ELECTRONIC, MAGNETIC AND OPTICAL PROPERTIES OF OXIDE SURFACES, HETEROSTRUCTURES AND INTERFACES: ROLE OF DEFECTS

LIU ZHIQI

(B. SC. Lanzhou University, CHINA)

A THESIS SUBMITTED

FOR THE DEGREE OF DOCTOR OF PHILOSOPHY IN SCIENCE

DEPARTMENT OF PHYSICS

NATIONAL UNIVERSITY OF SINGAPORE

2013

DECLARATION

I hereby declare that the thesis is my original work and it has been written by me in its entirety. I have duly acknowledged all the sources of information which have been used in the thesis.

This thesis has also not been submitted for any degree in any university previously.

_____

Liu Zhiqi

Acknowledgements

The PhD study in the past four years has been an extremely important stage in my life. During these four years, a lot of people have helped me to further my research and I am grateful to all of them. Especially, I would like to sincerely thank my supervisors Prof. Ariando and Prof. T. Venkatesan for educating and encouraging me. Prof. Ariando keeps me motivated in my research and persistently supports me without any reserve. It is well his infinite support that enables me to freely think and try in oxides research. However, what I have benefited from his education is far not only in academic research. Indeed, I have learned quite a lot about the attitude to life from frequent discussions with him which are not limited to research. Therefore, he is a supervisor in my research, and also a mentor in my life.

I always think that it is really my fortune to study under Prof. T. Venkatesan. He is so creative and enthusiastic in research. We have frequent discussions on academic research, even sometimes until midnight, and even sometime during weekends. During discussions, he can always come up with some amazing ideas which excite us a lot and I therefore enjoy discussions with him quite much. I had never seen a man like him who can easily connect the knowledge of different areas together as his brain is “a live library” of material science. It is well his creativity and enthusiasm that enlighten me to boldly and creatively

think in my own research. I will ever be indebted to Prof. Ariando and Prof. T. Venkatesan.

I would like to take this opportunity to thank Prof. J. M. D. Coey from Ireland, who has ever been a visiting professor in Nanocore for several months. He is an eminent material scientist. What impresses me is that he is so knowledgeable that he can explain many tough physical issues in material science by simple estimations based on fundamental physics. I would like to thank him for illuminating and fruitful discussions on my own studies.

Also, I would like to acknowledge Prof. Y. P. Feng in NUS and Prof. H. B. Su in NTU. They persistently support our studies with pertinent theoretical calculations, which make our work sound and convincing.

I would like to express my special gratitude to my senior Mr. Wang Xiao, who taught me various instruments in our lab when I first joined in Nanocore. That enables me to perform various experiments easily in my own research later. He is quite kind and discreet in conducting me on various experiments. Definitely, I would also like to thank Dr. W. M. Lü for teaching me significantly in various experimental processes and helping me a lot in my life during the past four years.

I would like to thank Dr. X. H. Huang, Dr. Z. Huang, Dr. K. Gopinadhan, Dr. S. Saha, Dr. M. Yang, Dr J. B. Yi and Dr X. P. Qiu for their consistent support in various experiments. Of course, there are a lot of talented lab mates who help me in my own studies from time to time. Hence I would also like to extend my gratitude to them, Mr. A. Annadi, Mr. S. W. Zeng, Mr. Y. L. Zhao,

Mr. J. Q. Chen, Mr. A. Srivastava, Mr. T. Tarapada, Mr. C. J. Li, and Dr. M. Motapothula.

I also warmly remember all the Internship and Final Year Project students who worked with me in Nanocore, the master student Ms. D. P. Leusink from University of Twente, Netherlands, the undergraduate student Ms. Y. T. Lin from NUS, the undergraduate students Ms. Poulami Das and Mr. Soumya Sarkar form NIT, India.

Finally, it would not have been possible for me to finish my PhD without invaluable love and patience from my *beloved* wife Ms. *Jing Wang*. Also, I thank my parents and my talented sister for their persistent support. It is their everlasting love and support that have been the source of confidence and strength in my research and life.

Table of Contents

Abstract

In this thesis, electrical and magnetotransport properties of reduced $SrTiO_3$ (STO) single crystals and $SrTiO_3$ thin films were investigated. In STO_{3-x} single crystals, the Fermi liquid exists; a magnetic-field induced resistivity minimum emerges due to the high mobility and the possible strengthening of the classical limit by mass enhancement of strong electron correlations; also, linear in-plane transverse MR was observed and attributed to the unusual quantum linear MR. In contrast, metal-insulator transition was observed in STO_{3-x} thin films. By comparing the electrical properties of STO_{3-x} single crystals and STO_{3-x} thin films, the distribution of oxygen vacancies in STO single crystals was found to be mostly on the surface. There is a large concentration gradient of oxygen vacancies from the STO single crystal surface to its interior, which leads to anisotropic 2D-like transport in reduced STO single crystals. In addition, high similarities between the carrier freeze-out observed in STO_{3-x} films and the spin glass state enable us to think the carrier freezing state as a kind of “charge glass” state.

Atomically flat interfaces between STO films and single-terminated $LaAlO_3$ (LAO) substrates were also achieved. The transport measurements displayed that this kind of interface is highly insulating. The reason for that could be the surface reconstruction of LAO single crystals or due to the interface epitaxial strain. Ultrathin STO_{3-x} films are insulating, which could be due to a large number of compensating defects. Besides, our work opens a way to achieve atomically flat film growth based on LAO substrates.

Furthermore, the quasi-2DEG (two-dimensional electron gas) could even also be tailored probably by means of vacuum reduction or Argon-ion milling after the realization of atomically flat nanoscale film growth on LAO substrates.

In addition, we studied the origin of the 2DEG at the LAO/STO interface a comprehensive comparison of (100)-oriented STO substrates with crystalline and amorphous overlayers of LAO of different thicknesses prepared under different oxygen pressures. By virtue of transport, optical, oxygen-annealing and Ar-milling studies, we conclusively found that oxygen vacancies account for the interface conductivity in amorphous LAO/STO heterostructures; both oxygen vacancies and electronic reconstruction contribute to the conductivity of crystalline LAO/STO heterostructures which have not been annealed in oxygen post deposition; the interface electronic reconstruction due to the potential build-up in LAO overlayers is ultimately responsible for the conductivity oxygen-annealed crystalline LAO/STO heterostructures. Moreover, our experiments demonstrate that the crystallinity of the LAO layer is crucial for the polarization catastrophe.

We also studied electrical and magnetic properties of Nb-doped $SrTiO_3$ (NSTO) single crystals. Reversible room-temperature ferromagnetism was observed in highly-doped ($\geq$ 0.5wt%) NSTO single crystals and found to be induced by oxygen vacancies and closely related to free carriers. We proposed the RKKY interaction to explain the ferromagnetism, where free electrons from Nb doping mediate the magnetic interaction among localized Ti 3*d* magnetic moments originating from oxygen vacancies. On the other hand, the use of this kind of substrate to search for novel ferromagnetism in oxide thin

films should be exercised with care due to the existence of ferromagnetism up to RT. Even though the ferromagnetic signal observed here is weak for a bulk single crystal, it is strong enough to mix up magnetic signals of thin films grown on it.

In this thesis, we have also studied the resistive switching of LAO films in metal/LAO/NSTO heterostructures and observed the electric-field-induced reversible MIT. The reversible MIT is ascribed to the population and depletion of quasi-conduction band (QCB) consisting of a wide range of defects states in LAO. The stable metallic state can be obtained only when the filling level of QCB inside the LAO aligns with the Fermi level of NSTO such that the wave functions of electrons inside the QCB and the conduction band of NSTO can overlap and interact with each other. The implications of this mechanism are far-reaching especially now the entire semiconductor industry is moving toward high$-k$ materials. For example, the use of multi-component oxides as insulators in devices, (*e.g.*, high-*k* dielectrics in silicon CMOS devices) must be exercised with caution because of the presence of multiple defect levels within their bandgap. Furthermore, we have demonstrated that the defect medicated quasi-conduction band model also applied to other large bandgap $RAlO_3$ (R = Pr, Nd, Y) oxide materials.

In this thesis, we have also studied the electronic and magnetic properties of $SrRuO_3/LaAlO_3$ (SRO/LAO) superlattices. By varying the thickness of SRO layers in the superlattices, we are able to modulate both electrical and magnetic properties of SRO films in SRO/LAO superlattices. For example, the ferromagnetic metal SRO can be tuned into a ferromagnetic insulator with a

much lower T_c of ~110 K as SRO layers are reduced to 2 uc in SRO/LAO superlattices. We have investigated the origin of the metal-insulator transition in ultrathin SRO films, which was found to be due to the interplay between dimensionality and dynamic spin scattering. Moreover, we have demonstrated field effect devices based on SRO/LAO superlattices, which reveals the possibility of realizing novel field effect devices based on multilayer structures.

Finally, we studied PL properties of $NdGaO_3$ (NGO) single crystals and thin films. The UV (~360 and ~390 nm) and blue emissions (~420 nm) were observed in both NGO single crystals and thin films. The PL emission of NGO is significantly enhanced at low temperatures and the high temperature activation energy is 35 meV. It was found that the crystallinity of NGO is essential for sharp emissions by virtue of Stark splitting. The observed UV and blue emissions can be understood based on the energy level diagram of the Nd^{3+} ion. Our observation is expected to open the path for NGO to be utilized as laser material or in photonic devices. In addition, the UV and blue emission in amorphous NGO films grown on commercial SiO_2/Si substrates is potential for large-scale photonic device applications.

List of Publications

(1) Physical Review X 3, 021010 (2013)

Z. Q. Liu, C. J. Li, W. M. Lü, X. H. Huang, Z. Huang, S. W. Zeng, X. P. Qiu, L. S. Huang, A. Annadi, J. S. Chen, J. M. D. Coey, T. Venkatesan, and Ariando

"*Origin of the two-dimensional electron gas at $LaAlO_3/SrTiO_3$ interfaces: The role of oxygen vacancies and electronic reconstruction*"

http://prx.aps.org/abstract/PRX/v3/i2/e021010

(2) Physical Review Letters 107, 146802 (2011)

Z. Q. Liu, D. P. Leusink, X. Wang, W. M. Lü, K. Gopinadhan, A. Annadi, Y. L. Zhao, X. H. Huang, S. W. Zeng, Z. Huang, A. Srivastava, S. Dhar, T. Venkatesan, and Ariando

"*Metal-insulator transition in $SrTiO_{3-x}$ thin films induced by frozen-out carriers*"

http://prl.aps.org/abstract/PRL/v107/i14/e146802

(3) Physical Review B: Rapid Communications 87, 220405(R) (2013)

Z. Q. Liu, W. M. Lü, S. L. Lim, X. P. Qiu, N. N. Bao, M. Motapothula, J. B. Yi, M. Yang, S. Dhar, T. Venkatesan, and Ariando

"*Reversible room temperature ferromagnetism in Nb-doped $SrTiO_3$ single crystals*"

http://prb.aps.org/abstract/PRB/v87/i22/e220405

(4) Physical Review B 84, 165106 (2011)

Z. Q. Liu, D. P. Leusink, W. M. Lü, X. Wang, X. P. Yang, K. Gopinadhan, Y. T. Lin, A. Annadi, Y. L. Zhao, A. Roy Barman, S. Dhar, Y. P. Feng, H. B. Su, G. Xiong, T. Venkatesan, and Ariando

"*Reversible metal-insulator transition in $LaAlO_3$ films mediated by intragap defects: an alternative mechanism for resistive switching*"

http://prb.aps.org/abstract/PRB/v84/i16/e165106

(5) Physical Review B 85, 155114 (2012)

Z. Q. Liu, W. M. Lü, X. Wang, Z. Huang, A. Annadi, S. W. Zeng, T. Venkatesan, and Ariando

"*Magnetic-field induced resistivity minimum with in-plane linear magnetoresistance of the Fermi liquid in $SrTiO_{3-x}$ single crystals*"

http://prb.aps.org/abstract/PRB/v85/i15/e155114

(6) AIP Advances 2, 012147 (2012)

Z. Q. Liu, Z. Huang, W. M. Lü, K. Gopinadhan, X. Wang, A. Annadi, T. Venkatesan, and Ariando.

"*Atomically flat interface between a single-terminated $LaAlO_3$ substrate and $SrTiO_3$ thin film is insulating*" (*Research Highlight in AIP Advances: Flipping a film*)

http://aipadvances.aip.org/resource/1/aaidbi/v2/i1/p012147_s1

(7) Applied Physics Letters 101, 223105 (2012)

Z. Q. Liu, Y. Ming, W. M. Lü, X. Wang, B. M. Zhang, Z. Huang, K. Gopinadhan, S. W. Zeng, A. Annadi, Y. P. Feng, T. Venkatesan, and Ariando

"*Tailoring the electronic properties of $SrRuO_3$ films in $SrRuO_3$/$LaAlO_3$ superlattices*"

http://apl.aip.org/resource/1/applab/v101/i22/p223105_s1?isAuthorized=no

(8) Nature Communications 2, 188 (2011)

Ariando, X. Wang, G. Baskaran, Z. Q. Liu, J. Huijben, J.B. Yi, A. Annadi, A. Roy Barman, A. Rusydi, S. Dhar, Y.P. Feng, J. Ding, H. Hilgenkamp, and T. Venkatesan

"*Electronic phase separation at the $LaAlO_3$/$SrTiO_3$ interface*"

http://www.nature.com/ncomms/journal/v2/n2/full/ncomms1192.html

(9) Nature Communications 4, 1838 (2013)

A. Annadi, Q. Zhang, X. Wang, N. Tuzla, K. Gopinadhan, W. M. Lü, A. Roy Barman, Z. Q. Liu, A. Srivastava, S.Saha, Y.L. Zhao, S.W. Zeng, S. Dhar, E. Olsson, B. Gu, S. Yunoki, S. Maekawa, H. Hilgenkamp, T. Venkatesan, and Ariando

"*Anisotropic two dimensional electron gas at the $LaAlO_3/SrTiO_3$ (110) interface*"

http://www.nature.com/ncomms/journal/v4/n5/full/ncomms2804.html

(10) Applied Physics Letters 99, 172103 (2011)

W. M. Lü, X. Wang, Z. Q. Liu, S. Dhar, A. Annadi, K. Gopinadhan, A. Roy Barman, H. B. Su, T. Venkatesan, and Ariando

"*Metal-insulator transition at a depleted $LaAlO_3/SrTiO_3$ interface: evidence for charge transfer induced by $SrTiO_3$ phase transitions*"

http://apl.aip.org/resource/1/applab/v99/i17/p172103_s1?isAuthorized=no

(11) Physical Review B 86, 085450 (2012)

A. Annadi, A. Putra, Z. Q. Liu, X. Wang, K. Gopinadhan, Z. Huang, S. Dhar, T. Venkatesan, and Ariando

"*Electronic correlation and strain effects at the interfaces between polar and nonpolar complex oxides*"

http://prb.aps.org/abstract/PRB/v86/i8/e085450

(12) Physical Review B 84, 075312 (2011)

X. Wang, W.M. Lü, A. Annadi, Z. Q. Liu, S. Dhar, K. Gopinadhan, T. Venkatesan, and Ariando

"*Magnetoresistance of 2D and 3D electron gas in $LaAlO_3/SrTiO_3$ Heterostructures: influence of magnetic ordering, interface scattering and dimensionality*"

http://prb.aps.org/abstract/PRB/v84/i7/e075312

(13) Physical Review B 87, 201102(R) (2013)

A. Annadi, Z. Huang, K. Gopinadhan, X. Renshaw Wang, A. Srivastava, Z. Q. Liu, H. Ma, T. Sarkar, T. Venkatesan and Ariando

"*Anisotropic magnetoresistance and planar Hall effect at $LaAlO_3/SrTiO_3$ heterointerfaces: Effect of carrier confinement on magnetic interactions*"

http://prb.aps.org/abstract/PRB/v87/i20/e201102

(14) Physical Review B 86, 045124 (2012)

S. W. Zeng, X. Wang, W. M. Lü, Z. Huang, M. Motapothula, Z. Q. Liu, Y. L. Zhao, A. Annadi, S. Dhar, H. Mao, W. Chen, T. Venkatesan, and Ariando

"*Metallic state in La-doped $YBa_2Cu_3O_7$ thin films with n-type charge carriers*."

http://prb.aps.org/abstract/PRB/v86/i4/e045124

(15) AIP Advances 2, 012129 (2012)

Y. L. Zhao, W. M. Lü, Z. Q. Liu, S. W. Zeng, M. Motapothula, S. Dhar, Ariando, Q. Wang, and T. Venkatesan

"*Variable-range hopping in TiO_2 insulating layers for oxide electronic devices*"

http://aipadvances.aip.org/resource/1/aaidbi/v2/i1/p012129_s1

(16) Applied Physics Letters 100, 241907 (2012)

Amar Srivastava, T.S. Herng, Surajit Saha, Bao Nina, A. Annadi, N. Naomi, Z.Q. Liu, S. Dhar, Ariando, J. Ding, and T. Venkatesan

"*Coherently coupled ZnO and VO_2 interface studied by photoluminescence and electrical transport across a phase transition*"

http://apl.aip.org/resource/1/applab/v100/i24/p241907_s1?isAuthorized=no&ver=pdfcov

(17) Applied Physics Letters 100, 241907 (2012)

Y. L. Zhao, M. Motapothula, N. L. Yakovlev, Z. Q. Liu, S. Dhar, A. Rusydi, Ariando, M. B. H. Breese, Q. Wang, and T. Venkatesan

"*Reversible ferromagnetism in rutile TiO_2 single crystals induced by nickel impurities*"

http://apl.aip.org/resource/1/applab/v101/i14/p142105_s1?isAuthorized=no

(18) Applied Physics Letters 101, 231604 (2012)

A. Annadi, A. Putra, A. Srivastava, X. Wang, Z. Huang, Z. Q. Liu, T. Venkatesan, and Ariando

"*Evolution of variable range hopping in strongly localized two dimensional electron gas at $NdAlO_3/SrTiO_3$ (100) heterointerfaces*"

http://apl.aip.org/resource/1/applab/v101/i23/p231604_s1?isAuthorized=no

(19) Superconductor Science and Technology 25, 124003 (2012)

S. W. Zeng, Z. Huang, X. Wang, W. M. Lü, Z. Q. Liu, B. M. Zhang, S. Dhar, T. Venkatesan, and Ariando

"*The influence of La substitution and oxygen reduction in ambipolar La-doped $YBa_2Cu_3O_y$ thin films*"

http://iopscience.iop.org/0953-2048/25/12/124003/

(20) Physical Review B: Rapid Communications 88, 161107(R) (2013)

Z. Huang, X. Renshaw, Wang, Z. Q. Liu, W. M. Lü, S. W. Zeng, A. Annadi, W. L. Tan, X. P. Qiu, Y. L. Zhao, M. Salluzo, J. M. D. Coey, T. Venkatesan, and Ariando

"*Conducting channel at the $LaAlO_3/SrTiO_3$ interface*"

http://prb.aps.org/abstract/PRB/v88/i16/e161107

List of Awards

(1) "**FIAP Outstanding Student Papers"** awarded by **American Physical Society (APS)**, March 2011, USA.

For the paper "*Nonlinear Insulator in Complex Oxides*"

(2) "Best Poster Award" awarded by **IEEE Magnetics Society**, October, 2011, Singapore.

For the poster "*Giant magnetic exchange interaction between epitaxial LSMO and a two dimensional electron gas at the LAO/STO interface*".

(3) "Best Poster Award" awarded by **Materials Research Society (MRS)**, March, 2012, Singapore.

For the poster "*Metal-insulator transition of $SrTiO_{3-x}$ films and highly anisotropic Fermi liquid in $SrTiO_{3-x}$ single crystals*".

(4) "President's Graduate Fellowship" awarded by **National University of Singapore,** June 2012, Singapore.

The President's Graduate Fellowship (PGF) is awarded to candidates who show exceptional promise or accomplishment in research.

(5) "Best Graduate Researcher Award" awarded by **Faculty of Science, National University of Singapore**, August 2012, Singapore.

(6) "Best Presentation Award" awarded by **Department of Physics, National University of Singapore**, August 2012, Singapore.

(7) "**CHINESE GOVERNMENT AWARD FOR OUTSTANDING SELF-FINANCED STUDENTS ABROAD**", awarded by **China Scholarship Council,** May 2013.

List of Tables

List of Figures

List of Symbols

ϵ_r	Relative Dielectric Constant	f_2	Finite Width Correction Factor
a	Lattice constant	R_s	Sheet Resistance
T_c	Curie Temperature	V_H	Hall Voltage
λ	Wavelength	n	Carrier density
k	Boltzman Constant	e	Elementary Charge
R_e	Equilibrium Deposition Rate	B	Magnetic Field
D_m	Supersaturation	R_H	Hall Coefficient
T	Temperature	μ	Mobility
k	Wave Vector	F	Lorentz Force
G	Reciprocal Lattice Vector	v	Speed
d	Lattice Plane Spacing	ω	Cyclotron Frequency
$\bar{d}$	Average Lattice Constant	$\hbar$	Reduced Planck Constant
Λ	Artificial Lattice Constant	τ	Relaxation Time
R	Resistance	E_n	Quantized Energy
ρ	Resistivity	E_F	Fermi Energy
t	Thickness	m_c	Cyclotron Mass
l	Length	m	Magnetic Moment
V	Voltage	T_N	Neel Temperature
I	Current	T_f	Spin Freezing Temperature
s	Area	E_p	Photo Energy
f_1	Thickness Correction Factor	E_g	Bandgap Energy

$n(\lambda)$	Refractive Index	ϵ	Activation Energy
m_D	Density-of-states Effective Mass	n_s	Sheet Carrier Density
n_c	Critical Carrier Density	σ_s	Sheet Conductance
a^*	Effective Bohr Radius	ϵ_0	Vacuum Dielectric Constant
m_0	Electron rest mass	H	Magnetic Field
T_{min}	Resistivity Minimum Temperature	M	Magnetization
E_B	Binding Energy	V_G	Gate Voltage
μ_B	Bohr Magneton	E_a	Activation Energy of PL emission

Chapter 1 Introduction

Oxide materials exhibit luxuriously abundant and exotic physical properties such as high temperature superconductivity [1,2], metal-insulator transition [3,4], colossal magnetoresistance [5,6], electronic phase separation [7–9], resistive switching [10–12], ferroelectricity [13] and multiferroicity [14]. They have broad applications in both large scale (such as the maglev train system, electricity grids, and high magnetic field generators) and various microscopic electronic devices (such as CMOS, optoelectronic, and memory devices), as well as chemical catalysis, lithium-batteries and solar energy conversion.

In the last decade, the resistive switching and interface physics in oxide heterostructures have been the research spotlights in the community of oxide electronics. In practice, rapid advances in information technology rely on high-speed and large-capacity nonvolatile memories and resistive switching in oxides is potential for the new generation of flash memory devices – resistance random access memory (ReRAM) with advantages of low power cost, fast write (of ~ns [15]) and read access. As the conventional memory unit scaling is expected to approach the technical and physical limits, ReRAM devices capable of multi-state storage become remarkably important.

Nevertheless, the gold rush in oxide heterostructures has been significantly stirred by novel functionalities created at interfaces [16]. Take several model systems for examples: a metallic two-dimensional electron gas at the interface between the two band insulators $SrTiO_3$ and $LaAlO_3$ [17], originating from the interface electronic reconstruction [18], shows superconductivity [19], the Kondo effect [20] and electronic phase separation [9]; ferroelectricity emerges in $SrTiO_3$ thin films grown on $DyScO_3$ substrates own to interface strain [21]; the bulk polarization of $BiFeO_3$ is modulated by interface coupling in $BiFeO_3/La_{0.7}Sr_{0.3}MnO_3$ heterostructures [22]; and a magnetic proximity effect shows up in $YBa_2Cu_3O_7/La_{0.7}Ca_{0.3}MnO_3$ superlattices [23].

Now looking back upon my own studies in the past four years, they also mainly fall into the above two areas, *i.e.*, resistive switching and oxide heterostructure interface physics. More interestingly, all my studies are, to some extent, all related to defects in oxide and oxide heterostructure. Basically, a defect in oxide materials is a break in the periodicity of a crystalline lattice. It extensively exists in crystalline materials in different terms such as point defects including vacancies, interstitial atoms, off-center ions, antisite defects and topological defects, line defects (*e.g.*, dislocations), planar defects including grain boundaries and stacking faults, and even bulk defects (voids or impurity clusters). Most of complex oxides have predominantly ionic bonds and prone to a variety of cationic and anionic point defects energetically favorable in such materials. Point defects could significantly affect the electronic, magnetic, optical and mechanical properties of materials.

However, the interface defect issue induced by combining different oxides together in oxide heterostructures is much more complicated. Generally such issue can be classified into the following categories: (i) the substrate surface roughness could result in island formation during thin film growth and loss of conducting percolation [24]; (ii) thermal interdiffusion may lead to interface atoms intermixing and even the formation of solid solutions; (iii) interfacial strain arising from mismatch in lattice constants may induce thermodynamic defects during high temperature growth in oxide thin films; (iv) structure reconstruction may occur due to electrostatic incongruity [25]; (v) charge depletion or accumulation can be driven at interfaces by the chemical potential difference of distinct oxide materials; (vi) polar discontinuity at the interface between a polar and a nonpolar oxide could stir up interface defects such as precipitates [26] and dislocations [27]; (vii) the optimized oxygen pressure during deposition could be largely different for various oxide materials, making some materials incompatible.

One point worth underlining is that not all defects in oxides are detrimental for applications. Instead, they have their own specific roles in determining the electronic, magnetic and optical properties of oxides and oxide heterostructures. For a simplest example, chemical doping could create high temperature superconductivity and colossal magnetoresistance.

This PhD thesis involves diverse research topics related to oxides and oxide heterostructures. What is common in all of my research topics is pulsed laser deposition, which was intensively used to fabricate oxide thin films and oxide interfaces. Various characterization techniques were also utilized to

explore the structural, electrical, magnetic and optical properties of the samples. As the research topics covered by this thesis are loosely interconnected, I therefore organize the main body of thesis into a research topic-based pattern and divide different research topics into separate chapters.

In this introduction chapter, a preview of what I have done in terms of different research topics will be presented, followed by the introduction to different oxide materials involved in this research.

1.1 Research Contents

1.1.1 Oxygen vacancy-mediated transport in $SrTiO_3$

Since the discovery of the two-dimensional electron gas at the interface between two band insulators $SrTiO_3$ and $LaAlO_3$ in 2004 [17], the role of oxygen vacancies in electrical properties of $SrTiO_3$ has again attracted a significant attention as it is of great importantance in various novel properties of the newly developed two-dimensional electron system. For this reason, we studied the effect of oxygen vacancies on the transport properties of $SrTiO_3$.

Oxygen vacancies are a kind of doping and they can convert an insulating $SrTiO_3$ into a metal. The mobile carriers have a high mobility due to the giant dielectric constant of $SrTiO_3$ at low temperatures and the resulting dielectric screening of ionic scattering potential. Consequently, a magnetic field-induced resistivity minimum can be seen at low temperatures. However, oxygen vacancies serve as doubly charge donor centers, the activation energy of which could be up to several ten meV. Therefore, the carrier freeze-out effect can

occur in oxygen deficient $SrTiO_3$, which induces a metal-insulator transition in $SrTiO_{3-x}$ films. The low temperature frozen state in $SrTiO_{3-x}$ thin films can be re-excited by electric field, Joule heating and magnetic field, which has been coined as a “charge glass”.

By comparing the electrical properties of reduced $SrTiO_3$ thin films with single crystals, it was found that oxygen vacancies in $SrTiO_3$ single crystals obtained by finite-time reduction are far from uniform due to the small diffusion constant of oxygen vacancies in $SrTiO_3$. Instead, there is a strong concentration gradient of oxygen vacancies from its surface to interior. As a result, highly anisotropic magnetotransport behavior as well as an inhomogeneity-induced quantum linear magnetoresistance is present in reduced $SrTiO_3$ single crystals. Overall, free electrons originating from oxygen vacancies in $SrTiO_3$ single crystals behave in a quasi-2D fashion on the $SrTiO_3$ surface region due to the confinement by inhomogeneity.

In addition, we succeeded in layer-by-layer growing ultrathin $SrTiO_3$ films (4-10 nm) on atomically flat $LaAlO_3$ substrates. Unlike the conducting heterostructures consisting of epitaxial $LaAlO_3$ films and $SrTiO_3$ substrates, such a heterostructure consisting of a $SrTiO_3$ thin film and a $LaAlO_3$ substrate is highly insulating. The reason was attributed to the surface reconstruction of $LaAlO_3$ single crystals and also possibly the interfacial strain. Metallicity is absent in ultrathin $SrTiO_{3-x}$ films obtained by vacuum reduction, which indicates that compensating defects such as Sr and Ti vacancies are dominant in thermally reduced ultrathin $SrTiO_{3-x}$ films.

The above results can shed light on the origin of the two-dimensional electron gas at the interface between $SrTiO_3$ and $LaAlO_3$. For example, the insulating interface between a $SrTiO_3$ film and a $LaAlO_3$ single crystal reveals that the intermixing of Sr/La and Ti/Al is not responsible for the conductivity in conducting crystalline $LaAlO_3/SrTiO_3$ heterostructures. Moreover, such studies provide a fundamental basis for exploring the origin of the two-dimensional electron gas at the $LaAlO_3/SrTiO_3$ interface. For instance, the carrier freeze-out effect observed in $SrTiO_{3-x}$ films is also present in unannealed crystalline $LaAlO_3/SrTiO_3$ heterostructures, which suggests that oxygen vacancies exist in $SrTiO_3$ substrates.

1.1.2 Origin of the two-dimensional electron gas at the $LaAlO_3/SrTiO_3$ interface – the role of oxygen vacancies and electronic reconstruction

Despite of a substantial body of novel properties unveiled by many research groups for the two-dimensional electron gas at the interface between $SrTiO_3$ and $LaAlO_3$, such as the electronically coupled complementary interfaces [28], the metal-insulator transition as the thickness of $LaAlO_3$ layer decreases to below 4 unit cells [29], the magnetic Kondo scattering at the interface [20], the low temperate two-dimensional superconductivity [19], the electric-field tunable ground state [30], the electronic phase separation [9], the coexistence of superconductivity and ferromagnetism [31–33], the large gate capacitance enhancement due to strong electron correlation [34], and the feasibility of integration with Si [35], its origin is still unclear.

Generally three different mechanisms have been proposed [36]. First is interface electronic reconstruction to avoid the polar catastrophe induced by the discontinuity at the interface between polar $LaAlO_3$ and nonpolar $SrTiO_3$ [18,37,38]. Second is doping by thermal interdiffusion of Ti/Al or La/Sr atoms at the interface [39]; A third possible mechanism is creation of oxygen vacancies in $SrTiO_3$ substrates during the deposition process [40–43]. Oxygen vacancies are known to introduce a shallow intragap donor level close to the conduction band of $SrTiO_3$ [44], and their action may be specific to this one substrate. The thermal interdiffusion mechanism was discounted in recent work [45], which studied the effect of a mixed interface layer. It is also in conflict with the experimental results that *p*-type $LaAlO_3/SrTiO_3$ interfaces [17] and interfaces created by growing $SrTiO_3$ films on $LaAlO_3$ [46] are insulating.

Metallic interfaces with similar electronic properties produced by amorphous oxide overlayers [47,48] on $SrTiO_3$ have further called in question the original polarization catastrophe model. We resolve the issue by a comprehensive comparison of (100)-oriented $SrTiO_3$ substrates with crystalline and amorphous overlayers of $LaAlO_3$ of different thicknesses prepared under different oxygen pressures, using photoluminescence to monitor the oxygen vacancy concentration created at the interface. For both types of overlayer, there is a critical thickness for the appearance of conductivity, but its value is always 4 unit cells (~1.6 nm) for the oxygen-annealed crystalline case, whereas in the amorphous case the critical thickness could be varied in the range 0.5 to 6 nm depending on the deposition

conditions. Subsequent ion milling of the overlayer restored the insulating state for the oxygen-annealed crystalline heterostructures but not for the amorphous ones. Oxygen post-annealing removes the vacancies, and the interfaces become insulating in the amorphous case, but the interfaces with a crystalline overlayer remain conducting but with a reduced carrier density.

Our data clearly demonstrate that oxygen vacancies are the dominant source of mobile carriers when the $LaAlO_3$ overlayer is amorphous, while both oxygen vacancies and polarization catastrophe contribute to the interface conductivity in unannealed crystalline LAO/STO heterostructures, and the polarization catastrophe alone accounts for the conductivity in oxygen-annealed crystalline LAO/STO heterostructures. Furthermore, it was found that the crystallinity of the LAO layer is crucial for the polarization catastrophe mechanism in the case of crystalline LAO overlayers.

1.1.3 Transport properties and defect-mediated ferromagnetism in Nb-doped $SrTiO_3$

Nb is a hydrogenic-type donor to $SrTiO_3$, which has inappreciable activation energy (~0.8 meV) due to the large dielectric constant of STO. The free electrons originating from Nb doping have high mobility due to the giant dielectric constant of $SrTiO_3$ at low temperatures and the resulting dielectric screening of ionic scattering potential. Consequently, a magnetic field-induced resistivity minimum can be observed in high mobility Nb-doped single crystals.

In addition, the search for oxide-based room-temperature ferromagnetism has been one of the holy grails in condensed matter physics. We observed room-temperature ferromagnetism in Nb-doped $SrTiO_3$ single crystals. The ferromagnetism can be eliminated by air annealing and can be recovered by subsequent vacuum annealing. The x-ray photoemission spectroscopy, the static time-of-flight and also the dynamic secondary ion mass spectroscopy measurements were performed to examine any possible magnetic impurities, but no impurity was seen. The temperature dependence of magnetic moment resembles the temperature dependence of carrier density, suggesting an intrinsic origin of the ferromagnetism – carrier-mediated Ruderman-Kittel-Kasuya-Yosida (RKKY) interaction, where free electrons from Nb doping mediate the magnetic interaction among the localized Ti 3*d* magnetic moments originating from oxygen vacancies.

Our experimental observation demonstrates an interesting system where defects together with carriers play important roles in room temperature ferromagnetism. Moreover, the use of this kind of single crystals as substrates to search for novel ferromagnetism in oxide thin films should be exercised with care due to the existence of ferromagnetism up to room temperature, which is strong enough to mix up the magnetic signals of thin films grown on them.

1.1.4 Resistive switching mediated by intragap defects

The insulating state is one of the most basic electronic phases in condensed matter. This state is characterized by an energy gap for electronic excitations

that makes an insulator electrically inert at low energy. However, for complex oxides, the concept of an insulator must be re-examined. Complex oxides behave differently from conventional insulators such as SiO_2, on which the entire semiconductor industry is based, because of the presence of multiple defect levels within their bandgap. As the semiconductor industry is moving to such oxides for high-dielectric (high-*k*) materials, we need to truly understand the insulating properties of these oxides under various electric field excitations.

In this part we demonstrate that the insulating properties of an insulator can be significantly changed due to its intragap defects by investigating the resistive switching properties of insulating $RAlO_3$ (R = La, Pr, Nd, Y) thin films in metal/$RAlO_3$/Nb-$SrTiO_3$ heterostructures. Resistive switching is a phenomenon occurring in metal/insulator/metal sandwich structures, where the resistance of such sandwich structures changes upon the excitation of current or voltage pulses. Reproducible and reversible transitions were observed between a low-resistance metallic state and a high-resistance non-metallic state when applying suitable voltages in metal/$RAlO_3$/Nb-$SrTiO_3$ heterostructures. The possibility of diffusion of the metal electrodes or oxygen vacancies into the $RAlO_3$ layer was excluded by low temperature measurements. Instead, the phenomenon is attributed to the formation of a quasi-conduction band in the defect states of $RAlO_3$ that forms a continuum state with the conduction band of the Nb-$SrTiO_3$. Once this continuum (metallic) state is formed, the state remains stable even when the voltage bias is turned off. An opposing voltage is required to deplete the charges from the defect states. The thickness dependent switch-on voltage and the constant

switch-off voltage strongly support our model. This model can provide an alternative mechanism for resistive switching in complex oxides. In addition, our ability to manipulate and control these defect states of complex oxides will open up a new path to develop novel devices.

1.1.5 Tailoring the electronic and magnetic properties of $SrRuO_3$ film in superlattices

Metallic oxides are essential to oxide electronic devices typically as electrodes and templates for integration of other oxide materials. $SrRuO_3$ is a conducting ferromagnetic oxide, which has been extensively utilized as a ferromagnetic metal in oxide Josephson junctions, ferromagnetic electrodes in magnetic tunnel junctions, and normal metal electrodes in resistive switching devices. Generally, technological scaling of electronic devices stresses the need of using such metallic oxides in terms of thin films. However, an important issue on using ultrathin films of metallic oxides is the substantially increased resistivity, which is clearly existent in SRO thin films.

The electronic and magnetic properties of $SrRuO_3/LaAlO_3$ superlatties with different thicknesses of $SrRuO_3$ layers were studied. As the thickness of $SrRuO_3$ layers in superlattices is reduced, $SrRuO_3$ films gradually transform into a more localized state from its original bulk metallic state, *i.e.*, from a bad metal to weak localization, then to metal-insulator transition and finally to strong localization. The critical thickness for a completely insulating state is two unit cells. The strain effect on the metal-insulator transition was also investigated by a serial of superlattices fabricated on different substrates. It

was found that although strain can obviously affect the resistance of superlattices, it does not change the evolution of electronic properties of $SrRuO_3/LaAlO_3$ superlatties with thickness.

To explore the origin of the metal-insulator transition in ultrathin $SrRuO_3$ films, first-principle density-functional calculations were performed. We found that although the density of states of $SrRuO_3$ at Fermi energy decreases with reduced thickness, it does not reach zero even as the $SrRuO_3$ thickness is reduced to one unit cell. We therefore concluded that the metal-insulator transition in ultrathin $SrRuO_3$ films is due to the interplay between dimensionality and dynamic spin scatterings which cannot be included in theoretical calculations.

All the superlattices, even those with $SrRuO_3$ layers as thin as two unit cells, are clearly ferromagnetic at low temperatures. Both the Curie temperature and ferromagnetic moment decrease with reducing thickness of $SrRuO_3$ layers and reach ~110 K and 0.15 μ_B/Ru, respectively, in superlattices with two unit cell $SrRuO_3$ layers. Moreover, we demonstrate field effect devices based on such multilayer superlattice structures, which reveals the possibility of realizing novel field effect devices based on multilayer structures.

1.1.6 Ultraviolet and blue emission in $NdGaO_3$

Ultraviolet emission and blue emission are of significant interest for applications in electroluminescence devices. Room temperature ultraviolet emissions (360 and 388 nm) and blue emission (420 nm) were observed in $NdGaO_3$ single crystals. The light emission increases significantly at low

temperatures and consequently blue emission is visible at low temperatures. Similar ultraviolet and blue emissions were achieved in polycrystalline $NdGaO_3$ thin films grown on Al_2O_3 and MgO substrates by pulsed laser deposition. Such emissions were also realized in single crystalline $NdGaO_3$ thin films depositing on $(LaAlO_3)_{0.3}(Sr_2AlTaO_6)_{0.7}$ and Nb-$SrTiO_3$-buffered $LaAlO_3$ substrates. Furthermore, ultraviolet and blue emissions were even obtained in amorphous $NdGaO_3$ thin films deposited on commercial SiO_2/Si substrates, which can lay the foundation for cheap and large-scale photonic device applications of $NdGaO_3$ such as oxide-based short wavelength photonic devices for high resolution full color displays.

1.2 Perovskite oxide materials

1.2.1 $SrTiO_3$

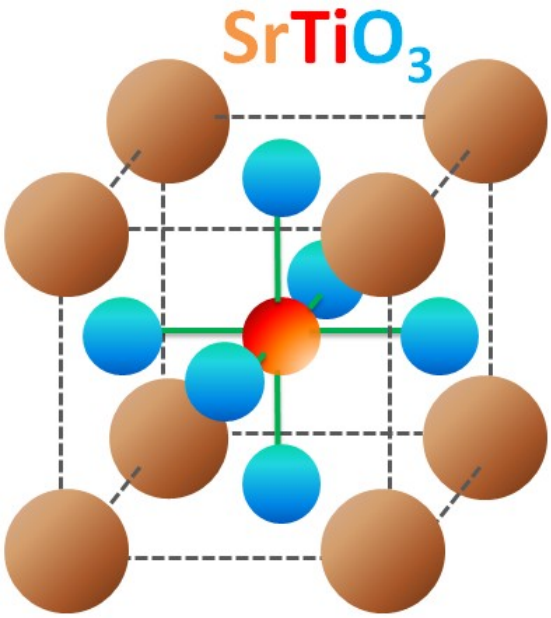

Figure 1.1. Schematic of the $SrTiO_3$ crystal structure.

$SrTiO_3$ is a cubic perovskite with a lattice constant of 3.905 Å, in which Ti is centered in the octahedron surrounded by six oxygen atoms as schematized in Fig. 1.1. At 105 K, it undergoes a structural phase transition into a tetragonal phase. It is chemically stable. The melting point of $SrTiO_3$ is high up to 2080 °C and hence it is also thermally stable. It is a band insulator with an indirect bandgap of 3.25 eV and a direct bandgap of 3.75 eV [49]. A remarkable property of $SrTiO_3$ is its large dielectric constant (ϵ_r = 300 at room temperature and > 20000 below 4 K) [50]. It is therefore extensively utilized as gate material in oxide transistor devices. Stoichiometric $SrTiO_3$ is diamagnetic as a result of the absence of unpaired electrons. Moreover, owing to its large bandgap, it is transparent to visible light. The refractive index of $SrTiO_3$ is strongly dispersive, which changes from 2.5 at 400 nm to 2.1 at 1500 nm [51].

The surface termination of $SrTiO_3$ single crystals can be controlled by chemical treatments [52]. For instance, TiO_2-terminated surface can be achieved by buffered HF-etching followed by thermal annealing. Hence $SrTiO_3$ single crystals are extensively used as substrates for engineering oxide electronics by atomic control.

1.2.2 $LaAlO_3$

$LaAlO_3$ is a rhombohedral perovskite with the lattice constant a = 5.357 Å and α = 60.1°. However, it has a pseudocubic structure with a lattice constant a = 3.79 Å. Above 435 °C, it is cubic with a = 3.82 Å. $LaAlO_3$ is chemically and thermally stable with a melting point of 2110 °C. It has a large bandgap of 5.6

eV and transparent to visible light. $LaAlO_3$ has a room temperature dielectric constant of 24 and remarkably small dielectric loss tangents tanδ of 5×10^{-6} at 8.6 GHz and 77 K [53]. Therefore, it is of high interest in high-*k* material studies and low loss microwave and dielectric resonance applications. Moreover, it is an excellent substrate for epitaxial growth of various perovskite oxide thin films.

Macroscopic twins are present in $LaAlO_3$ single crystals during cooling down after crystal growth due to the structural phase transition at 435 °C and twin lines are visible on the surface. However, atomically flat surface with uniform single-terminated steps can be achieved within twins by annealing [46] or chemical treatment [54].

1.2.3 $SrRuO_3$

$SrRuO_3$ has an orthorhombic structure with lattice constants a = 5.53 Å, b = 5.57 Å and c = 7.85 Å, and a slightly distorted pseudocubic unit cell of a = 3.93 Å. It undergoes a structural phase transition at 820 K and becomes tetragonal. Another structural phase transition into a cubic phase occurs at 920 K. The melting point of $SrRuO_3$ is high up to 2300 °C [55]. It is an itinerant ferromagnetic metal with a bulk Curie temperature T_c of ~160 K. Its room temperature resistivity is ~280 μΩ·cm and therefore $SrRuO_3$ is broadly used as electrode material in various oxide electronic devices.

1.2.4 $NdGaO_3$

$NdGaO_3$ is an orthorhombic perovskite with lattice constants a = 5.43 Å, b = 5.50 Å and c = 7.71 Å, and a pseudocubic unit cell of a = 3.87 Å. The crystal structure of $NdGaO_3$ is stable in a wide temperature range. Its melting point is 1600 °C. $NdGaO_3$ has a large bandgap of 3.8 eV [56] and the room temperature dielectric constant is 25. It is a widely used substrate for high-temperature superconductor and various perovskite oxide thin film depositions. $NdGaO_3$ is a strong paramagnet, which undergoes a magnetic phase transition into an antiferromagnetic phase at ~1 K [57]. Despite of its large bandgap, $NdGaO_3$ has selective absorption to visible light due to abundant energy levels of the rare earth element Nd. The transimittance spectrum of a (110)-oriented $NdGaO_3$ single crystal is shown in Fig. 1.2. The refractive index of $NdGaO_3$ is ~2.13 [58].

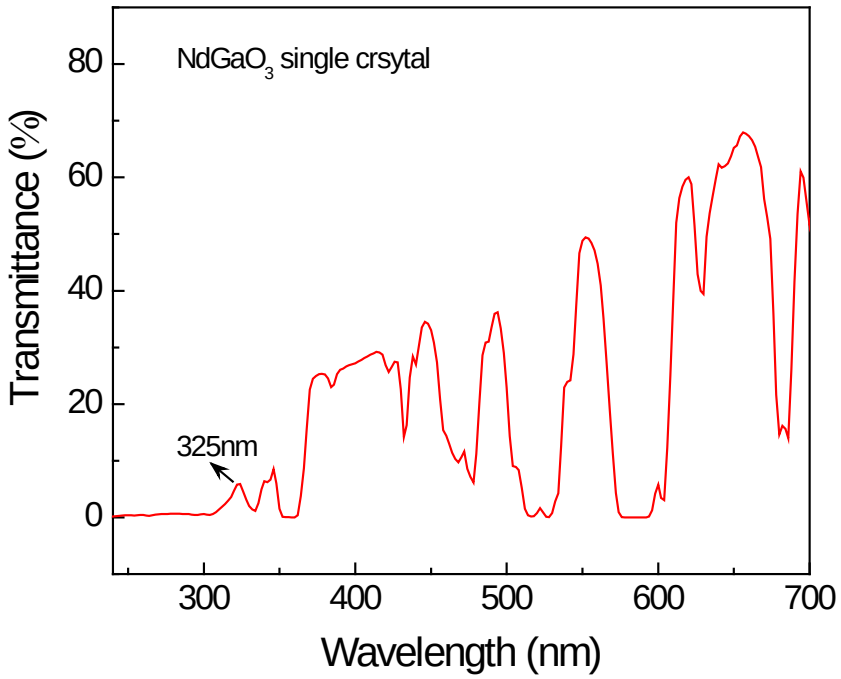

Figure 1.2. Room temperature transmittance spectrum of a (110)-oriented $NdGaO_3$ single crystal.

1.2.5 $DyScO_3$

$DyScO_3$ has an orthorhombic perovskite structure with lattice constants a = 5.43 Å, b = 5.50 Å and c = 7.71 Å, and a pseudocubic unit cell of a = 3.94 Å. The crystal structure of $DyScO_3$ is stable and no structural phase transition is present up to 1200 °C [59]. The melting point of $DyScO_3$ crystal is ~2100 °C. $DyScO_3$ has a large bandgap of 5.7 eV and a room temperature dielectric constant of 21. $DyScO_3$ is a strong magnet and has intriguing magnetic anisotropy at low temperatures below 4 K. Along the [1-10] direction (refer to Fig. 2.39), it shows spin glass behavior. But along the [100] direction, $DyScO_3$ exhibits a sharp antiferromagnetic transition at 4.5 K as shown below in Fig. 1.3.

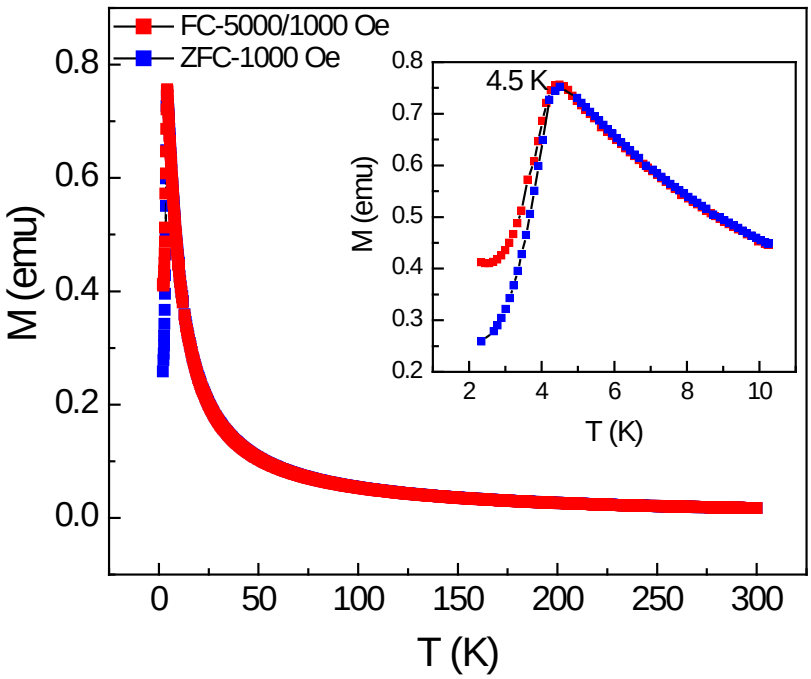

Figure 1.3. Magnetic moment of a (110)-oriented $DyScO_3$ single crystal along the in-plane [100] direction measured in different procedures, *i.e.*, field cooling (FC) with a 5000 Oe field and measured by a 1000 Oe, and zero-field cooling (ZFC) with a 1000 Oe measurement field. Inset: magnetic data below 10 K.

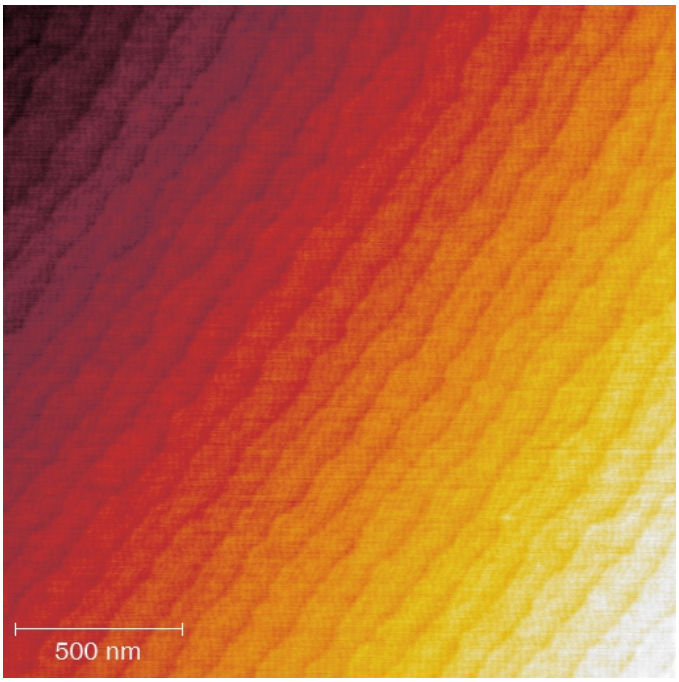

Figure 1.4. Atomic force microscopy image of a 5×5×0.5 mm^3 (110)-oriented $DyScO_3$ single crystal annealed in air at 1000 °C for 2 h. The average step width is ~110 nm.

Similar to $NdGaO_3$, $DyScO_3$ has selective absorption to visible light owing to the existence of Dy element. The surface of (110)-oriented $DyScO_3$ single crystals can be thermally annealed (at 1000 °C in air for 2 h) to generate atomically flat surface with uniform steps. An atomic force microscopy image is shown in Fig. 1.4.

1.2.6 $(LaAlO_3)_{0.3}$ $(Sr_2AlTaO_6)_{0.7}$

$SrTiO_3$ is an excellent substrate for high temperature superconducting film depositions and it has a large dielectric constant. However, its dielectric loss tangents are quite large up to 6×10^{-2} at 8.6 GHz and 77 K [53], which is detrimental for microwave applications. Compared with $SrTiO_3$, $LaAlO_3$ has remarkably small dielectric loss tangents of 5×10^{-6} at 8.6 GHz and 77 K. Nevertheless, it suffers from twins and twin boundaries which affect the

quality of thin films and their microwave applications. To overcome the disadvantages of $SrTiO_3$ and $LaAlO_3$ as substrates for high temperature superconductor microwave applications, a new crystal - $(LaAlO_3)_{0.3}(Sr_2AlTaO_6)_{0.7}$ (LSAT) was synthesized by Tidrow *et al.* [60] in 1996 via a 30/70 mole % solid solution between $LaAlO_3$ and Sr_2AlTaO_6. It is cubic with a = 3.868 Å and twin-free. The room temperature dielectric constant is 22. Its structural phase transition occurs at a low temperature of 150 K from cubic to tetragonal phase [61]. That is the reason why no twin is formed during cooling down after crystal growth. The melting point of LSAT is lower (1840 °C) relative to $LaAlO_3$ and $SrTiO_3$. Moreover, LSAT has low dielectric loss tangents, $\sim 2\times10^{-4}$ at 8.68 GHz and 77 K [62]. It has good lattice match with various perovskite oxide materials.

LSAT is an ideal diamagnet and can be used to explore novel magnetic properties of thin films. It has a large optical bandgap of ~4.7 eV [63] as an annealed LSAT single crystal shows an absorption edge of 268 nm. Moreover, its refractive index is 2.02 at 600 nm [64].

Chapter 2 Sample fabrication and characterization

In this chapter, I will first introduce the principal sample fabrication technique – pulsed laser deposition. Following that, various characterization techniques will be discussed together with instances.

2.1 Pulsed laser deposition

2.1.1 History

Shortly upon the technical realization of the first ruby laser by Theodore H. Mainman at Hughes Research Laboratories in California in 1960 [65], a ruby laser was utilized by F. Breech and L. Cross to vaporize and excite atoms from a solid surface, which was presented at the International Conference on Spectroscopy at the University of Maryland in June of 1962 [66] and published as an abstract in *Applied Spectroscopy* **16**, 59 (1962). Due to the rapid development of laser technology, the availability of reliable electronic *Q*-switches for generation of short optical pulses enabled the deposition of a variety of thin films using a ruby laser in vacuum by Howard M. Smith and A. F. Turner in New York in 1965 [67]. This marked the birth of laser film growth.

Nevertheless at that time, thin films obtained from laser ablation were still not able to compete with those grown by other techniques such as molecular beam epitaxy and chemical vapor deposition due to inferior film quality. As subsequent development in laser technology gave rise to high efficient harmonic generator and excimer laser with powerful UV radiation, the laser ablation of solid target materials became more efficient. As a result, the number of studies on laser assisted film deposition grew linearly in the 1970s and exploded in the early 1980s [68].

However, the substantial breakthrough in laser film growth was achieved by T. Venkatesan's group at Bell Communications Research Laboratory in 1987 [69], four months after the discovery of high temperature superconducting Y-Ba-Cu oxides [2], where high temperature superconducting $YBa_2Cu_3O_7$ thin films with more superior quality than those obtained by other techniques were successfully fabricated using pulsed laser evaporation. In a later paper by Venkatesan *et al.* [70], such a technique was coined as "pulsed laser deposition". Since then, pulsed laser deposition (PLD) has attained its reputed fame and been extensively utilized to fabricate high quality crystalline films including oxide thin films, nitride films, metallic multilayers, various superlattices and even to synthesize nanotubes [71], nanoparticle [72] and quantum dots [73].

2.1.2 Mechanism

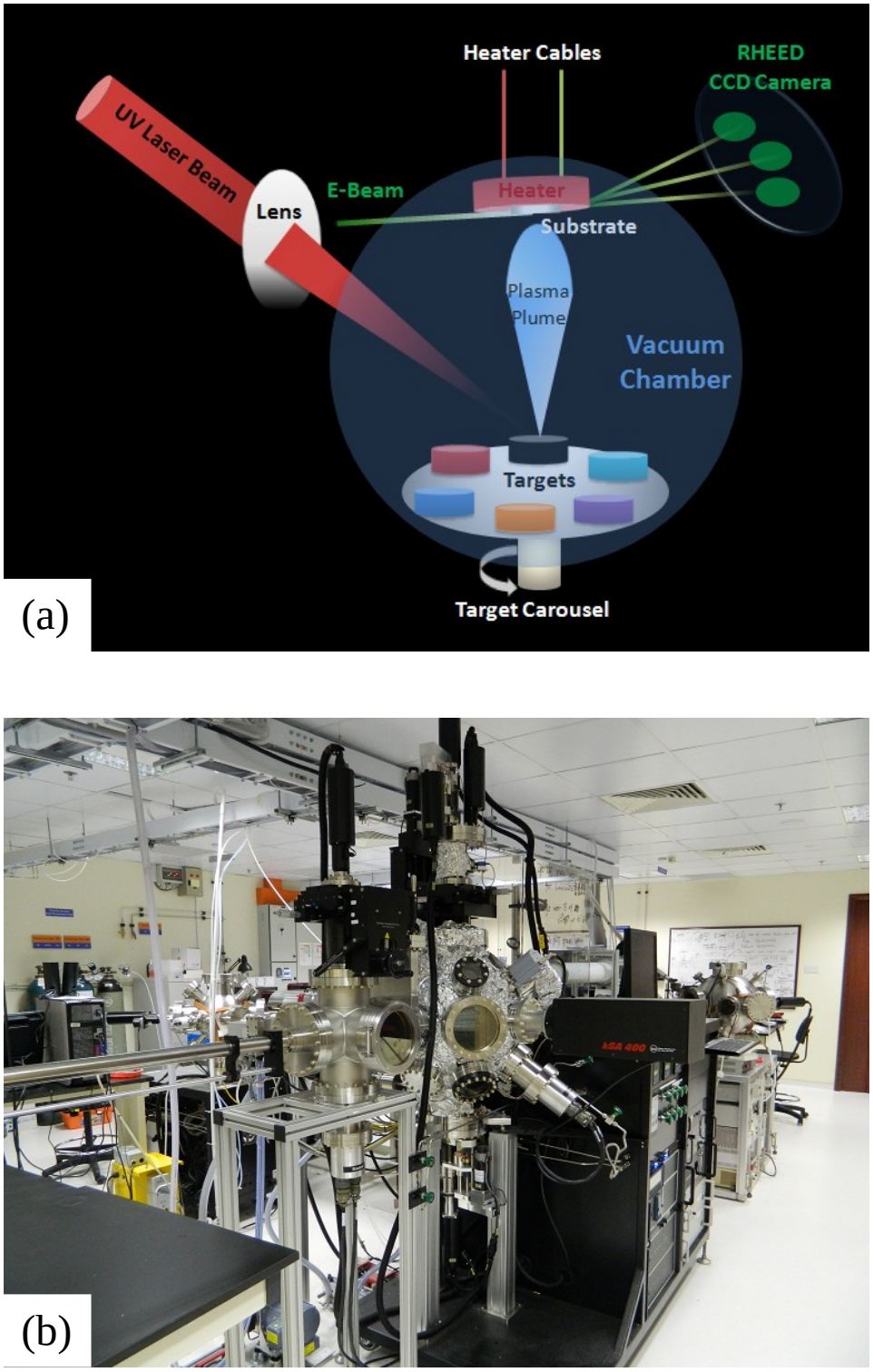

Figure 2.1. (a) Schematic of a typical PLD system. (b) Photograph of one of PLDs in our lab.

A schematic of PLD setup as well as a photo of the PLD in our lab is shown in Figure 2.1. The mechanism of PLD is complicated including the ablation of target material by pulsed and focused high energy ultraviolet laser beam, the development of a plasma plume by laser irradiation, and then the nucleation and growth of target material on substrates. When the laser pulse is absorbed by the target, energy is first converted to electronic excitation and then into thermal, chemical and mechanical energy resulting in evaporation, ablation, plasma formation and even exfoliation (Pulsed Laser Deposition of Thin Films, edited by Douglas B. Chrisey and Graham K. Huble, John Wiley & Sons, 1994).

Generally, then entire PLD process can be divided into the following steps, (i) laser ablation: the incident ultraviolet laser (typically λ = 248 nm) short pulse (pulse duration of ~10 ns) penetrates into the surface of the material within the penetration depth of typically 10 nm for most materials; the resulting strong electric field generated by the laser beam can remove electrons from the bulk material of the penetrated volume; and the free electrons oscillate within the electromagnetic field of the laser light and collide with the atoms of the bulk material, thus transferring energy to lattice and heating up the surface of the target to be vaporized. (ii) plume formation: heating of the surface yields significantly high local temperature up to ~10^5 K, resulting in plasma formation; the ablated material with plasma expands in the form of plume which is normal to the target surface due to strong Coulomb repulsion from the target surface and contains a variety of energetic species including atoms, molecules, electrons, ions, clusters, particulates and also

melted globules. (iii) deposition: the high energetic species sputter some of the surface atoms and a collision region is formed between the incident flow and the sputtered atoms; the collision region serves as a source for condensation of particles; film growth starts as the condensation rate is higher than the supply rate of particles from ablation so that thermal equilibrium conditions can be satisfied.

Nucleation and growth of thin films depends on several parameters including laser fluence, laser spot size, the ionization degree of ablated material, substrate surface temperature, target-to-substrate distance, background pressure and the physicochemical properties of target and substrate materials. A large supersaturation emerges on the substrate during the pulse duration, giving rise to a large nucleation density on the substrate surface. That can suppress the roughness of thin films. Indeed, the main two thermodynamic parameters influencing the growth are substrate surface temperature T and supersaturation D_m, where the former affects the mobility of vapor atoms (from the plume) on the substrate surface while the latter is associated with nucleation density. They are related to each other by the following equation:

$$D_m = kTln\left(R/R_e\right) \tag{2-1}$$

where k is the Boltzman constant, R is the practical deposition rate and R_e is the equilibrium value at the temperature T.

Depending on the above deposition parameters, two-dimensional (2D) and three-dimensional (3D) growth can occur in PLD thin film growth. In 2D growth, there are two modes including step-flow growth and layer-by-layer growth. They are schematized and elaborated as below.

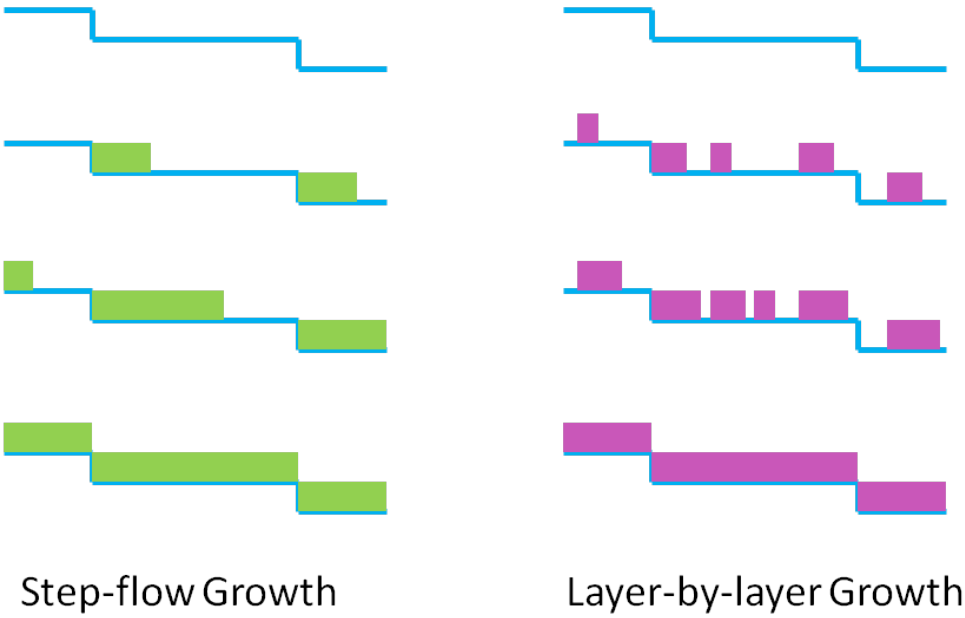

Figure 2.2. Schematics of 2D growth modes: step-flow growth and layer-by-layer growth.

The 2D growth modes: (i) step-flow growth - atomic steps exist on the surface of a crystalline substrate owing to a miscut angle relative to its nominal crystallography plane. Atoms land on the substrate surface and thermally diffuse to such step edges before they can nucleate to form surface islands. The growth process can be viewed as step edges are flowing or steps are expanding along the surface. This process occurs when the miscut of a substrate is large or the substrate temperature is sufficiently high so that adatom (vapor atoms) are mobile enough to move to step edges and nucleate. (ii) layer-by-layer growth - atoms nucleate into 2D islands on the surface. As

more material is added, the islands start to grow and merge into each other. This is referred as coalescence. At that time, a large number of pits exist on the surface. As addition material is added, the atoms diffuse into the pits so that one layer can be completed. This process appears at lower temperatures so that atoms are not fast enough to move to step edges to nucleate.

The 3D growth mode: once atoms nucleate on the surface forming islands, additional atoms will nucleate on the former islands. The entire growth continues in a 3D fashion rather than a 2D one. This mostly happens when the substrate roughness is large or the lattice of film is pronouncedly distinct from that of substrate or the substrate temperature is too low.

The advantages of PLD are versatility, the capability of maintaining target composition, low cost (compared with molecular beam epitaxy) and cleanness. In addition, the rapid deposition of the energetic ablation species enhances the substrate surface temperature. In this respect, crystalline thin film growth by PLD tends to demand a lower substrate temperature. A drawback of PLD is that highly energetic plume ions may cause structural defects in substrates and thin films. Moreover, it suffered from the small cross section of laser plume, limiting itself to research environment. However, large area and uniform thin film deposition by PLD can be achieved by shifting the laser beam and rotating the substrate during deposition, potential for industrial applications. A 4-inch wafer PLD system is available in our lab.

2.1.3 RHEED

RHEED is the abbreviation of reflection high-energy electron diffraction. Nowadays, more and more PLD systems are equipped with RHEED, which is used to characterize the surface of a crystalline material and *in situ* monitor the thin film growth. Accordingly, a PLD system equipped with RHEED is also referred as PLD-MBE. The high energy beam diffraction is similar to x-ray diffraction, while in the RHEED setup an electron beam shines on the sample with a grazing incident angle and therefore only surface atoms contribute to the diffraction pattern.

Generally there are two kinds of diffraction contributing to the RHEED patterns, including elastic and inelastic scatterings. For the elastic scattering, the energy of electrons keeps constant before and after scattering, which is termed kinematic scattering [A. Ichimiya and P. I. Cohen, Reflection high energy electron diffraction. Cambridge University Press: Cambridge, UK (2004)]. In contrast, the energy of electrons partly loses because of interactions with the crystal lattice in inelastic scatterings.

Regarding to the elastic scattering, the RHEED pattern is a construction of the Ewald's Sphere related to the reciprocal lattice of a crystalline material. However, it differs from the reciprocal lattice of bulk crystals consisting of a series of points. As only the sample surface contributes to the diffraction, the out-of-plane dimension is not involved. Hence, the RHEED pattern of a crystal is only associated with the reciprocal lattice of a 2D lattice, which consists of a set of infinite rods.

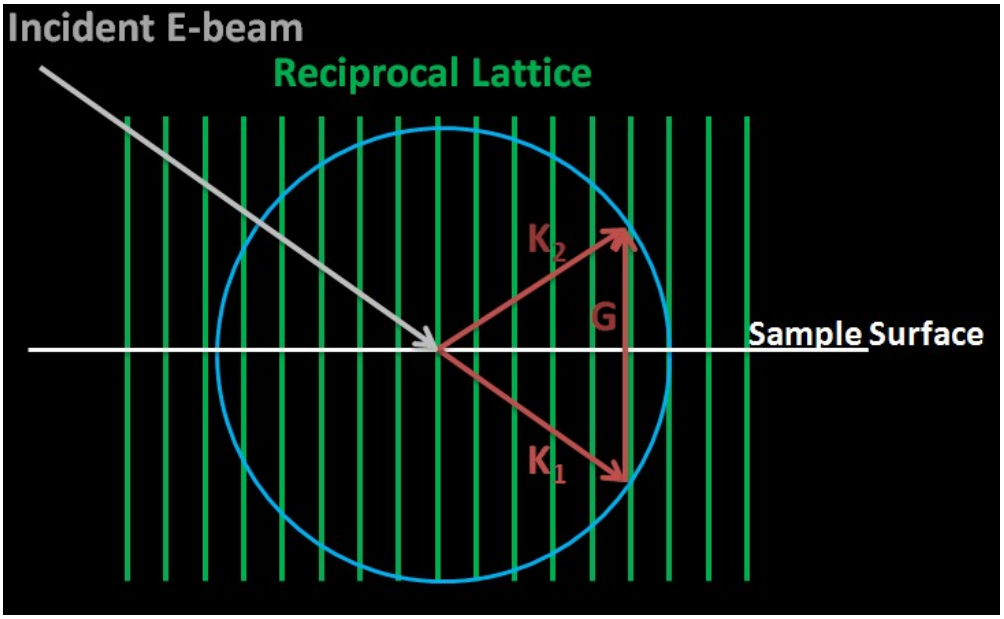

Figure 2.3. Schematic of the Ewald's Sphere at the sample surface. In the figure, $\boldsymbol{k_1}$ is the wave vector of an incident electron beam and $\boldsymbol{k_2}$ is the wave vector of a diffracted electron beam.

As schematized in Figure 2.3, the radius of the Ewald's Sphere is the reciprocal of the wavelength, which can be expressed by the following equation

$$\boldsymbol{k_1} = \frac{2\pi}{\lambda}, \tag{2-2}$$

where λ is the wavelength of the incident electron beam. Following the Laue diffraction conditions, constructive diffraction occurs where the rods of reciprocal lattice intersect the Ewald's sphere. The conditions can be expressed by the following equations:

$$|\boldsymbol{k_1}| = |\boldsymbol{k_2}| \tag{2-3}$$

$$\boldsymbol{G} = \boldsymbol{k_2} - \boldsymbol{k_1} \tag{2-4}$$

where $\boldsymbol{G}$ is an arbitrary reciprocal lattice vector.

The inelastic scattering determines the brightness of a point on the detector screen. Part of inelastically scattered electrons penetrate the bulk crystal and approach Bragg diffraction conditions, consequently leading to kikuchi diffraction patterns. Kikuchi lines intersect the principal elastic diffraction circles in the RHEED pattern and appear to radiate from the center of the pattern.

For an ideal incident electron beam with an accurate energy, the radius of the Ewald's sphere $\boldsymbol{k_1}$ is precise and therefore the thickness of the Ewald's sphere is infinitely small. Also for an ideal surface lattice the rods in its reciprocal lattice is infinitely thin. In such a case, the elastic diffraction points originating from the intersections of the Ewald's sphere and the reciprocal lattice rods are infinitely sharp singular points. However, the electron beam energy in reality has a certain fluctuation and the lattice of a crystal surface is not ideally periodic, leading to a finite thickness for both the Ewald's sphere wall and the reciprocal lattice rods. As a result, the intersections between the Ewald's sphere and the reciprocal lattice rods typically exhibits streaked and elongated points, which are common in practical RHEED patterns.

In the following, we will discuss how the RHEED is utilized to monitor the thin film growth in PLD. In the layer-by-layer growth mode, the RHEED intensity integrated over a selected area on the specular point first decreases as the material is grown until one layer is half finished. That is because the surface roughness increases and reaches its maximum when the substrate is

half covered, corresponding to the appearance of a large number of pits on the surface. As subsequent adatoms will diffuse into those pits to complete the layer in the latter half layer growth, the RHEED intensity gradually recovers. Such process is repeated as the thin film growth continues and consequently RHEED oscillations are obtained during the layer-by-layer growth. Each oscillation represents one unit cell of crystalline thin films. In what follows, I will show some examples of RHEED patterns and oscillations.

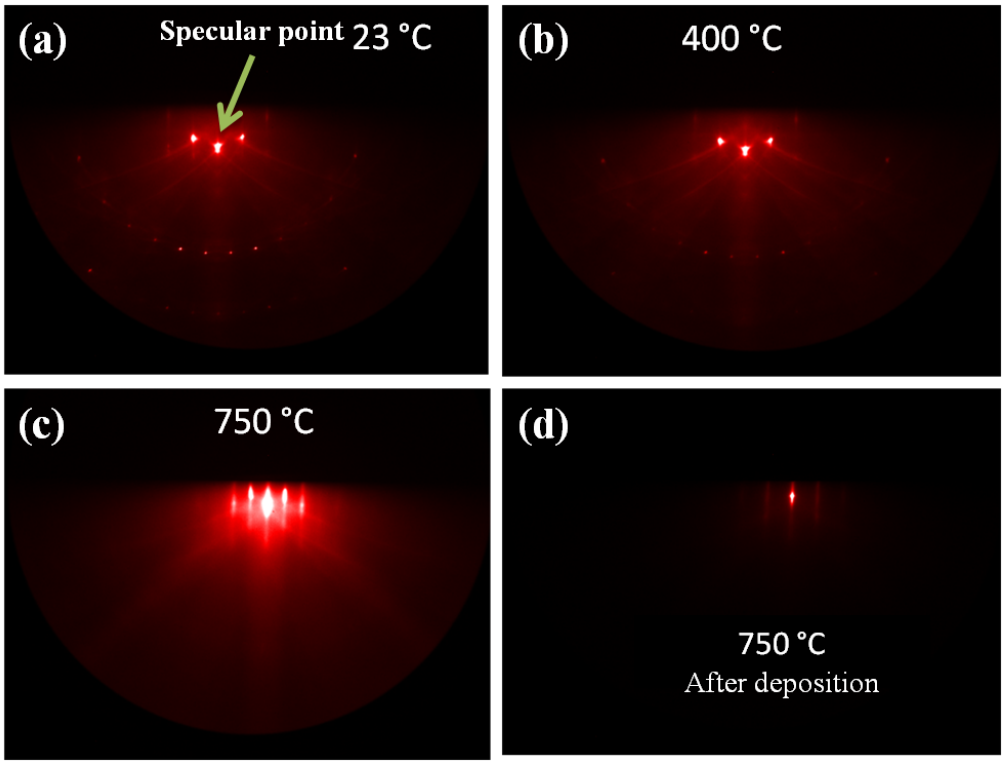

Figure 2.4. RHEED patterns of a TiO_2-terminated $SrTiO_3$ (100) surface at different temperatures (a)-(c) and after the deposition of a 9 unit cell $LaAlO_3$ layer (d).

Figure 2.4 shows RHEED patterns of a TiO_2-terminated $SrTiO_3$ (100) substrate surface at different temperatures (a)-(c) and after the deposition of a 9 unit cell $LaAlO_3$ layer (d). In the RHEED patterns at low temperatures,

sharp diffraction points as well as Kikuchi lines are visible. As the temperature of the $SrTiO_3$ substrate increases to 750 °C, the RHEED pattern becomes streaky. That is because the electron beam energy fluctuation increases as a result of the high temperature and thermal disturbance. In addition, streaky RHEED patterns indicate a flat sample surface and also a dominant 2D surface diffraction.

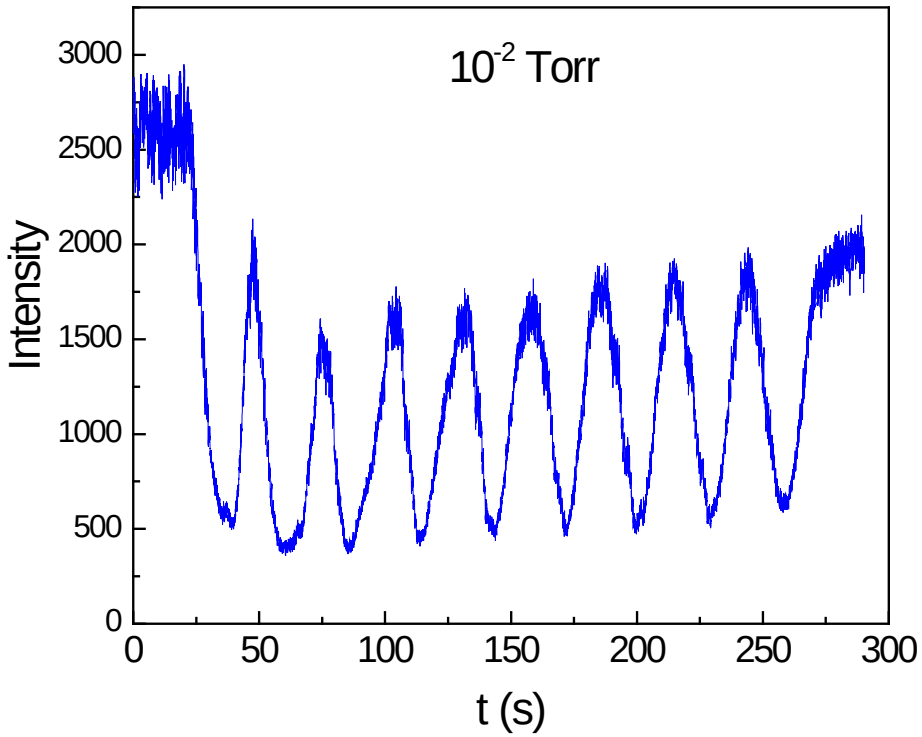

Figure 2.5. RHEED oscillations of a $LaAlO_3$ film grown on a TiO_2-terminated $SrTiO_3$ (100) substrate at 750 °C and 10^{-2} Torr oxygen partial pressure.

The RHEED intensity by integrating over a selected area on the specular spot during the deposition of a $LaAlO_3$ layer is recorded in Figure 2.5. The periodic RHEED intensity oscillations indicate a layer-by-layer growth mode. After the deposition, the RHEED pattern shown in Figure 2.4(d) is obviously streaky, suggesting a flat surface of the film. Indeed, the step-flow growth can also result in a streaky RHEED pattern as it is 2D growth too and the smooth

surface can be maintained. In terms of RHEED intensity, the layer-by-layer growth and the step-flow growth are distinctly different. The RHEED intensity in the step-flow growth mode does not oscillate with time while it periodically varies with time in the layer-by-layer growth mode. Moreover, in the step-flow growth, the RHEED intensity obviously recovers with time once the deposition process is interrupted due to the high mobility of adatoms, whereas the RHEED intensity keeps almost constant in the layer-by-layer growth mode after stopping the deposition in between because of the low mobility of adatoms [74].

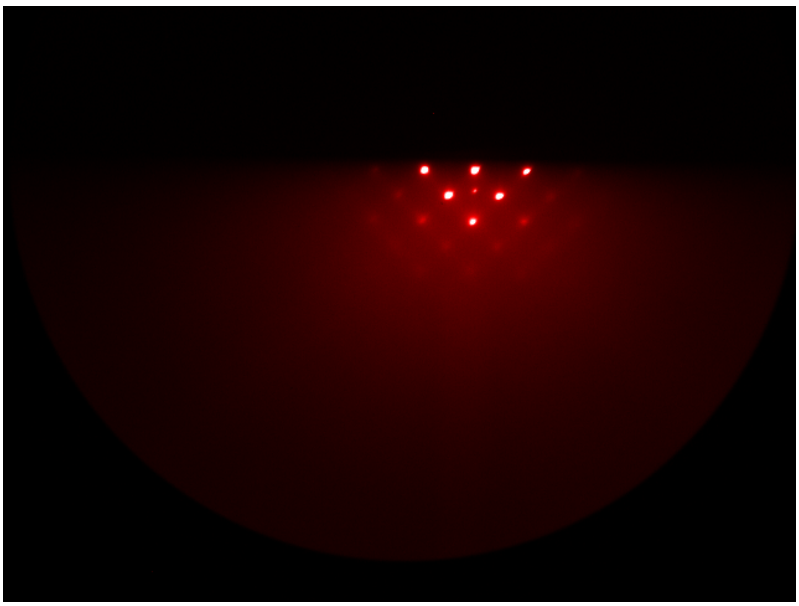

Figure 2.6. RHEED pattern of a CuO film grown on a TiO_2-terminated $SrTiO_3$ (100) substrate at 750 °C and 10^{-2} Torr oxygen partial pressure, indicating a 3D growth.

For a 3D film growth mode, the RHEED pattern is no longer 2D diffraction. Instead, the high energy electron can penetrate the islands of thin film, yielding a 3D diffraction pattern consisting of a set of points. An

example RHEED pattern when depositing CuO films on $SrTiO_3$ substrates is shown in Figure 2.6.

From what is elaborated above, one can easily distinguish the growth mode of a thin film by RHEED pattern combined with the RHEED intensity evolution with time. Hence RHEED is a powerful tool to monitor thin film growth in PLD.

2.2 Sample characterization techniques

2.2.1 Structural characterization

For the structural characterization of oxide heterostructure samples, the growth quality of crystalline thin films is typically examined by x-ray diffraction; the surface morphology of thin films is analyzed by atomic force microscopy while the oxide interface can be explored by transmission electron microscopy. In this part, I will briefly introduce the above three main techniques for structural characterization utilized during my research.

2.2.1.1 X-ray diffraction

X-ray diffraction (XRD) is a rapid and nondestructive technique to detect the crystallographic structure of a periodic atom lattice. Considering lattice planes spaced by *d*, the constructive diffraction happens when the following equation is fulfilled,

$$2dsin\theta = n\lambda \tag{2-5}$$

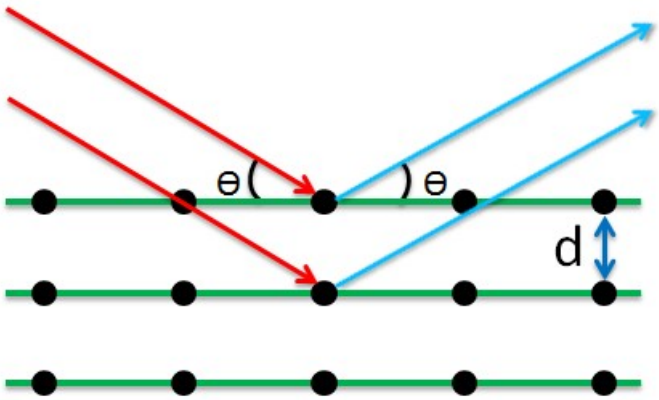

Figure 2.7. Schematic of elastic x-ray diffraction.

where θ is the incident angle of the x-ray relative to the crystalline plane, n is the order number of diffraction pattern and λ is the wavelength of x-ray. The above equation is known as Bragg's law.

X-ray is used to detect the crystal structure of a lattice as its wavelength is comparable or smaller than the typical crystal lattice spacing of Å. For example, the wavelength of Cu k_α x-ray is 1.54056 Å, which is extensively used in XRD setup. By virtue of XRD, one can readily determine the crystal structure and calculate the lattice constant d according to the peak position. In our lab, a Bruker XRD system with a 2D detector (shown in Figure 2.8) was used.

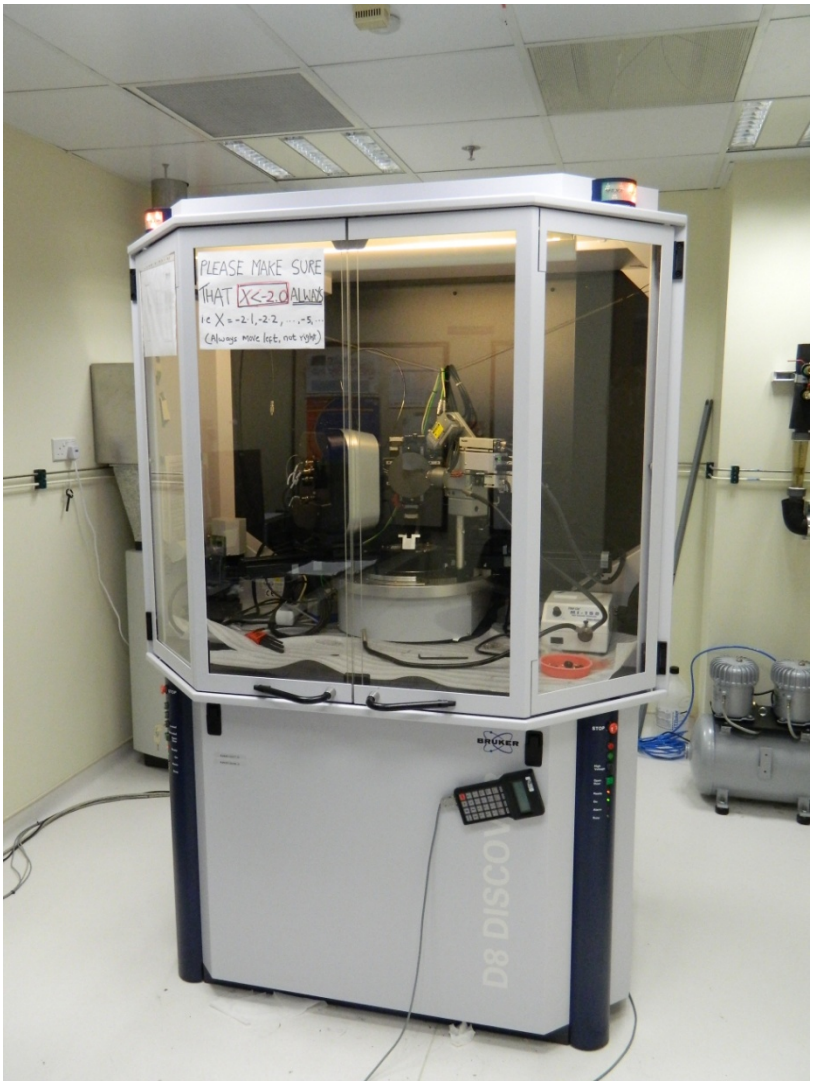

Figure 2.8. Photograph of the x-ray diffraction (XRD) setup with a 2D detector in our lab.

With a 2D detector, one can intuitively identify whether oxide films are polycrystalline or single-crystalline as the XRD diffraction pattern of a single crystal film displays a series of sharp points corresponding to a certain lattice orientation while the XRD pattern of a polycrystalline film exhibits a series of diffraction circles. As examples, the diffraction patterns of a single crystal $YBa_2Cu_3O_7$ film grown on a $SrTiO_3$ substrate and a polycrystalline $NdGaO_3$

film grown on an MgO substrate are shown in Figures 2.9 and 2.10, respectively.

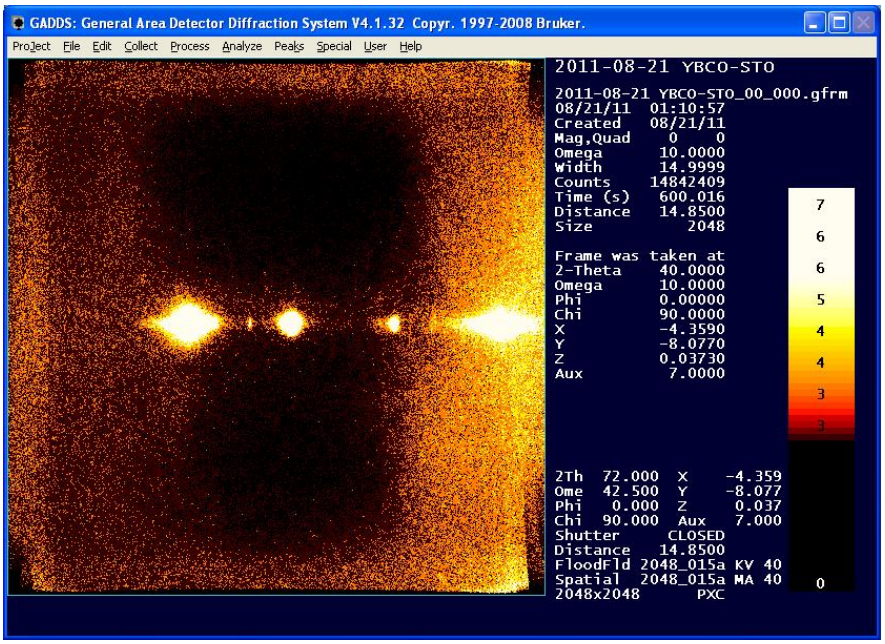

Figure 2.9. 2D XRD pattern of a single crystal $YBa_2Cu_3O_7$ thin film deposited on a $SrTiO_3$ substrate at 750 °C and 200 mTorr oxygen partial pressure.

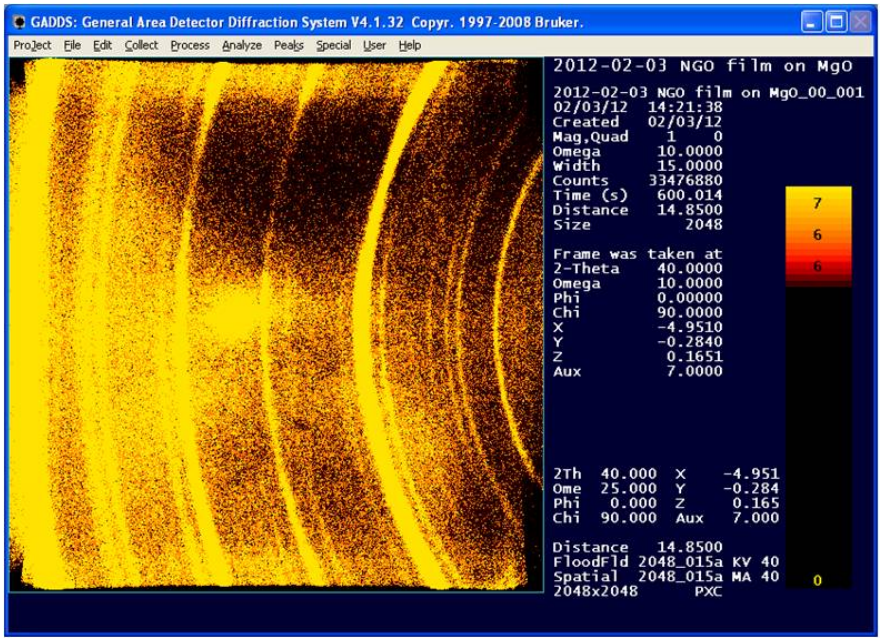

Figure 2.10. 2D XRD pattern of a polycrystalline $NdGaO_3$ thin film deposited on an MgO substrate at 700 °C and 10^{-2} Torr oxygen partial pressure.

Not only is it useful for single layer thin films, XRD is also capable of characterizing multilayer oxide heterostructures such as superlattices [75]. In superlattices, additional periodicity in layered materials is added and the high angle ($\theta > 15°$) peak positions can be indexed by the following equation:

$$2\frac{sin\theta}{\lambda} = \frac{1}{\bar{d}} \pm \frac{n}{\Lambda} \quad (2\text{-}6),$$

where $\bar{d}$ is the average lattice constant of the entire superlattice and Λ is the distance between the artificially periodic layer structure. Accordingly, the artificial lattice constant Λ of this periodicity can be obtained from the peak positions of satellite peaks. For example, the $\theta - 2\theta$ scan profile of a $[(SrRuO_3)_7/(LaAlO_3)_7]_{20}$ superlattice fabricated on a TiO_2-terminated $SrTiO_3$ substrate is shown in Figure 2. 11.

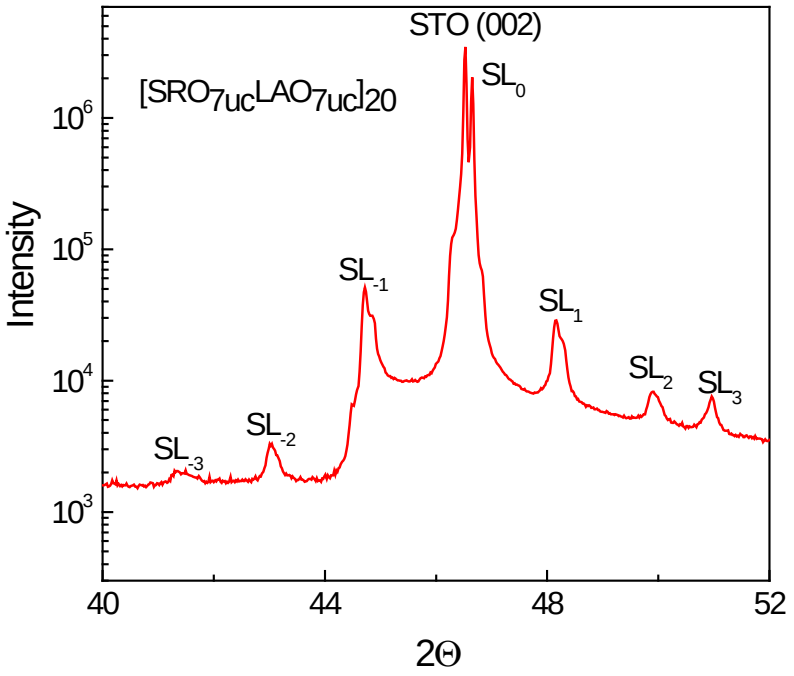

Figure 2.11. A *Θ-2Θ* scan profile of a $[(SrRuO_3)_7/(LaAlO_3)_7]_{20}$ superlattice fabricated on a TiO_2-terminated $SrTiO_3$ substrate. SL represents satellite peaks.

Satellite peaks up to the third order can be seen. If we plot the order number n as a function of $2\frac{sin\theta}{\lambda}$, it should show a straight line with a slope of Λ. The linear fitting of the above $\theta - 2\theta$ scan profile is shown in Figure 2.12.

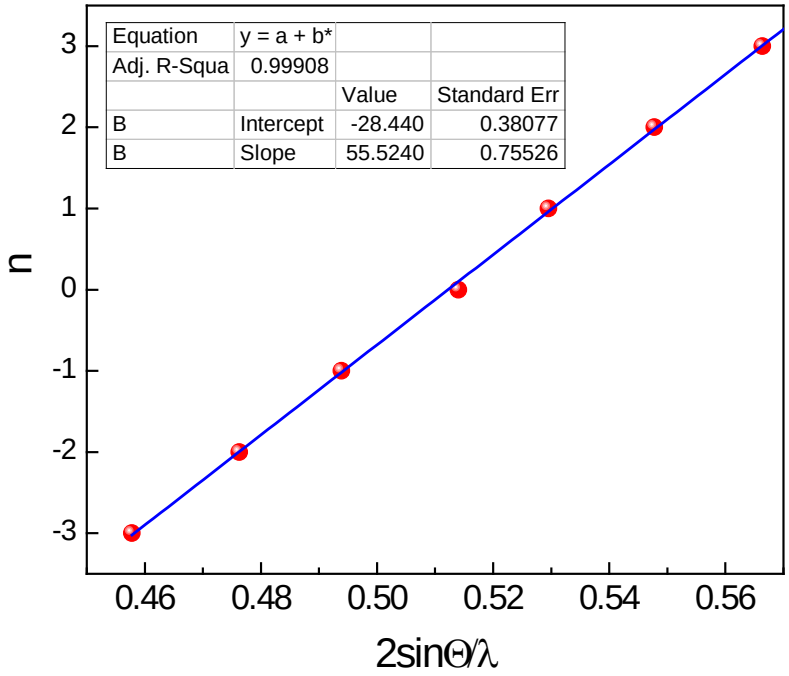

Figure 2.12. Linear fitting of superlattice satellite peaks. The fitted slope Λ is 55.5 Å, close to the nominal thickness of 7 unit cell $LaAlO_3$ plus 7 unit cell $SrRuO_3$ (54 Å = 7 × 3.79 Å + 7 × 3.93 Å).

What we have discussed above is all about the $\theta - 2\theta$ scan, which is an examination of out-of-plane lattice periodicity of crystalline thin films or superlattices. Besides, XRD is a versatile technique with other multiple capabilities for broad applications in thin film studies, such as rocking curve for thin film crystallinity check, reciprocal lattice mapping for in-plane lattice constant and interface strain study, reflectivity measurement for film thickness determination and pole figures for texturing effect analysis.

2.2.1.2 Atomic force microscopy

Based on scanning tunneling microscopy, Binnig, Quate and Gerber invented atomic force microscopy (AFM) in 1986. In AFM, the localized mechanical interaction between a sharp tip and the sample surface is utilized for mapping the sample topography. A schematic and a photograph of an AFM setup are shown in Figure 2.13 and Figure 2.14, respectively. As schematized in Figure 2.13, a laser beam is reflected from the backside of the cantilever, on the end of which the sharp tip is mounted, onto a quadruple photodiode array. The vertical displacement resulting from normal atomic force and the lateral twist owing to friction force can be obtained by analyzing the relative light intensity detected by the four diodes. Feedback electronics and piezoelectric scanner are used to maintain a constant tip-sample force or constant oscillation amplitude during topography mapping.

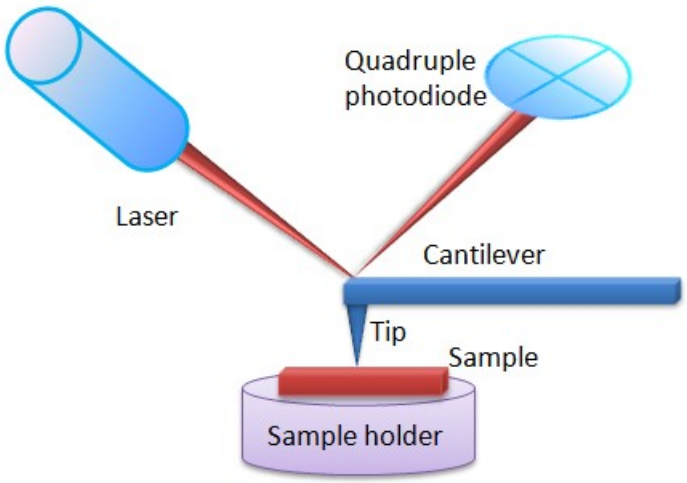

Figure 2.13. Schematic of an atomic force microscopy (AFM) setup.

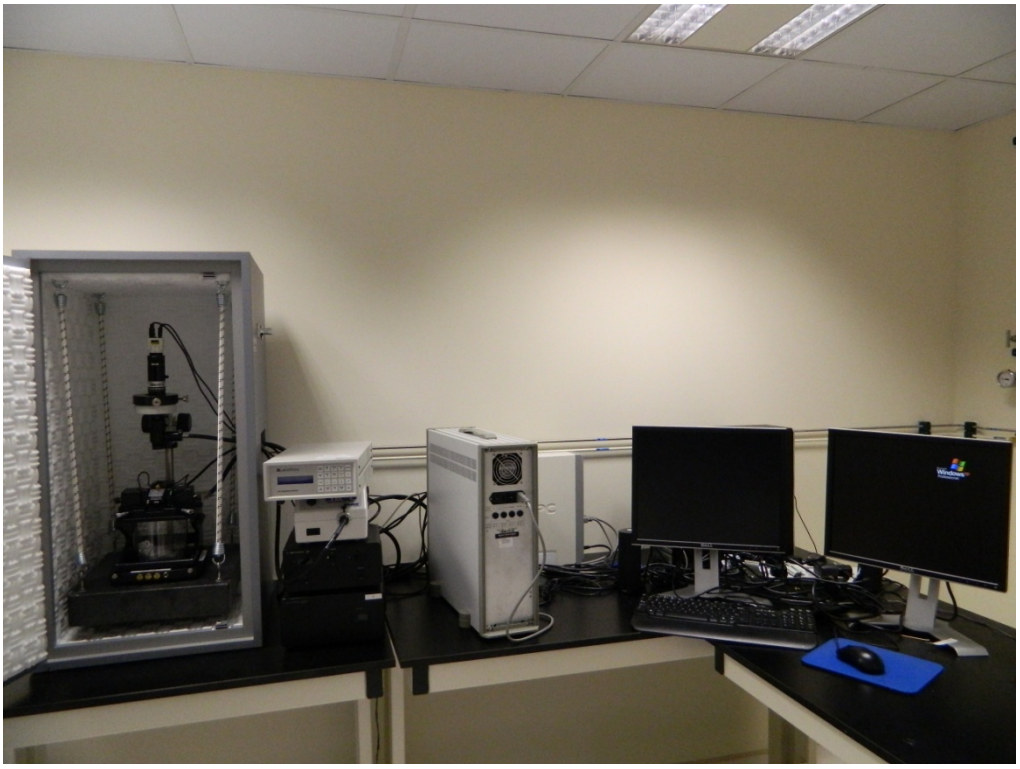

Figure 2.14. Photograph of the AFM in our lab.

The V-shaped cantilever tip, typically fabricated by lithographing Si-based material, has a spring constant of 10^{-2}–10^{2} N/m. With a displacement detection sensitivity of 0.1 Å, the minimal detectable force is ~10^{-12} N. In some specific cases, atomic resolution in AFM can be achieved. The primary operation modes for AFM are contact mode and tapping mode. In the contact mode, the cantilever is dragged over the surface by the van der Waals forces and the surface is mapped directly by virtue of the deflection of the cantilever. In the tapping mode, the cantilever is driven to oscillate at a frequency close to its resonance frequency and the amplitude of such oscillation is typically 100-200 nm. The oscillation amplitude, phase and resonance frequency are affected by the tip-surface interaction forces, which is used to construct the sample surface

contours. The tapping mode is gentle enough to avoid damaging the sample surface and even able to image the biomolecules in a liquid medium.

For example, an AFM image of a TiO_2-terminated $SrTiO_3$ substrate obtained by the contact mode is shown in Figure 2.15. As can be seen, the surface is atomically flat with uniform step flows. The steps are smooth with a step height of ~4 Å and an average width of ~500 nm, corresponding to the thickness of one unit cell $SrTiO_3$ 3.9 Å. Nanoscale defects such as holes and clusters can be clearly seen.

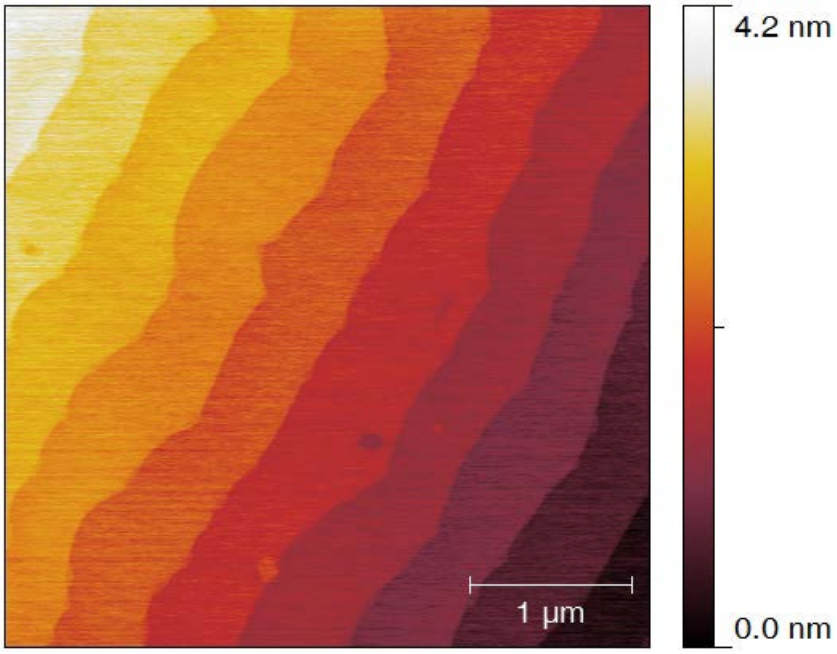

Figure 2.15. A 4 μm×4 μm AFM image of a TiO_2-terminated $SrTiO_3$ substrate.

As one of the foremost tools for surface studies, AFM is easy to be applied to nanostructure imaging. For example, the surface topography of a CuO film grown on a $SrTiO_3$ substrate is shown in Figure 2. 16. The CuO nanowires

with the diameter of 100-300 nm originating from 3D island growth (refer to Figure 2.6) can be clearly visualized.

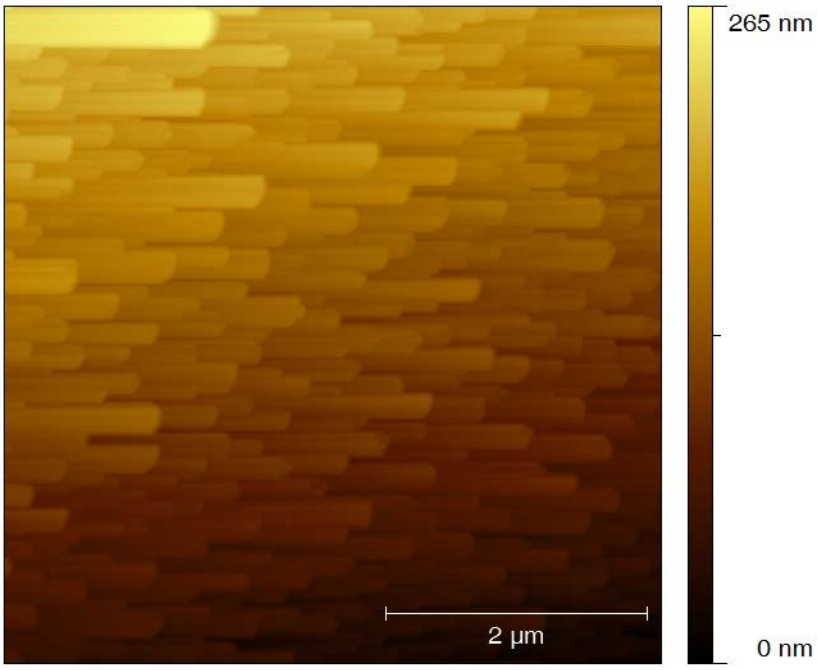

Figure 2.16. A 5 μm×5 μm AFM image of the CuO film deposited on a $SrTiO_3$ substrate (refer to Figure 2.6), showing nanopillar structures of CuO.

2.2.1.3 Transmission electron microscopy

Transmission electron microscopy (TEM) is an imaging technique by virtue of the interaction between an electron beam and an ultrathin sample during the transmission of the electron beam through the sample. It is a direct probe to the crystalline lattice on an atomic scale. In TEM, an ultrathin sample is irradiated by a high-energy (typically 100-500 keV) coherent electron beam and the image is realized by a sophisticated electron optic system, which can be operated either in a diffraction mode or an imaging mode. In the diffraction mode, a diffraction pattern of the ultrathin sample can be observed on the

fluorescent screen. A TEM diffraction pattern of an $NdGaO_3$ film grown on a $SrTiO_3$ substrate is shown in Figure 2.17.

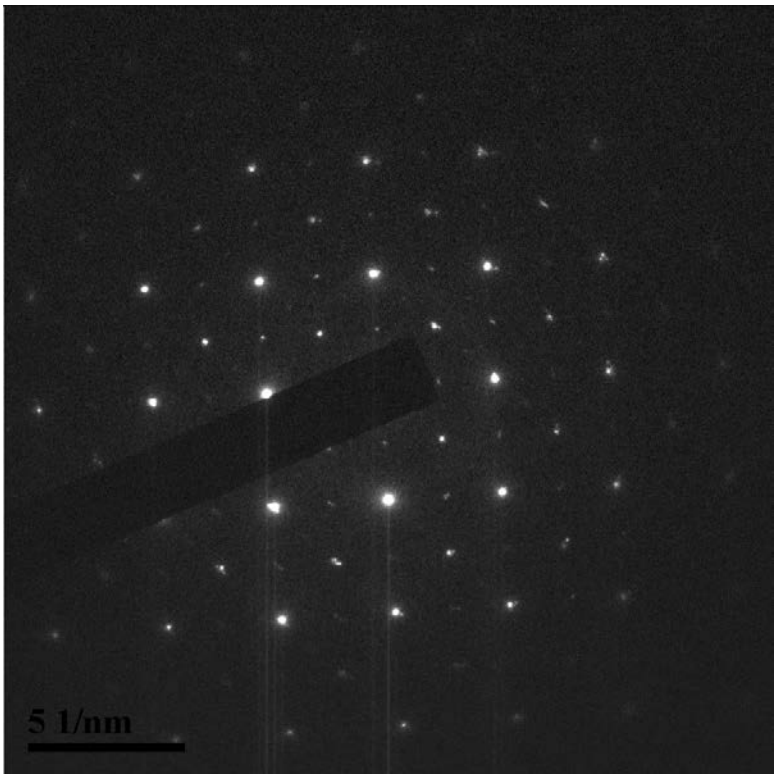

Figure 2.17. Transmission electron microscopy (TEM) diffraction pattern of a 300 nm $NdGaO_3$ film grown on a $SrTiO_3$ substrate at 700 °C and 10^{-2} Torr oxygen partial pressure.

In the imaging mode, a real-space image can be obtained from part of diffraction spots. Depending on the diffraction spots selected for imaging, there are two types of imaging modes, *i.e.*, bright field imaging and dark field imaging. In the bright field mode, the specular diffraction spot is selected for imaging. The regions in the sample with high crystalline quality typically have a low scattering rate and consequently show high intensity in the image, whereas the regions with defects exhibit relatively low intensity. In this mode, high-resolution imaging with atomic resolution can be achieved due to the interference of the specular beam and other Bragg diffracted beams. In the

dark field imaging, non-specular diffraction spots or scattered spots are chosen, where the structures yielding those diffraction or scattering patterns display as bright regions. This image mode is typically used to identify grain boundaries or textures or domains in crystalline samples.

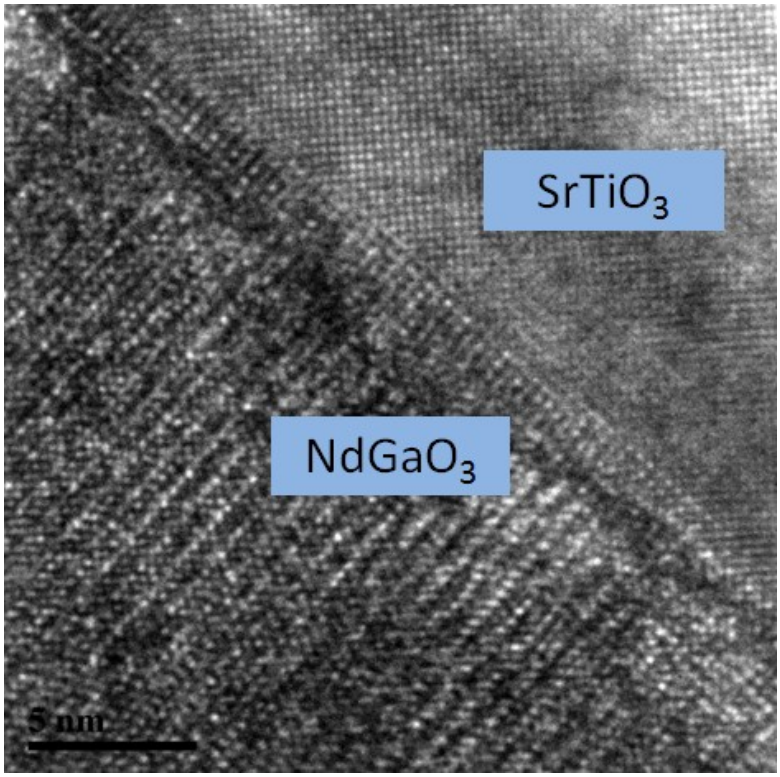

Figure 2.18. Cross-section TEM image of an $NdGaO_3$ film grown on a $SrTiO_3$ substrate.

One of the most critical processes in TEM for high quality image is sample preparation. Oxide heterostructures are typically built on bulk crystalline substrates, which need to be thinned down to hounded of nm so that the electron beam can be transmitted through. Mechanical polishing followed by Ar-ion milling is typically utilized for sample preparation. Of course, optical instrumental settings are also critical to the image quality. Up to date, TEM

has been the most powerful tool for exploring the cross-section atomic structures at interfaces between thin films and substrates.

A cross-section TEM image of an $NdGaO_3$ film grown on a $SrTiO_3$ substrate is shown in Figure 2.18. A zoom-in TEM image of the $NdGaO_3$ film shown in Figure 2.19 reveals a uniform crystal lattice .

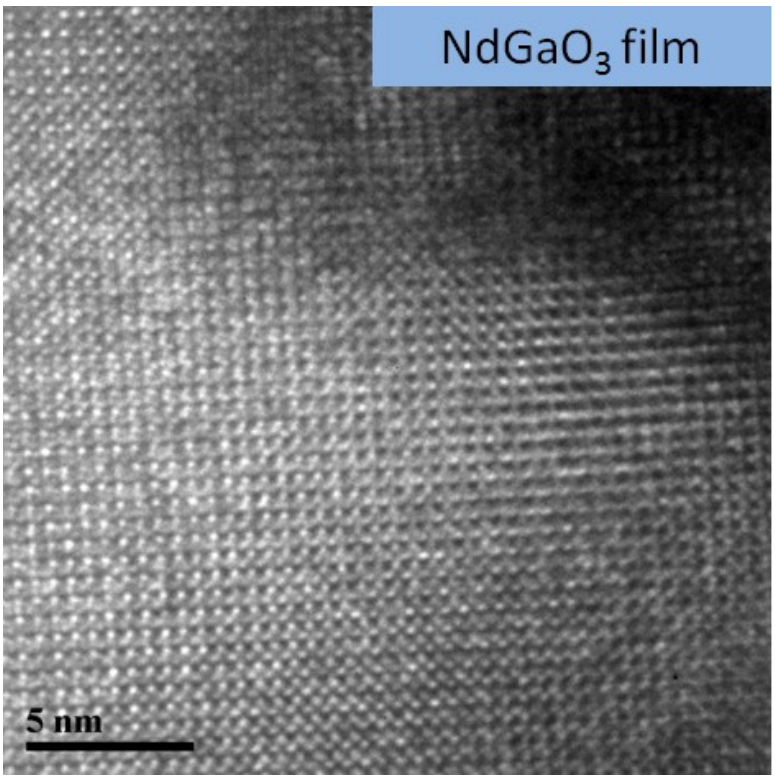

Figure 2.19. Zoom-in TEM image of the $NdGaO_3$ film.

Additionally, information on elemental composition can be obtained by analyzing electron energy loss spectra (EELS) or energy dispersive x-ray (EDX) generated by high energy electron beam. An EDX spectrum of the $NdGaO_3/SrTiO_3$ heterostructure is shown in Figure 2.20.

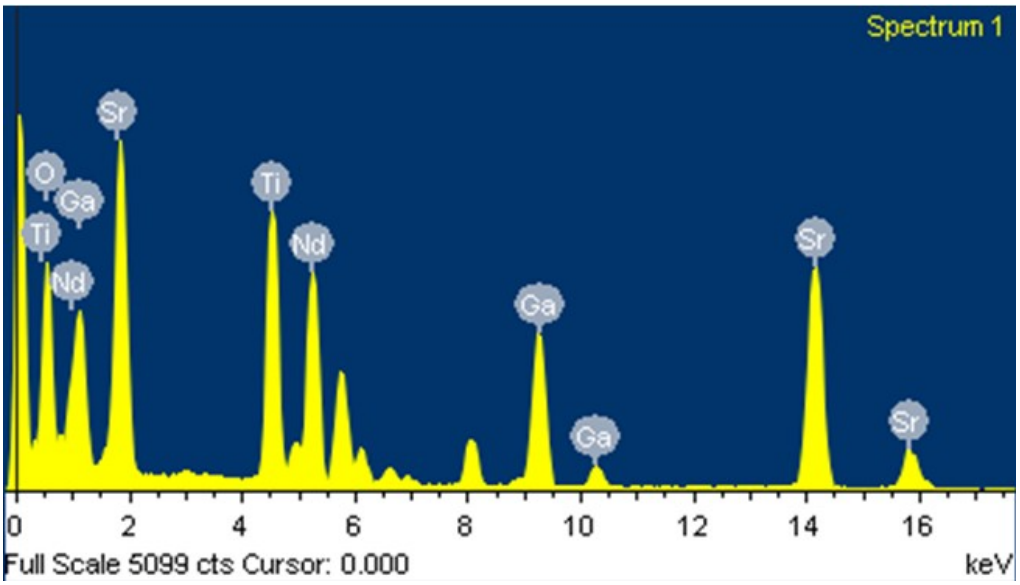

Figure 2.20. Energy dispersive x-ray spectrum of the $NdGaO_3/SrTiO_3$ heterostructure.

2.2.2 Electrical characterization

Generally, there are three categories of electrical measurements involved in my research: resistance measurements, Hall measurements and magnetoresistance measurements. All these measurements can be readily accomplished by a physical properties measurement system (PPMS) shown in Figure 2.21. I will briefly introduce the fundamental basis for them one by one in this part.

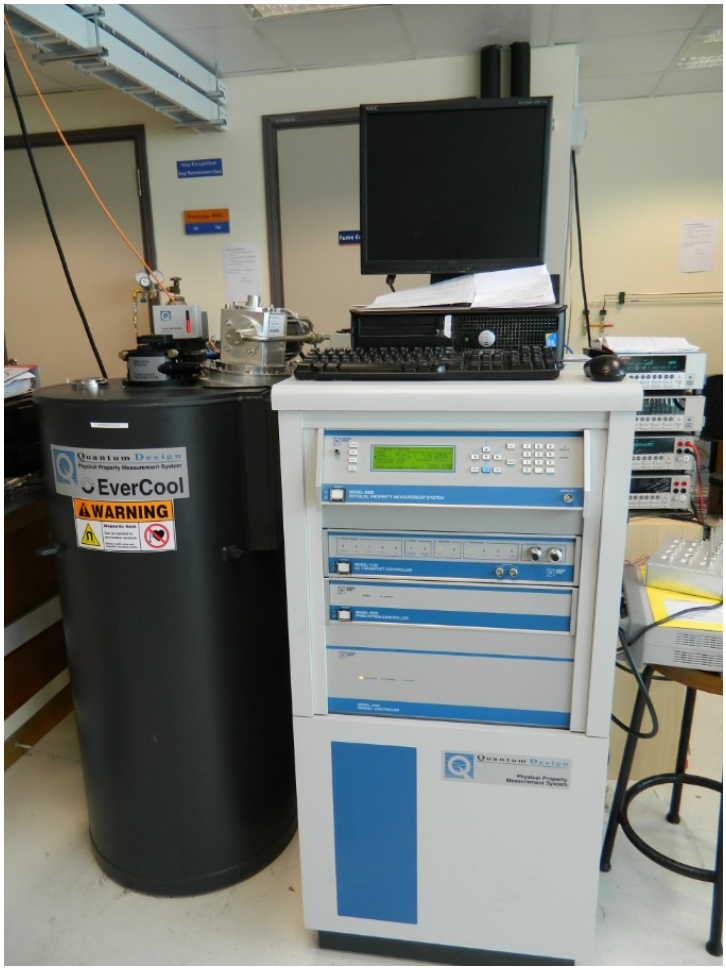

Figure 2.21. Photograph of the physical properties measurement system machine in our lab.

2.2.2.1 Resistance measurements

A four-point probe is typically used in thin film resistance measurements to avoid contact resistance between connection wires and thin films. There are two commonly used geometries, *i.e.*, linear geometry and van der Pauw geometry. A four-probe linear geometry is schematized for a thin film with the thickness of t in Figure 2.22. Due to the finite size effect, the applied current I cannot uniformly flow along the entire film cross section and therefore the

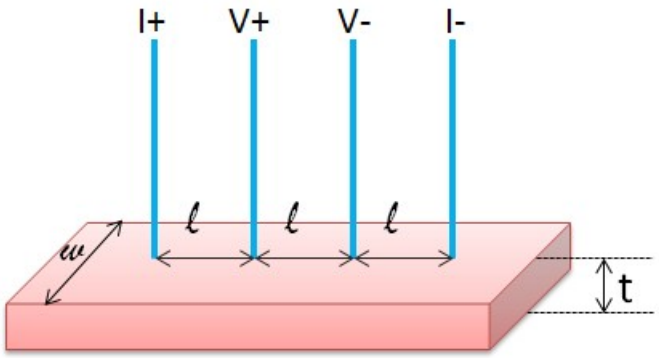

Figure 2.22. Schematic of the four-probe linear geometry for resistance measurements.

resistivity ρ of the thin film cannot be simply determined by the following equation:

$$R = \rho \frac{l}{s} \qquad (2\text{-}7),$$

where R is the resistance determined by the measured voltage V divided by the applied current I, l is the distance between the two voltage electrodes and s is the area of the thin film cross section perpendicular to the linear line. Instead, with the electrodes centered on a very wide ($l \ll w$) and very thin ($t \ll l$) film, the resistivity ρ is given by:

$$\rho = \frac{\pi}{\ln(2)} t\left(\frac{V}{I}\right) = 4.5324t\left(\frac{V}{I}\right) \qquad (2\text{-}8)$$

For a thin film with non-negligible thickness and finite width the above expression should be further rectified by geometrical correction factors f_1 and f_2.

$$\rho = \frac{\pi}{\ln(2)} t\left(\frac{V}{I}\right) f_1 f_2 = 4.5324t\left(\frac{V}{I}\right) f_1 f_2 \qquad (2\text{-}9)$$

where $f_1 = f_1(\frac{t}{l})$ is non-negligible thickness correction and $f_2 = f_2(\frac{w}{l})$ is finite width correction. Typically for a thin film, $t \ll l$ is always satisfied and $f_1 = 1$. While finite width correction usually exists and therefore the resistivity of a thin film can be expressed by

$$\rho = \frac{\pi}{\ln(2)} t(\frac{V}{I}) f_2 = 4.5324 t(\frac{V}{I}) f_2 \quad (2\text{-}10)$$

and correspondingly the sheet resistance can be expressed by

$$R_s = \frac{\pi}{\ln(2)} (\frac{V}{I}) f_2 = 4.5324 (\frac{V}{I}) f_2 \quad (2\text{-}11)$$

in the four-probe linear geometry. The finite width correction factors can be found for thin films with different shapes in [76].

For example, a 200 nm thick Sn-doped In_2O_3 (ITO) thin film grown on a $LaAlO_3$ substrate (5×5 mm^2) at 200 mTorr and 750 °C has a measured resistance of 3.76 Ω at room temperature with the electrode spacing of 1 mm. The finite width correction factor for $\frac{w}{l} = 5$ and a square sample is 0.65. Therefore, the sheet resistance is $R_s = 3.76\ \Omega \times 4.53 \times 0.65 = 11.07\ \Omega/\square$. Finally, the corresponding room temperature bulk resistivity is $\rho = R_s t = 2.22\times10^{-4}\ \Omega\cdot$cm.

In the PPMS machine, the temperature of a sample can be varied by the cooling system and the resistance can be recorded as a function of temperature. Thus the temperature dependence resistivity ($\rho - T$) can be obtained. The $\rho - T$ curve of the ITO thin film is shown in Figure 2. 23. The resistivity of

the ITO thin film changes with temperature and shows a low temperature upturn at ~100 K.

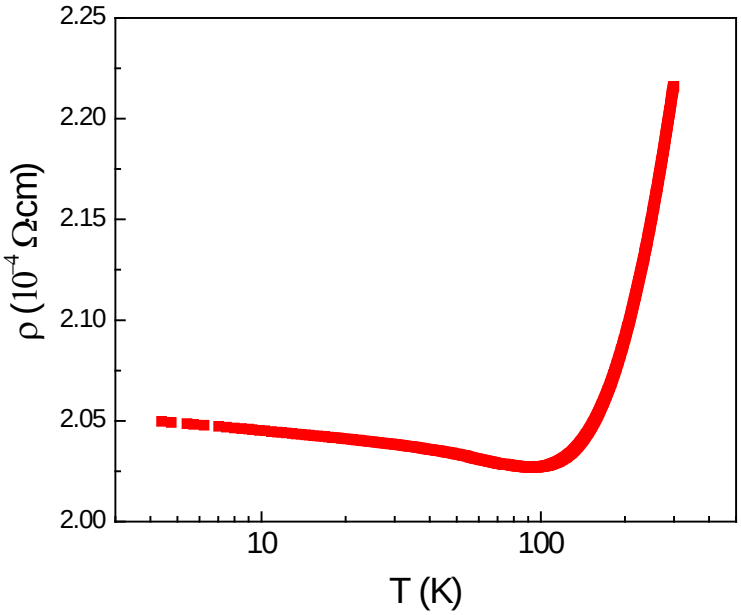

Figure 2.23. Temperature dependence of the resistivity (ρ-T) of a 200 nm Sn-doped In_2O_3 (ITO) thin film deposited on a $LaAlO_3$ substrate at 750 °C and 200 mTorr oxygen pressure.

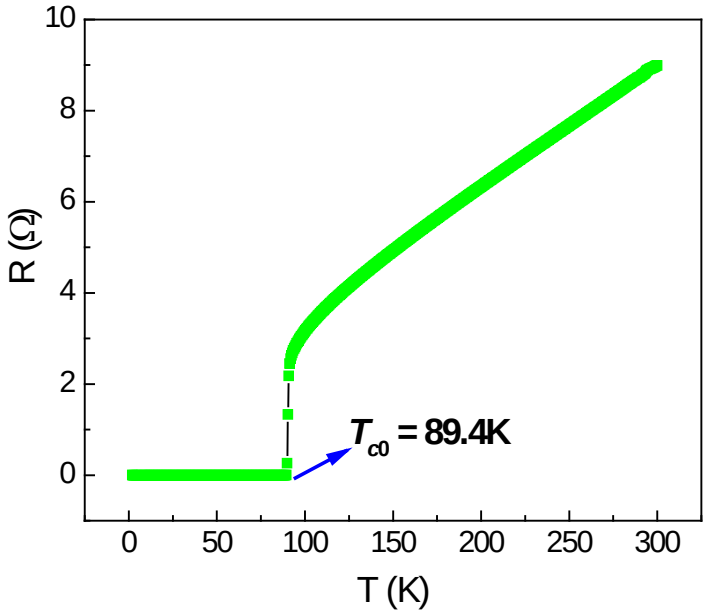

Figure 2.24. Temperature dependent resistance (R-T) of a 100 nm $YBa_2Cu_3O_7$ thin film deposited on a $SrTiO_3$ substrate at 750 °C and 200 mTorr oxygen pressure followed by air-annealing at 600 °C for 30 mins.

The temperature dependent resistance (*R-T*) of a thin film of the most famous high temperature superconductor $YBa_2Cu_3O_7$ is shown in Figure 2.24. At 89.4 K, the resistance drops down to zero, which means the material has transformed into a superconducting state.

The other four-probe resistance measurement geometry is van der Pauw geometry, where the two voltage electrodes are parallel to the two current probes but not in a line. A typical van der Pauw measurement geometry is drawn in Figure 2.25 for a square sample. A current is injected along the edge

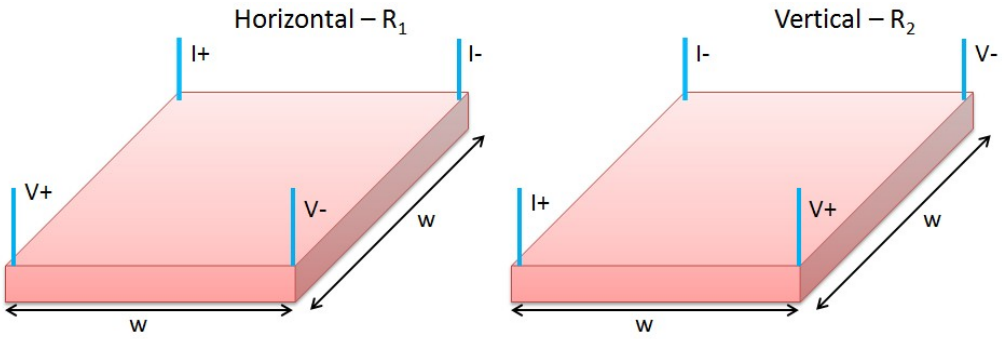

Figure 2.25. Schematic of the van der Pauw measurement geometry for a square sample.

of the sample and the voltage across the opposite edge is collected. The intrinsic sheet resistance R_s of a square sample can be deduced from the van der Pauw equation:

$$e^{-\pi R_1/R_s} + e^{-\pi R_2/R_s} = 1 \qquad (2\text{-}12)$$

where R_1 and R_2 are resistance measured along two different directions as drawn in Figure 2.25.

In general the van der Pauw equation cannot generate a specific function for sheet resistance calculation. In the simplest case, $R_1 = R_2 = R$, then the sheet resistance can be simplified as:

$$R_s = \frac{\pi}{\ln(2)} R \tag{2-13}$$

In practice, R_1 is always different from R_2 and therefore the van der Pauw equation has to be numerically solved to obtain R_s. An example of a van der Pauw measurement of the 2DEG at $LaAlO_3/SrTiO_3$ interface is shown in Figure 2.26, where R_1 differs from R_2 over the whole temperature range.

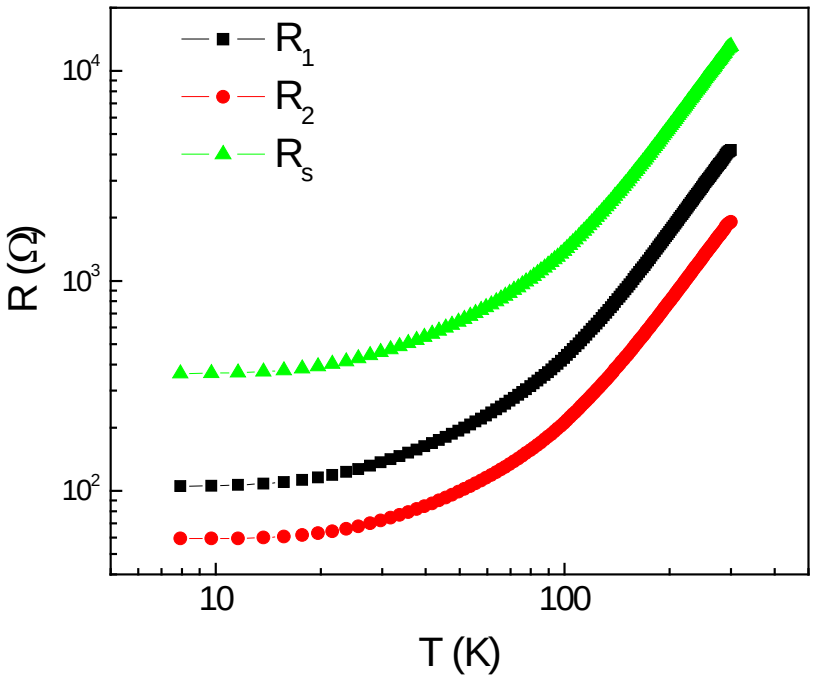

Figure 2.26. *R-T* curves of a $LaAlO_3/SrTiO_3$ heterostructure (fabricated by depositing 10 unit cells of $LaAlO_3$ on a TiO_2-terminated $SrTiO_3$ substrate at 750 °C and 10^{-2} oxygen partial pressure) measured in the van der Pauw geometry. R_s is deduced from R_1 and R_2 by solving the van der Pauw equation using an iterative method.

2.2.2.2 Hall measurements

Hall measurement is based on the Hall effect (Figure 2.27), which is a generation of voltage V_H transverse to the injected current I by a perpendicular magnetic field $\boldsymbol{B}$. For a semiconductor or a metal sample with only one type of charge carrier the Hall voltage is given by:

$$V_H = -\frac{IB}{net} \tag{2-14}$$

where n is the carrier density, e is the elementary charge and t is the thickness of the sample. The Hall coefficient R_H is defined as:

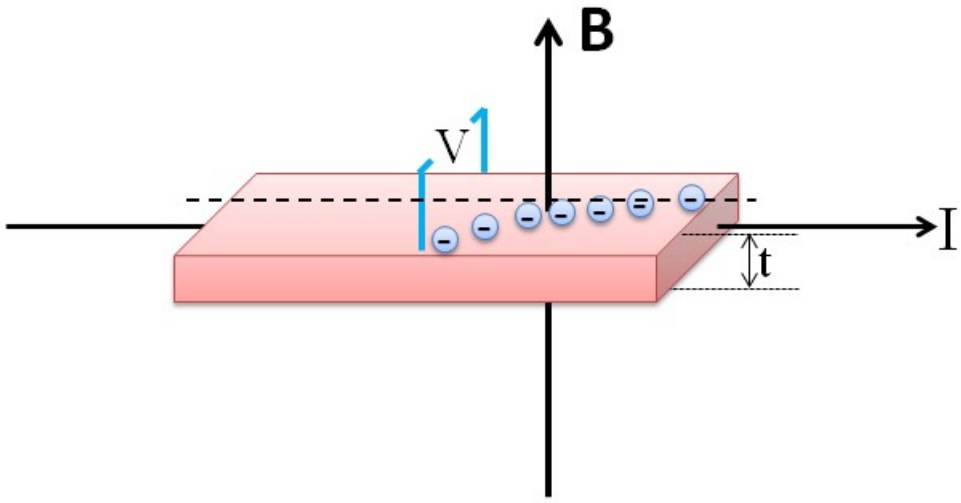

Figure 2.27. Schematic of the Hall effect. The electrons initially move following the dashed line. However, they deviate from that due to Lorentz force generated by the applied magnetic field $\boldsymbol{B}$. Consequently, the electrons accumulate on the one lateral edge of the sample, leading to a voltage across the sample and transverse to the current.

$$R_H = \frac{V_H t}{IB} = -\frac{1}{ne} \tag{2-15}$$

where the unit of Hall coefficient is m^3/C or Ω·cm/G. The Hall effect is commonly used for carrier density determination.

For a thin film sample, van der Pauw geometry (Figure 2.28) is typically used for Hall measurements, where the two voltage electrodes are perpendicular to the two current electrodes. The measured resistance $R = {}^{V_H}/_{I}$

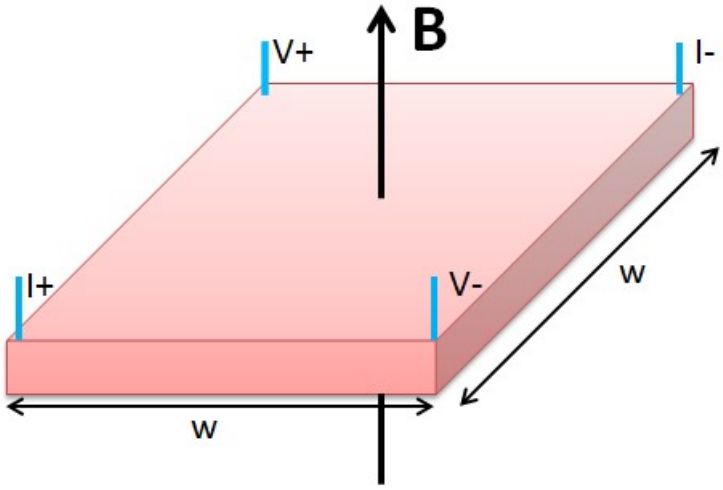

Figure 2.28. Schematic of Hall measurement in the van der Pauw geometry for a square sample.

can be expressed as by

$$R = {}^{V_H}/_{I} = -\frac{B}{net} \tag{2-16}$$

and therefore is a linear function of the applied magnetic field B for a sample with only one type of carrier. The Hall measurement data at 300 K for a 200 nm ITO film deposited on a $LaAlO_3$ substrate at 750 °C and 200 mTorr oxygen pressure is shown in Figure 2.29. The measured resistance is linearly proportional to the magnetic field and the fitted slope is 0.05 Ω/T, which

corresponds to -1/*net* and thus the room temperature bulk carrier density of the ITO film is determined to be -6.23×10^{20} cm^{-3}.

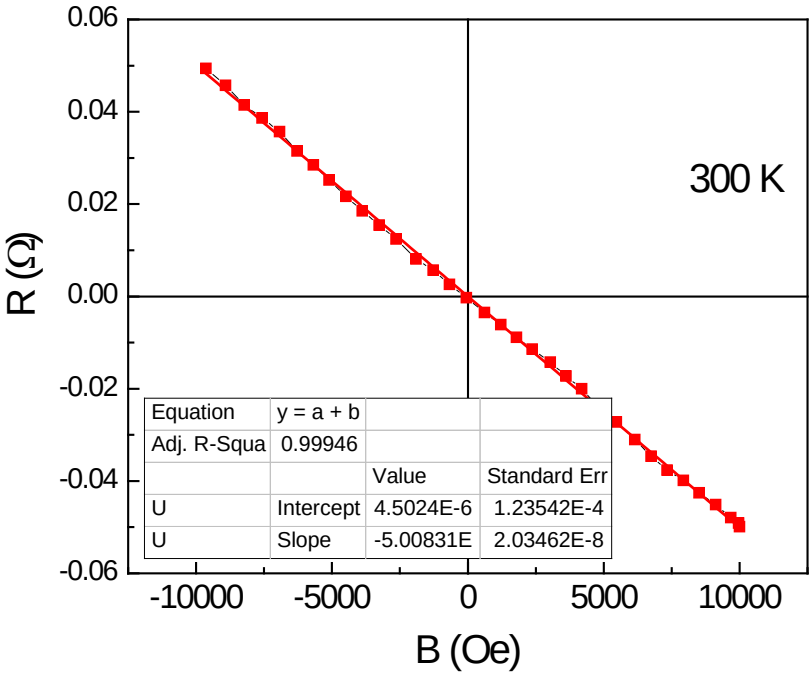

Figure 2.29. Hall measurement data at 300 K for a 200 nm ITO film (red diamonds). The black line is a fitted line.

As the resistivity ρ, carrier density n and mobility μ are related to each other by

$$\rho = 1/(ne\mu) \tag{2-17}$$

and accordingly the room temperature mobility of the ITO film can be deduced from the resistivity and carrier density values. Considering the room temperature bulk resistivity of ITO film is $\rho = R_s t = 2.22\times10^{-4}$ Ω·cm (refer to 2.2.2.1), the mobility at 300 K is $1/\rho ne = 1/(2.22\times10^{-4}\ \Omega\cdot cm \times 6.23\times10^{20}\ cm^{-3} \times 1.602\times10^{-19}\ C) = 44.63\ cm^2/(V\cdot s)$.

A linear dependence of resistance on the magnetic field is the simplest case in Hall measurements. Nevertheless, a nonlinear Hall effect can occur for a sample with multiple types of carriers either with different mobility or with different effective mass. Moreover, the anomalous Hall effect could emerge in ferromagnetic materials, which originates from the superposition of internal magnetization and the external magnetic field. For example, the Hall measurement data at 2 K of a 100 nm $SrRuO_3$ film deposited on a $SrTiO_3$ substrate at 750 °C and 200 mTorr oxygen pressure is shown in Figure 2.30. As $SrRuO_3$ is ferromagnetic below ~160 K, it exhibits an anomalous Hall effect with a hysteresis loop similar to its ferromagnetic loop.

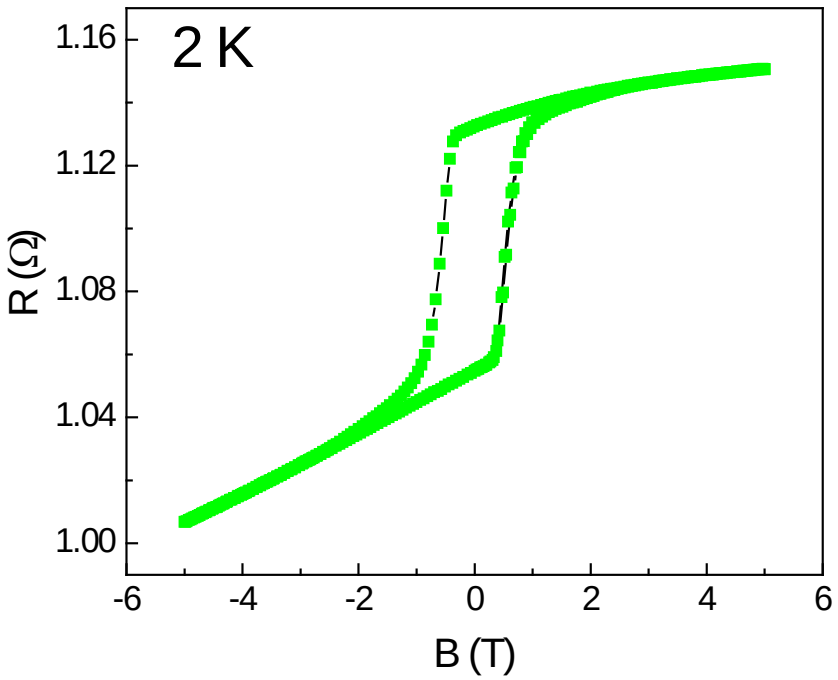

Figure 2.30. Hall measurement data at 2 K for a 50 nm $SrRuO_3$ film grown on a $SrTiO_3$ substrate at 750 °C and 200 mTorr oxygen pressure.

2.2.2.3 Magnetoresistance measurements

Magnetoresistance (MR) is a relative resistance change typically defined as

$$MR = \frac{R(B)-R(0)}{R(0)} \tag{2-18}$$

It is an examination of the effect of an external magnetic field on the transport properties of carriers, by which transport mechanisms and magnetic energy levels can be explored. In a weak magnetic field, electron travelling transverse to the field are scattered by Lorentz force $\boldsymbol{F}$ given by

$$\boldsymbol{F} = q\boldsymbol{v} \times \boldsymbol{B} \tag{2-19}$$

and the effective mean free path of electrons decreases as they are deflected away from the initial current direction. In general, the resistance of a material increases under a magnetic field. In such a case, the MR can be expressed by Kohler's rule

$$MR = \alpha(\mu B)^2 \tag{2-20}$$

where μ is mobility and α is a material and temperature dependent parameter.

Under a strong magnetic field, as originally pointed out by Landau, the motion of a conduction electron is quantized. The effect of the quantization on the MR measurement is most pronounced at low temperatures and high magnetic fields, so that the conditions

$$\omega\tau \gg 1 \tag{2-21}$$

and

$$\hbar\omega \gg kT \tag{2-22}$$

can be satisfied, where ω is the cyclotron resonance frequency, τ is the relaxation time, $\hbar$ is the Planck constant and k is the Boltzmann constant.

The quantized energy levels is expressed by

$$E_n = (n + \tfrac{1}{2})\hbar\omega \tag{2-23}$$

for non-relativistic particles. As E_n reaches E_F, the system energy peaks and the resistance reaches its minimum, where

$$E_n = \left(n + \frac{1}{2}\right)\hbar\omega = \left(n + \frac{1}{2}\right)\hbar\frac{eB_n}{m_c} = E_F \tag{2-24}$$

and therefore

$$\frac{1}{B_n} - \frac{1}{B_{n-1}} = \frac{\hbar e}{m_c E_F} \tag{2-25}$$

where m_c is the cyclotron mass. In such a case, the system resistance oscillates with $1/B$ at a period of $\hbar e/m_c E_F$, which is referred as Shubnikov-de Haas Oscillations [77]. The amplitude of the oscillations A is dependent on temperature, magnetic field and the cyclotron mass

$$A \propto TB^{1/2} exp(-2\pi^2 kT/\beta^* B) \tag{2-26}$$

with

$$\beta^* = \frac{\hbar e}{m_c} \tag{2-27}$$

being the effective double Bohr magneton. For a fixed *B*, the plot of *ln*(*A*/*T*) as a function of *T* yields a straight line and the cyclotron mass m_c can be fitted from the slope, the so called Dingle Plot [78,79].

For relativistic particles, the quantized energy is expressed by

$$E_n = sgn(n)\sqrt{2e\hbar {v_F}^2|n|B} \tag{2-28}$$

where v_F is the Fermi velocity. Thus the quantum oscillations in MR is expressed as follows:

$$\frac{1}{B_n} - \frac{1}{B_{n-1}} = \frac{8\hbar e}{{m_c}^2 {v_F}^2} \tag{2-29}$$

by virtue of which the cyclotron mass m_c can be obtained from fitting the oscillation period [80].

The condition (2-22) $\hbar\omega \gg kT$ to ensure that all electrons are in the lowest quantum magnetic level has been coined as “quantum limit” by Argyres and Adams [81]. In such a case, the MR is positive and linearly proportional to *B*. On the contrary, when $\hbar\omega \ll kT$, the motion of electrons is characterized by large quantum numbers. According to the correspondence principle, the quantum treatment yields the same results with the semi-classical treatment, which neglects the quantization.

Moreover, MR could be negative, which mostly appears in ferromagnetic materials, Kondo scattering systems and weak localization systems. The origin of the negative MR in ferromagnetic and Kondo systems are all because magnetic (or spin-dependent) scatterings are suppressed by an external

magnetic field as magnetic field can align randomly-oriented or antiparallelly-aligned spins. The MR of a ferromagnetic $SrRuO_3$ thin film is shown in Figure 2.31, showing a butterfly loop due to its internal magnetic hysteresis. However, the negative MR in weak localization systems originates from the destruction of the coherent self-intersecting interference of electrons by a

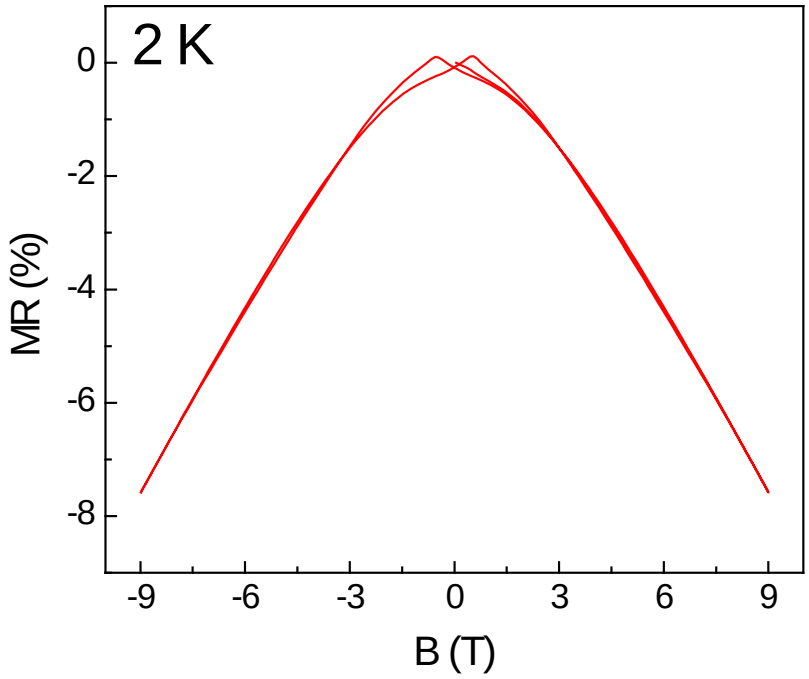

Figure 2.31. Magnetoresistance (MR) of a 50 nm $SrRuO_3$ film (deposited on a $SrTiO_3$ substrate at 750 °C and 200 mTorr oxygen pressure) at 5 K. The magnetic field is applied parallel to the current.

magnetic field. Specifically, a perpendicular magnetic field adds an additional phase to the electron wave function of an electron travelling along a circle (Aharonov-Bohm-**AB** effect). In a weak localization system, an electron is elastically scattered back by disorders and a coherent interference occurs for it at the intersecting point of the electron path. The interference leads to the increase in resistivity (refer to Figure 2.23). An example of the negative MR in a weakly localized ITO film is shown in Figure 2.32. Such a quantum

interference effect typically yields a MR of a few percents and only the magnetic field perpendicular to the electron orbital plane works.

Regarding MR measurements, another important aspect is anisotropic MR (AMR), which means MR varies with the angle between magnetic field and current. Obviously, as elaborated above, the MR of a 2D weak localization system is strongly anisotropic since a negative MR effect occurs

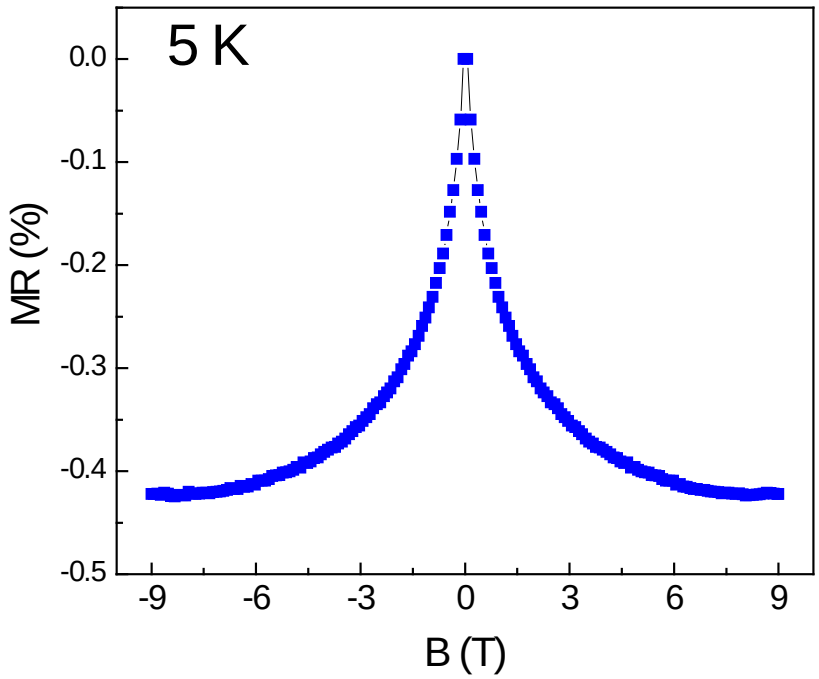

Figure 2.32. Magnetoresistance (MR) of a 200 nm ITO film (deposited on a $LaAlO_3$ substrate at 750 °C and 200 mTorr oxygen pressure) at 5 K, showing a negative MR, evidence for the weak localization. The magnetic field is normal to the film surface.

only as the magnetic field is perpendicular to the sample surface. On the contrary, a Kondo system typically shows an isotropic MR although it can also lead to a low temperature resistance upturn in *R-T* curves similar to the weak localization [82]. Other well-known sources [83] for AMR are orbital

scattering due to Lorentz force, Fermi surface effects and spin-orbit interactions. The MR in orbital scattering can be denoted as

$$MR \propto (Bsin\theta)^2 \tag{2-30}$$

where θ is the angle between the magnetic field and current. Fermi surface effect can generate sharp AMR features with the symmetry of the crystal for clean metals at high magnetic fields, which occurs as the angle of the applied field changes the Fermi surface orbit in momentum space from closed to open [84]. The MR is linearly proportional to B for closed orbits while proportional to B^2 for open orbits. Such Fermi surface effects demand $\omega\tau \gg 1$. AMR due to spin-orbit interaction mostly appears in ferromagnetic systems, which is closely related to magnetization and disappears above Curie temperature [83].

2.2.3 Magnetic characterization

Magnetic measurements are to detect magnetic moments in a system. What is available in our lab for magnetic measurements is a Quantum Design Superconducting Quantum Interference Device — Vibrating Sample Magnetometer (SQUID-VSM), which is shown in Fig. 2.33.

It has a sensitivity of 10^{-8} emu. The maximum magnetic field is 7 T and the lowest temperature is 2 K. SQUID-VSM combines the speed of a VSM with the sensitivity of a SQUID.

Figure 2.33. Photograph of the Quantum Design superconducting quantum interference device – vibrating sample magnetometer in our lab.

By controlling the temperature and magnetic field, the magnetic moment *m* of a sample can be measured as a function of temperature (*m*-*T*) and magnetic field (*m*-*H*). Typically, a ferromagnetic sample exhibits hysteresis loops in *m*-*H* curves. Below its Curie temperature T_c, the magnetic moment increases with lowering temperature dramatically and tends to saturate at low temperatures, while it is much less affected by temperature above T_c. On the contrary, the magnetic moment of an antiferromagnetic sample decreases with lowering temperature below its Neel temperature T_N. The total magnetic moment of a diamagnet is always negative, which indeed means the direction

of magnetic moments is opposite to that of the applied magnetic field. Moreover, the magnetic moment of a paramagnet linearly scales with 1/*T*.

An *m*-*T* curve measured by a 1000 Oe magnetic field is shown for a ferromagnetic $SrRuO_3$ thin film in Figure 2.34, which displays a Curie temperature of ~165 K. For comparison, an *m*-*T* curve of antiferromagnetic CuO is shown in Figure 2.35. Below 230 K, the magnetic moment apparently decreases with lowering temperature. Nevertheless, the characteristic of *m*-*T* curve of a diamagnet is much simpler as the magnetic moment of a diamagnet is almost independent of temperature. The magnetization of a pristine $SrTiO_3$ single crystal is illustrated in Figure 2.36, which is an ideal diamagnet.

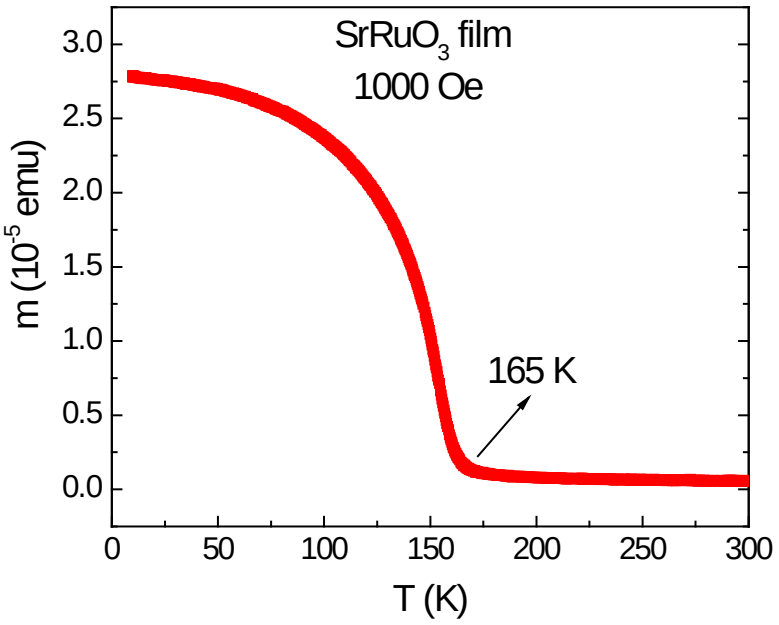

Figure 2.34. Temperature dependent magnetic moment (*m*-*T*) of a $SrRuO_3$ film (deposited on a $SrTiO_3$ substrate at 750 °C and 200 mTorr oxygen pressure)

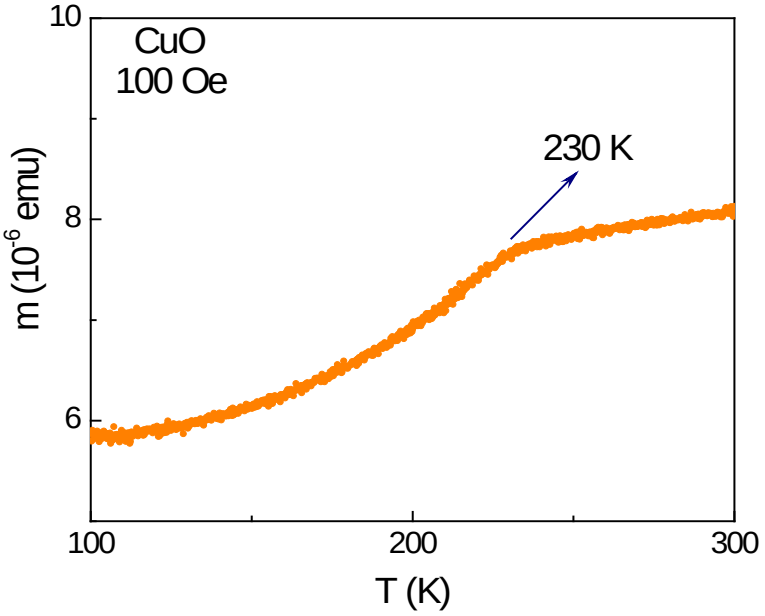

Figure 2.35. *m-T* of CuO powder measured by a 100 Oe magnetic field.

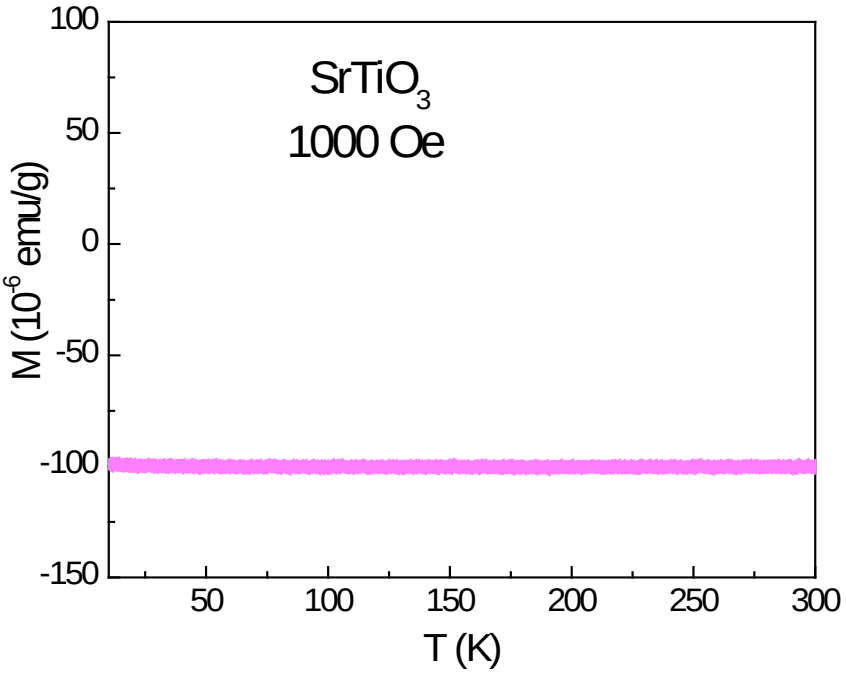

Figure 2.36. Mass magnetization (measured by a 1000 Oe magnetic field) as a function of temperature for a $SrTiO_3$ single crystal.

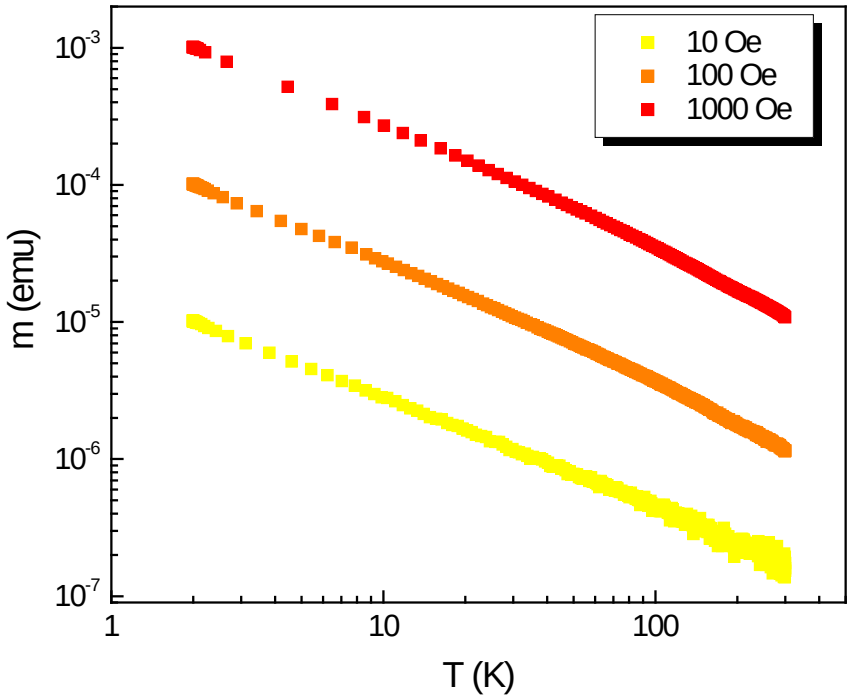

Figure 2.37. *m-T* curves of Cu-doped $LaAlO_3$ measured by different fields.

As an example for paramagnetism, I would like to show *m-T* curves of Cu-doped $LaAlO_3$ in Figure 2.37. As can be seen, the logarithmic plots display linear *m-T* curves, characteristic of paramagnetism.

The *m-T* measurement is a useful approach to examine the superconducting state due to the Meissner effect. A superconductor is a diamagnet below its T_c. The *m-T* curve of a $YBa_2Cu_3O_7$ thin film grown on a $LaAlO_3$ substrate is shown in Figure 2.38, where a diamagnetic transition at its critical temperature of ~91 K can be clearly seen.

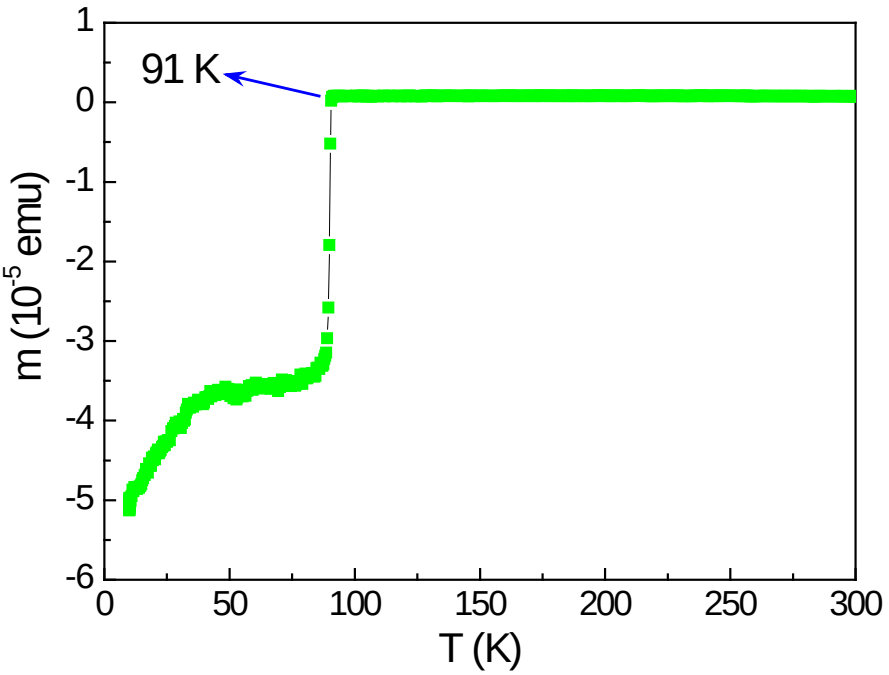

Figure 2.38. *m-T* curve of a 100 nm $YBa_2Cu_3O_7$ thin film depoisted on a $LaAlO_3$ substrate at 750 °C and 200 mTorr oxygen partial pressure.

In some materials, a new magnetic state could emerge due to magnetic frustrations disorders, where spins are frozen in random directions below a certain temperature called spin freezing temperature T_f. Above T_f, spins are fluctuating but below T_f spins are frozen in random directions determined by

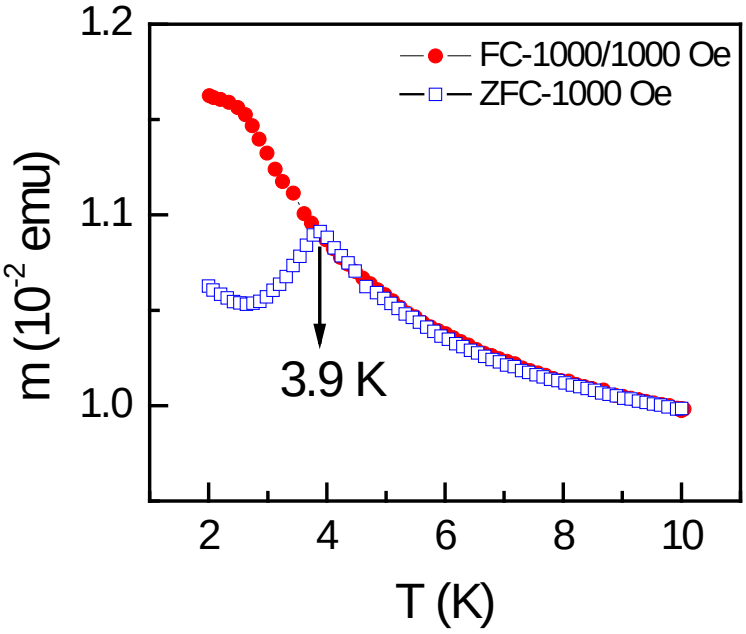

Figure 2.39. *m-T* curves of a (110)-oriented $DyScO_3$ single crystal (5×5×0.5 mm^3) measured along its in-plane (1-10) direction via different measurement procedures.

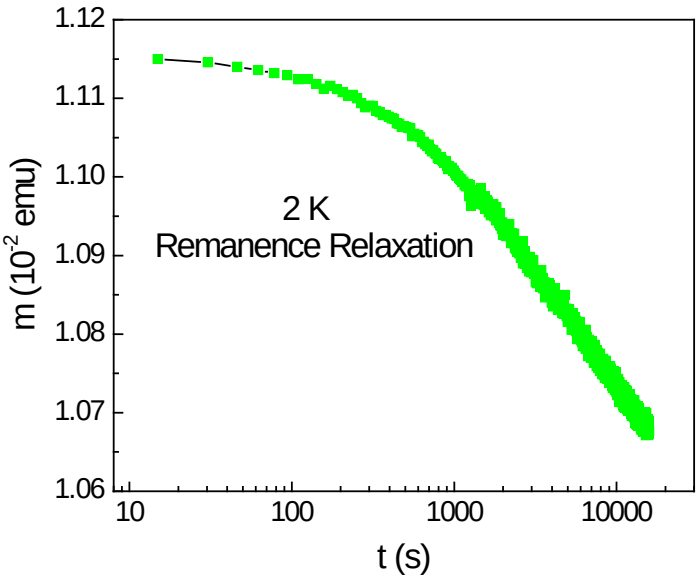

Figure 2.40. Time dependence of thermoremanent magnetization at 2 K for the $DyScO_3$ single crystal, signature of spin glass.

local magnetic anisotropy. Such materials are named spin glasses. A spin glass system shows distinct peak at T_f in zero-field-cooled (ZFC) magnetization, while field-cooled (FC) magnetization increases or keeps flat below T_f.

Therefore, there is a bifurcation in ZFC and FC *m*-*T* curves at T_f (seen in Figure 2.39). It is worth mentioning that the bifurcation in ZFC and FC *m*-*T* curves could be suppressed by a large measuring field. Typically there are three main characteristics for a spin glass system. They are (i) frozen-in magnetic moments below a freezing temperature T_f and hence a peak in the frequency-dependent susceptibility shifting with frequency; (ii) lack of periodic long-range magnetic order; (iii) remanence and magnetic relaxation (seen in Figure 2.40) on macroscopic time scales below T_f [85].

2.2.4 Optical characterization

The main optical characterization techniques utilized in my research are ultraviolet visible near-infrared spectroscopy and photoluminescence spectroscopy. I will discuss these two techniques one by one in this section.

2.2.4.1 Ultraviolet visible near-infrared spectroscopy

For short, ultraviolet visible near-infrared spectroscopy is referred as UV-Vis-NIR, which can be used to detect the absorption and transmittance of oxide materials. Typically, UV-Vis radiation is useful to detect the electronic band gap of large bandgap oxide materials. A UV-Vis-NIR spectrometer in our lab is shown in Figure 2.41. A classical semiconductor with an electronic bandgap exhibits a minimal optical absorption for photons with energy less than the bandgap and high optical absorption for photons with energy higher than the bandgap. Consequently, there is a sharp increase in absorption or (decrease in

transmittance) at photon energy close to the bandgap, which is known as an absorption edge. Under the parabolic band approximation, the estimation of

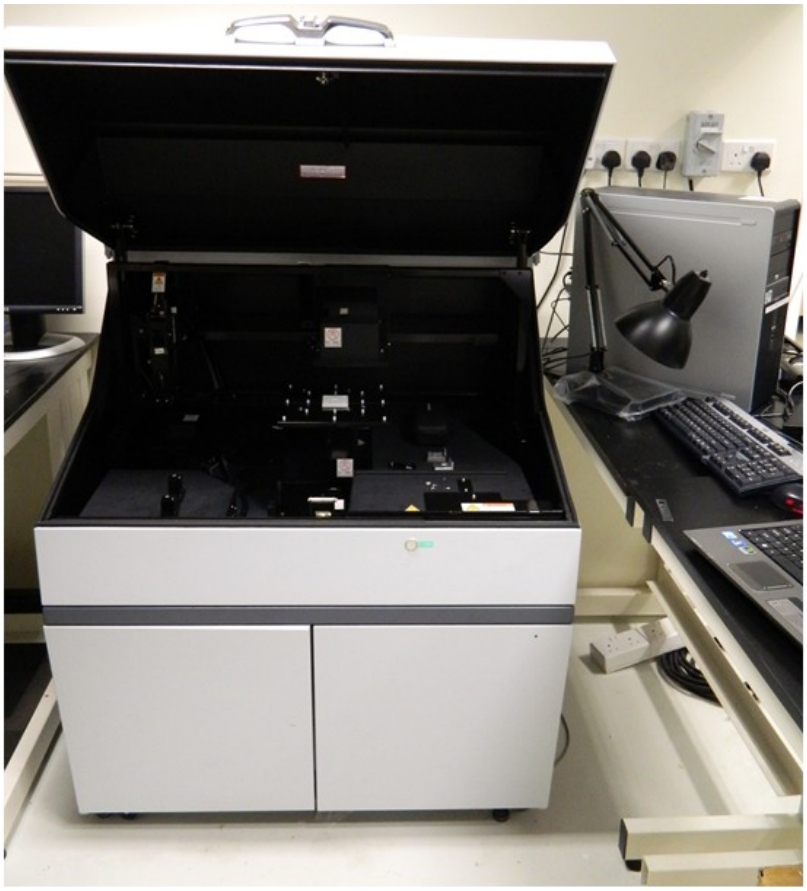

Figure 2.41. Photograph of the ultraviolet visible (UV-Vis) near-infrared spectrometer in our lab.

the bandgap can be performed by using the following formula:

(i) for direct bandgap semiconductors:

$$\alpha \propto \frac{\sqrt{E_p - E_g}}{E_p} \tag{2-31}$$

where α is the absorption coefficient, E_p is the photo energy, and E_g is the band gap energy. E_g is the intercept of the straight line obtained by plotting $(\alpha E_p)^2$ versus E_p.

(ii) for indirect bandgap semiconductors:

$$\alpha \propto \frac{(E_p - E_g)^2}{E_p} \tag{2-32}$$

In this case, E_g is the intercept of the straight line obtained by plotting $\sqrt{\alpha E_p}$ versus E_p.

It is worth noticing that all above formula are under the precondition that the optoelectronic transition occurs in semiconductors between parabolic bands [86]. For some materials which cannot fulfill the parabolic band approximation, the above estimations are invalid.

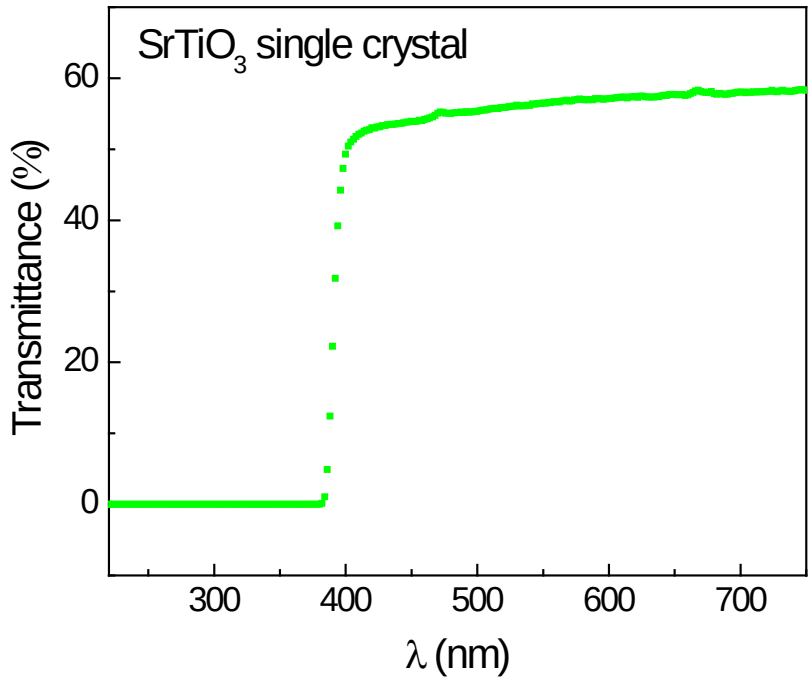

Figure 2.42. UV-Vis transmittance spectra of a $SrTiO_3$ single crystal at room temperature.

The transmittance spectra of a $SrTiO_3$ single crystal is shown in Figure 2.42, which manifests an obvious absorption edge at ~384 nm, corresponding to its indirect bandgap 3.25 eV. UV-Vis-NIR spectroscopy can also be used to

determine thin film thickness by virtue of the Fabry-Perot interference when the thin film surface is sufficiently smooth. When the following condition

$$2n(\lambda)d = m\lambda \tag{2-33}$$

is satisfied, the transmittance peaks, where $n(\lambda)$ is refractive index, d is film thickness and m is an integer and the order of the fringe. Accordingly, the plot of transmittance oscillates with $1/\lambda$ with a period of $1/2n(\lambda)d$. As a result, the thin film thickness can be extracted out. For example, the transmittance of a 2-μm-thick $NdGaO_3$ film grown on a SiO_2 single crystal substrate (Figure 2.43) exhibits oscillations, which periodically oscillates with $1/\lambda$ (Figure 2.44).

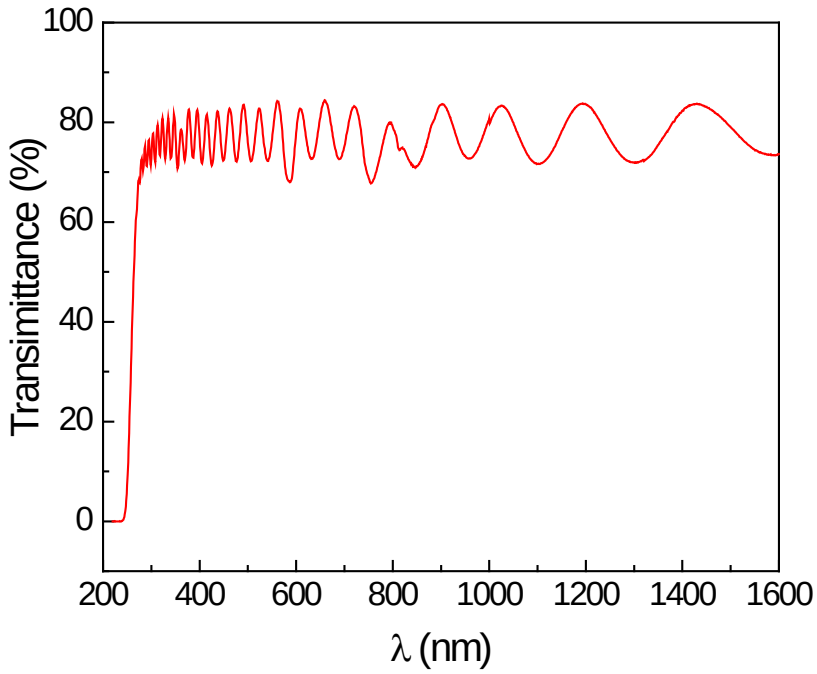

Figure 2.43. UV-Vis-NIR transmittance spectra of an $NdGaO_3$ film grown on a SiO_2 substate at 700 °C and 10^{-2} oxygen pressure.

The nd fitted from Figure 2.44 is 4126 nm. As the average refractive index n is 2.13 [58], the fitted thickness is 1937 nm.

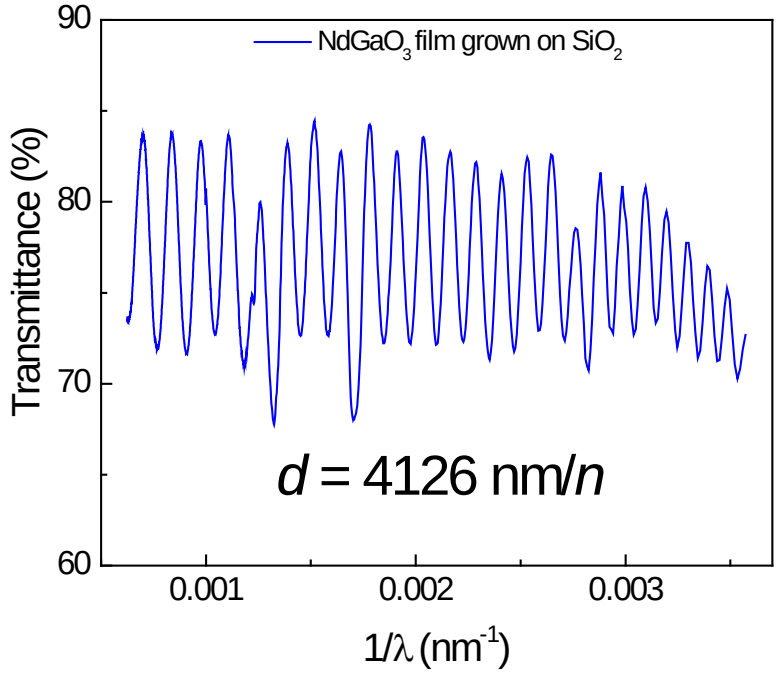

Figure 2.44. Film thickness extracted by fitting a plot of transmittance versus $1/\lambda$.

2.2.4.2 Photoluminescence Spectroscopy

Photoluminescence (PL) in semiconductor materials is a process that the electrons are excited by an incident light (typically a laser light) from the valence band to high energy levels or the conduction band and then decay into lower energy levels or the valence band to recombine with holes, leading to light emission during transitions. Hence, PL spectroscopy is very useful to determine the band gap and intragap defect energy levels in semiconductor materials. It is a contactless and nondestructive method to probe the electronic structure of materials. The PL intensity provides a measure of the relative rates of radiative and non-radiative recombinations as recombination transitions include both radiative and non-radiative processes. Thereinto, non-radiative

recombination is an undesired process in optoelectronic materials, which lowers the light emission efficiency and increases heat loss.

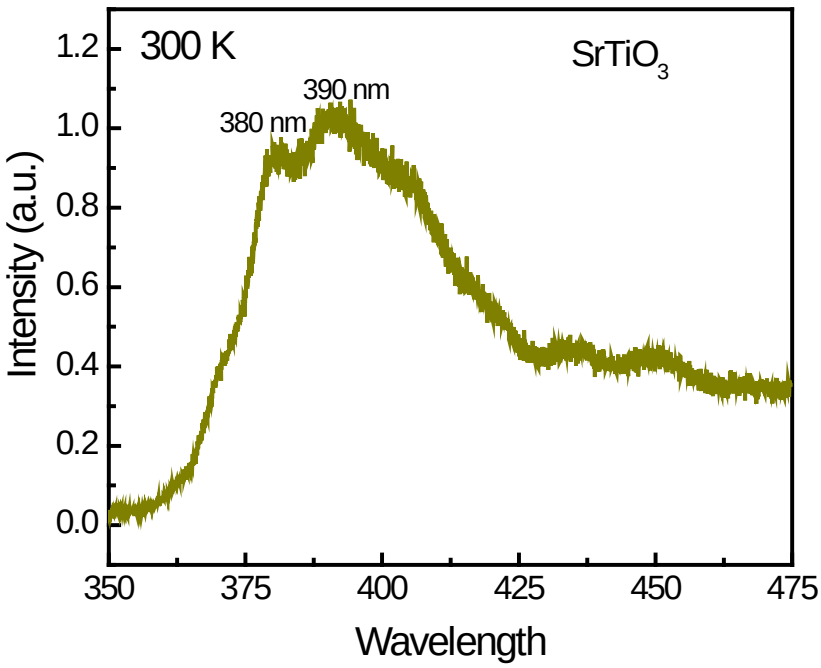

Figure 2.45. Room temperature photoluminescence spectrum of a $SrTiO_3$ single crystal excited by a 325 nm laser.

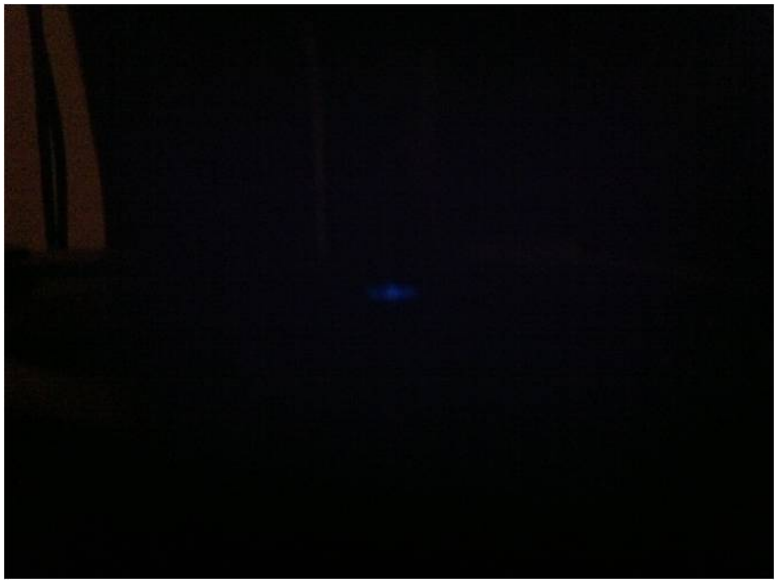

Figure 2.46. Room temperature blue emission of the $SrTiO_3$ single crystal excited by a 325 nm laser.

For example, the room temperature PL spectra of a $SrTiO_3$ single crystal excited by a 325 nm laser is shown in Figure 2.45, where a broad emission peak at ~390 nm can be clearly seen. Correspondingly, it shows visible blue emission at room temperature in Figure 2.46. The emission peak at 380 nm corresponds to an energy interval of 3.26 eV, coinciding with the indirect band gap [49] of $SrTiO_3$. Nevertheless, the emission at a longer wavelength of 390 nm pertains to a lower energy interval of 3.17 eV, originating from shallow defect donor level of oxygen vacancies [87].

Chapter 3 Oxygen vacancy-mediated transport in $SrTiO_3$

$SrTiO_3$ (STO) is the most important workhorse in modern oxide electronics. It is a striking material since it becomes an intrinsic quantum paraelectric below 4 K with a giant dielectric constant ϵ_r [50]. It is a band insulator with a large bandgap of 3.25 eV and therefore stoichiometric STO is electrically insulating. However, extrinsic doping such as Nb [88] and oxygen vacancies [89] can convert it into a metal as long as the carrier density originating from doping hits the Mott critical carrier density of STO. Generally, electrons in STO possess high mobility (> 10 000 $cm^2V^{-1}s^{-1}$) at low temperatures and a large density-of-states effective mass $m_D \approx 5\text{-}6m_0$ [77,88] as well as a large cyclotron mass $m_c \approx 1.5\text{-}2.9m_0$ [77], where m_0 is the electron rest mass. In this chapter, we will discuss the transport properties of oxygen-deficient STO single crystals and STO thin films.

The critical carrier density for the metal-insulator transition in a carrier system is generally given by Mott's criterion

$$n_c \approx (0.25/a^*)^3 \tag{3-1}$$

where

$$a^* = 4\pi \epsilon_r \epsilon_0 \hbar^2/(m_D e^2) \tag{3-2}$$

is the effective Bohr radius. Again considering at room temperature $\epsilon_r \approx 300$ and $m_D \approx 5m_0$ for STO, the Mott critical carrier density is $n_c \sim 4.9\times10^{17}$ cm^{-3}.

3.1 Transport properties of $SrTiO_{3-x}$ single crystals

Magnetic quantum effects such as Shubnikov-de Haas oscillations usually can be observed in high-mobility systems. However, the additional conditions on Femi energy

$$E_F = (\hbar^2/2m_D)(3\pi^2 n)^{2/3} >> kT \tag{3-3}$$

and magnetic energy (Equation 2-22) must also be satisfied, where E_F is Fermi Energy, n is carrier density, and B is magnetic field. Taking $m_c = 2m_0$ for example, the magnetic energy $\hbar w_c$ of 9 T is 0.52 eV and starts to exceed thermal energy kT from $T \approx 6$ K. Therefore it is still, to some extent, possible to observe magnetic quantum effects from the viewpoint of the magnetic quantization under usual laboratory magnetic fields.

3.1.1 Magnetic field induced resistivity minimum

Stoichiometric (100)-oriented STO single crystals were reduced in 10^{-7} Torr vacuum at 950°C [88,90] for annealing time varied from 1 to 8 h. The electrical contacts were made by wire bonding through aluminum wires. The temperature dependences of the resistivity (ρ-T), carrier density (n-T) and mobility (μ-T) of a sample reduced for 1 h are shown in Fig. 3.1. As seen in Fig. 3.1(a), the sample shows metallic behavior over the whole temperature range from 300 to 2 K. The measured carrier density at 300 K is ~1.5×10^{18} cm^{-}

^{3}, more than three times the critical carrier density n_c ~ 4.9×10^{17} cm^{-3} for metal-insulator transition. That explains why the sample is metallic. Additionally, it is of particular interest that the resistivity below ~80 K is well described by $\rho = \rho_0 + AT^2$ as fitted in the inset of Fig. 3.1(a), indicative of a strongly correlated Fermi liquid.

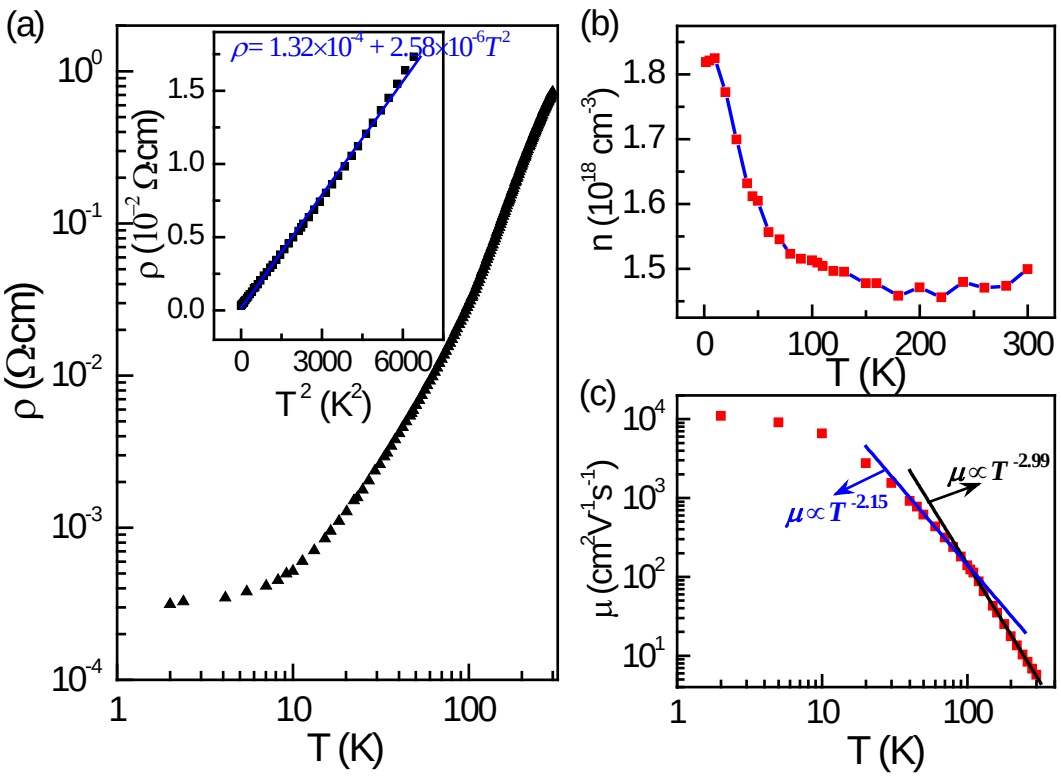

Figure 3.1. Temperature dependences of (a) resistivity (ρ-T), (b) carrier density (n-T), and (c) mobility (μ-T) of a reduced STO single crystal. Inset of (a): linear fitting of T^2 dependence of the resistivity.

The elaborated carrier density in Fig. 3.1(b) was determined by low field (from -2000 Oe to 2000 Oe) Hall measurements, which show an ideal characteristic of an electron-doped system over the whole temperature range. The carrier density changes with temperature although the variation is much smaller than one order of magnitude. At high temperatures, it slightly

fluctuates; surprisingly, the carrier density obviously increases with decreasing temperature at low temperatures especially between 100 and 10 K.

The increase of carrier density with lowering temperature is unusual as the typical thermal activation can only result in the opposite result. This indicates that another mechanism dominates in the temperature dependence of the carrier density in reduced STO single crystals. One of the unique properties of STO is that its dielectric constant increases with lowering temperature (especially below ~100 K) and saturates below 4 K because of the quantum-mechanical stabilization of the paraelectric phase [50]. It seems plausible to assume that in reduced STO part of electrons are trapped by the Coulomb potentials of lots of positively charged defects due to the strongly ionic nature of the lattice. Thus as the dielectric constant increases, the Coulomb potentials will be suppressed due to dielectric screening (or polarization shielding), in which a screened Coulomb potential [91] is inversely proportional to ϵ_r. Hence the increase of dielectric constant could serve as a kind of detrapping mechanism and consequently account for the increase of carrier density at low temperatures.

The temperature dependence of mobility is plotted on a logarithmic scale in Fig. 3.1(c). The high mobility, up to ~ 11,000 $cm^2\ V^{-1}\ s^{-1}$ at 2 K, decreases with temperature rapidly and varies in accordance with certain power laws above 30 K, where the scattering of electrons by polar optical phonons dominates and results in a power law dependence of mobility on temperature $\mu \propto T^{\alpha}$ [89,92,93]. The effect of the structural phase transition in STO at ~105 K

on the mobility can be apparently seen from the linear fittings owing to the variation of phonons induced by the structural phase transition. Below 30 K, the scattering of electrons is dominated by ionized defects potentials [89] and/or the electron-electron Umklapp scattering because of the Fermi liquid behavior [94] at low temperatures, leading to the deviation of the mobility change with temperature from any power law. However, the electron-electron scattering should be strengthened with increasing carrier density, so the ionized defects scattering should be the predominant mechanism in this case.

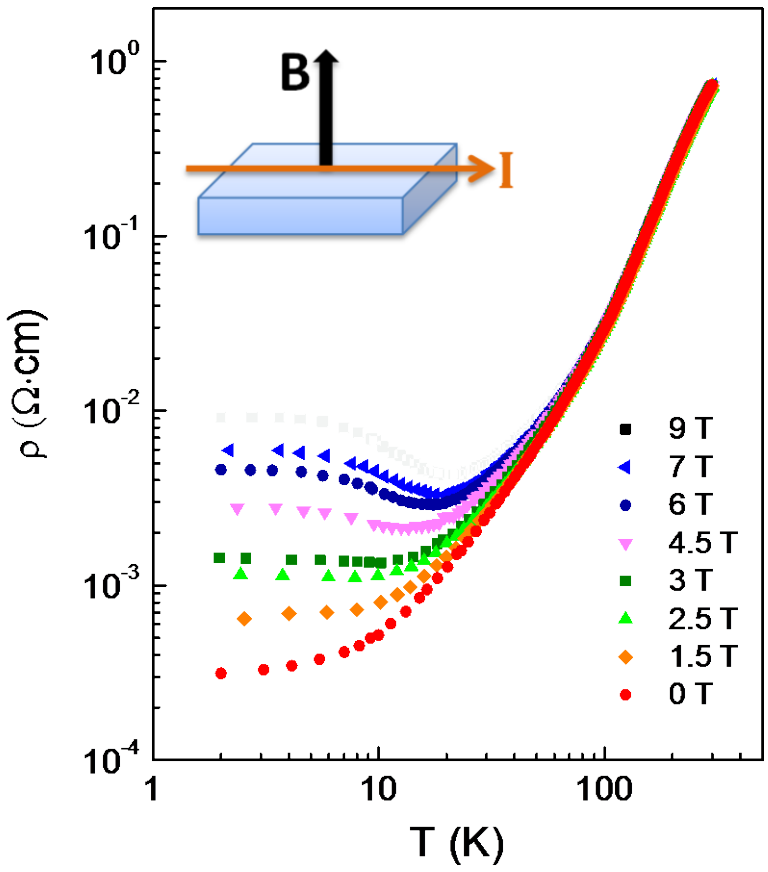

Figure 3.2. *ρ-T* curves of the reduced STO single crystal under different magnetic fields.

Similarly, the mobility further increases with decreasing temperature from 30 K due to the dielectric screening of ionized scattering potentials and also the

increase of the dielectric constant of STO. Finally, saturation appears to present below 5 K, corresponding to the quantum paraelectric phase in STO.

The ρ-T curves under different magnetic fields perpendicular to the sample surface are shown on a logarithmic scale in Fig. 3.2. The transverse MR $\Delta\rho/\rho(0) = [\rho(B)- \rho(0)]/\rho(0)$ is notable only below ~50 K and always positive. Interestingly, the ρ-T curves under sufficient strong magnetic fields equal or larger than 2.5 T show Kondo-like behavior at low temperatures with a resistivity minimum at a certain intermediate temperature T_{min}. The T_{min} increases with magnetic field monotonically as plotted in Fig. 3.3.

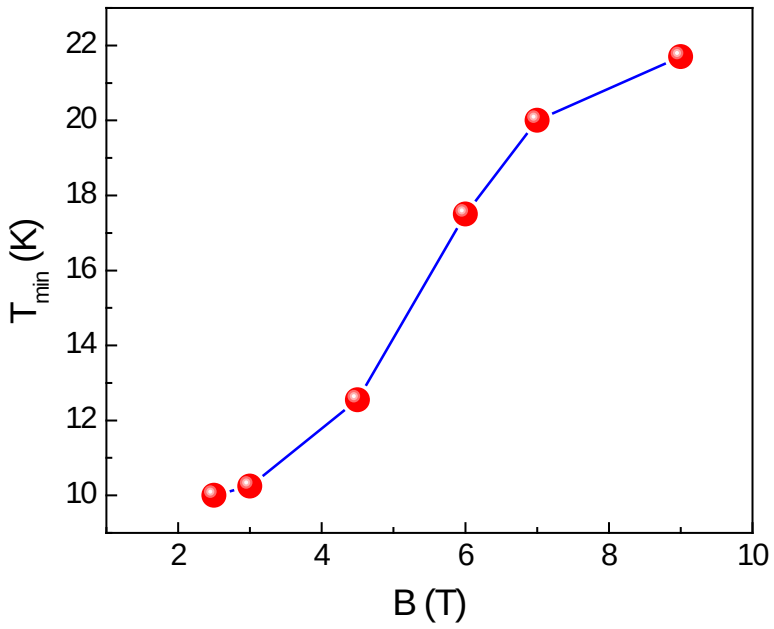

Figure 3.3. Extracted temperature of the resistivity minimum from Fig. 3.2 versus magnetic field.

This resistivity minimum cannot pertain to a Kondo behavior or weak localization because they are inherently antagonistic towards magnetic fields. A possible mechanism responsible for this behavior could be the magnetic field induced carrier freeze-out due to the considerable shrinking of electron

wave functions if the magnetic field strength is much larger than the Coulomb forces [95]. One of the important parameters for magnetic freeze-out is the binding energy E_b, which is proportional to $1/(m_D\ a^*)$ under high fields approximation [96]. Due to the large effective mass and dielectric constant, the binding energy in STO is very small, corresponding to the thermal energy of ~1.4 K even under 10 T as estimated in [96]. That means the magnetic freeze-out can only happen at a temperature smaller than 1.4 K. However, T_m for all the magnetic fields ranging from 2.5 to 9 T is much higher than 1.4 K. On the other hand, the magnetic freeze-out gives rise to the increase of Hall coefficient under strong magnetic fields. To examine this, the high field Hall measurement was performed up to 5 T at 2 K. As seen in Fig. 3.4, the linear Hall effect manifests that large magnetic field is not affecting the carrier density.

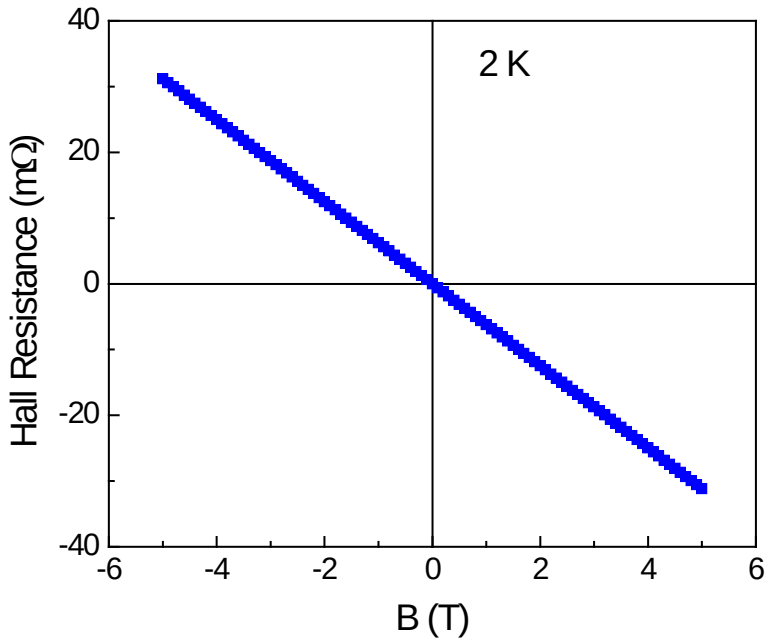

Figure 3.4. Hall effect of the reduced STO at 2 K up to ±5 T.

To further explore the unusual response of the Fermi liquid to the external magnetic field, the low temperature MR was measured up to 9 T with the same measurement geometry as shown in the inset of Fig. 3.2 at 2 and 10 K. As seen in Fig. 3.5, both the 2 and 10 K MR curves show a quadratic dependence, which indicates the classical orbital scattering.

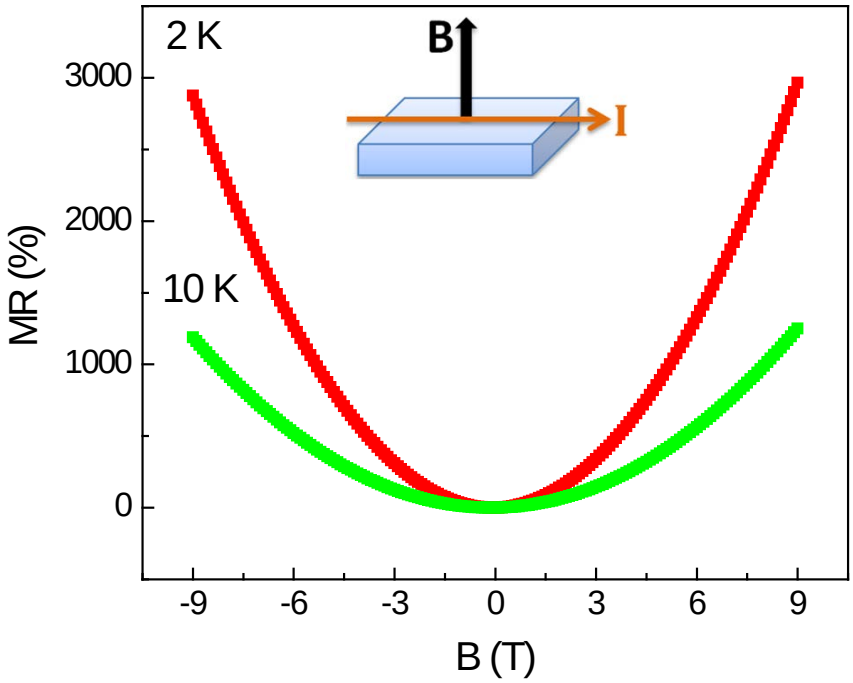

Figure 3.5. Out-of-plane MR of the reduced STO at 2 K and 10 K up to 9 T. Inset: schematic of the measurement geometry.

In spite of the high mobility at 2 K, no any signature of quantum oscillations in MR is seen. The Fermi energy at 2 K is $E_F \approx 1.08$ meV and more than $6kT$ (2 K) if we take $m_D \approx 5m_0$ as before, corresponding to a degenerate gas sate ($E_F \geq kT$). Therefore, there should be a large possibility to observe the quantum MR. However, as a result of the Fermi liquid behavior at low temperatures, both the electron masses m_D and m_c can be largely enhanced by strong electron correlations. The initially assumed degenerate gas seems actually be a non-degenerate ($E_F \leq kT$) "liquid" and the occupation of

magnetic energy levels by electrons may well be smeared out by thermal fluctuations.

The MR of 9 T at 2 K is huge, more than 2900% and decreases to ~1200% at 10 K. The resulting classical transverse orbital scattering can be described by the Kholer's rule $\Delta\rho/\rho(0) = \alpha\mu^2B^2$, where the constant α depends on the properties of the material being considered and μ is carrier mobility. By fitting the MR curves of 2 and 10 K to the Kholer's rule, the average value of α is obtained to be ~3.2×10^{-9} (the mobility and magnetic field are in units of $cm^2V^{-1}s^{-1}$ and T, respectively, during fitting), which is comparable to $\alpha \sim 3.8\times10^{-9}$ in *n*-type InSb [78].

As the mobility at 2 K is larger than that of 10 K in virtue of the dielectric screening, the MR of 2 K is far larger than that of 10 K as shown in Fig. 3.5. Moreover the high mobility at low temperatures yields a large difference in μ^2 of two certain temperature points T_1 and T_2 ($T_2 > T_1$) even with a fixed $\Delta\mu$ as $\mu_1^2 - \mu_2^2 = \Delta\mu(\mu_1 + \mu_2)$. Hence under a sufficiently high magnetic field, the MR difference [MR (T_1) – MR (T_2)] is so large that the overall resistivity $\rho(B, T) = \rho(0, T) + \alpha\mu^2B^2\rho(0, T)$ at a lower temperature T_1 could become larger than that at a higher temperature T_2 although $\rho(0, T_1)$ is smaller than $\rho(0, T_2)$ in the normal metallic state of a Fermi liquid. In this way, the intriguing resistivity minimum under a large magnetic field could be realized.

For a clear comparison, the magnetic field dependences of the resistivity (ρ-B) at 2 and 10 K are depicted in Fig. 3.6, which shows a crossover (data shown only up to 5 T to make it clear) between the two ρ-B curves at ~2.5 T,

above which the resistivity of 2 K exceeds the resistivity of 10 K. The critical magnetic field is well consistent with the one observed in Fig. 3.2.

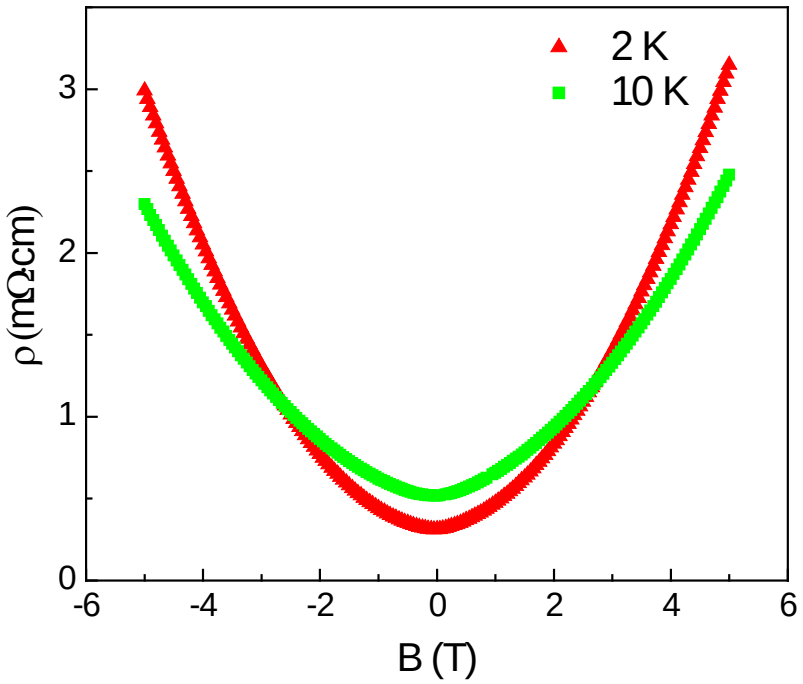

Figure 3.6. Magnetic field dependence of resistivity (ρ-B) for the reduced STO at 2 and 10 K up to 5 T.

Based on the above analysis, the low temperature resistivity $\rho(B, T) = \rho(0, T) + \alpha\mu^2B^2\rho(0, T)$ can be easily simulated up to 80 K by considering the T^2 dependence of $\rho(0, T)$ and mathematically representing the mobility below 30 K with a good exponential fitting. The simulated results are shown in Fig. 3.7, which contains all the main features as in Fig. 3.2; this suggests that the above analysis is not only true for the resistivity comparison between 2 and 10 K but also valid for the other temperatures. Finally, we conclude that the magnetic field induced resistivity minimum is due to the extremely large MR and its pronounced increase with decreasing temperature at low temperatures. The large MR is achieved by fairly high mobility, sufficiently large magnetic fields

and the stabilization of the low-field classical region by strong electron correlations of the Fermi liquid.

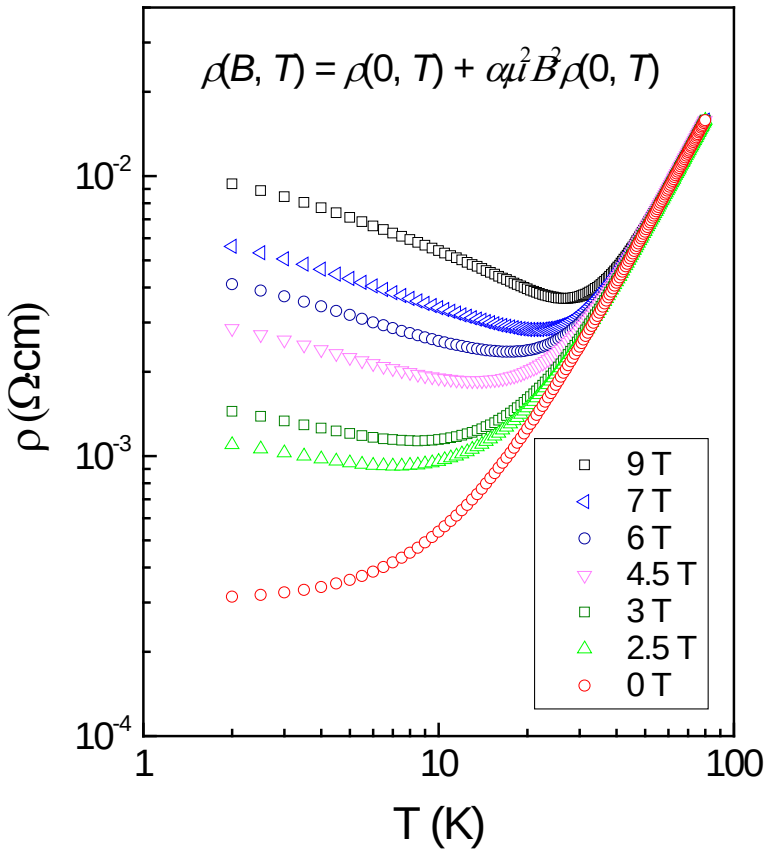

Figure 3.7. Simulated ρ-T curves under magnetic fields $\rho(B, T) = \rho(0, T) + \alpha\mu^2B^2\rho(0, T)$ by taking the power law dependence of the mobility above 30 K as well as the T^2 dependence of $\rho(0, T)$.

A similar behavior was also observed in STO single crystals reduced for 2 h (Fig. 3.8), but with a larger room temperature carrier density ~1.85×10^{18} cm^3 and higher mobility at 2 K. The Fermi liquid behavior, *i.e.* the T^2 dependence of the resistivity, exists in the sample below ~65 K. Nevertheless, as the reducing time was prolonged to 8 hours for a STO single crystal, the obtained room temperature carrier density reaches ~6×10^{18} cm^3 and consequently the mobility at 2 K is only ~2500 $cm^2V^{-1}s^{-1}$. As a result there is no observable resistivity minimum even under a 9 T magnetic field.

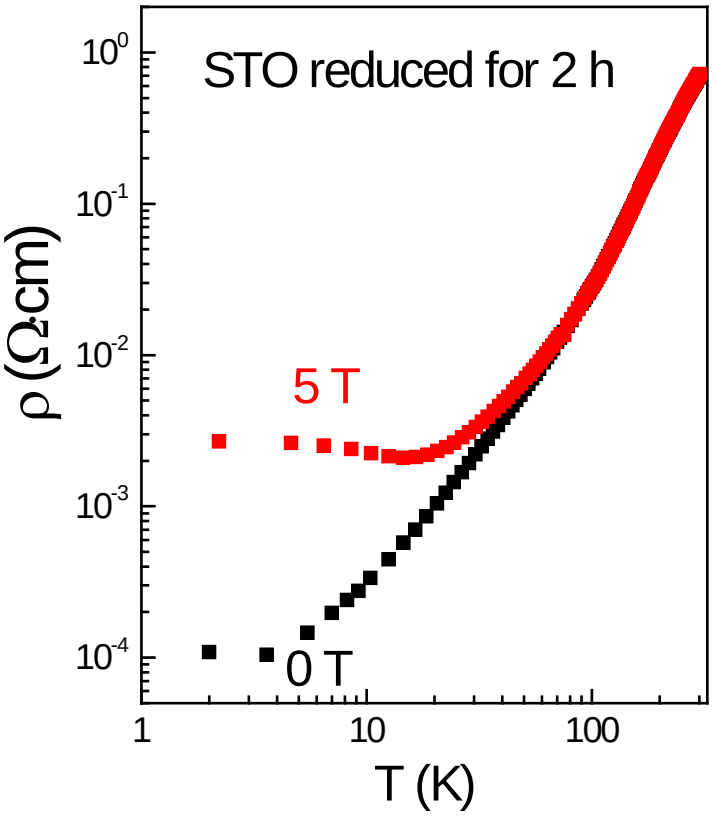

Figure 3.8. ρ-T curves of a reduced STO single crystal (reduced for 2 h at 950 °C and 10^{-7} Torr vacuum) under zero and a perpendicular 5 T field.

3.1.2 Quantum linear magnetoresistance

The condition for the strong-field region $\hbar w_c >> kT$, in which most of carriers are in the lowest Landau magnetic quantum level, was coined as "quantum limit" by Argyres and Adams [81]. The theoretical analysis indicates that for both degenerate and non-degenerate statistics [78], the transverse MR has a quadratic field dependence in the classical low-field case with $\hbar w_c << kT$ but a linear dependence (see also [97,98]) in the quantum limit. Moreover, the other criterion [98]

$$n \ll \left(\frac{eB}{\hbar}\right)^{3/2} \tag{3-4}$$

should also be fulfilled as in high mobility InSb, PbTe and germanium systems [78,99–101] and also in graphite [102]. As shown in Fig. 3.9, the MR curves exhibit highly linear field dependence while the magnetic field is applied in plane and remains transverse to the current. The magnitude of the in-plane MR under 9 T field at 2 and 10 K are ~92% and 66%, respectively, which are much smaller (~30 times for 2K and ~20 times for 10 K) than the out-of-plane values. Accordingly, no crossover in the ρ-B curves (inset of Fig. 3.9) and also no magnetic field induced resistivity minimum was observed. In our case, the

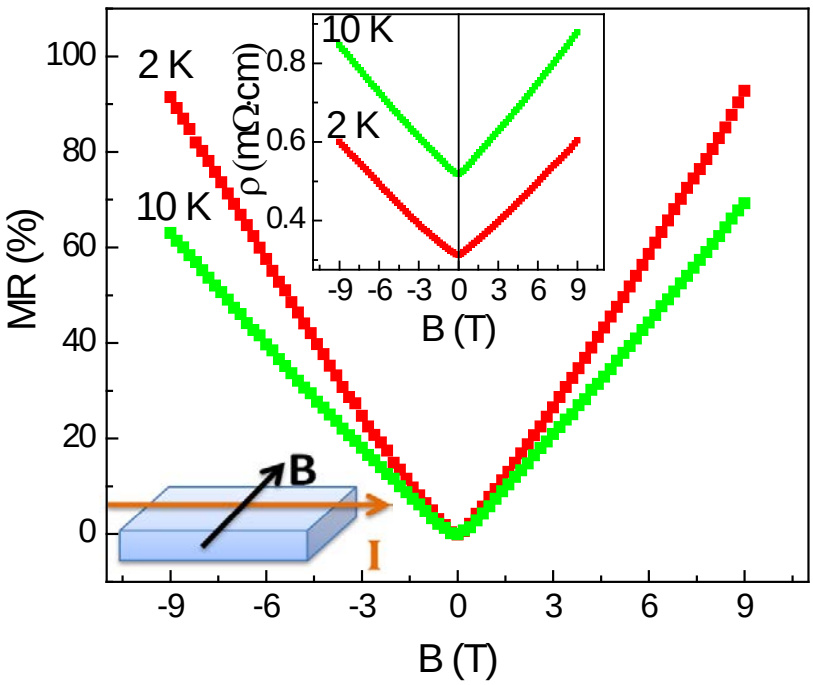

Figure 3.9. In-plane transverse MR of the reduced STO (reduced for 1 h) at 2 and 10 K up to 9 T. The upper and lower insets are the corresponding ρ-B curves of the two temperatures and the schematic of measurement geometry, respectively.

linear MR starts from a very small field < 0.5 T, which corresponds to a critical carrier density of ~1.36×10^{17} cm^{-3} for the usual quantum linear MR. The average carrier density at 2 K in our case is 1.85×10^{18} cm^{-3}, which is one

order of magnitude larger than the critical carrier density for metal-insulator transition. Thus, the linear MR we observed may be out of the usual quantum linear MR picture.

The linear MR starting from small fields was also observed previously in non-stoichiometric silver chalcogenides $Ag_{2+x}Se$ and $Ag_{2+x}Te$ by Xu *et al.* [103]. In those cases, the criteria for the usual quantum linear MR could not be fulfilled either. However, Abrikosov [98,104] proposed another model of quantum linear MR for the $Ag_{2+x}Se$ and $Ag_{2+x}Te$ cases with two assumptions: (i) The substance is inhomogeneous, consisting of clusters of excess silver atoms with a high electron density, surrounded by a medium with a much lower electron density; (ii) in this medium the electron energy spectrum is similar to a gapless semiconductor with a linear dependence of energy on momentum and thereby it can explain all the data in [103] satisfactorily. Our scenario seems quite close to the above cases since the inhomogeneity of oxygen vacancies in $SrTiO_{3-x}$ single crystals has been a long-standing issue [44,105]. Moreover, the oxygen vacancy clustering in $SrTiO_{3-x}$ has been well studied both theoretically by Cuong *et al.* [106] and experimentally by Muller *et al.* [107]. Similar to clusters of excess silver atoms in non-stoichiometric silver chalcogenides, oxygen vacancy clusters have a high electron density. Thus, the linear MR in our case could be another example for the unusual quantum linear MR induced by inhomogeneities and conductive clusters.

Considering the further spin-orbital splitting of the Landau magnetic levels, the energy scale $\mu_B B$ is involved, where μ_B is the Bohr magneton. The

dimensionless parameter $\frac{\rho_B}{\rho_0} \cdot \frac{kT}{\mu_B B}$ is theoretically predicted to be independent of temperature for the quantum limit as illustrated in [99]. This parameter is plotted in Fig. 3.10 as a function of field for two different temperatures and it does approach a constant value. This demonstrates a quantum linear MR behavior for the in-plane transverse MR, corresponding to a much smaller cyclotron mass m_c relative to the out-of-plane case.

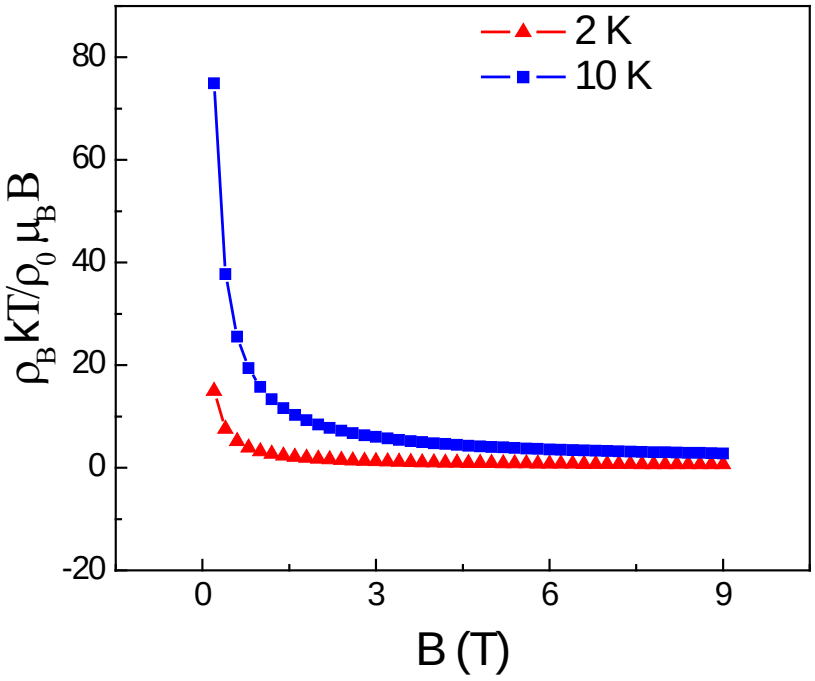

Figure 3.10. The parameter $\rho_B kT/\rho_0 \mu_B B$ plotted as a function of magnetic field.

Although the free electrons are apparently distributed in three dimensional bulk of the reduced STO, the extremely large anisotropy in both MR and also the cyclotron mass strongly suggest that the Fermi liquid dominating the transport properties of reduced STO has a quasi-2D nature. The oxygen vacancies in reduced STO single crystals are far from uniform; contrarily, there is a large concentration gradient from the surface to the interior of the crystals, and the transport properties are dominated by the well surface

area [44]. Therefore the quasi-2D nature of the surface Fermi liquid could be understood by considering the large inhomogeneity of oxygen vacancies and thus the carrier density along the out-of-plane direction due to strong interlayer scatterings. Pushing this mechanism into an extreme case, *i.e.*, assuming there is an extremely sharp gradient in the concentration of donors, the free electrons will be well confined into a quasi-2D electron gas as recently reported [108,109].

The extremely large anisotropy in both MR and the electron cyclotron mass indicates that the observed Fermi liquid dominating the transport properties of reduced STO has a quasi-2D nature. By this work, we demonstrate the crossover between the classical and quantum limit in one system and a simple route to approach the quantum limit, *i.e.*, the possible quasi-2D confinement of carriers in virtue of inhomogeneities.

To examine the effect of inhomogeneity on the in-plane transverse MR, the MR curves of STO single crystals reduced for 1, 2 and 8 h are plotted together in Fig. 3.11. As the reduction time increases, the depth profile of oxygen vacancy concentration becomes flatter and expands into a deeper region. Thus, the confinement of electrons at the surface is suppressed. As a result, the in-plane transverse MR gradually transforms into a quadratic shape.

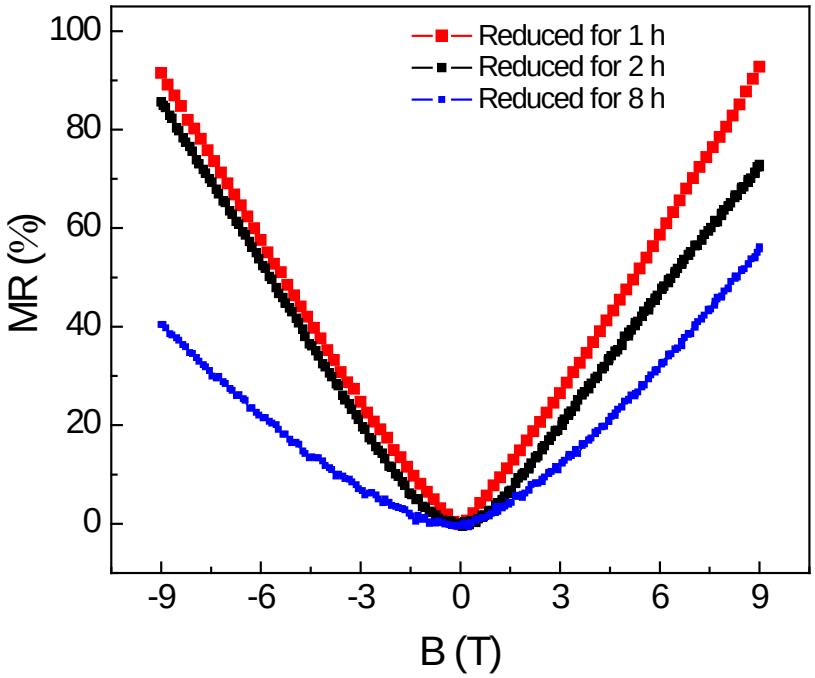

Figure 3.11. In-plane transverse MR at 2 K for STO single crystals reduced for 1, 2 and 8 h.

3.1.3 Summary

In conclusion, we studied the electrical and magnetotransport properties of STO_{3-x} single crystals. It was found that the Fermi liquid exists at low temperatures and the dielectric constant of STO plays an important role in carrier density and mobility. A magnetic-field induced resistivity minimum was observed and it was found to originate from the high mobility and the possible strengthening of the classical limit by mass enhancement due to strong electron correlations. The linear in-plane transverse MR, potential for linear MR sensors, was observed and attributed to the unusual quantum linear MR due to the inhomogeneity of oxygen vacancies and also oxygen vacancy clustering. The large anisotropy in transverse MRs reveals the strong surface interlayer scattering due to the inhomogeneity of oxygen vacancies at the

surface of STO_{3-x}. By this work, we demonstrate a potential route to quantum linear MR by virtue of inhomogeneities.

3.2 Metal-insulator transition in $SrTiO_{3-x}$ thin films induced by carrier freeze-out effect

STO is one of the most fascinating oxides due to its giant dielectric constant. It plays an important role in novel oxide electronics as substrate because of the close lattice match to a wide range of other perovskite oxides [17,110,111] as well as its excellent thermal and chemical stability. STO is a typical nonpolar band insulator with an indirect band gap of ~3.27 eV, but oxygen deficient STO can show a metallic phase with a flexible tunability in electrical conductivity depending on the concentration of oxygen vacancies. More attractively, oxygen deficient STO is the first oxide discovered to be superconductive [90] with the T_c between 0.1 K and 0.6 K [112]. Shubnikov-de Haas (SDH) oscillations [77] are also observed under usual laboratorial magnetic fields due to the high mobility [89] of free electrons. As a result of the large effective mass of the electrons at the bottom of the conduction band, oxygen deficient STO possesses a large Seebeck coefficient of ~890 μV/K at room temperature (RT) [88], thus being a focus point in solid state thermoelectric too.

Although so many interesting properties in oxygen deficient STO, the inhomogeneity of oxygen vacancies obtained by reducing bulk single crystals in vacuum and at high temperature is always an existing issue [77,88–

90,112,113]; that is because the diffusion process of oxygen ions is usually proportional to the square root of time and the diffusion coefficient of oxygen ions in STO is small, namely ~10^{-10} cm^2/s at 950°C [114]. For example, taking 1 h as the annealing time at 950°C, the diffusion length of oxygen ions in single crystal STO will be only ~6 μm in accordance to $l = \sqrt{Dt}$, where D is the diffusion coefficient and t is the annealing time. Tufte and Chapman [89] found that the reduced STO samples begin to reoxidize from a very low temperature of ~500 K; Frederikse *et al.* [77] observed SDH oscillations in reduced STO samples, which theoretically and also experimentally prefer to appear in a system close to a high mobility two-dimensional electron system; these observations suggest that the oxygen vacancies may mostly exist near the surface rather than uniformly over the whole bulk material.

The values of some physical quantities [88–90,112,113] including resistivity and carrier density, derived from the thickness of the whole bulk sample, which was used to characterize the dimension of the conducting area, would be of dubious validity. On the other hand, the intrinsic properties of the material are closely related to these physical parameters. For example, the superconducting transition temperature of oxygen deficient STO apparently depends on the carrier density [112,113]. Additionally, the inhomogeneities could generate significant influence on electrical and galvanomagnetic measurements, and can even give rise to quantum effect – linear magnetic field dependence of the transverse magnetoresistance [115,116]. Nowadays, various fabrication techniques enable us to conveniently prepare high quality

single crystal STO thin film with the thickness smaller than the diffusion length of a feasible annealing time.

3.2.1 Fabrication of $SrTiO_{3-x}$ films

In this work we observed a metal-insulator transition (MIT) in oxygen deficient STO films, in which oxygen vacancies are expected to uniformly distribute. As a highly interesting subject in condensed matter physics, MIT has various intriguing mechanisms [4]. However the MIT observed here is ascribed to the deionization effect of oxygen vacancies with decreasing temperature, which serve as doubly charged donor centers to make STO metallic at high temperatures. Both the resistivity and carrier density are significantly different from the ones of the bulk samples with the carrier freeze-out phenomenon [89], *i.e.*, several ten times smaller and larger, respectively. The frozen non-metallic state can be re-excited by electric field and Joule heating. Surprisingly, it was found that the low temperature carrier freeze-out can also be suppressed by large magnetic fields, leading to negative magnetoresistance (MR).

In this work, the pulsed laser deposition technique was used to fabricate a STO film from a single crystal STO target on a (100)-oriented $LaAlO_3$ (LAO) single crystal substrate with both sides polished. The deposition was carried out at 800°C and 6×10^{-3} Torr O_2. During deposition, the fluence of laser energy was kept at 4 J/cm^2 and the repetition rate of laser was 4 Hz; a shadow mask was used to cover a small part at the corner of the LAO substrate to facilitate the later determination of film thickness. The deposition was

conducted for a long time of 6 h to achieve a film thickness of the order ~μm, which is to keep the properties of the film akin to bulk STO. Cooling to RT was performed at a quite slow ramping rate of 3°C/min to avoid possible cracking of the film, which may occur due to the mismatch of the thermal expansion coefficients of LAO and STO.

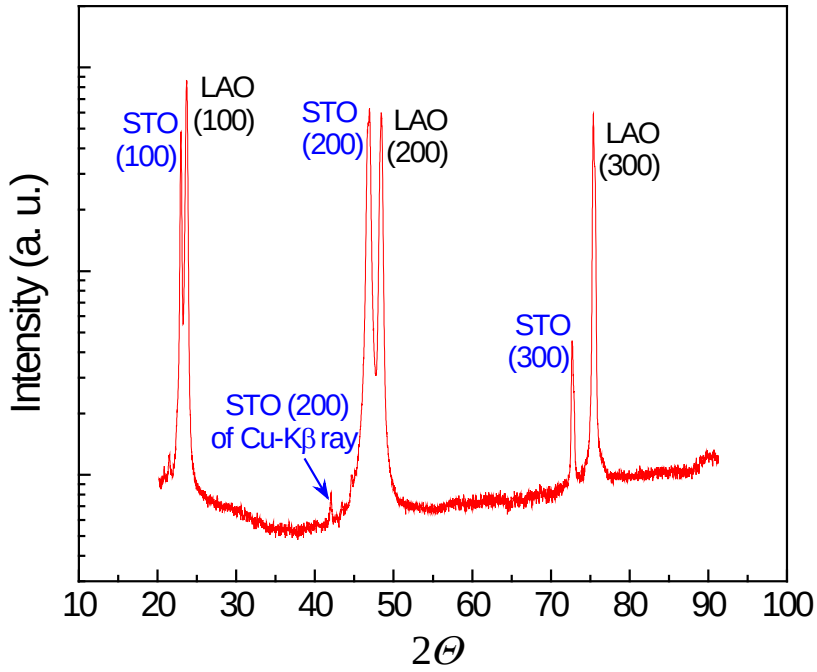

Figure 3.12. X-ray diffraction of an as-grown STO film on a $LaAlO_3$ (LAO) substrate.

The x-ray diffraction (Cu-Kα_1 ray) pattern of the as-deposited STO film on the LAO substrate is shown in Fig. 3.12. The adjacent double diffraction peaks of the film and the substrate for each order indicate the typical characteristic of epitaxial growth. Although there are plenty of twins in LAO single crystals and thus visible twin lines on the surface, the locally flat film can still be obtained. The 3D atomic force microscope image of the topography of the STO film (Fig. 3.13) shows the variation of the *z*-dimension is less than 6 nm. The root mean square value of the surface roughness in this 1 μm×1 μm area

is only ~0.541 nm, revealing a quite flat surface considering the film thickness of ~2.6 μm determined by surface profile measuring system.

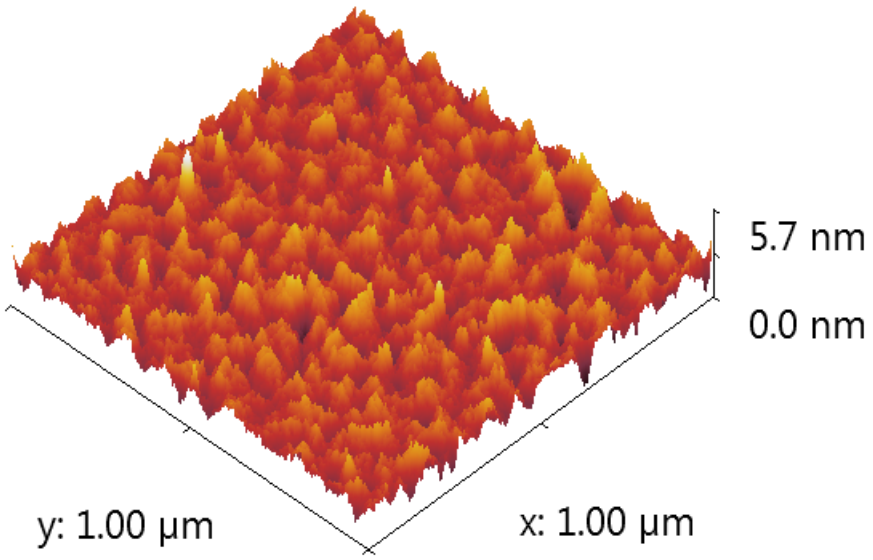

Figure 3.13. 3D atomic force microscope image of an 1×1 μm^2 area of the as-grown STO film.

The deposited STO film was reduced by annealing the sample at 950°C and ~1×10^{-7} Torr vacuum for 1 h. The transmittance spectrum (Fig. 3.14) of the oxygen deficient STO film was measured through ultraviolet-visible (UV) spectroscopy from 240 to 1600 nm. The absorption edge is ~380 nm, well corresponding to the band gap of STO. This suggests that after vacuum annealing the lattice structure of the STO film is still preserved.

The optical spectrum displays an interference pattern with relatively high transmittance above 380 nm, which pertains to a scenario where the thick and highly smooth STO film serves as a Fabry-Perot interferometer. So the transmittance will show a peak when the wavelength of the incident optical wave meets the condition (2-33). To simply estimate the film thickness from the oscillations, take an intermediate refractive index 2.05 [51] to keep *n* as a

constant. Thus if the transmittance data of the wavelength from 380 to 1600 nm are plotted versus $1/\lambda$ as shown in the inset of Fig. 3.14, the average period of the oscillations in $1/\lambda$ will be $1/2n(\lambda)d$. The fitted average period is 9.664×10^{-5} nm^{-1} and therefore the derived thickness is 2.524 μm. The value is consistent with the directly measured one but slightly smaller since the intrinsic refractive index should be smaller than that of a usual STO film due to the oxygen vacancies [117].

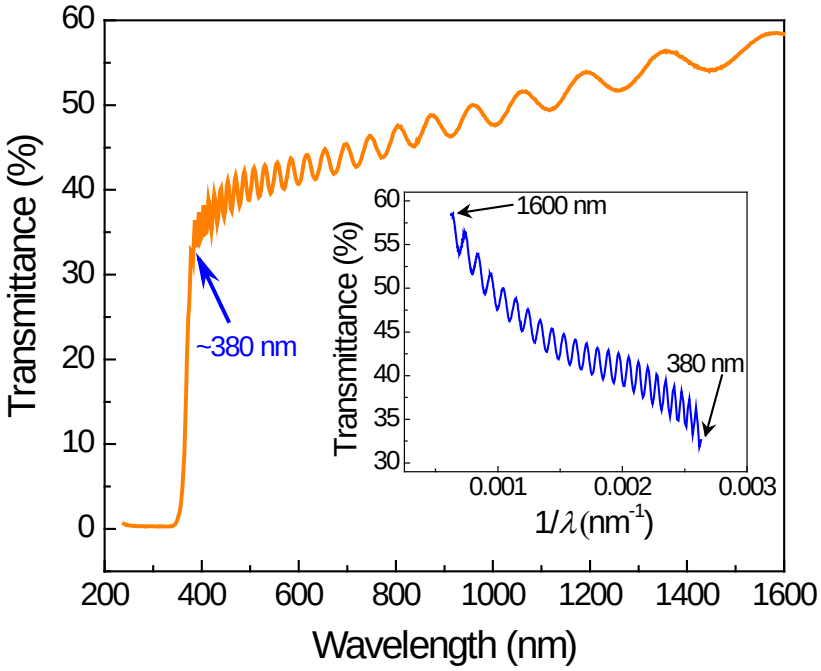

Figure 3.14. Room temperature ultraviolet-visible-infrared spectroscopy of the reduced STO film (obtained by annealing in ~1×10^{-7} Torr vacuum at 950°C for 1 hour) from 240 to 1600 nm. (Inset) The transmittance data plotted versus the reciprocal of the wavelength from 380 to 1600 nm.

The optical absorption of free electrons generated from oxygen vacancies is not seen in the UV spectroscopy, which typically leads to a decrease in transmittance especially in the long wavelength region and is likely buried by the strong interference here. However, the multiple photoluminescence (PL) emission peaks mostly from the oxygen vacancies [87] can be clearly seen

(Fig. 3.15). The three PL peaks correspond to the energy intervals 2.95, 2.86, and 2.76 eV, respectively.

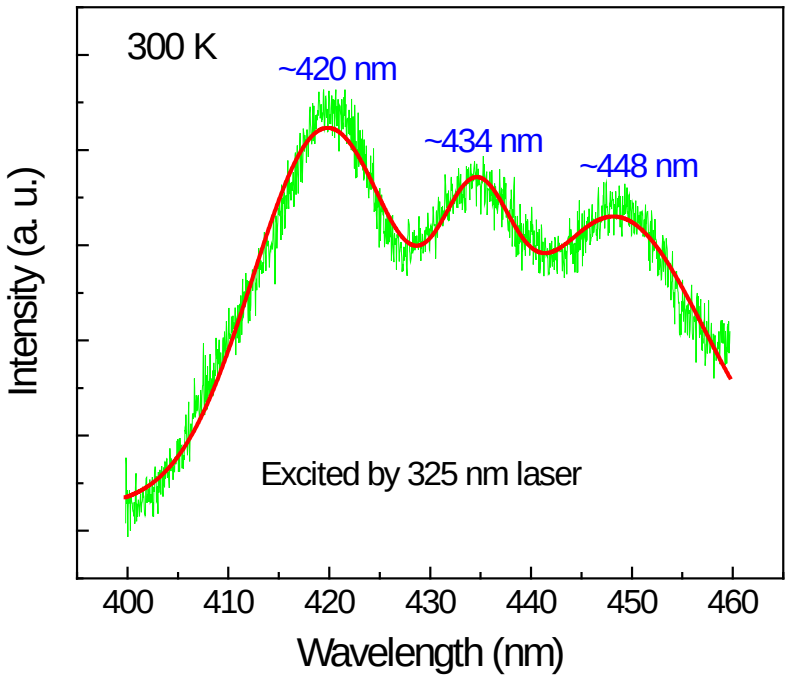

Figure 3.15. Room temperature photoluminescence spectroscopy of the reduced STO film between 400 and 460 nm.

3.2.2 Metal-insulator transition in $SrTiO_{3-x}$ thin films

The transport properties of the vacuum-annealed STO film were measured by a Quantum Design PPMS machine. Aluminum wires were used through wire bonding for contacts. The temperature dependence of the resistivity (ρ-T) measured by 10 μA is shown on a logarithmic scale in Fig. 3.16. There is no observable difference between the cooling down and warming up ρ-T curves. The ρ-T curves reveal an obvious metal-insulator transition at ~78 K: at higher temperatures above 78 K, the resistivity is small and presents metallic behavior; nevertheless, the resistivity begins to increase with decreasing

temperature dramatically from 78 K and reaches nearly six times the RT resistivity at 2 K.

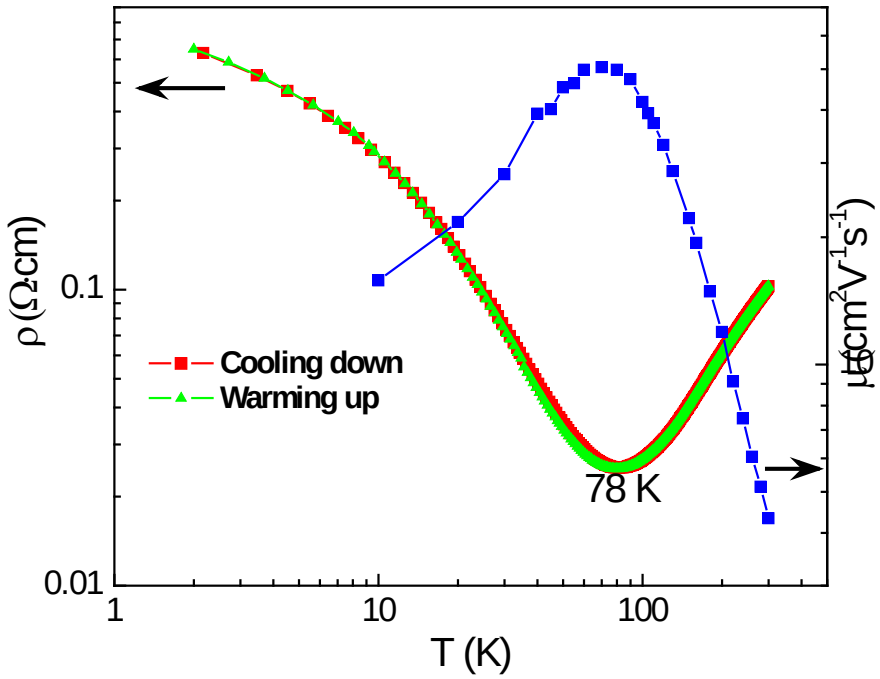

Figure 3.16. *ρ-T* curves from 300 to 2 K during cooling down and warming up as well as its carrier mobility over the temperature range of 300 to 10 K.

Detailed Hall measurements were performed to determine the temperature dependence of the carrier density. It was found that the carrier density considerably decreases with the decrease of temperature, resulting in more than one order of magnitude variation in carrier density from 300 to 10 K (Fig. 3.17). Below 10 K, Hall measurements become disordered possibly because the intrinsic carrier density gets far smaller and therefore the gained Hall voltage starts to approach the measurement limit of the utilized commercial instruments. These resemble the characteristics of the carrier freeze-out effect [89,118]; the density of donors (oxygen vacancies here) is low such that the donor level is separated from the bottom of the conduction band. Hence,

once the temperature decreases to some extent, most of free electrons will go down to the lower donor level and get trapped.

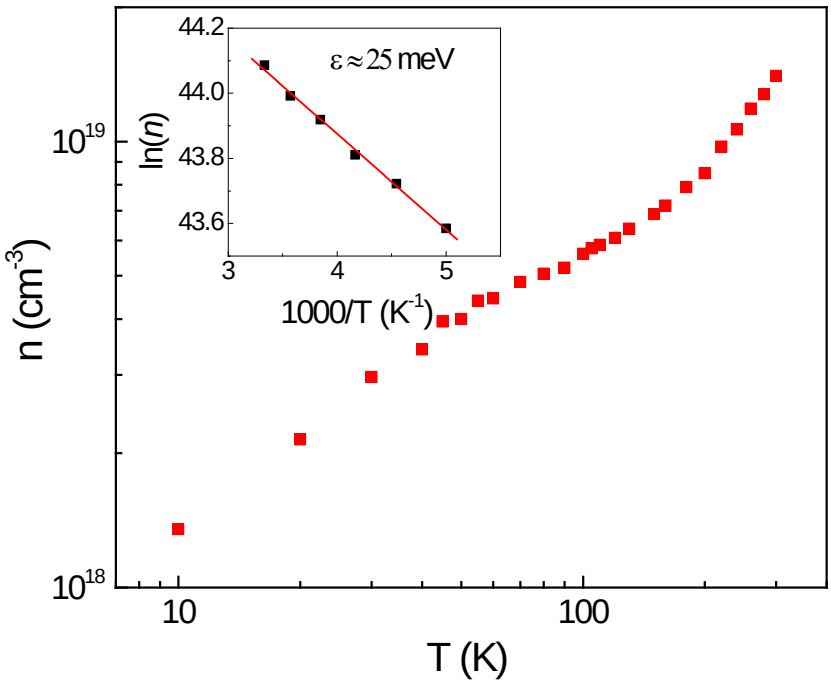

Figure 3.17. *n-T* curve of the reduced STO film. Inset: the Arrhenius plot of ln(*n*) for the temperature range 300 to 200 K and the linear fitting.

The activation energy ϵ at high temperatures fitted according to the relation of carrier density $n \propto e^{-\epsilon/K_B T}$ is ~25 meV (inset of Fig. 3.17), close to the RT thermal energy. Simply taking this value to characterize the energy interval between the donor level and the bottom of the conduction band bottom, an energy band diagram of the oxygen deficient STO film can be obtained as depicted in Fig. 3.18 on the basis of the PL emission peaks (Fig. 3.15). The defect levels close to the valence band of STO is consistent with what Kan *et al.* [87] reported. The resistivity ~0.1 Ω·cm and carrier density 1.4×10^{19} cm^{-3} at RT derived from the measured film thickness, which is within the diffusion length of oxygen ions in 1 h vacuum annealing at 950°C and expected to represent the dimension of the uniform area more accurately, are

respectively 30~50 times smaller and ~30 times larger than the values of the bulk samples with the similar carrier freeze-out phenomenon [89]. These strongly suggest that the uniform area of the oxygen vacancies in a bulk STO is at most of the order of one tenth of the whole single crystal thickness rather than the entire sample. So all the previous data of the resistivity and carrier density [88–90,112,113] related to the bulk STO should be re-considered carefully.

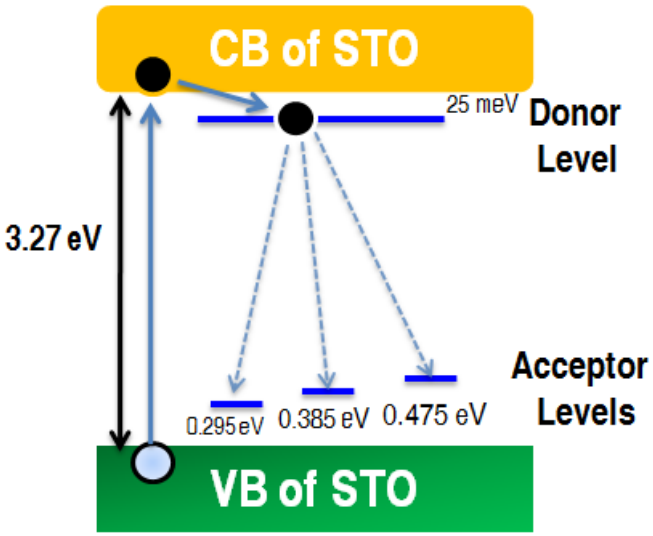

Figure 3.18. Band diagram of the STO_{3-x} film and the possible light emission mechanism. The energy intervals are not drawn to scale.

The corresponding carrier mobility from 300 to 10 K (Fig. 3.16) is overall small and peaks around the phase transition temperature below which the mobility decreases with decreasing temperature due to the carrier freezing. At high temperatures the linear power law dependence of the mobility on temperature is more obvious. However, the influence of STO structural phase transition at ~105 K on the mobility [119] is not apparent, likely due to the disruption of the carrier freeze-out.

3.2.3 Electrical re-excitation and thermal effect

The frozen state can be re-excited by larger electric fields at low temperatures. As shown in Fig. 3.19, the resistivity decreases with increasing measurement current especially below 10 K. At 2 K, the resistivity obtained from d*I*/d*V* measurement clearly displays a large negative electroresistance originating from the electrical excitation to trapped electrons, which can be defined as [$\rho(I)$-ρ(0)]/$\rho(0)$ and reaches ~-50% when the excitation current is 2 mA [inset of Fig. 319(a)].

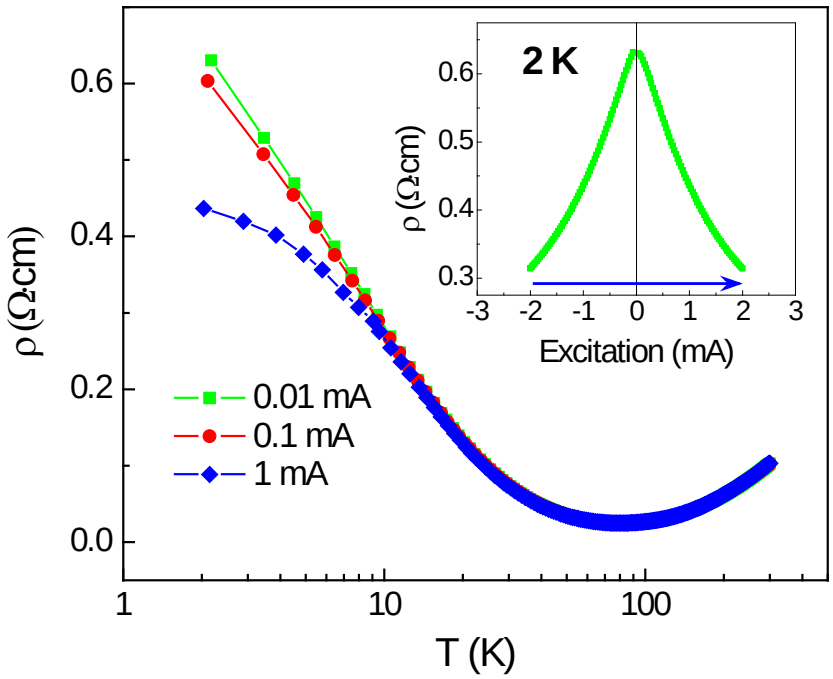

Figure 3.19. *ρ-T* curves of the oxygen deficient STO film measured by the different currents, *i.e.*, 0.01, 0.1 and 1 mA. (Inset) The resistivity at 2 K (obtained by the d*V*/d*I* measurement) versus the measurement current from -2 to 2 mA.

Additionally, it was found that there is also a time dependence of the resistivity for the frozen state. As seen from Fig. 3.20, the resistivity at 2 K relaxes with the continuous measurement time, which suggests that the

thermal effect is playing an important role during measurement. It can be understood by the ideas that the thermal conductivity of STO is low and after reduction there will be a significant decrease [120] due to the scattering of phonons from oxygen vacancies. Therefore the local temperature on the sample surface would increase as a result of the Joule heat accumulation, eventually yielding a decrease in resistivity under the low temperature frozen non-metallic state. However, the thermal effect at 2 K is much weaker than the electrical re-excitation.

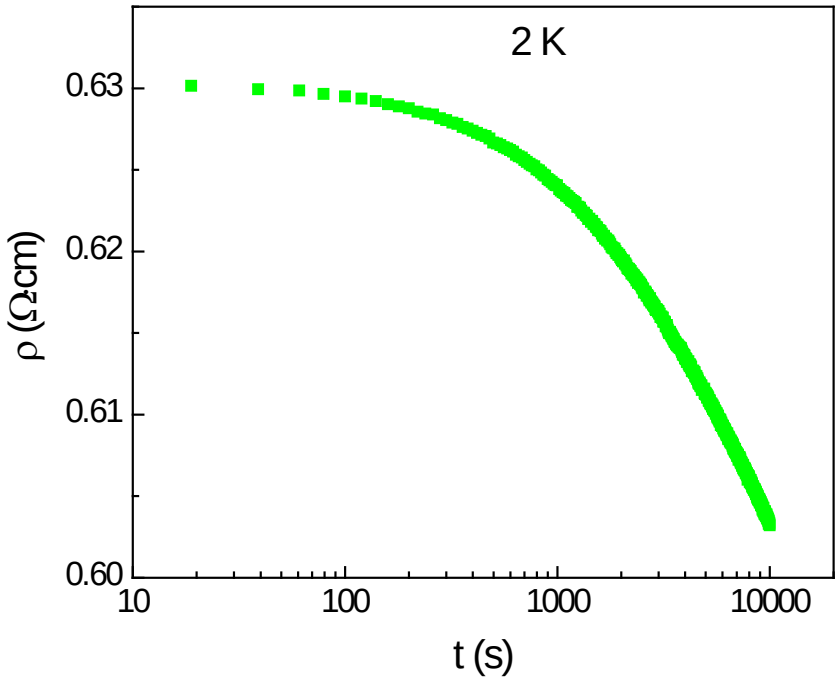

Figure 3.20. Time dependence of the resistivity at 2 K determined by 0.01 mA for a continuous measurement up to 10,000 s.

To further confirm the thermal effect, time dependence of the relative resistivity change of the STO_{3-x} film was measured at different temperatures. Below the transition temperature 78 K, the resistivity change is negative in the insulating state (Fig. 3.21) while it becomes positive in the metallic state

above 78 K (Fig. 3.22). This corroborates that the resistivity change is due to the thermal effect.

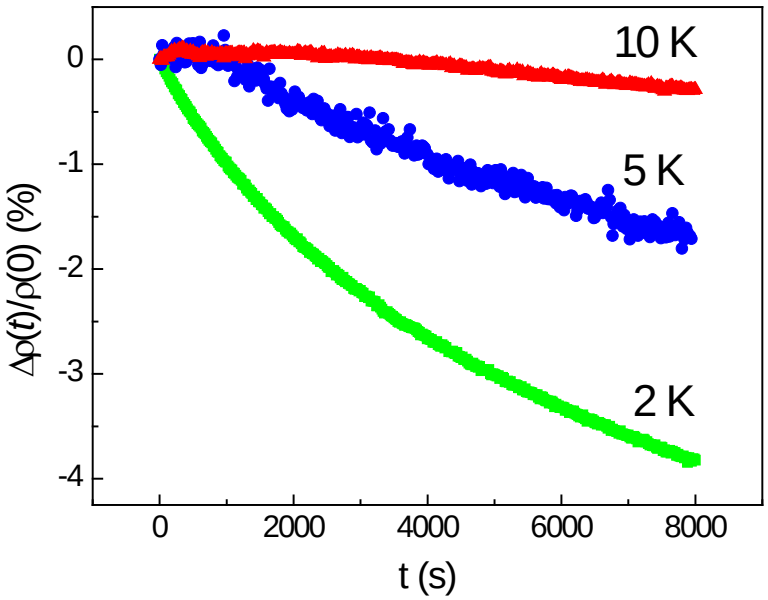

Figure 3.21. Time dependence of the relative resistive change below 78 K.

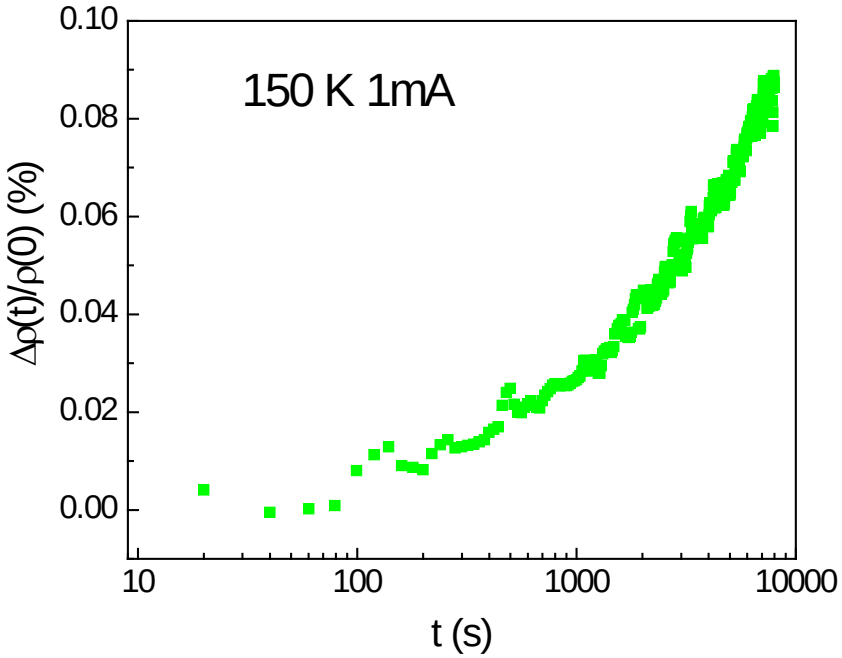

Figure 3.22. Time dependence of the relative resistive change at 150 K.

3.2.4 Negative Magnetoresistance

The response of the resistivity to a 9 T magnetic field applied perpendicular to the STO film surface yields a negative MR although it is relatively small and can only be seen below 5 K in the ρ-T curves. The MR curve up to 9 T at 2 K is shown in Fig. 3.23. It was found there was an asymmetry in the first curve obtained by scanning field from -9 to 9 T. To examine whether the asymmetry was due to an improper measuring geometry, the sample was warmed up to RT and then cooled down to 2 K again to repeat the measurement but with field scanned from 9 T to -9 T.

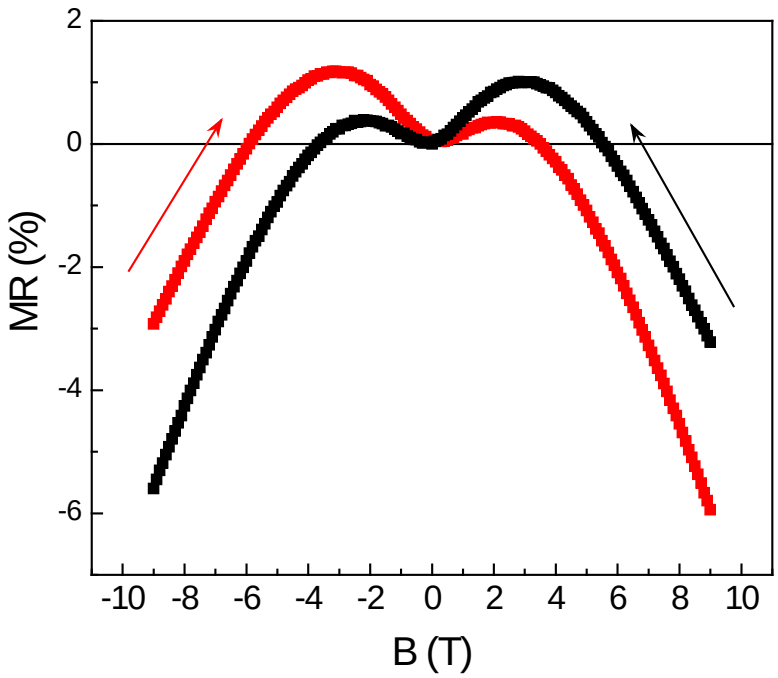

Figure 3.23. MR of the reduced STO film at 2 K.

It was found there is always an asymmetry generated from an additional overall decrease in resistivity over the measuring time regardless of the scanning sequence of magnetic field; this indicates the asymmetry in the MR curves is from the thermal effect rather than the measurement geometry. For

example, a continuous measurement generates a gradually decreasing resistivity as seen in Fig. 3.24.

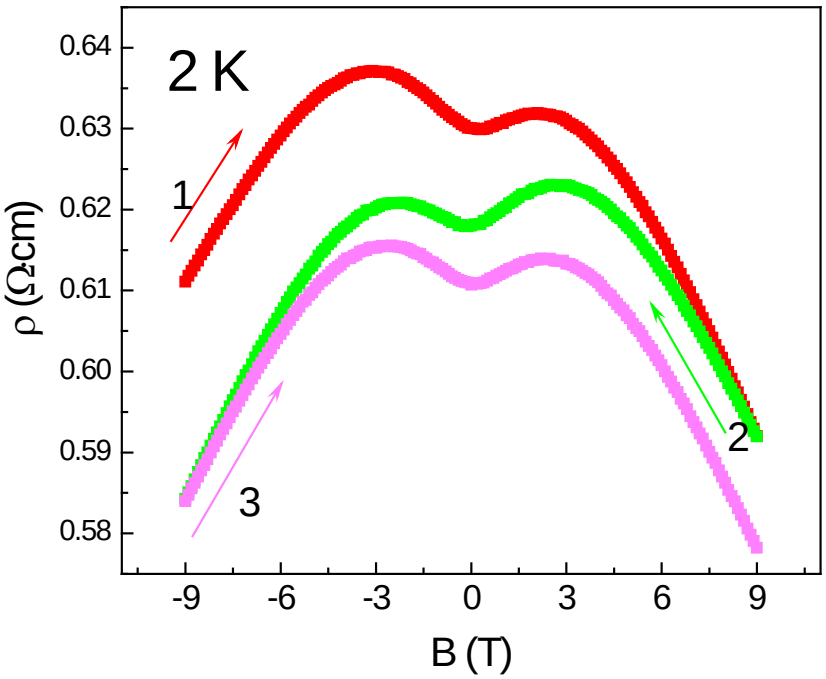

Figure 3.24. Resistivity of the STO_{3-x} film during a continuous scanning of magnetic field at 2 K.

After deducting the thermal effect, the shape of the MR curve at 2 K would resemble 'M'. The positive MR under small magnetic fields can be easily elucidated by Lorentz scattering because the magnetic field is perpendicular to the current. The positive MR is very small because of the poor mobility of the charge carriers in the frozen state. However, there should still be another mechanism competing with Lorentz scattering to account for the negative MR. Considering that the resistance at low temperatures is predominantly due to the trapping of carriers, so it is plausible to imagine that the large magnetic field could help to physically detrap the localized electrons from the trapping centers via electric field through excitation induced by the Lorentz force. On the other hand, the Kondo scattering originating from

localized Ti 3*d* magnetic moments could also be responsible for the negative MR.

The bulk STO single crystal, vacuum-annealed together with the STO film, is metallic over the whole temperature range of 300-2 K. The quadratic MR at 2 K (Fig. 3.5) is quite large up to ~2800% at 9 T because of an extremely high mobility exceeding 10, 000 $cm^2V^{-1}s^{-1}$ and does not show any signature of a negative MR up to 9 T. This strengthens the idea that the negative MR of the oxygen deficient STO film is closely related to the carrier freezing state. Additionally, the bulk STO seems to be more conducting than the STO film since there is no carrier freeze-out in it. This evinces that the local concentration of oxygen vacancies in the bulk STO surface is larger than that in the STO film although they were decreased simultaneously, which strongly suggests that there is a sharp gradient in the concentration of oxygen vacancies in the bulk STO sample from the surface to the interior of single crystals. Thus all the electrical properties related phenomena in oxygen deficient bulk STO should be mostly just the local properties of the near surface area.

Interestingly, the behavior of the carrier freeze-out observed here is quite comparable to the spin glass behavior [85], for example, the carrier freezing transition, the relaxation of the frozen resistivity (although here is due to the thermal effect), and the suppression of the frozen state by the external fields. Considering these, we can also coin this as “charge glass” to more vividly represent its characteristics.

3.2.5 Summary

In summary, we argued the uniformity of oxygen vacancies in the bulk STO single crystals by studying the high quality STO single crystal film via various means. It was found the actual uniform thickness of the bulk STO is around several ten times smaller than the whole thickness and all the intriguing electrical phenomena of the oxygen deficient bulk STO could only be the local surface properties due to the obvious gradient in the concentrations of oxygen vacancies from surface to its interior. Moreover, we investigated the MIT observed in the oxygen deficient STO film. The low temperature frozen state can be remarkably re-excited by the applied electric field. The thermal effect in oxygen deficient STO film during the electrical measurements is pronounced due to its poor thermal conductivity although the re-excitation of thermal effect to the low temperature frozen state is far less effective than the electric field. It was also found that large external magnetic fields can suppress the carrier freezing and generate negative MR. The possible mechanism proposed for that is the magnetic field can detrap the localized electrons under the frozen state through Lorentz force with the help of an electric excitation. The high similarity between the various behaviors of the carrier freeze-out and the spin glass state enables us to think the carrier freezing state as a kind of “charge glass” state.

3.3 Insulating state in ultrathin $SrTiO_{3-x}$ films

3.3.1 Surface of $LaAlO_3$ single crystal substrates

STO is a widely used substrate for atomically flat interface engineering not only because of its excellent chemical and thermal stabilities and the lattice match with other perovskite oxides, but also the atomically controllable surface termination [52]. Similar to STO, LAO is also an excellent substrate and extensively utilized for oxide thin film growth. Moreover, it is extremely difficult to generate conductivity in LAO by thermal treatment because the diffusion coefficient of oxygen vacancies in LAO is very low [121]. In addition, oxygen vacancies in LAO, if there is any, are energetically favored to be in a energy level of ~2.6 eV below the conduction band [122], which is too low to serve as a donor level at room temperature. This is well in contrast to STO, in which the defect level of oxygen vacancies is only 25 meV below the conduction band [44], and hence gives an advantage over STO for high temperature oxide film deposition.

The surface termination of (100)-oriented LAO single crystals has been previously investigated by Yao *et al.* [123] and Wang *et al.* [124] with multiple surface-sensitive techniques, *e.g.*, time-of-flight scattering and recoiling spectrometry, atomic force microscopy (AFM), low-energy electron diffraction, Auger electron spectroscopy, x-ray photoelectron spectroscopy and reflection electron microscopy. They found that the surface termination of a LAO single crystal is strongly temperature-dependent: the surface is

exclusively terminated in an Al-O layer from room temperature up to ~150 °C and a La-O layer above ~250°C; Only in the intermediate temperature region between 150 and 250 °C, mixed terminations exist. Using AFM they also demonstrated an atomically flat LAO surface with uniform one-unit-cell step flow [123], providing the possibility to prepare an atomically flat interface based on a LAO substrate.

The as-received (100)-oriented LAO single crystals (CrysTec GmbH, Germany) with two sides polished were examined by AFM at room temperature, and indeed the steps on the surfaces were able to be seen (Fig. 3.25), which is consistent with the earlier report.

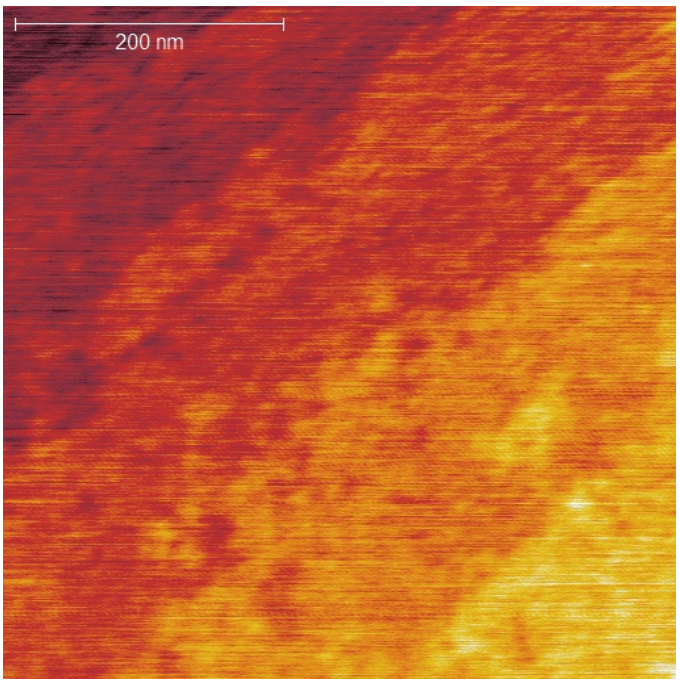

Figure 3.25. Room temperature AFM image of an as-received $LaAlO_3$ substrate.

Moreover, the surface topography of LAO was largely improved by the later air annealing for 2 h. The AFM images of LAO single crystals annealed

at different temperatures are shown in Fig. 3.26. For LAO annealed at 900 °C, the steps are not ideally flat but there are nanosize particles and wrinkles. On the other hand, a LAO single crystal annealed at 1000 °C has flat and uniform steps. A LAO single crystal annealed at 1050 °C also exhibits obvious steps. However, a LAO single crystal annealed at the elevated temperature of 1100 °C suffered from physical holes.

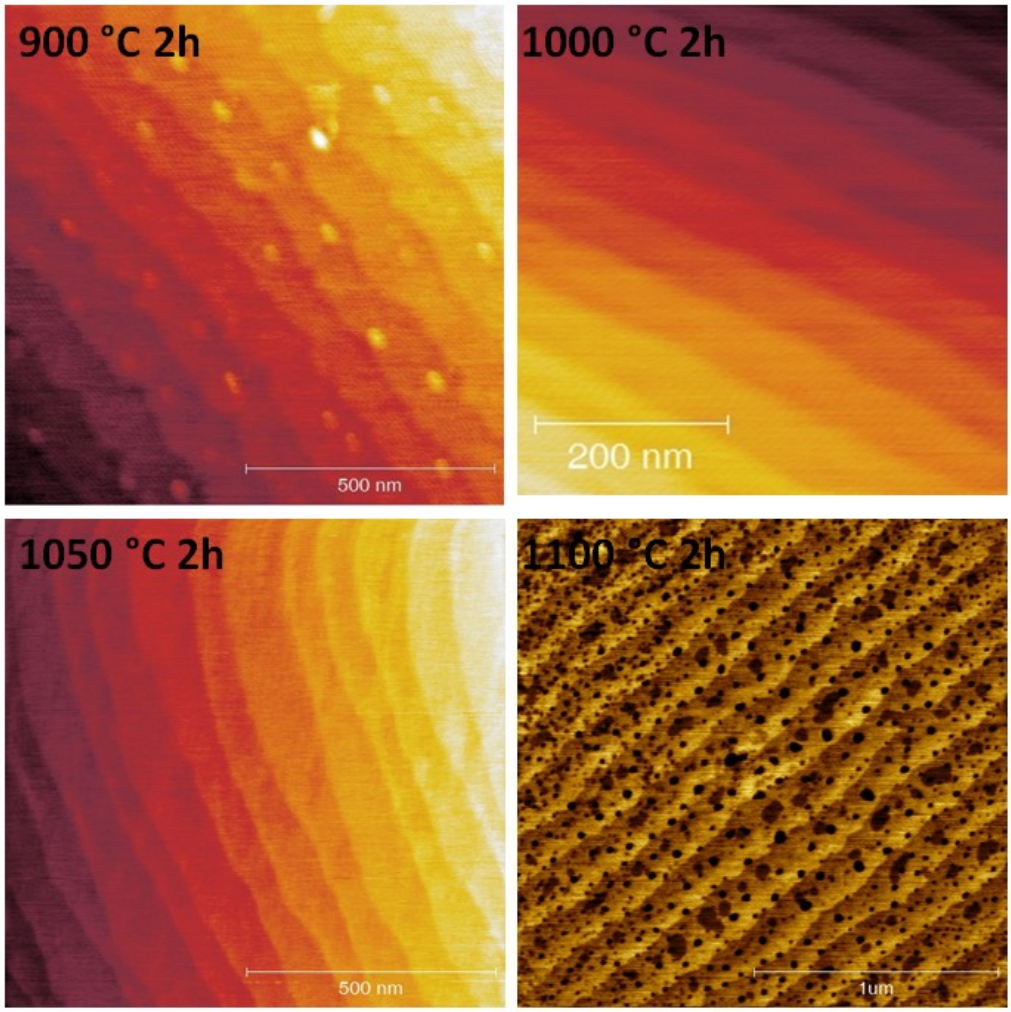

Figure 3.26. AFM images of LAO single crystals annealed in air for 2 h at different temperatures.

LAO single crystal substrates annealed for 2 h at 1000 °C were utilized for STO ultrathin film deposition. As can be seen in the inset of Fig. 3.27, the

surface of such LAO substrate is single-terminated and atomically flat with uniform steps. The height profile data in Fig. 3.27 corresponding to the cross line mark by '1' in the inset displays the average terrace width of ~60 nm and the average step height of ~ 4 Å pertaining to 1 uc LAO height.

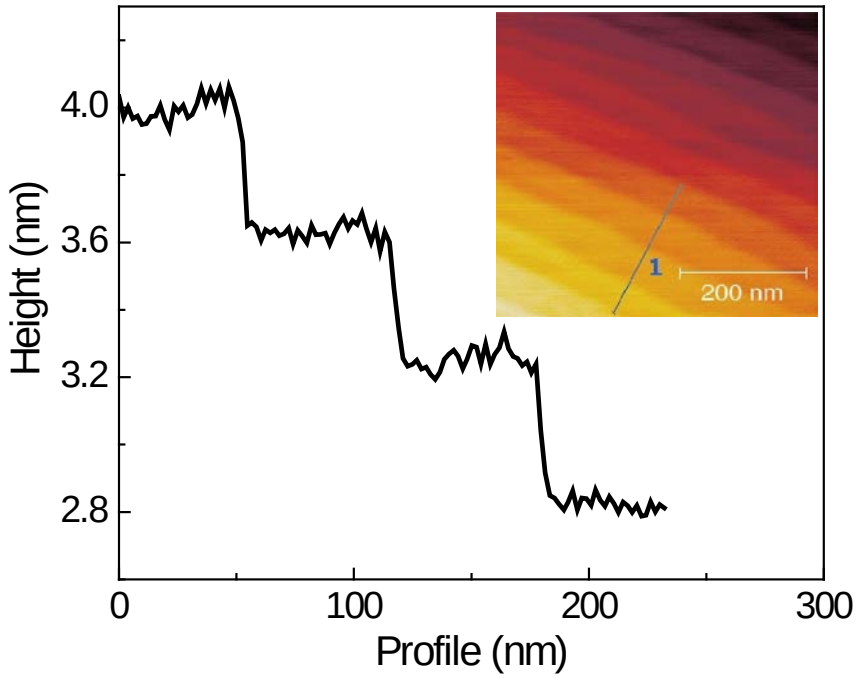

Figure 3.27. Height profile of the cross line "1" in the inset. Inset: AFM image of a (100)-oriented LAO single crystal substrate annealed in air at 1000 °C for 2 h.

3.3.2 Layer-by-layer growth of $SrTiO_3$ on $LaAlO_3$

Pulsed laser deposition with a KrF excimer laser (λ = 248 nm) was used to fabricate STO ultrathin films from a single crystal STO target on fully-terminated LAO single crystal substrates at 800 °C and oxygen pressure of 5×10^{-4} mbar, which are typical conditions for 2DEG growth. Before deposition, LAO substrates were kept under the deposition conditions for 30 mins for the stabilization of surface termination. The RHEED was utilized to

monitor the entire growth process. The RHEED pattern of a LAO substrate at 800 °C before deposition is shown in Fig. 3.28(a).

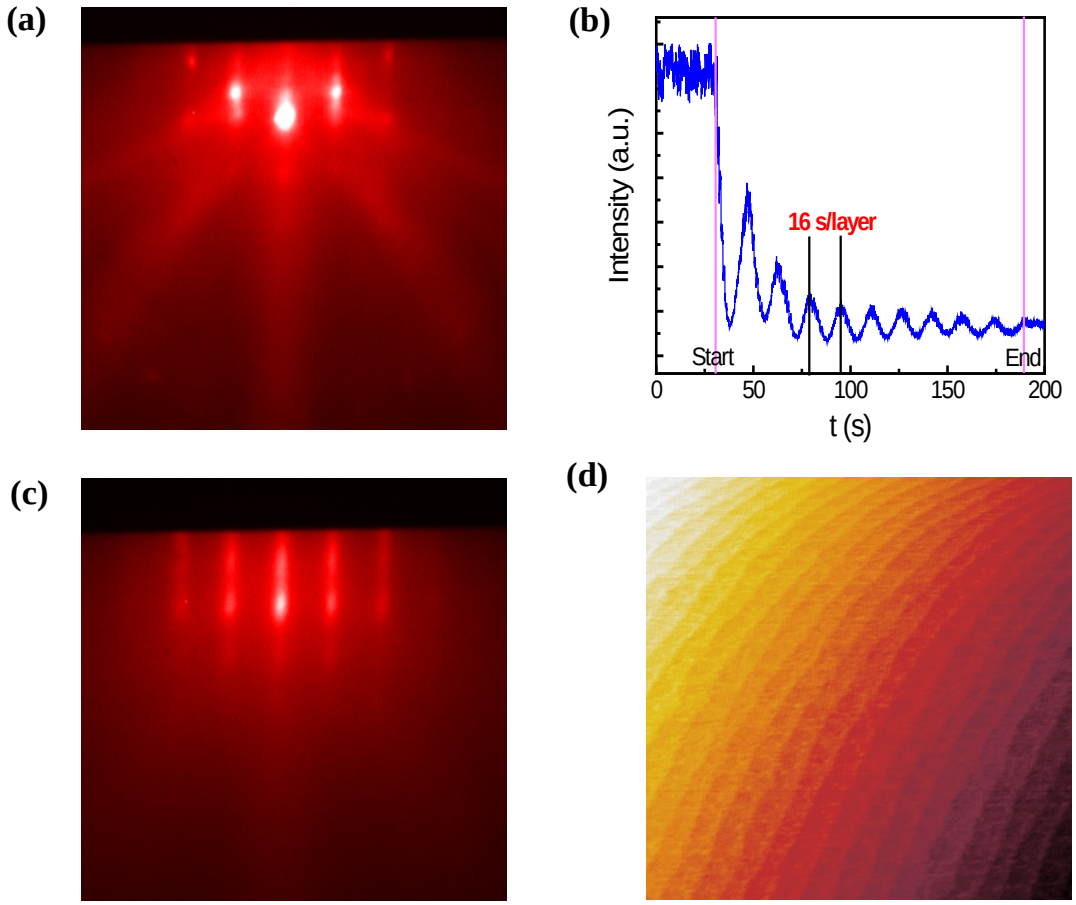

Figure 3.28. (a) RHEED pattern of a LAO single crystal at 800 °C before deposition. (b) RHEED oscillations of a 10 unit cells (uc) $SrTiO_3$ (STO) film grown on a fully-terminated LAO substrate. (c) RHEED pattern after 10 uc STO film deposition. (d) AFM image of an as-deposited 10 uc STO film (1 μm × 1 μm).

During the deposition, the fluence of laser energy was 1.5 J/cm^2 and the frequency was 1 Hz. Consequently, the layer-by-layer growth of STO films on LAO substrates was achieved. In Fig. 3.28(b), the RHEED oscillation of a 10 uc STO is shown with an accurate periodicity of 16 s/layer, indicating a layer-by-layer growth mode. The RHEED pattern after 10 uc STO film deposition is shown in Fig. 3.28(c), where streaky peaks are typical of a two dimensional

growth. The surface topography of an as-deposited 10 uc STO sample was examined by AFM and the terraces can be clearly seen in Fig. 3.28(d) with analogous signatures of a single-terminated LAO substrate. Similarly, 25 uc STO samples were also fabricated based on single-terminated LAO substrates.

Upon heating to the deposition temperature of 800 °C, the surface termination of a LAO substrate experiences a transition from an Al-O layer at room temperature to a La-O layer possibly due to the creation of surface oxygen deficiencies during heating [123]. Therefore, the (LaO)-(TiO_2) interface is expected to form in our case, which is similar to the *n*-type interface as in the typical 2DEG LAO/STO heterostructure.

Not only can STO films be layer-by-layer grown on a fully-terminated LAO substrate, the high quality atomically flat growth can also be obtained for some other perovskite materials like $NdAlO_3$ and $PrAlO_3$. This demonstrates an approach to achieve atomically flat interfaces based on LAO substrates, which are robust and nearly free of oxygen-vacancy-induced conductivity.

3.3.3 Insulating interface between $SrTiO_3$ thin film and a $LaAlO_3$ substrate

Subsequently, the transport properties of both 10 and 25 uc STO samples were examined by simple four-probe linear DC resistance measurement with a typical distance between voltage electrodes of ~1 mm. The samples were contacted using Al wires and the measuring current was 5 nA. Nevertheless, it was found that all the samples are highly insulating and the resistance of them

is of the order of GΩ at room temperature, in contrast to the metallicity of the *n*-type interface of 2DEG. The temperature dependence of resistance (*R*-*T*) for a 10 uc STO sample is shown in Fig. 3.29, which exhibits a characteristic behavior of insulators.

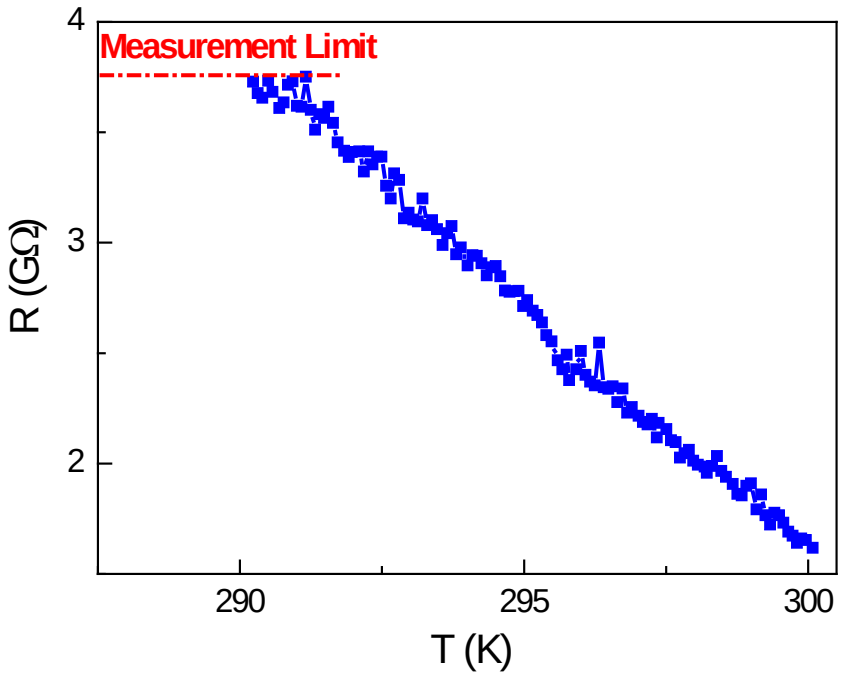

Figure 3.29. *R*-*T* of a heterostructure with 10 uc STO film grown on a single-terminated LAO substrate. The distance between voltage electrodes in four-probe resistance measurements was ~1 mm.

Microscopically the internal atomic layers of a LAO single crystal, *i.e.*, AlO_2- and LaO-layers, are polar, but the (100) surface of a polar LAO bulk single crystal is likely experience surface reconstruction [124–126] to be nonpolar [127,128]. Thus, the growth of STO films on LAO substrates can be explained by a scenario that a nonpolar material is grown on another nonpolar surface as schematized in Fig. 3.30. Therefore, the nonexistence of polar discontinuity at the interface between STO films and LAO substrates could be responsible for the highly insulating behavior. On the other hand, the epitaxial

interface strain for STO films grown on LAO substrates works in the opposite direction compared to the case of LAO films grown on STO substrates, which could also affect the interface conductivity and hence account for the highly insulating behavior. However, the nanoscale mixing of interface atoms [39] cannot be used to clarify the highly insulating behavior here.

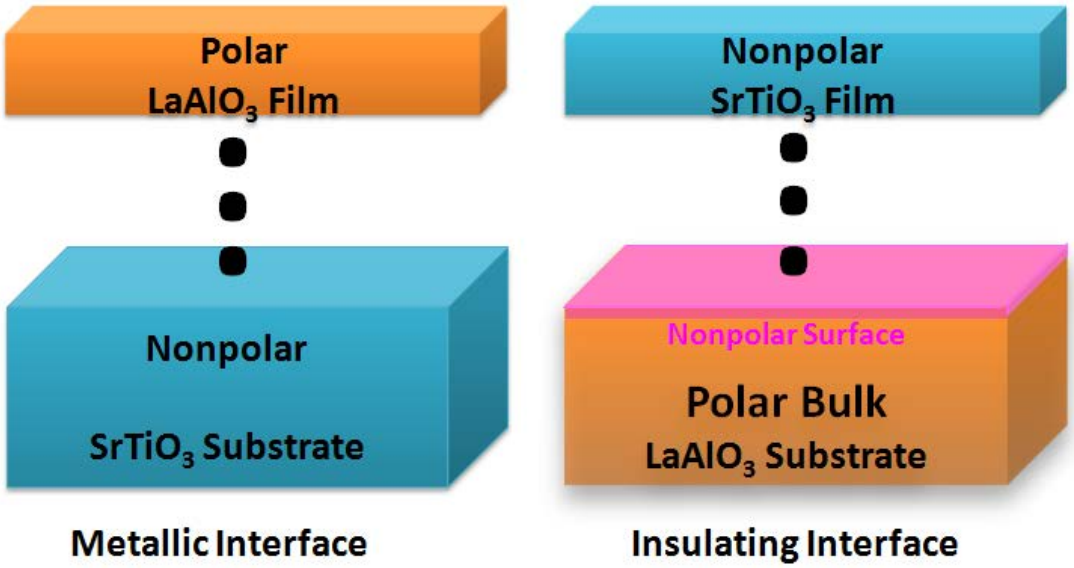

Figure 3.30. Schematics of two types of interfaces with and without polar discontinuity.

3.3.4 Variable-range hopping in ultrathin $SrTiO_{3-x}$ films

To investigate the effect of oxygen vacancies in STO films on the transport properties of such heterostructures, a 25 uc (~10 nm) STO sample was thermally reduced in a vacuum of 10^{-7} Torr at 950 °C for 1 h. The resistance measurement was then performed with the same measurement geometry as for Fig. 3.29. The *R-T* curve from 300 to 10 K as shown on a semi-logarithmic scale in Fig. 3.31 represents an insulating behavior although the room temperature resistance decreases by four orders of magnitude relative to the

initial resistance (after the reduction, the LAO substrate was still extremely high insulating, which was checked from the backside of the crystal).

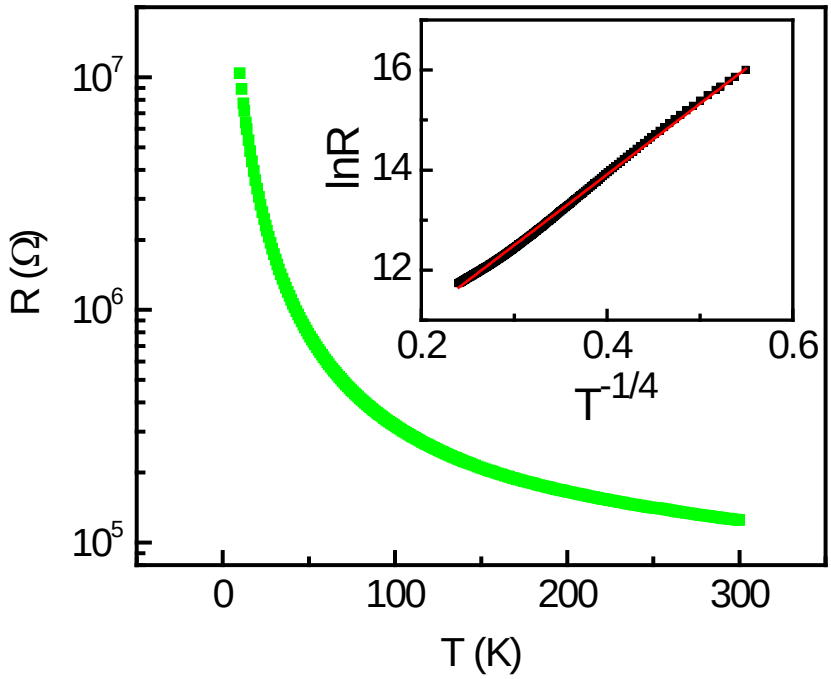

Figure 3.31. *R-T* curve of the 25 uc STO/LAO heterostructure after 1 h thermal reduction at 950 °C and 10^{-7} Torr vacuum. (Inset) Fitting plot in terms of three-dimensional variable-range hopping of Mott law.

The room temperature Hall measurement displays that the areal carrier density is ~ 2.12×10^{12} cm^{-2}. Furthermore, it was found that the *R-T* curve can be well fitted by the variable-range hopping of Mott law, *i.e.*, $lnR \propto T^{-\frac{1}{4}}$, over the whole temperature range as plotted in the inset of Fig. 3.31, which reveals that the *R-T* curve belongs to the three-dimensional transport property. Hence considering the thickness of 25 uc STO, the areal carrier density is converted into a volume density of being 2.17×10^{18} cm^{-3}. The value is smaller than the experimental critical carrier density of ~5×10^{18} cm^{-3} [44] of the metal-insulator transition for a reduced STO film, so this can also explain why the film is still insulating. Such an insulating state is likely due to significant

compensating defects such as Ti and Sr vacancies accompanying a large number of oxygen vacancies created during vacuum annealing.

3.3.5 Summary

In summary, we demonstrated atomically flat interfaces between STO films and single-terminated LAO substrates. The transport measurements displayed that this kind of interface is highly insulating. The reason for that could be the surface reconstruction of LAO single crystals or due to the interface epitaxial strain. Ultrathin STO_{3-x} films are insulating, which could be due to a large number of compensating defects. Besides, our work opens a way to achieve atomically flat film growth based on LAO substrates. Furthermore, the quasi-2DEG could also be tailored by means of vacuum reduction or Argon-ion milling after the realization of atomically flat nanoscale film growth on LAO substrates.

Chapter 4 Origin of the two-dimensional electron gas at the $LaAlO_3/SrTiO_3$ interface – the role of oxygen vacancies and electronic reconstruction

The high mobility two-dimensional electron gas (2DEG) at the interface between LAO films and TiO_2-terminated STO substrates was discovered by Ohtomo and Hwang [17]. Since then, 2DEG at the LAO/STO interface has attracted a huge amount of attention from the community of oxide electronics and been one of the most fascinating topics in the contemporary condensed matter physics. Plenty of intriguing physical properties have been unveiled by different groups at this interface system, for example, the electronically coupled complementary interfaces [28], the transition from metallic to insulating phase as the thickness of LAO films decreases to less than 4 unit cells (uc) [29], the magnetic Kondo scattering at the interface [20], the low temperature two-dimensional superconductivity [19], and the large gate capacitance enhancement [34] due to strong electron correlations (the 2DEG at the LAO/STO interface was also proposed as a kind of electron 'liquid', *i.e.*, 2DEL well because of strong electron-electron interactions [129]).

For a long time whether the ground state of 2DEG is ferromagnetic or superconducting was a physically fundamental issue under debate. However,

Ariando *et al*. [9] recently found the coexistence of the ferromagnetic state and a superconducting-like state and proposed electronic phase separation for the 2DEG at the LAO/STO interface. Later the coexistence of superconductivity and ferromagnetism in this system was observed by Dikin *et al*. [31], Li *et al*. [32] and [130]. The theoretical origin for this coexistence is attributed to the localization and strong spin-orbit coupling of Ti 3*d* interface electrons [131]. In addition, the successful integration of 2DEG with Si by Park *et al*. [35] has pushed this functional oxide interface system toward nanoelectronic device applications significantly.

As to the origin of the metallic conductivity at the LAO/STO interface, generally three kinds of different mechanisms have been developed. One is polar discontinuity induced interface charge transfer to overcome polar catastrophe [18,37,38]; the second one is oxygen vacancies [40–43] on the STO side generated due to the growth oxygen pressure or the bombardment during the growth process [132], which could behave similarly as in thermally reduced bulk STO [89] and thus lead to metallicity; the third one is thermal intermixing of atoms at the interface [39] since La-doped STO is metallic [133]. However, the thermal interdiffusion mechanism was discounted in recent work [45], which studied the effect of a mixed interface layer. It is also in conflict with the experimental results that *p*-type LAO/STO interfaces [17] and interfaces created by growing STO films on LAO are insulating [46]. In addition, the study on the epitaxial interface strain [134] indicated that the epitaxial strain at the interface could be playing an important role in the interface conductivity.

In 2007, Shibuya *et al.* [132] associated the metallic conductivity at interfaces between room temperature-deposited amorphous $CaHfO_3$ films and STO single crystal substrates with the bombardment of STO substrates by the plume during the pulsed laser deposition process. Later, Chen *et al.* [47] demonstrated metallic interfaces between STO substrates and various amorphous oxide overlayers including LAO, STO and yittria-stablized zirconia thin films fabricated by pulsed laser deposition. The origin of the 2DEG in such crystalline/amorphous heterostructures was attributed to formation of oxygen vacancies at the surface of the STO. Moreover, metallic interfaces between Al-based amorphous oxides and STO substrates have also been realized by other less energetic deposition techniques such as atomic layer deposition [48] and electron beam evaporation [135]. The electronic properties of STO-based amorphous heterostructures [47,48] are, to some extent, similar to those of crystalline LAO/STO heterostructures [20,29], including the metallicity accompanied by the presence of Ti^{3+} ions and a sharp metal-insulator transition as a function of overlayer thickness. These results call into question the polarization catastrophe model.

In this chapter, we present a detailed comparison of amorphous and crystalline LAO/STO heterostructures based on electrical and optical measurements. By comparing the electronic properties of these two interfaces, we are able to distinguish the two different mechanisms mainly responsible for the 2DEG observed in amorphous and crystalline LAO/STO heterostructures.

4.1 Amorphous $LaAlO_3/SrTiO_3$ heterostructures

Amorphous LAO films were deposited from a single crystal LAO target on untreated (100)-oriented STO substrates by pulsed laser deposition (KrF laser λ = 248 nm) at room temperature and different oxygen partial pressures. Crystalline LAO films were fabricated on TiO_2-terminated (100)-oriented STO substrates at 750 °C in 10^{-3} Torr oxygen partial pressure. During deposition, the repetition rate of the laser was kept at 5 Hz and the laser fluence was fixed at 1.3 J/cm^2. The deposition rate of amorphous LAO films was calibrated by transmission electron microscopy measurements and the growth of crystalline LAO films was monitored *in situ* by RHEED. Electrical contacts onto 5 × 5 mm^2 samples were made with Al wires using wire bonding and electrical measurements were performed in a Quantum Design physical property measurement system. While the sheet resistance and Hall effect of all LAO/STO heterostructures was measured in the *van der Pauw* geometry, the magnetoresistance measurements were performed in the four-probe linear geometry.

Figure 4.1 shows a cross-section transmission electron microscopy image of a 20 nm amorphous LAO film deposited on an untreated STO substrate at room temperature and 10^{-6} Torr oxygen partial pressure. The LAO layer is seen to uniformly cover the STO substrate. The zoom-in image of an interface region in Fig. 4.2 demonstrates the amorphous feature of the LAO overlayer, with one or two oriented layers at the interface, which confirms the room-temperature amorphous growth of LAO films on crystalline STO substrates.

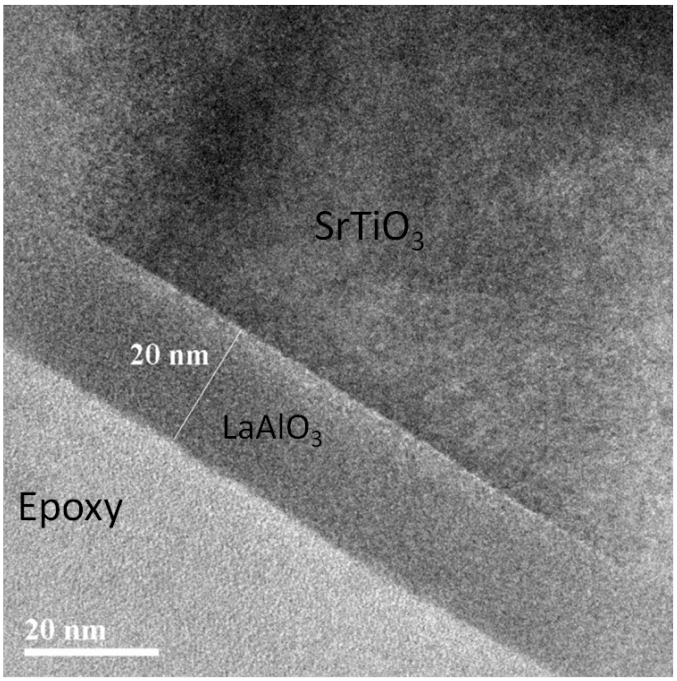

Figure 4.1. TEM image of a $LaAlO_3$ (LAO) film deposited on an untreated STO substrate at room temperature and 10^{-6} Torr oxygen pressure.

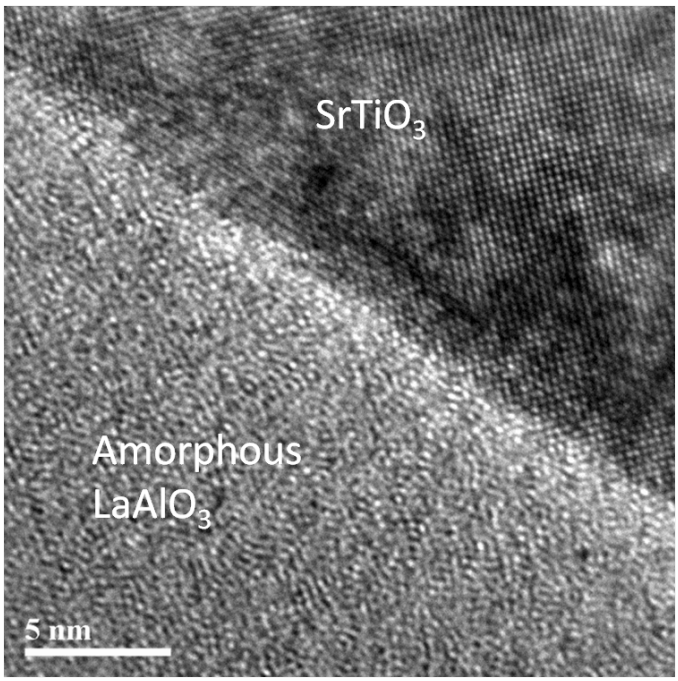

Figure 4.2. Zoom-in image of an interface region.

The first monolayer of the LAO is well oriented, while subsequent layers are increasingly disordered.

4.1.1 Photoluminescence spectra

The photoluminescence (PL) spectra (excited by a 325 nm laser with energy density of 1 MW/cm^2) of an as-received STO substrate and 20 nm amorphous LAO films deposited on STO substrates at different oxygen partial pressure ranging from 10^{-1} to 10^{-6} Torr are shown in Fig. 4.3. Although the PL intensity of the as-received STO substrate is weak, the characteristic PL peaks of oxygen vacancies at wavelengths ranging from 380 to 420 nm [44,87] in STO can still be seen.

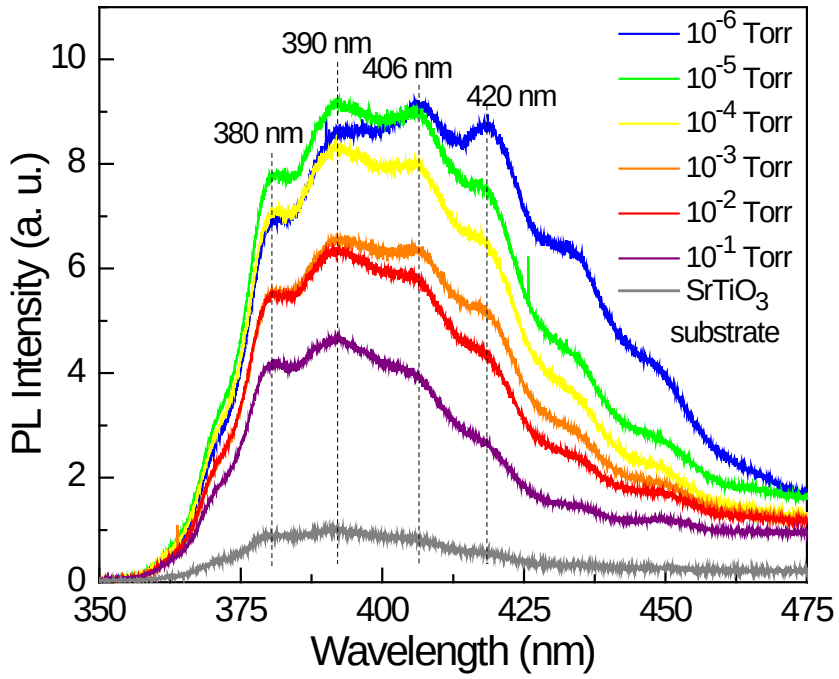

Figure 4.3. Room-temperature photoluminescence (PL) spectra of an as-received STO substrate and 20 nm amorphous LAO films deposited on untreated STO substrates at different oxygen partial pressure ranging from 10^{-1} to 10^{-6} Torr.

The PL intensity of amorphous LAO/STO heterostructures is enhanced by a factor of 5 to 9, relative to the as-received STO substrate, depending on the oxygen partial pressure used during the growth. At the same time, the multiple

PL emission peaks are much more pronounced, and the PL intensity increases with decreasing oxygen partial pressure.

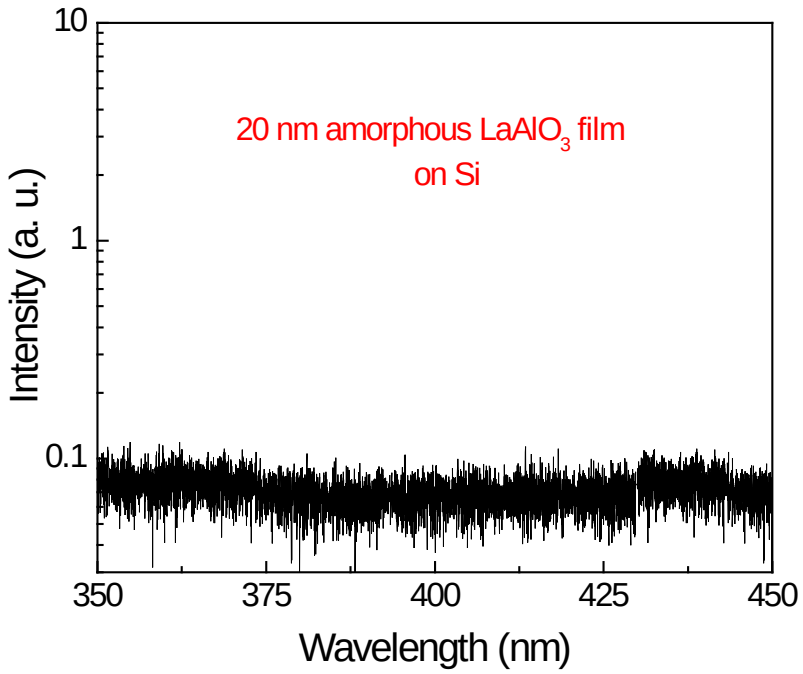

Figure 4.4. PL of a 20 nm amorphous $LaAlO_3$ film deposited on a Si substrate at 10^{-3} Torr and room temperature using pulsed laser deposition. The PL spectra reveal that there is no pronounced emission from the 20 nm amorphous $LaAlO_3$ film.

Considering that 20 nm amorphous LAO films grown on Si substrates present no PL signal (Fig. 4.4) and the PL peaks from various defects in LAO bulk crystals appear only at ~600 nm and above [136], we are able to attribute the large enhancement of PL intensity between 350 and 475 nm in amorphous LAO/STO heterostructures to the creation of oxygen vacancies in the STO substrates near their interface during the deposition process.

4.1.2 Transport properties

The temperature-dependent sheet resistance (R_s-T) of the 20 nm amorphous LAO/STO heterostructures fabricated in different oxygen partial pressures

from 10^{-3} to 10^{-6} Torr is shown in Fig. 4.5. As can be seen, the heterostructures exhibit metallic behavior in the whole temperature range. The room temperature sheet resistance increases with oxygen partial pressure.

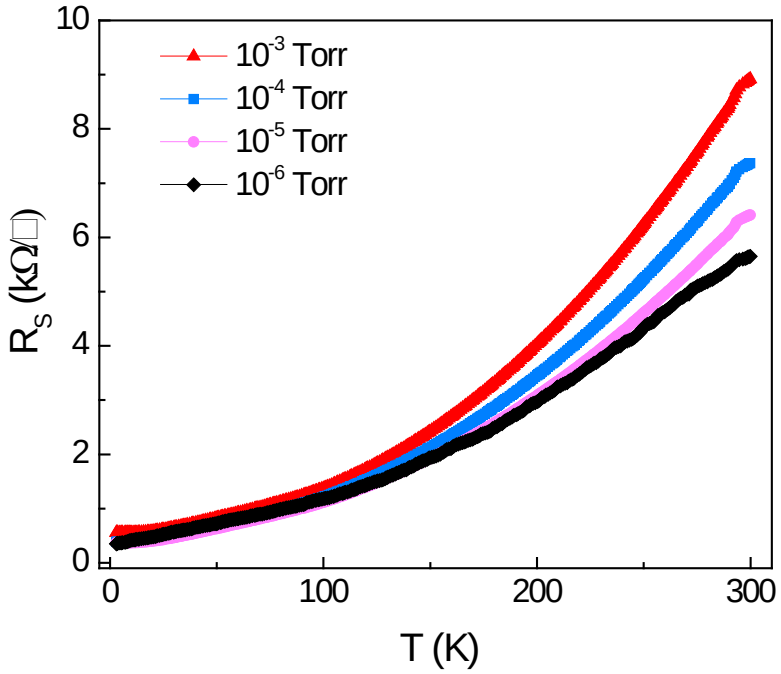

Figure 4.5. Temperature dependence of sheet resistance (R_s-T) for 20 nm amorphous LAO/STO heterostructures fabricated at different oxygen pressures from 10^{-3} to 10^{-6} Torr.

The corresponding carrier density and mobility data are illustrated in Fig. 4.6. The room-temperature carrier density of ~10^{14} cm^{-2} is comparable to that of unannealed crystalline LAO/STO heterostructures [9,20], which were directly cooled down to room temperature in the deposition oxygen pressure after high temperature growth. Moreover, both the temperature-dependent carrier density (n_s-T) and mobility of such amorphous LAO/STO heterostructures are similar to those of unannealed crystalline LAO/STO heterostructures [9,20,28], including the carrier freeze-out effect below ~100 K.

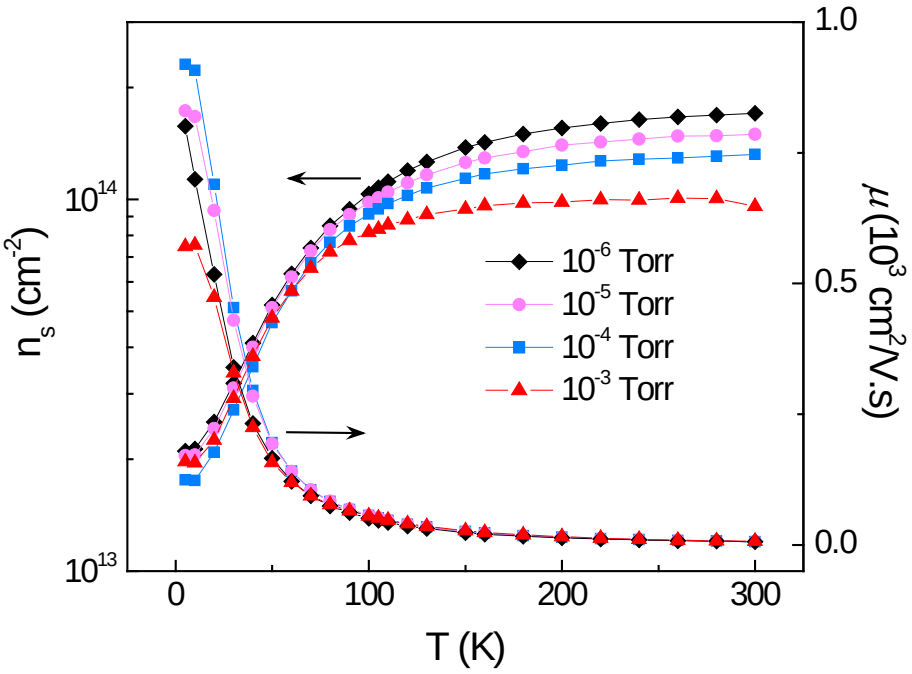

Figure 4.6. Temperature dependences of sheet carrier density (n_s-T) and the corresponding mobility for 20 nm amorphous LAO/STO heterostructures fabricated at different oxygen pressures from 10^{-3} to 10^{-6} Torr.

To examine the conductivity and band gap of amorphous LAO, we deposited 150 nm amorphous LAO films on large band gap substrates MgO and Al_2O_3. By electrical and ultraviolet-visible spectroscopy measurements, it was found that amorphous LAO is highly insulating with a band gap greater than 5 eV (Fig. 4.7), similar to crystalline bulk LAO. In addition, any issue of polar discontinuity in amorphous LAO-STO heterostructures should be minor and only confined to the first few quasi-crystalline layers of LAO at the interface. The PL spectra in Fig. 4.3 indicate the presence of oxygen vacancies in STO substrates. We are therefore led to conclude that the conductivity emerging at the interface between amorphous LAO films and STO substrates originates mainly from oxygen vacancies created in STO near the interface during film deposition.

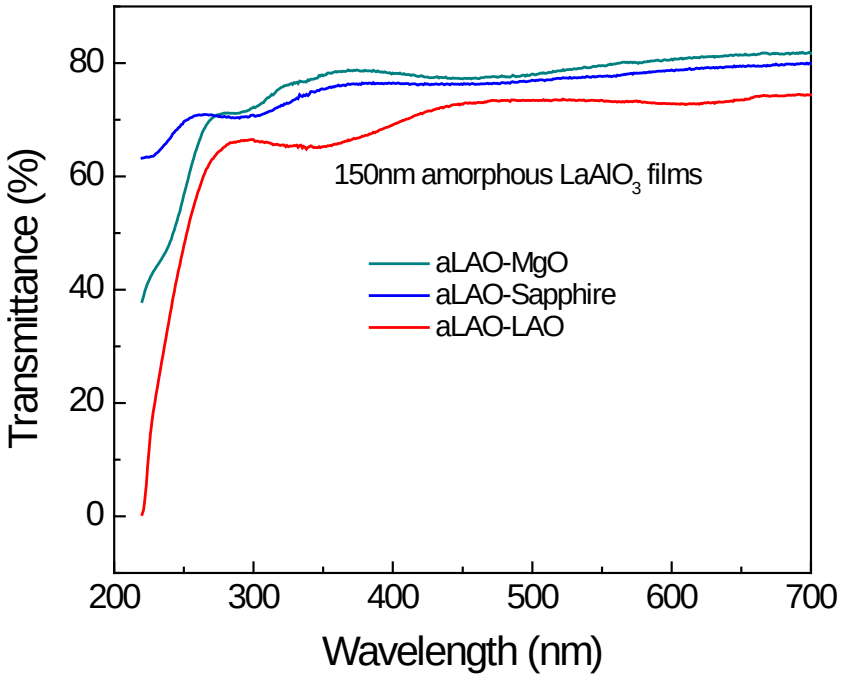

Figure 4.7. Ultraviolet-visible-infrared spectra of 150 nm amorphous $LaAlO_3$ films grown on MgO, Al_2O_3 and $LaAlO_3$ substrates.

The out-of-plane MR of amorphous LAO/STO heterostructures is plotted in Fig. 4.8. Indeed, there is a common feature in the MR curves of all amorphous heterostructures, *i.e.*, MR is quadratic at low field but linear at high magnetic field, as shown in Fig. 4.8(a). Such a feature is also seen in crystalline LAO/STO heterostructures [9,137]. The out-of-plane MR of amorphous LAO/STO samples fabricated at lower oxygen pressure (10^{-4}~10^{-6} Torr) is larger than that of the samples deposited at higher pressure (10^{-2}~10^{-3} Torr) at 9 T.

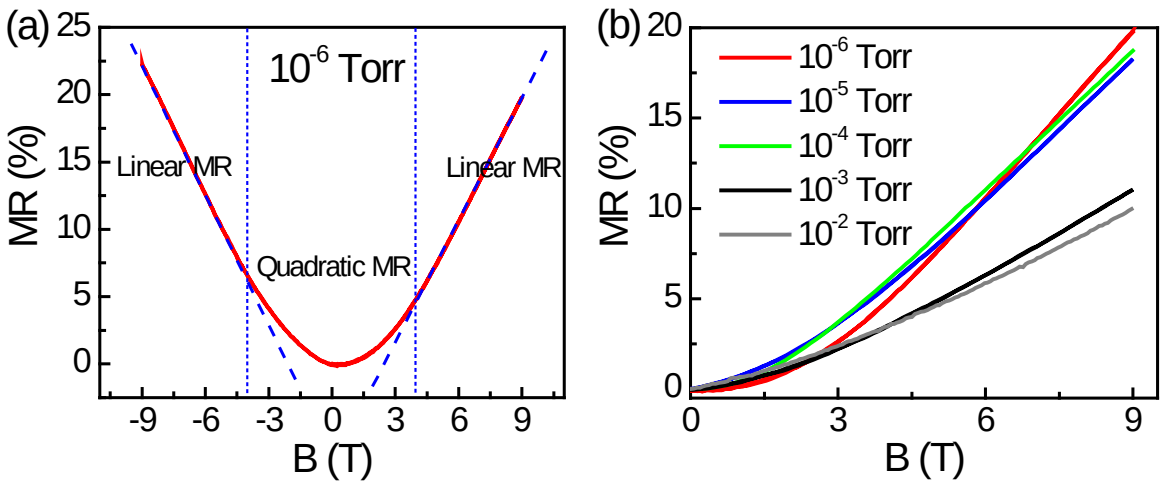

Figure 4.8. (a) Out-of-plane MR of an amorphous LAO/STO heterostructure fabricated at 10^{-6} Torr oxygen pressure. Linear lines are guides to the eye. (b) Out-of-plane MR of amorphous LAO/STO samples fabricated at different oxygen pressures.

4.1.3 Kondo effect and electric field effect

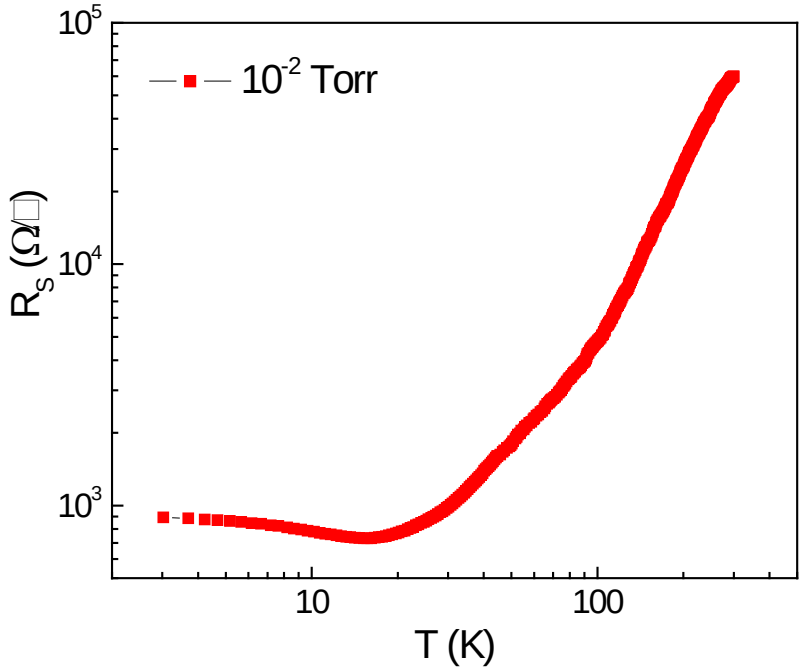

Figure 4.9. R_s-T of a 20 nm amorphous LAO/STO heterostructure fabricated at 10^{-2} Torr oxygen partial pressure.

The R_s-T curve of a 20 nm amorphous LAO/STO heterostructure (Fig. 4.9) fabricated at 10^{-2} Torr behaves differently from other heterostructures

fabricated at lower oxygen pressure. There is a resistance minimum at ~18 K, which tends to saturate at low temperatures.

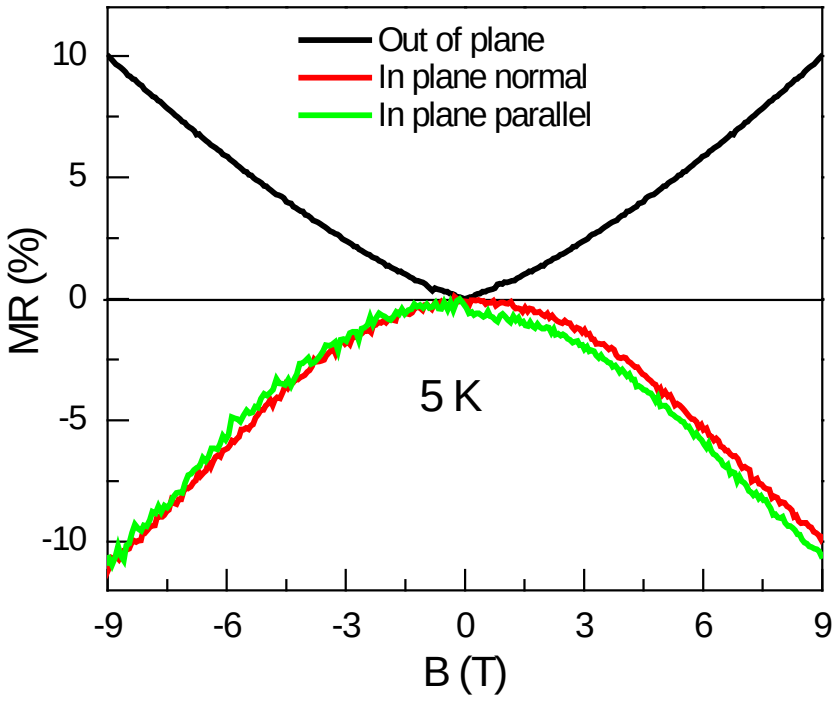

Figure 4.10. Out-of-plane and in-plane MR of the 10^{-2} Torr amorphous LAO/STO heterostructure.

The typical mechanisms proposed to explain the low temperature resistivity minimum are weak localization and Kondo scattering. To distinguish between these two, we performed MR measurements. As shown in Fig. 4.10, the out-of-plane MR is positive, which can be understood by orbital scattering [119] due to the Lorentz force. However, when the magnetic field ***B*** is applied parallel to the sample surface, the MR is negative, regardless of current direction, *i.e.*, the relative angle between ***B*** and current. Even when ***B*** is in plane and perpendicular to current, positive MR is absent. The anisotropy between out-of-plane and in-plane transverse MR indicates that the conductivity is quasi-two-dimensional (quasi-2D) rather than three-

dimensional because the orbital effect is suppressed in a 2D system when ***B*** is in-plane. Hence, the in-plane negative MR is associated with Kondo scattering, since for quasi-2D weak localization the negative MR appears only when ***B*** is perpendicular to the sample surface (or electron orbital plane) [137]. Moreover, the in-plane isotropy of the MR further confirms the Kondo effect [82].

Similar to the Kondo effect observed in crystalline LAO/STO heterostructures [20] as well as electric-field-controlled STO single crystals [138], the Kondo effect in amorphous LAO/STO heterostructures can be associated with localized Ti^{3+} moments. Recent calculations by Pavlenko *et al.* [139] show that oxygen vacancies at titanate interfaces can generate a two-dimensional magnetic state due to the interface orbital reconstruction. The Kondo effect is indeed a demonstration of the magnetic scattering of mobile carriers by localized magnetic moments [140]. The density of mobile carriers of the 10^{-2} Torr heterostructure is lower than those prepared at lower oxygen partial pressure. That could be the reason why we observe a more pronounced Kondo effect in the 10^{-2} Torr sample.

Figure 4.11 demonstrates the electric field tuning of the electron gas in an amorphous LAO/STO heterostructure at 5 K using a back gate. The large tunability in the sheet resistance (60% variation between ±60 V) and in the MR [Fig. 4.11(b)] are comparable to the electric field effect in a 2DEG confined at the interface in a crystalline heterostructure [141]. That further confirms the quasi-2D nature of the electron gas in amorphous LAO/STO heterostructures.

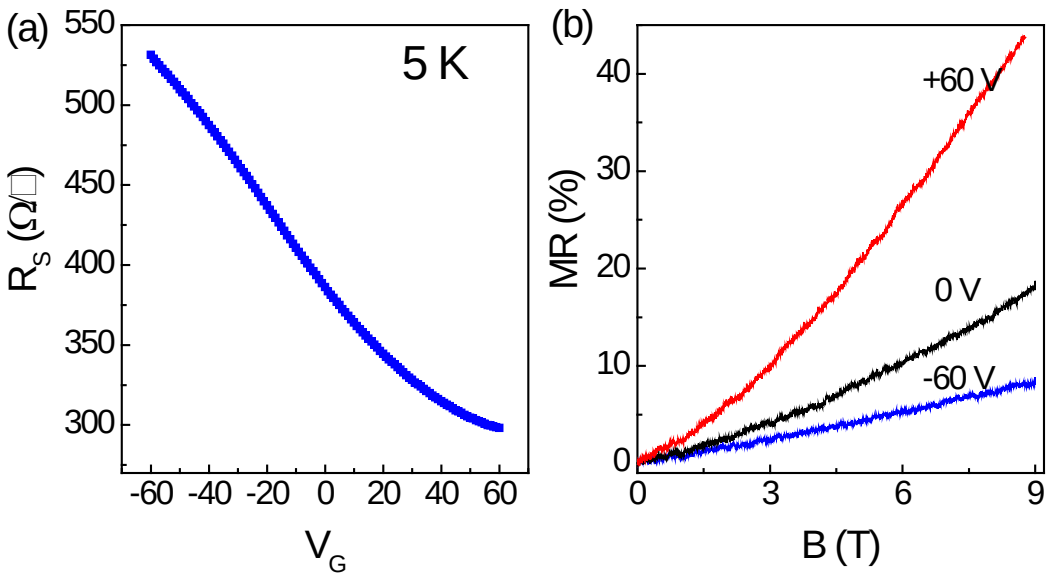

Figure 4.11. (a) Sheet resistance and (b) MR of a 20 nm amorphous LAO/STO heterostructure prepared at 10^{-4} Torr as a function of back gate voltage at 5 K.

4.1.4 Critical thickness for appearance of conductivity

We systematically examined the LAO layer thickness dependence of sheet resistance for amorphous LAO/STO heterostructures fabricated in different oxygen partial pressures ranging from 10^{-1} to 10^{-6} Torr. For samples deposited at 10^{-1} Torr, no measurable conductivity was ever detected up to a 100 nm LAO layer thickness. As shown in Fig. 4.12(a), for samples prepared at 10^{-2} Torr and lower pressure, a sharp drop by more than four orders of magnitude in sheet resistance occurs at a certain LAO layer thickness, which strongly depends on oxygen pressure [Fig. 4.12(b)].

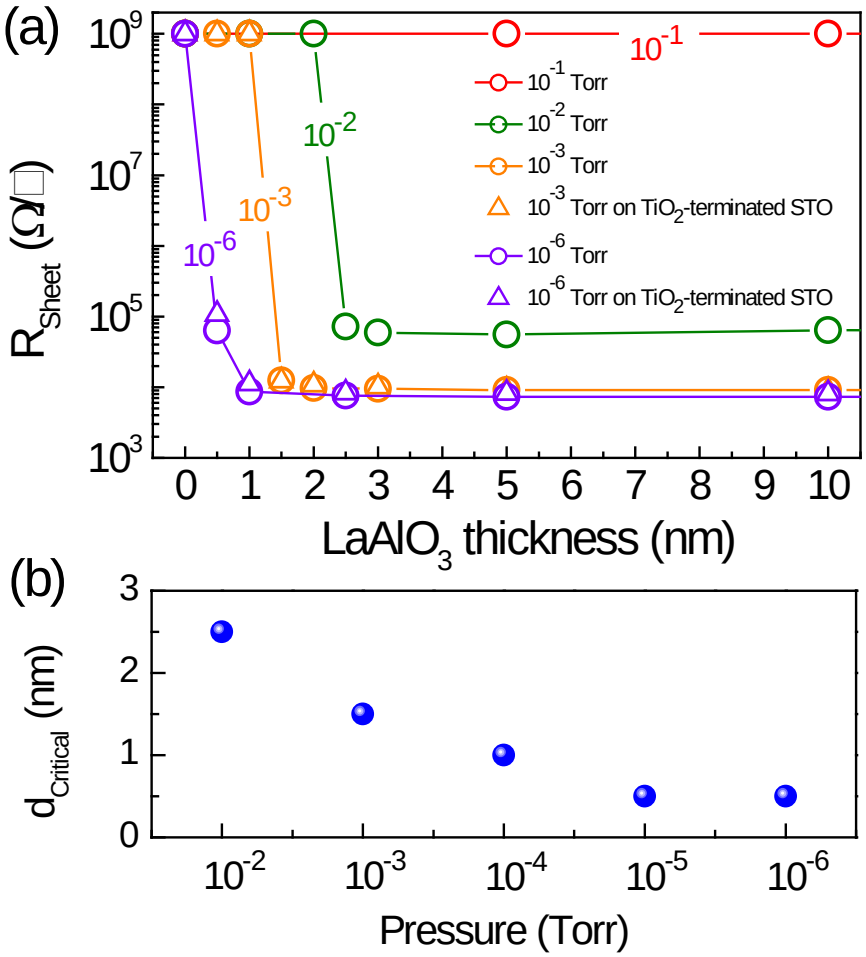

Figure 4.12. (a) Thickness dependence of room-temperature sheet resistance of amorphous LAO/STO heterostructures prepared at different oxygen pressures and on different STO substrates. Triangle symbols represent TiO_2-terminated STO substrates, while circles represent untreated STO substrates. (b) Critical thickness as a function of deposition oxygen pressure.

A similar sharp transition in resistance as a function of overlayer thickness was observed by Chen *et al.* [47] and Lee *et al.* [48]. However, the critical thickness for different pressures in our case is different from those reported by Chen *et al.* This is in contrast to the oxygen-annealed crystalline LAO/STO case, where the critical thickness of 4 uc [29] is robust over a large oxygen pressure range from 10^{-2} to 10^{-5} Torr. We also found that the critical thickness in the amorphous case depends on some other factors such as laser energy and substrate-target distance. For example, as we increased the substrate-target

distance in our experimental setup by a factor of two and lowered the laser fluence from 1.3 to 0.7 J/cm^2, the critical thickness at 10^{-3} Torr changed from 1.5 to 6 nm. There is no pronounced difference in the sheet resistance when the amorphous heterostructures are fabricated on TiO_2-terminated instead of randomly-terminated STO.

There are three intriguing features in Fig. 4.12 that demand explanation –i) the sharp conductivity transition, ii) the oxygen pressure dependence of the critical thickness, and iii) the saturation of the sheet resistance with the amorphous overlayer thickness. When depositing the overlayer, chemically reactive species such as Al [142] have a strong propensity to attract oxygen ions from the surface of the STO, even at room temperature. The conductivity transition is explained by percolation of the electrons associated with the oxygen vacancies. The wave function of these electrons will be Bohr-like orbitals with radii of a few nm (3.2 nm for STO), resulting from the large dielectric constant of STO (ε_r = 300 at 300 K) and the large effective mass (~5m_e) [143]; the percolation carrier density is ~10^{13} cm^{-2} in one monolayer. The oxygen-depletion process from the STO surface will depend on how much reactive oxygen is available in the ambient atmosphere during deposition, thereby explaining why the critical thickness decreases at lower oxygen pressures. At the carrier densities required for percolation, the vacancy concentration at the STO surface is of the order of a few percent, a value that is already high and the further formation of vacancies will be inhibited [144]. This explains the saturation of the sheet resistance.

4.2 Oxygen annealing experiment

4.2.1 Oxygen annealing of amorphous $LaAlO_3/SrTiO_3$

The conductivity of all the amorphous LAO/STO heterostructures vanishes after a 1 h post-anneal at 600 °C in flowing oxygen (1 bar), as can be seen in Fig. 4.13(a). At the same time, the PL intensity of all oxygen-annealed amorphous LAO/STO heterostructures decreases significantly and approaches the intensity of the as-received substrate [Fig. 4.13(b)]. This confirms that oxygen vacancies in STO create the conductivity.

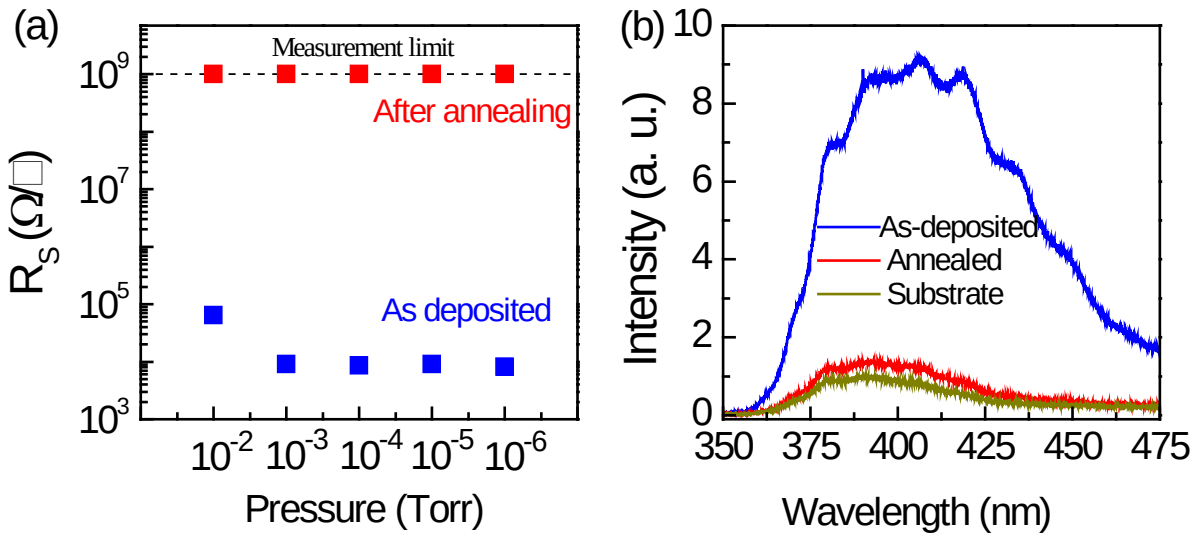

Figure 4.13. (a) Room-temperature sheet resistance of 20 nm amorphous LAO/STO heterostructures prepared at different oxygen pressures before and after oxygen-annealing in 1 bar of oxygen gas flow at 600 °C for 1 h. (b) PL intensity of the 20 nm amorphous LAO/STO heterostructures fabricated at 10^{-6} Torr before and after oxygen-annealing.

4.2.1 Oxygen annealing of crystalline $LaAlO_3/SrTiO_3$

To compare the amorphous and crystalline LAO/STO heterostructures, 10 uc crystalline LAO films were grown on TiO_2-terminated STO substrates under typical growth conditions, at 750 °C and 10^{-3} Torr, and then post-annealed in oxygen as described above. They remain conductive, although there is a decrease in carrier concentration and the room-temperature sheet resistance increases by a factor of seven (Fig. 4.14); for example, an unannealed crystalline sample has a room temperature carrier density of 8.26×10^{13} cm^{-2}, which decreases to 1.62×10^{13} cm^{-2} after post-annealing.

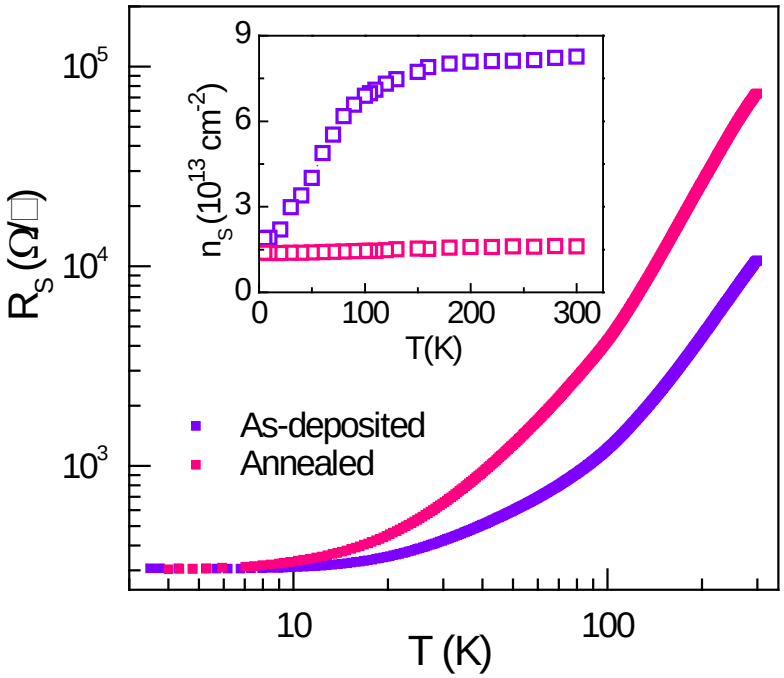

Figure 4.14. R_s-T and (inset) n_s-T of a 10 uc crystalline LAO/STO heterostructure prepared at 10^{-3} Torr and 750 °C before and after oxygen-annealing in 1 bar of oxygen gas flow at 600 °C for 1 h.

Moreover, the n_s-T of the unannealed crystalline LAO/STO sample shows carrier freeze-out below about 100 K, with n_s dropping to $1.90 \times 10^{13}$$cm^{-2}$ at 5 K. In contrast, the carrier density of the post-annealed crystalline sample

exhibits little temperature dependence, changing from 1.62 × 10^{13}cm^{-2} at 300 K to 1.38× 10^{13}cm^{-2} at 5 K. Such post-annealing experiments are reproducible (Fig. 4.15).

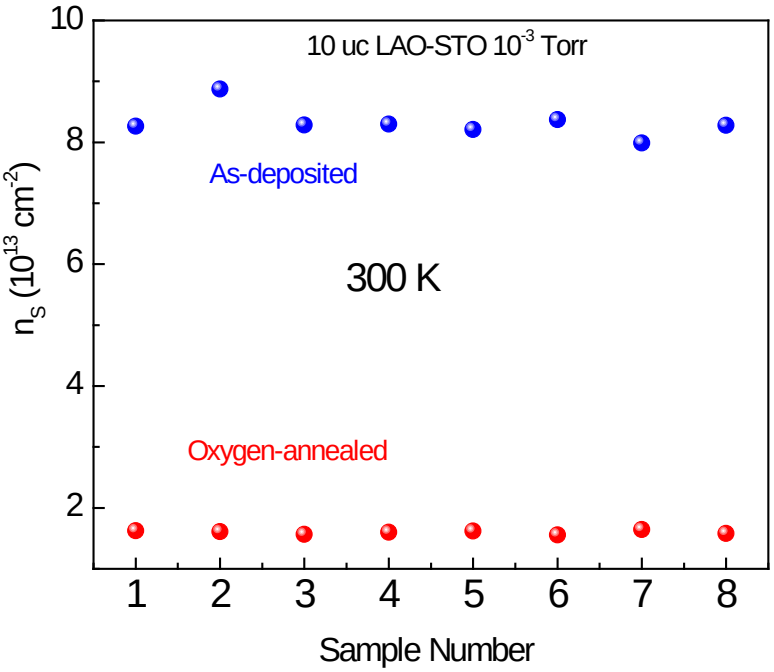

Figure 4.15. Room temperature sheet carrier density of eight crystalline LAO/STO heterostructures before and after oxygen annealing.

The carrier freeze-out effect in unannealed crystalline LAO/STO samples, which also exists in oxygen-deficient STO films [44], is characterized by an activation energy ϵ of 4.2 meV (fitted by $n_s \propto e^{-\epsilon/k_B T}$). In contrast, the activation energy of carriers in oxygen-annealed crystalline LAO/STO samples is even smaller, 0.5 meV.

As shown in Fig. 4.16, the PL intensity of the unannealed crystalline sample is greatly enhanced compared to that of its TiO_2-terminated STO substrate, which reveals the creation of a substantial amount of oxygen vacancies here too during deposition. After post-annealing, the PL intensity

falls back to the substrate level, similar to the effect of post-annealing on the PL signal of amorphous samples.

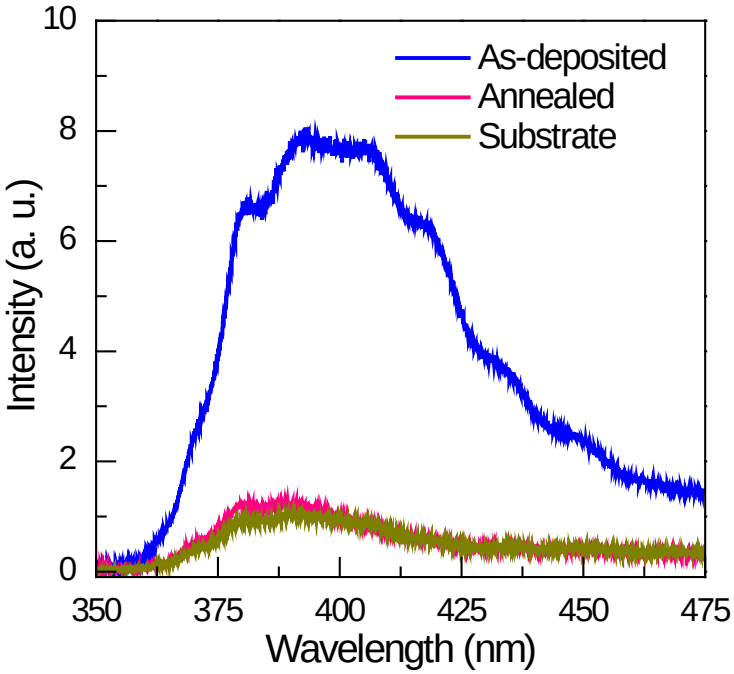

Figure 4.16. PL spectra of a 10 unit cell (uc) crystalline LAO/STO heterostructure prepared at 10^{-3} Torr and 750 °C before and after oxygen-annealing in 1 bar of oxygen gas flow at 600 °C for 1 h.

We conclude at this point that oxygen vacancies contribute significantly to the conductivity in *both* amorphous and unannealed crystalline LAO/STO heterostructures. Specifically, for amorphous LAO/STO samples, the existence of oxygen vacancies in STO substrates is the principal origin of the interface conductivity. For unannealed crystalline LAO/STO samples, oxygen vacancies are only partially responsible for a part of the interface conductivity, which can be eliminated by oxygen-annealing.

4.3 Ar-milling experiment

To further explore the different mechanisms responsible for the interface conductivity in amorphous and oxygen-annealed crystalline LAO/STO heterostructures, we performed Ar-milling experiments for both types, fabricated at 10^{-3} Torr. In the Ar-milling experiment an INTEL VAC Ion-Beam Milling System was used. Ar^{+} ions beam accelerated at 200 V at 4 ml/min and irradiated perpendicularly onto the samples mounted on a 6-inch Si wafer. The Ar pressure was kept as 4.8×10^{-4} Torr during milling. The milling rates of LAO layers were calibrated by an *in situ* secondary ion mass spectroscopy setup, which were 1.7 and 0.8 Å/s for amorphous LAO layer and crystalline LAO layer, respectively.

4.3.1 Ar milling of crystalline $LaAlO_3/SrTiO_3$

Figure 4.17 shows a typical thickness dependence of the conductivity (solid red squares) for oxygen-annealed crystalline heterostructures with a critical thickness of 4 uc. We then used a 4 uc sample in the Ar-milling experiments. After removing the top unit cell of LAO, the conductivity disappears, as shown by the hollow red diamonds. This result agrees with previous reports [30,145]. Moreover, step-by-step Ar milling of an oxygen-annealed 10 uc crystalline LAO/STO sample generates the same critical thickness of 4 uc for maintaining the interface conductivity (black hollow stars). On the other hand, Ar-milling the unannealed crystalline heterostructure from 10 uc down

to 2 uc produces little change in conductance (blue circles) and R_s-T curves (Fig. 4.18), indicating that the conduction is dominated by oxygen vacancies.

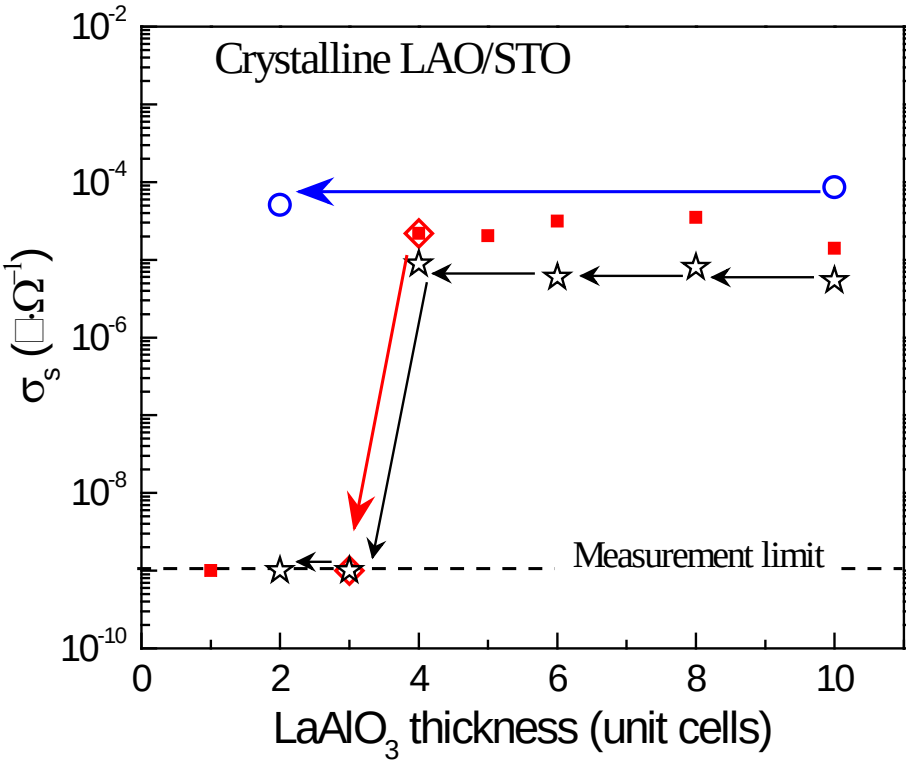

Figure 4.17. Thickness dependence (red solid squares) of room-temperature sheet conductance of oxygen-annealed crystalline LAO/STO heterostructures fabricated at 10^{-3} Torr and 750 °C, showing a critical thickness of 4 uc. The red hollow diamonds denote the sheet conductance of the 4 uc sample before and after the removal of the top 1 uc LAO by Ar-milling. Moreover, the blue hollow circles represent the conductance of an unannealed 10 uc crystalline LAO/STO heterostructure and after the removal of the top 8 uc LAO by Ar-milling. The black hollow stars represent the conductance of another oxygen-annealed 10 uc crystalline LAO/STO sample after step-by-step Ar milling.

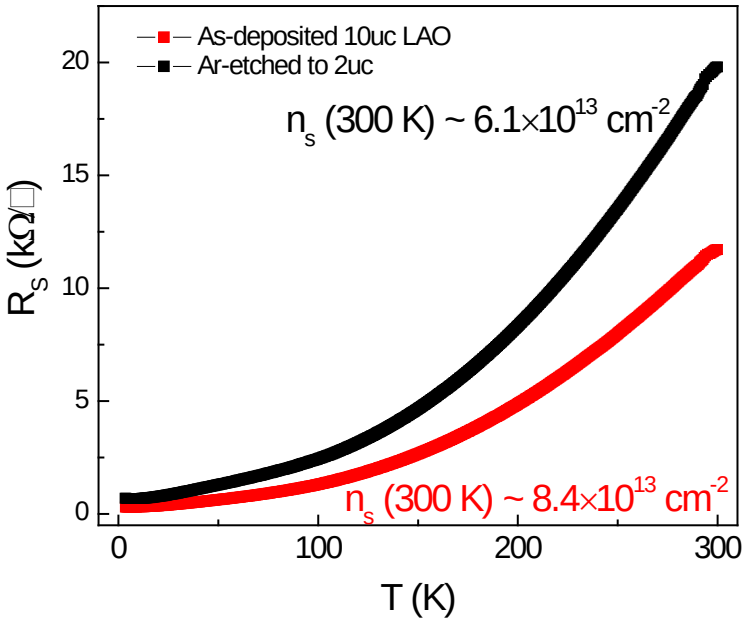

Figure 4.18. Temperature dependence of sheet resistance of 10 uc as-deposited crystalline LAO/STO samples before and after Ar-milling.

4.3.2 Ar milling of amorphous $LaAlO_3/SrTiO_3$

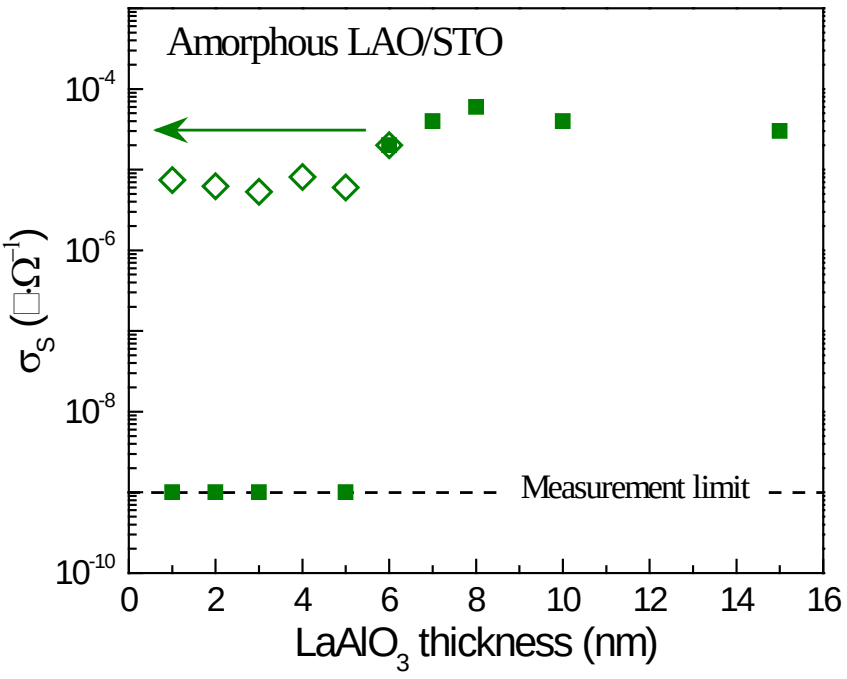

Figure 4.19. Thickness dependence (green solid squares) of room-temperature conductance of amorphous LAO/STO heterostructures fabricated at 10^{-3} Torr, showing a critical thickness of 6 nm. The green hollow diamonds represent the conductivity of the 6 nm sample that remains after the removal of the top LAO

layer 1 nm at a time by Ar-milling. All the arrows represent the Ar-milling process.

To facilitate control of the Ar-milling rate in the amorphous overlayer case, where the milling rate of LAO was more than twice that of the crystalline case, we intentionally arranged the critical thickness of heterostructures to be 6 nm by increasing the substrate-target distance and decreasing the laser fluence. Figure 4.19 illustrates the LAO layer thickness dependence of conductivity (green solid squares) for amorphous LAO/STO samples. As the top amorphous LAO layer is removed, one nm at a time, from a 6 nm LAO/STO sample, the conductivity of the heterostructures is retained (green hollow diamonds).

To check the possible effect of the Ar milling on the conductivity of STO single crystals, an insulating 2 nm amorphous LAO/STO sample was used as reference. After the removal of the top 1 nm of amorphous LAO, the heterostructure remains insulating. This proves that no conductivity is created by the Ar-milling process.

The Ar-milling experiment further confirms that the conductivity in amorphous LAO/STO heterostructures originates principally from oxygen vacancies in the STO substrate. However, the appearance of conductivity in oxygen-annealed crystalline LAO/STO samples is reversible across the critical thickness of 4 uc. Hence this must be closely associated with the interface electronic reconstruction due to the potential build-up in the crystalline LAO overlayer [18,37,38]. This is consistent with the electronic reconstruction at

the interface and also the built-in potential in the polar LAO layer observed by Singh-Bhalla *et al*. [146] and Huang *et al.* [147].

4.4 Re-growth experiment

To explore whether the conductivity of a milled crystalline LAO/STO sample can be restored by depositing a new LAO layer, we re-grew LAO on a crystalline LAO/STO heterostructure after the LAO layer was milled from 4 to 3 uc. After the Ar milling (n×2) surface reconstruction was observed in RHEED patterns both before and after deposition [Fig. 4.20(a)-(b)]. No periodic RHEED oscillation was seen during the deposition [Fig. 4.20(c)], which was likely caused by the surface reconstruction of LAO after Ar ion milling.

The thickness of the newly deposited LAO layer was estimated to be 2 uc. Although the re-grown sample shows a measurable room temperature sheet resistance of ~190 kΩ/□, its R_s-T curve exhibits a semiconducting behavior as seen in Fig. 4.20(d). Oxygen annealing in 600 °C and 1 bar of oxygen flow for 1 h only results in a slight change in sheet resistance, which proves that the partially restored conductance is not from oxygen vacancies. Instead, the partially restored conductance suggests that the polarization catastrophe mechanism still works for the re-grown sample but is limited by the poor crystallinity of the re-grown LAO layer.

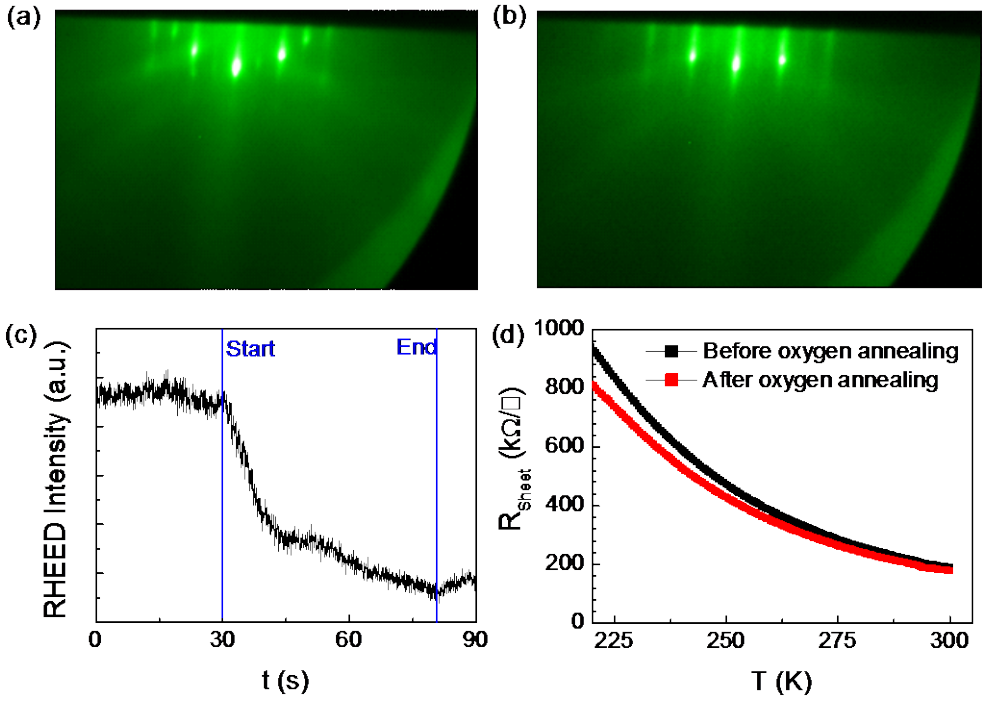

Figure 4.20. (a) RHEED pattern of a crystalline LAO/STO heterostructure with the LAO layer etched to 3 uc. (b) RHEED pattern after a new LAO deposition. (c) RHEED intensity during re-growth. (d) Temperature dependent sheet resistance of the re-grown sample before and after oxygen annealing.

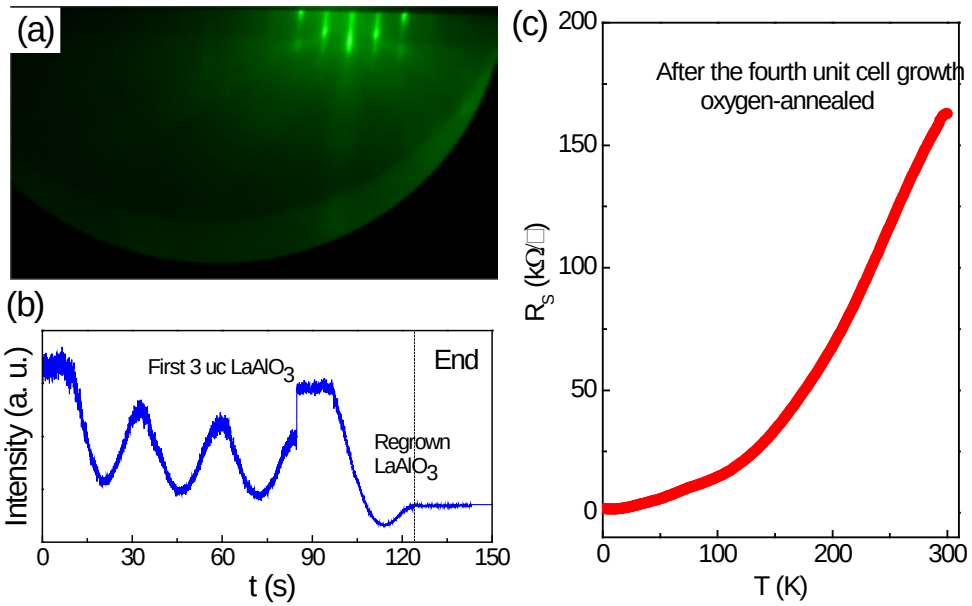

Figure 4.21. (a) RHEED pattern after depositing one uc LAO on a 3 uc crystalline LAO/STO heterostructure. (b) RHEED oscillations of the first deposition of 3 uc $LaAlO_3$ and the re-growth of the fourth uc. (c) Sheet resistance of the re-grown sample after oxygen annealing as a function of temperature.

For comparison, another re-growth experiment was performed. We first fabricated a 3 uc crystalline LAO/STO heterostructure, which was *ex situ* measured to be highly insulating. Then one more unit cell of LAO was deposited on such a heterostructure. No surface reconstruction was seen over the entire deposition process [Fig. 4.21(a)]. During the re-growth, periodic RHEED intensity oscillation was obtained [Fig. 4.21(b)]. The re-grown sample was subsequently oxygen-annealed and the R_s-T curve shows a typical metallic behavior [Fig. 4.21(c)]. Such re-growth experiments demonstrate that the good crystallinity of the LAO layer is crucial for the polarization catastrophe mechanism in the case of crystalline LAO overlayers.

4.5 Summary

In conclusion, despite there being a critical overlayer thickness of LAO for appearance of conductivity at the LAO/STO interface for both crystalline and amorphous forms of LAO, the explanation in the two cases is different. Unlike the 4 uc critical thickness for the oxygen-annealed crystalline heterostructures, there is no universal critical thickness when the LAO is amorphous. The critical thickness then depends sensitively on deposition conditions, and oxygen vacancies in the STO substrate account for the interface conductivity. Oxygen vacancies also contribute substantially to the conductivity of crystalline LAO/STO heterostructures which have not been annealed in oxygen post deposition. The reversible thickness dependence of conductivity across the critical thickness of 4 uc in oxygen-annealed crystalline heterostructures indicates that the interface electronic reconstruction due to the

potential build-up in LAO overlayers is ultimately responsible for the conductivity in that case. Moreover, our experiments demonstrate that the crystallinity of the LAO layer is crucial for the polarization catastrophe.

Chapter 5 Transport properties and defect-mediated ferromagnetism in Nb-doped $SrTiO_3$

5.1 Transport properties of Nb-doped $SrTiO_3$ single crystals

5.1.1 Electrical transport properties

Niobium (Nb) has multiple oxidation states including +5, +4, +3, +2 and -1, while the chemical valence of +5 is the most stable one. In STO, Ti has a chemical valence of +4. The introduction of Nb and the substitution of Ti by Nb in STO and the resulting substitution of Ti by Nb yield redundant electrons. These electrons are mostly free as the dielectric constant of STO is large and consequently the bound energy E_B of a hydrogenic-type donor is negligibly small, which is represented as follows

$$E_B = -\frac{m_D e^4}{8h^2 {\epsilon_r}^2 {\epsilon_0}^2} \quad (5\text{-}1)$$

Considering the dielectric constant $\epsilon_r = 300$ and $m_D = 5m_0$ for STO, the bound energy is 0.8 meV, much smaller than the room temperature thermal energy of 26 meV.

5.1.1.1 Resistivity

Nb-doped STO (NSTO) single crystals are commercially available with a large concentration ranging from 0.01wt% to 1wt%. The electrical resistivity of 5×5×0.5 mm^3 NSTO single crystals (0.01wt% from Japan; 0.05~0.5wt% from CrysTec GmbH, Germany; 0.7wt% from MTI, USA) with different dopings were measured as a function of temperature, which is shown in Fig. 5.1.

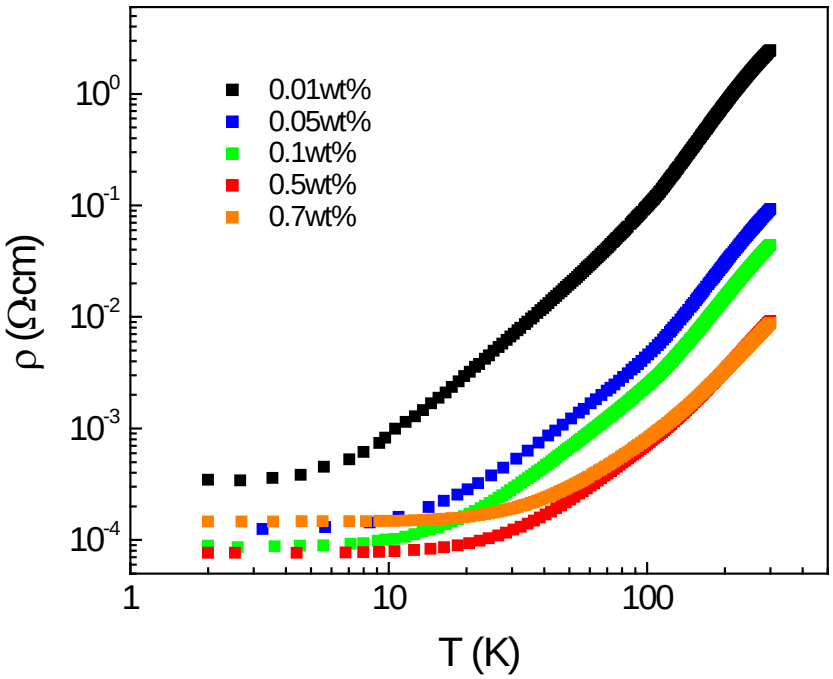

Figure 5.1. ρ-T curves of Nb-doped $SrTiO_3$ (NSTO) single crystals with with different dopings

All the NSTO single crystals are metallic over the entire temperature range of 300 to 2 K. The room temperature resistivity of NSTO single crystals is drawn in Fig. 5.2 as a function of doping concentration. The resistivity obviously decreases with doping in the doping range from 0.01wt% to 0.5wt%, while it only slightly changes with doping above 0.5wt%. On one hand, NSTO

single crystals from different manufacturers could be different in quality. On the other hand, a too high concentration of doping could result in compensating defects [148] in STO crystals such as Sr and Ti vacancies which then limits the increase of its carrier density.

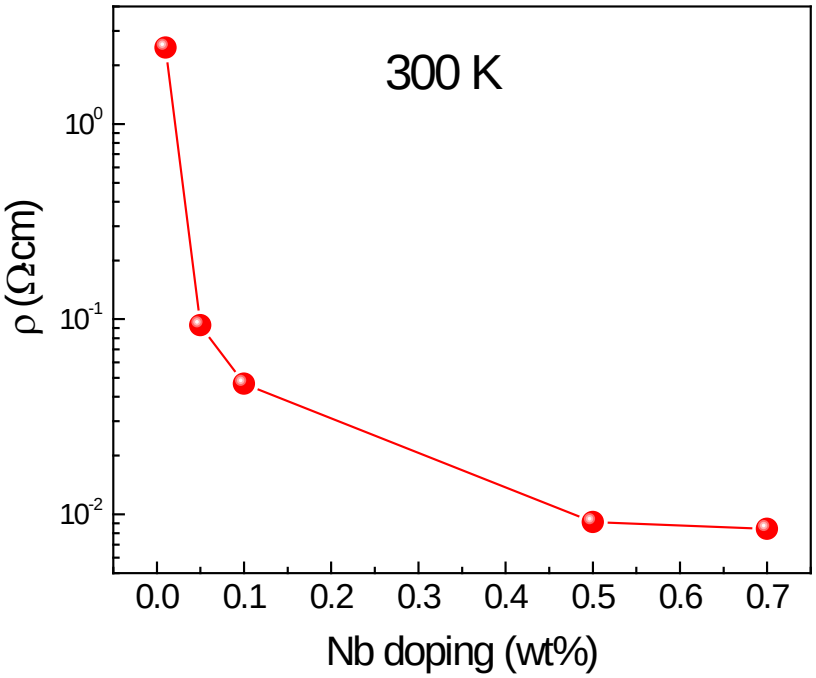

Figure 5.2. Room temperature resistivity of NSTO single crystals.

The room temperature resistivity of 0.01wt% NSTO is pronouncedly higher than others and reaches 25 times that of 0.05 wt% NSTO. This could be due to the low substitution rate of Ti and the poor uniformity for a too low concentration of Nb doping. To examine that, the carrier density of 0.01wt% NSTO was determined by Hall measurements. The *n*-*T* curve of 0.01wt% is shown in Fig. 5.3. The carrier density is 7×10^{17} cm^{-3} at room temperature, which is only one fifth of the nominal carrier density of 0.01wt% NSTO (3.4×10^{18} cm^{-3} provided that Nb atoms are fully occupying Ti sites). This

suggests that almost 80% Nb atoms are interstitial but not serve as substitution atoms in the case of 0.01wt% NSTO.

5.1.1.2 Carrier density and mobility

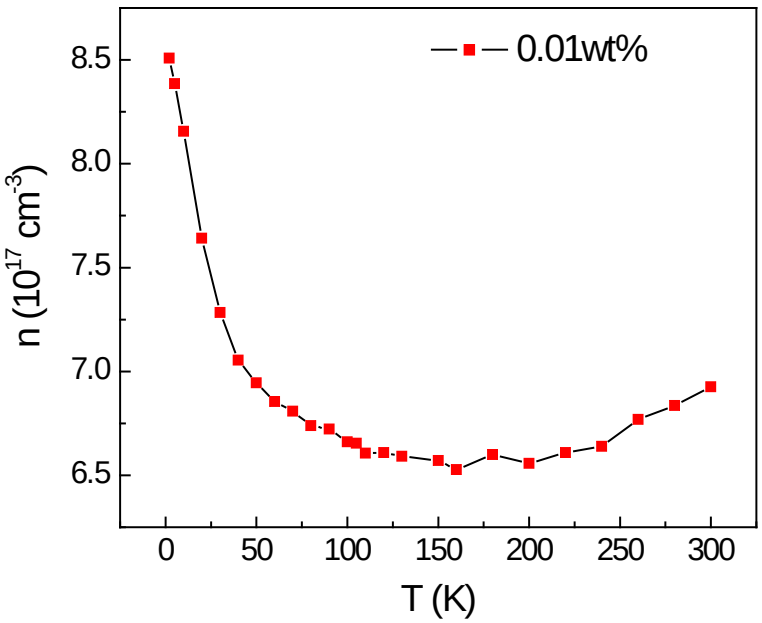

Figure 5.3. Temperature dependent carrier density of 0.01wt% NSTO.

The carrier density of 0.01wt% NSTO decreases with lowering temperature at high temperatures above 150 K and surprisingly increases at low temperatures especially below 100 K. Such an increase in carrier density was also observed in others' measurements [88,149]. This unexpected behavior is nearly unphysical from the typical thermal activation of carriers viewpoint. So definitely, there is at least one more intrinsic mechanism affecting the temperature response of carrier density, which is competing with the thermal activation in STO and becomes dominant at low temperatures in this case.

One of the unique properties of STO is that its dielectric constant increases with lowering temperature (especially below ~100 K) and saturates below 4 K because of the quantum-mechanical stabilization of the paraelectric phase [50]. It seems plausible to assume that in reduced STO part of electrons are trapped by the Coulomb potentials of lots of positively charged defects due to the strongly ionic nature of the lattice. Thus as the dielectric constant increases, the Coulomb potentials will be suppressed due to dielectric screening (or polarization shielding), in which a screened Coulomb potential [91] is inversely proportional to ϵ_r. Hence the increase of dielectric constant could serve as a kind of detrapping mechanism and consequently account for the increase of carrier density in STO at low temperatures.

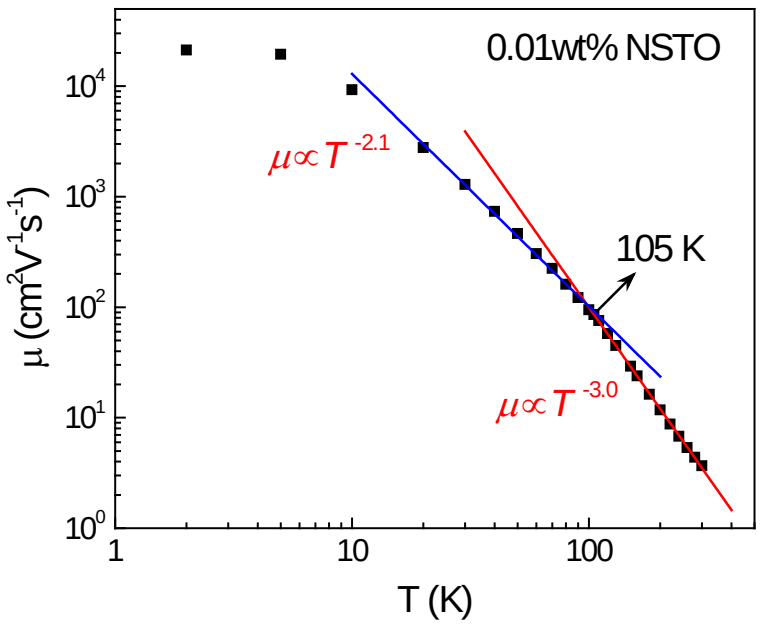

Figure 5.4. Temperature dependence of mobility of 0.01wt% NSTO. Solid lines are power law fittings.

The temperature dependence of mobility of 0.01wt% NSTO deduced from the resistivity and carrier density is shown on a logarithmic scale in Fig. 5.4.

The high mobility, up to 21,190 $cm^2V^{-1}s^{-1}$ at 2 K, decreases with temperature rapidly and varies in accordance with certain power laws above 20 K, where the scattering of electrons by polar optical phonons dominates and results in power law dependence of mobility on temperature $\mu \propto T^{-\beta}$ [89,92,93]. The effect of the structural phase transition in STO at ~105 K on the mobility can be apparently seen from the linear fittings owing to the variation in phonon vibration modes induced by the structural phase transition. Below 20 K, the scattering of electrons is dominated by ionized defect potentials [89]. The mobility further increases with decreasing temperature from 20 K due to the dielectric screening of ionized scattering potentials. That is because the scattering potential of ionized defects is inversely proportional to the dielectric constant and the dielectric constant of STO increases at low temperatures. Finally, saturation appears from 4 K and below probably corresponding to the quantum paraelectric phase in STO.

The temperature dependence of carrier density for 0.05wt% NSTO is shown in Fig. 5.5. It shows similar features as that of 0.01wt% NSTO, i.e., the carrier density increase with decreasing temperature. However, it peaks at 40 K. This could be due to the interplay between thermal activation and dielectric screening. The room temperature carrier density is 1.4×10^{19} cm^{-3}, close to the ideal carrier density of 1.7×10^{19} cm^{-3}. Its mobility is shown in Fig. 5.6. The power law variation at 105 K can be clearly seen although the exponents both above and below 105 K become smaller compared to those of 0.01wt% NSTO. Similarly, the mobility is dominated by ionized defect scatterings below 20 K and phonons above 20 K.

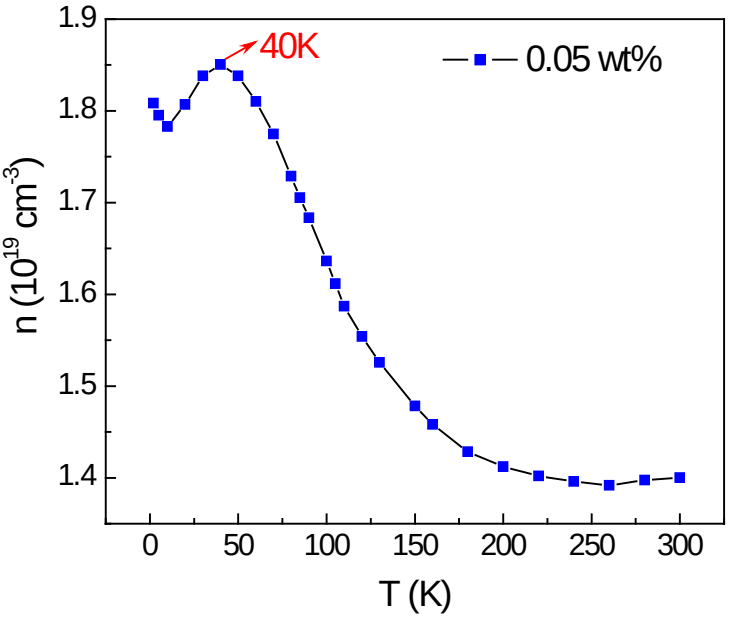

Figure 5.5. Temperature dependent carrier density of 0.05wt% NSTO.

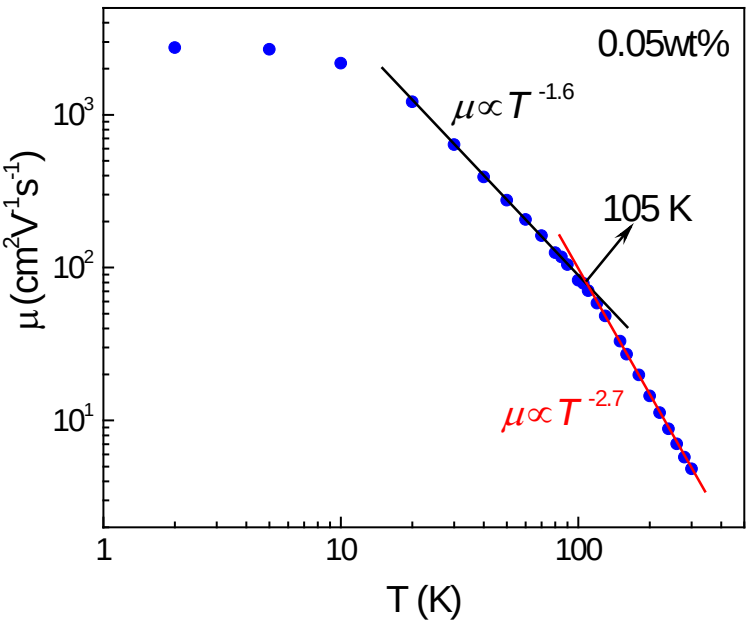

Figure 5.6. Temperature dependence of mobility of 0.05wt% NSTO. Solid lines are power law fittings.

The *n-T* curve of 0.1wt% NSTO is shown in Fig. 5.7. The carrier density increases with lowering temperature and peaks at 50 K. The room temperature carrier density is 2.7×10^{19} cm^{-3}, less than the ideal carrier density of 3.4×10^{19}

cm^{-3}. The corresponding temperature dependence of mobility is drawn in Fig. 5.8, which also shows the variation in power laws at 105 K. Below 20 K, the mobility is dominated by ionized defect scatterings.

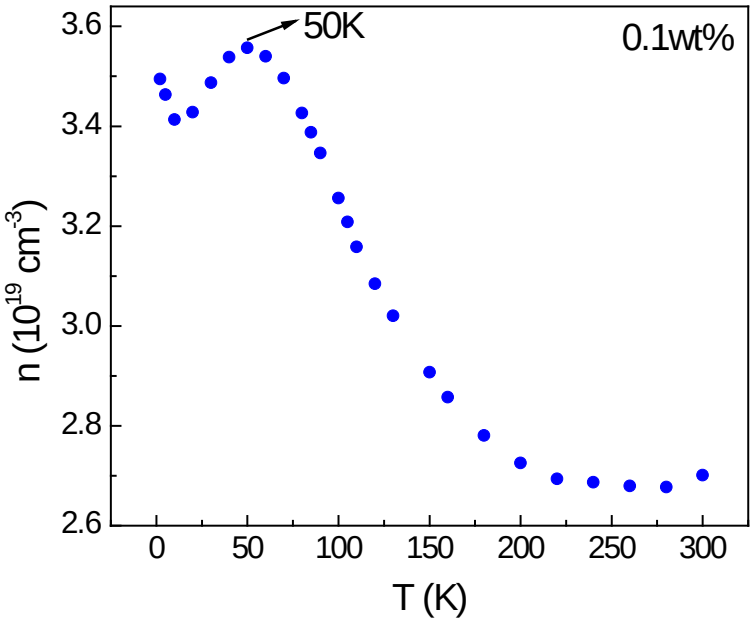

Figure 5.7. Temperature dependent carrier density of 0.1wt% NSTO.

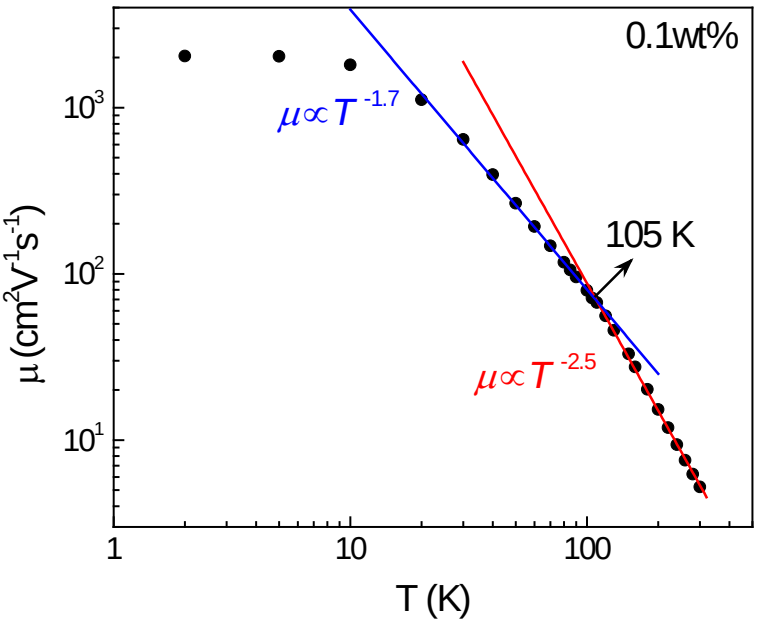

Figure 5.8. Temperature dependence of mobility of 0.1wt% NSTO. Solid lines are power law fittings.

The carrier density of 0.5wt% NSTO measured as a function of temperature is shown in Fig. 5.9. The room temperature carrier density is

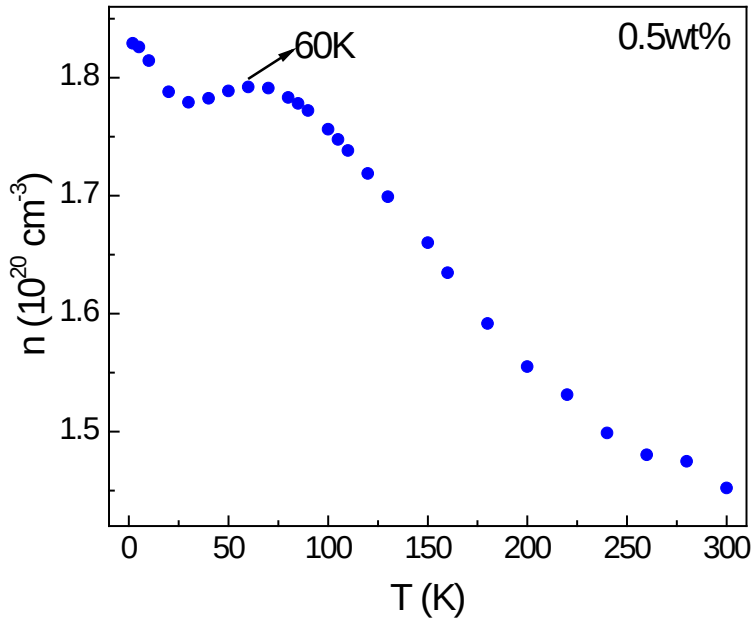

Figure 5.9. Temperature dependent carrier density of 0.5wt% NSTO.

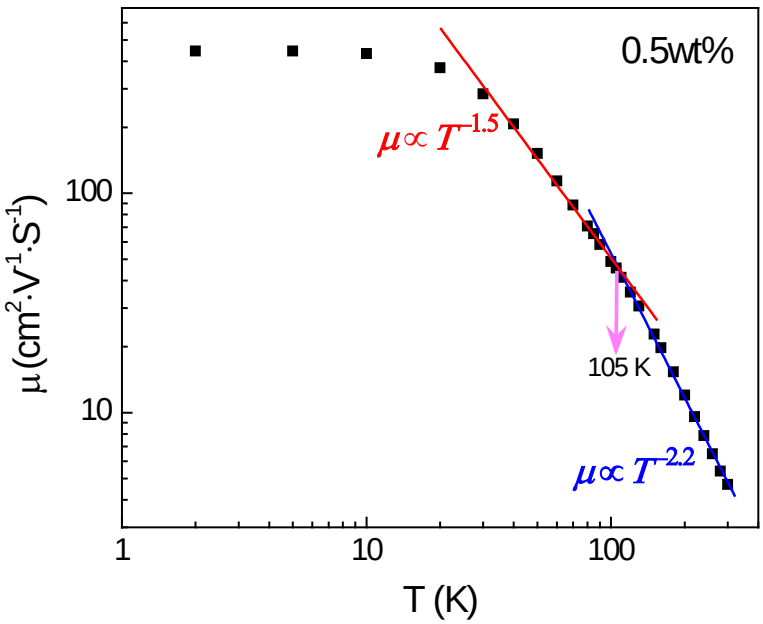

Figure 5.10. Temperature dependence of mobility of 0.5wt% NSTO. Solid lines are power law fittings.

1.4×10^{20} cm^{-3}. The carrier density decreases with lowering temperature, which is likely due to the dielectric screening. Its mobility is demonstrated in Fig. 5.10. Below 30 K, the mobility is dominated by ionized defect scatterings.

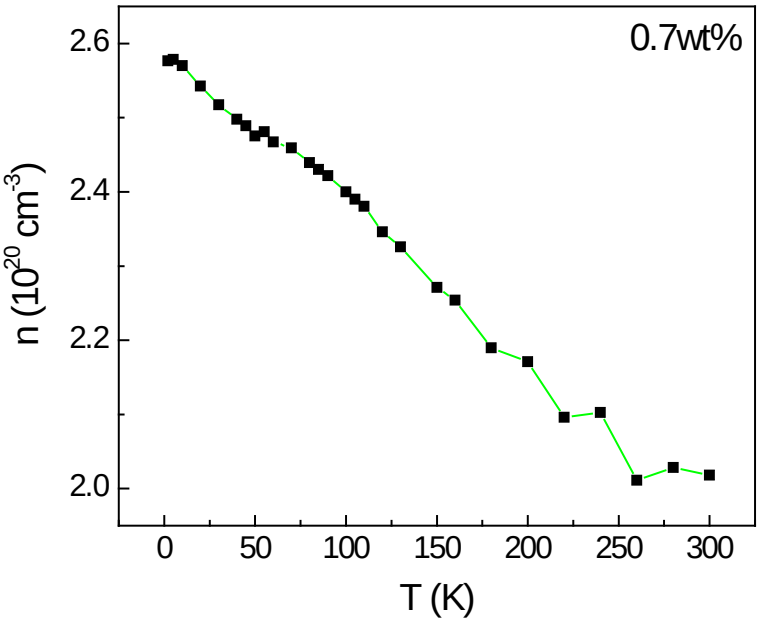

Figure 5.11. Temperature dependent carrier density of 0.7wt% NSTO.

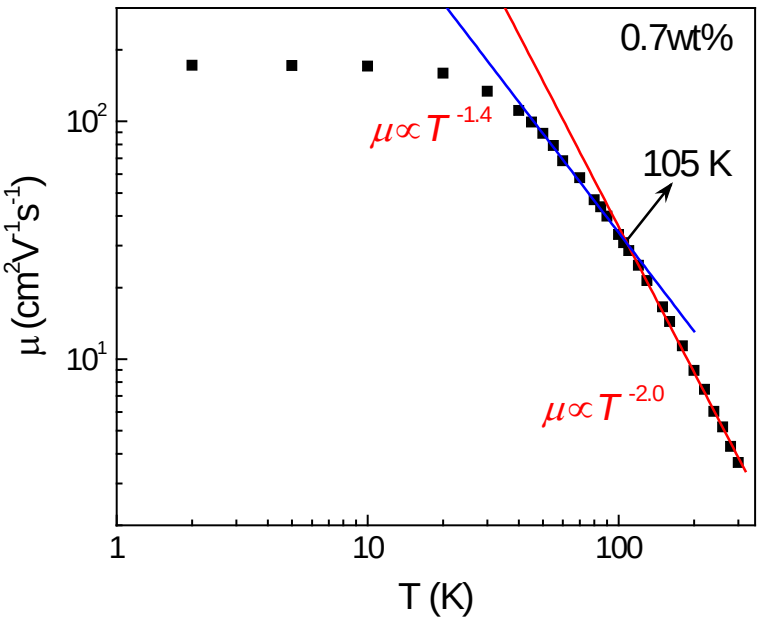

Figure 5.12. Temperature dependence of mobility of 0.7wt% NSTO. Solid lines are power law fittings.

The carrier density of 0.7wt% NSTO almost linearly decreases with temperature (Fig. 5.11). At room temperature, it is 2.0×10^{20} cm^{-3}. The mobility of 0.7wt% NSTO is quite low, less than 200 $cm^2V^{-1}s^{-1}$ at 2 K (Fig. 5.12). Above 40 K, the mobility is dominated by phonon scatterings.

To summarize, the room temperature carrier density of NSTO single crystals is plot together with their ideal carrier density (assuming that all Nb atoms have substituted Ti atoms) for different dopings in Fig. 5.13. As can be seen, the room temperature carrier density almost linearly scales with doping concentration. The carrier density is larger than the Mott critical carrier density 4.7×10^{20} cm^{-3}, which explains why all the NSTO single crystals are metallic as shown in Fig. 5.1. In addition, the difference between measured

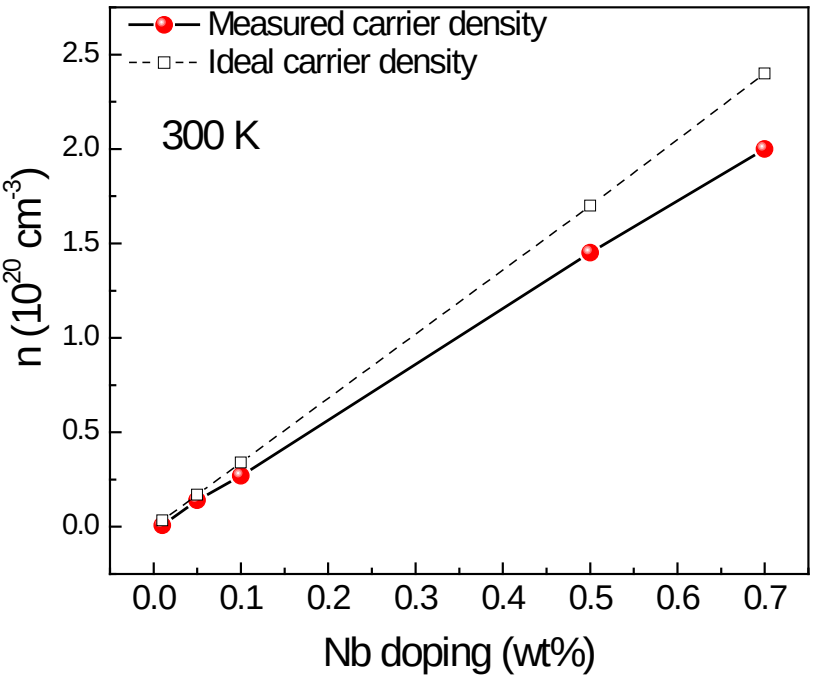

Figure 5.13. Room temperature carrier density of NSTO single crystals with different dopings. The carrier density considering 100% substitution is illustrated by hollow squares for different dopings.

and ideal values increases with doping concentration, which indicates the rise of compensating defects in highly doped NSTO single crystals.

The room temperature and low temperature mobility are shown in Fig. 5.14 on a logarithmic scale for NSTO single crystals. The room temperature mobility is small, ranging from 3.6 to 5.2 $cm^2V^{-1}s^{-1}$. However, the low temperature mobility is several orders of magnitude larger. Moreover, it nearly exponentially decays with doping concentration, which indeed demonstrates that the low temperature mobility in NSTO is strongly affected by carrier density due to electron-electron scatterings.

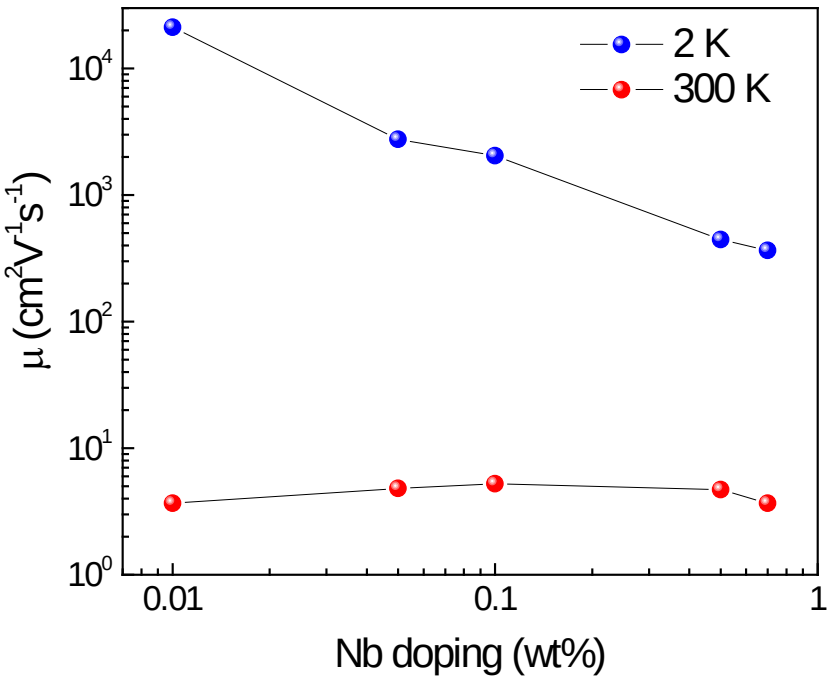

Figure 5.14. Room temperature and low temperature mobility of NSTO single crystals.

5.1.1.3 Fermi liquid

To corroborate the existence of electron-electron scatterings, the low temperature resistivity of NSTO is plotted as a function of T^2 (Fig. 5.15).

Highly linear dependence of resistivity on T^2 is a direct demonstration of the Fermi liquid behavior and thus strong electron-electron scatterings.

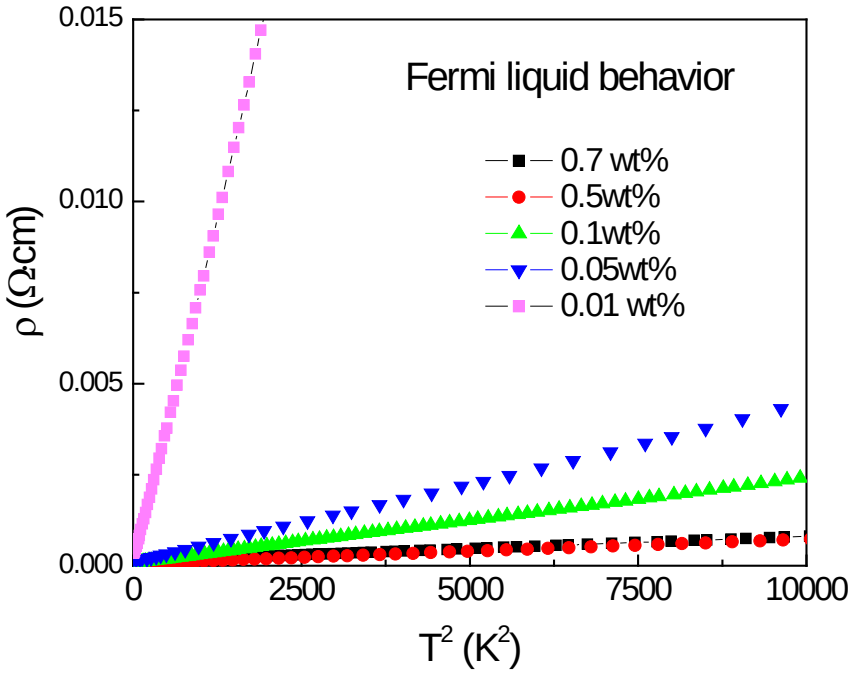

Figure 5.15. Low temperature resistivity of NSTO single crystals versus T^2.

5.1.2 Magnetotransport properties

The magnetoresistance (MR) of a 0.01wt% NSTO single crystal was measured up to ±5 T at low temperatures. According to the Kohler's law, MR typically has a quadratic magnetic field dependence because of the orbital effect. In this case, MR is proportional to μ^2. As the mobility of 0.01wt% NSTO is remarkably high up to 21,190 $cm^2V^{-1}s^{-1}$ at 2 K (Fig. 5.4), the positive MR at 2 K is extremely large, which is 4000% at 5 T on average. The MR at 10 K is far less due to the lower mobility, close to 620% at 5 T (Fig. 5.16).

The measured MR is asymmetric. To examine the origin of this asymmetry, the MR measurements were subsequently performed by scanning field from

the opposite direction, *i.e.*, from 5 T to 0. The MR curve coincides with that measured by scanning field from -5 to 5 T, which indicates the asymmetry is induced by geometrical misalignment.

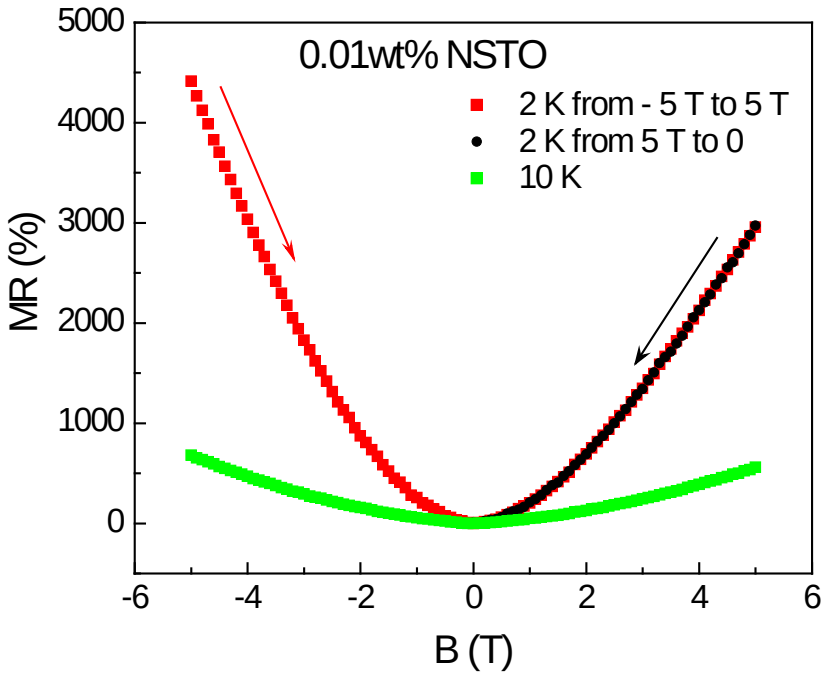

Figure 5.16. Magnetoresistance (MR) of 0.01wt% NSTO at 2 K and 10 K. The magnetic field is perpendicular to the sample surface.

The resistance of 0.01wt% NSTO at 2 and 10 K is plotted together in Fig. 5.17 as a function of magnetic field. It clearly shows a resistance crossover at ~1.5 T, above which the resistance at 2 K exceeds that at 10 K. Thus a resistivity upturn should exist in the ρ-T curves of 0.01wt% NSTO under a magnetic field greater than 1.5 T. To examine this, ρ-T curves were measured under different magnetic fields up to 9 T and the low temperature resistivity upturns were observed under magnetic fields larger than 1.5 T (Fig. 5.18).

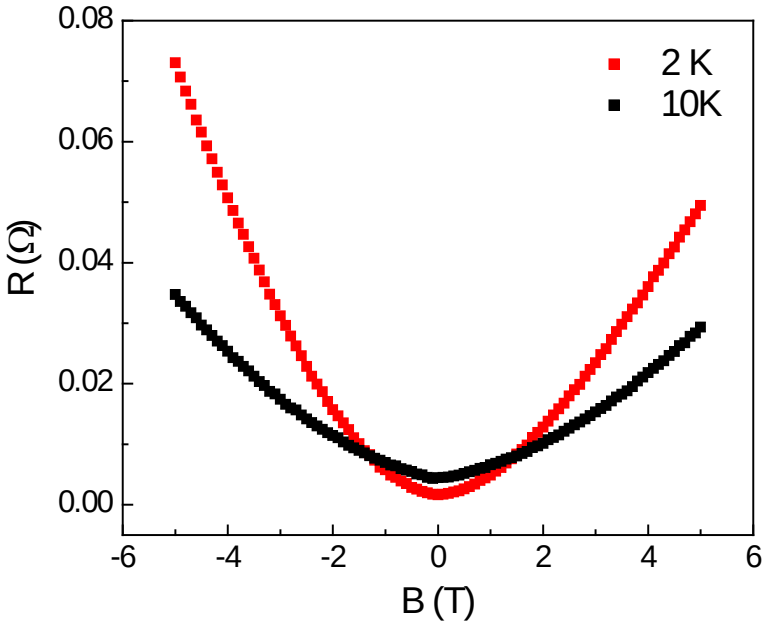

Figure 5.17. Resistance of 0.01wt% NSTO at 2 K and 10 K versus magnetic field.

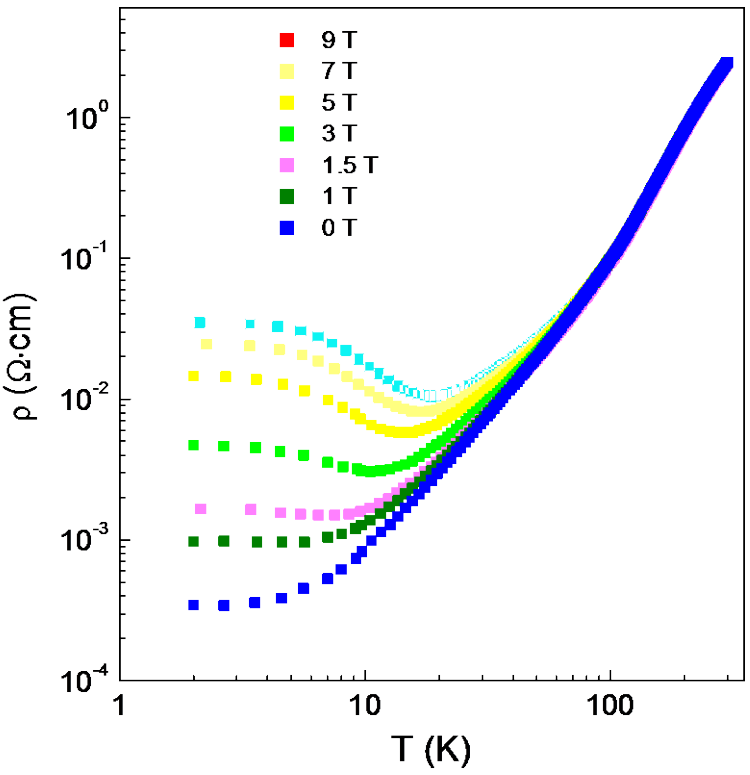

Figure 5.18. *ρ-T* curves of a 0.01wt% NSTO single crystal under different magnetic fields normal to the sample surface.

Such a magnetic field induced resistivity minimum is only seen in high mobility 0.01wt% NSTO single crystals. The low temperature MR of other NSTO single crystals is plotted together in Fig. 5.19, which decreases dramatically as the doping concentration increases as a result of the exponentially reduced mobility.

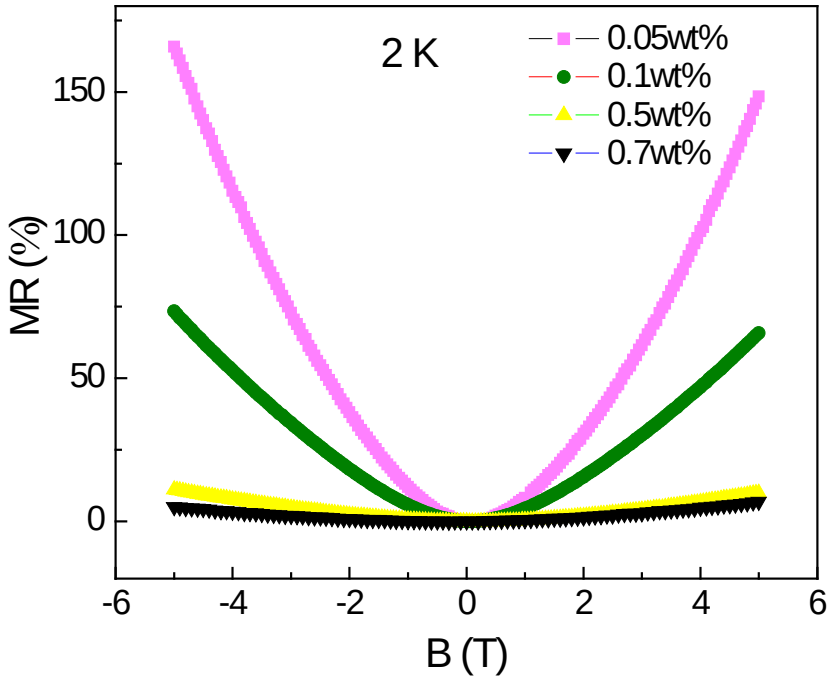

Figure 5.19. MR of NSTO single crystal with doping from 0.05wt% to 0.7wt% at 2 K with magnetic field normal to the sample surface.

5.1.3 Summary

We studied the electrical and magneto transport properties of NSTO single crystals with different dopings. It was found that all the NSTO single crystals are metallic and the Fermi liquid exists in NSTO single crystals at low temperatures. The room temperature resistivity decreases with doping and the room temperature density linearly scales with doping concentration. However, the low temperature mobility exponentially decays with the doping

concentration due to the strong electron-electron scatterings. The effect of structural phase transition of STO at 105 K on the mobility can be clearly seen in all NSTO single crystals. The carrier mobility in 0.01wt% NSTO is highest, up to 21,190 $cm^2V^{-1}s^{-1}$ at 2 K. The MR in NSTO crystals is quadratic and complies with the classical orbital scattering, which can be well described by Kholer's rule. Consequently, a large MR resulting from the high mobility at low temperatures leads to a resistivity minimum in ρ-T curves.

5.2 Defect-mediated ferromagnetism in Nb-doped $SrTiO_3$ crystals

The potential for discovering new magnetic interactions with possible applications in spintronic devices has been the main driver for the search of oxide-based room temperature ferromagnetism (RTFM) [150,151]. Since the theoretical prediction of RTFM in Mn-doped ZnO [152] and the experimental observation of RTFM in Co-doped TiO_2 [153], dilute magnetic semiconductors (DMS) has attracted significant attention from the community of oxide electronics. Typically, DMS are fabricated by introducing magnetic ions into wide bandgap semiconductors including ZnO, TiO_2, SnO_2 [154] and In_2O_3 [155]. However, since the finding of unexpected ferromagnetism in insulating HfO_2 thin films by Venkatesan *et al*. in 2004 [156], RTFM has been also observed in pristine TiO_2 [157,158], In_2O_3 [158], ZnO [159] and SnO_2 [160] thin films without magnetic dopings, which is generally attributed to oxygen vacancies or other ionic defects.

STO in oxide electronics is equivalent to silicon in semiconductor industry for oxide electronics due to its chemical and thermal stabilities, as well as the lattice match to a large number of functional perovskite materials. Pristine STO is a typical nonpolar band insulator with an indirect band gap of 3.25 eV and a direct band gap of 3.75 eV. However, the slight doping of Nb can shift the Fermi level of STO up or even into the bottom of its conduction band, thus giving an *n*-type semiconducting or metallic phase. Nb-doped $SrTiO_3$ (NSTO) itself is a highly interesting system as it is a low temperature two-band superconductor [161], with strong interactions among electrons, plasmons, phonons and polarons [162,163]. Moreover, it is one of the most used substrates for oxide film deposition and electronic device application.

Pure STO is an ideal diamagnet in the insulating phase due to the absence of unpaired electrons. The Nb doping replaces some of Ti atoms and the resultant Ti^{3+} ions with unpaired electrons can generate a paramagnetic response to external magnetic field. Here we report RTFM observed in NSTO single crystal substrates, which is found to be induced by oxygen vacancies and mediated by the free electrons from Nb doping. We examined the transport and the magnetic properties of 5 mm×5 mm×0.5 mm two-side-polished NSTO single crystals with different dopings, *i.e.*, 0.05 wt%, 0.1 wt%, 0.5 wt% (from CrysTec GmbH, Germany), 0.7 wt% (from Hefei Kejing Material Technology Co., Ltd., China) and 1 wt% (from MTI, USA). The transport and the magnetic properties were measured by a Quantum Design PPMS and a Quantum Design SQUID-VSM tool, respectively.

5.2.1 Ferromagnetism in Nb-doped (≥ 0.5wt%) $SrTiO_3$ single crystals

Magnetic moment versus temperature (*M-T*) measurements were performed for NSTO single crystals using 1000 Oe with the magnetic field parallel to the surface of samples. The zero-field-cooled (ZFC) *M-T* curves of NSTO single crystals are shown in Fig. 5.20. For 0.05 and 0.1 wt% dopings, the negative magnetic moments over the whole temperature range as seen in Fig. 5.20 indicate the diamagnetism from the STO matrix is dominant. The magnetic moment versus magnetic field (*M-H*) curves measured up to 2000 Oe did not show hysteresis even at low temperatures down to 2 K as seen in the inset of Fig. 5.20. That indicates only the diamagnetism and paramagnetism coexist in the 0.05 and 0.1 wt% NSTO single crystals. The increase in the *M-T* curves with decreasing temperature is due to the paramagnetic contribution to the magnetic moment.

The ZFC *M-T* curve of a two-side-polished 0.5 wt% NSTO single crystal is shown in Fig. 5.21, which is evidently distinct from the *M-T* curves of single crystals with lighter doping. Unexpectedly, the magnetic moment peaks at ~60 K and ferromagnetic hysteresis loops can be seen from 2 to 300 K as shown in Fig. 5.22. The average coercivity field is around 300-400 Oe. The saturation ferromagnetic moment at 2 K is ~5×10^{-6} emu and the corresponding magnetization for the whole 5 mm×5 mm×0.5 mm single crystal is 4×10^{-4} emu/cm^3, which is quite small, equivalent to ~ 5×10^{-3} Oe. The average ferromagnetic moment for each Nb atom (or roughly each free electron) and

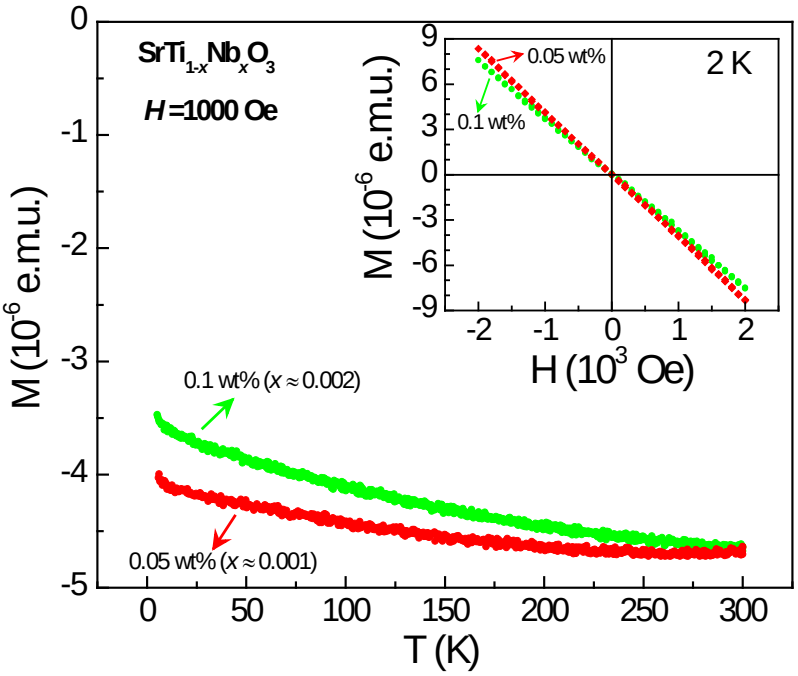

Figure 5.20. Zero-field-cooled (ZFC) *M-T* curves of 0.05 wt% and 0.1 wt% NSTO. (Inset) *M-H* curves at 2 K.

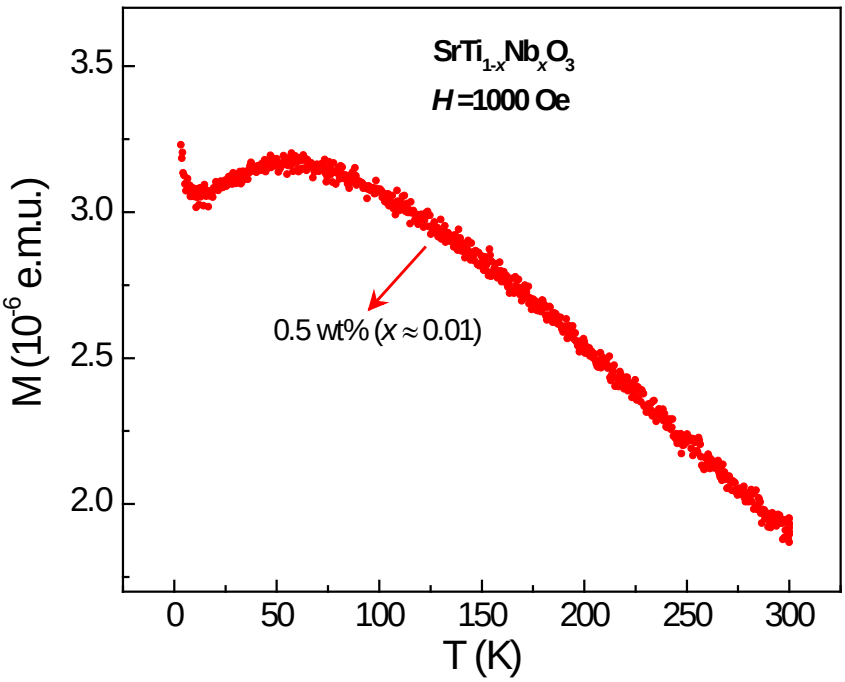

Figure 5.21. ZFC *M-T* curve of 0.5 wt% NSTO.

each unit cell of NSTO is ~2.65×10^{-4} and ~2.59×10^{-6} μ_B respectively, which are two orders of magnitude smaller than the ferromagnetism of free-electron gas, (0.07 μ_B/electron) as reported by Young *et al*. [164].

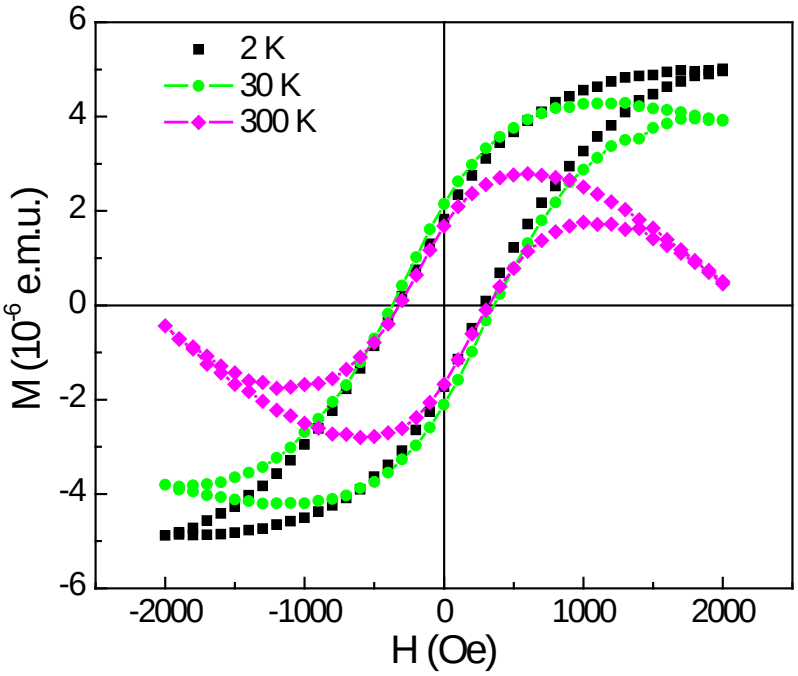

Figure 5.22. *M-H* curves of 0.5 wt% NSTO at 2 K, 30K and 300 K.

Different 0.5 wt%-doped NSTO single crystals both from the same and from a different batch (CrysTec GmbH) were checked.

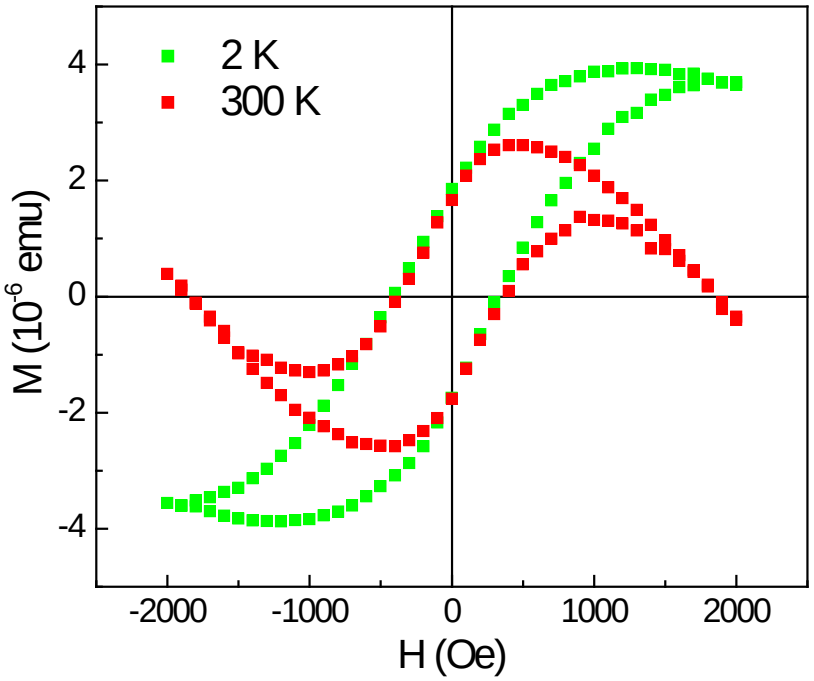

Figure 5.23. *M-H* curves of another 0.5wt% NSTO from CrysTec.

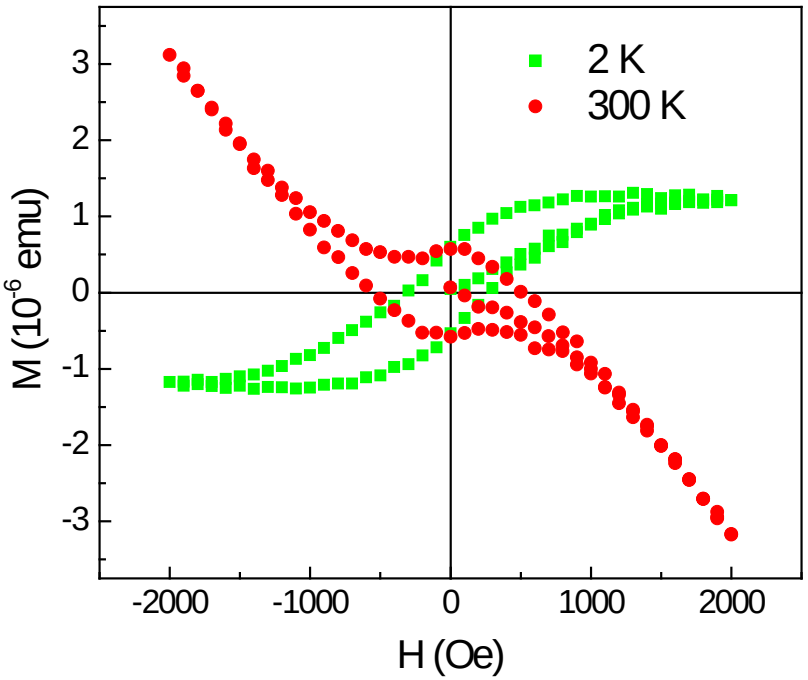

Figure 5.24. *M-H* curves of a 0.5wt% NSTO single crystal in another batch from CrysTec. All samples are with the dimensions of 5 mm×5 mm×0.5 mm.

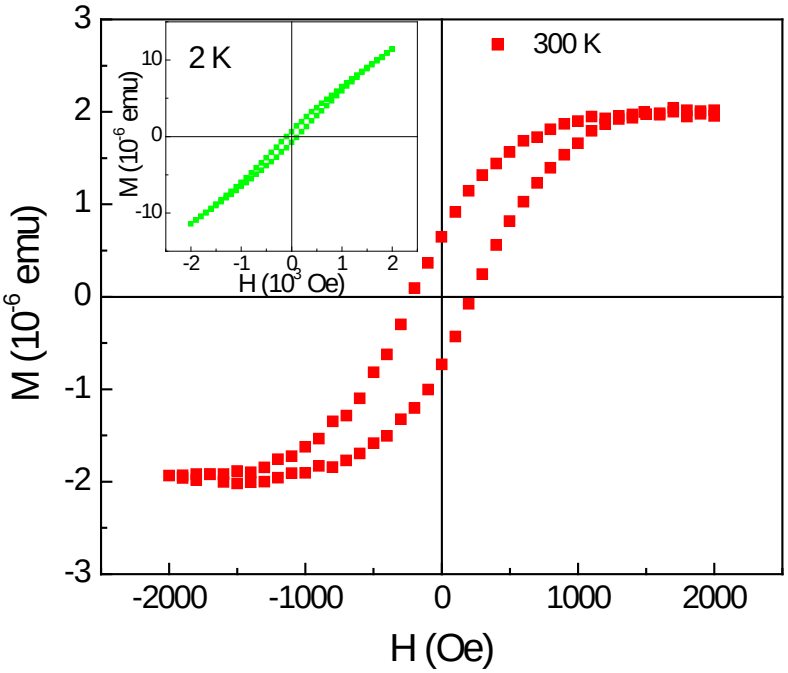

Figure 5.25. *M-H* curves at 300 K of a 0.7wt% NSTO single crystal (5 mm×5 mm×0.5 mm) from Hefei Kejing, China. (Inset) *M-H* curve at 2 K.

It was found all of them show ferromagnetic hysteresis loop with the same order of magnitude of the magnetic moment at both 2 and 300 K (Figs. 5.23 & 5.24). Moreover, 0.7 wt% NSTO from Hefei Kejing Material Technology Co., Ltd., China) and 1 wt% NSTO (from MTI, USA) single crystals also show similar ferromagnetic hysteresis loops both at 2 and 300 K (Fig. 5.25 and Fig. 5.26).

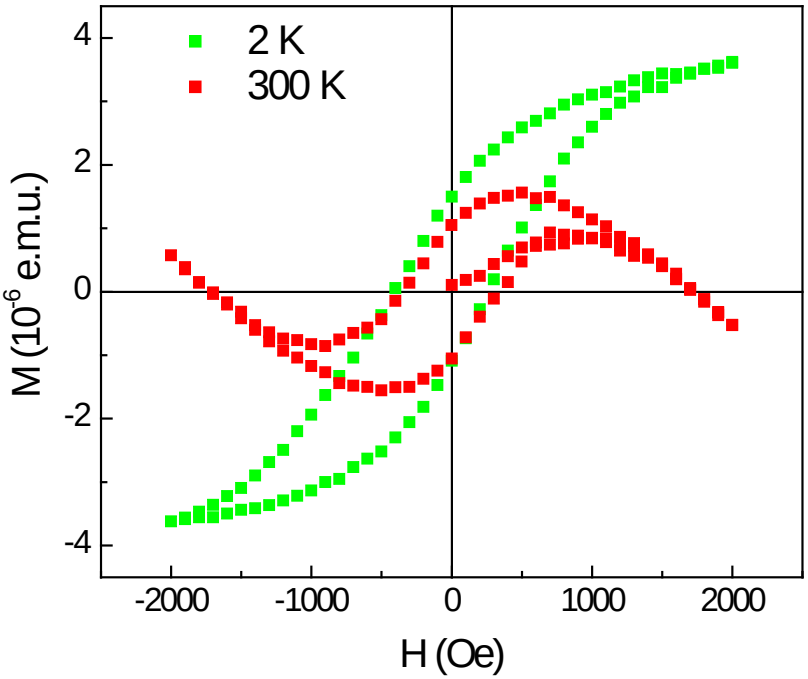

Figure 5.26. *M-H* curves at 300 K and 2 K of a 1wt% NSTO single crystal (5 mm×5 mm×0.5 mm) from MTI, USA.

5.2.2 Impurity examination

Assuming that the ferromagnetism originates from some ferromagnetic artifacts, such as Fe, which can at maximum supply 2.2 μ_B/atom to ferromagnetism, the corresponding minimum density of Fe impurity in 0.5 wt% NSTO is ~1.96×10^{16} atoms/cm^3. It is within the typical detection limit of static time-of-flight SIMS. SIMS analysis of possible Fe, Co, Ni, Cr, Mn and Cu elements were performed down to more than 400 nm below the surface at different regions of the sample but only trace of them on the noise level was seen (Fig. 5.27).

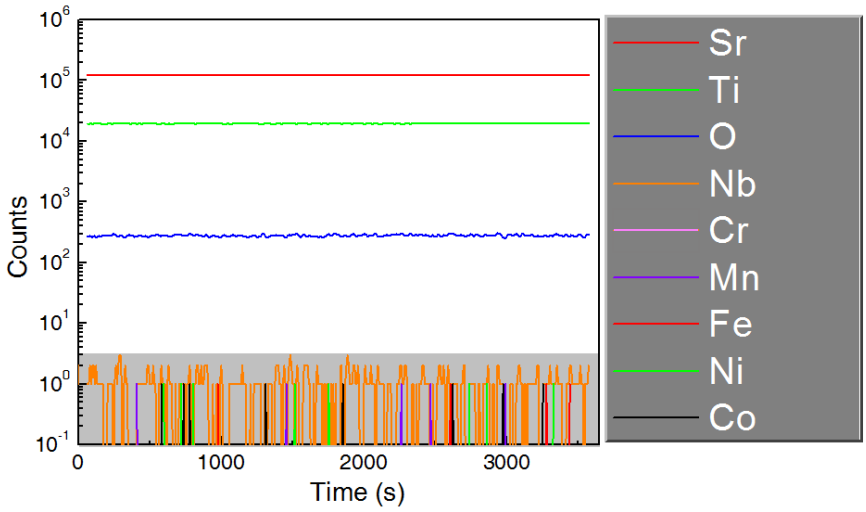

Figure 5.27. Counts versus etching time (corresponding to depth) for all elements during 3700 s etching by Ar ion beam milling with the ion energy of ~3 KeV. The gains of all the possible impurity elements are within the noise level of SIMS.

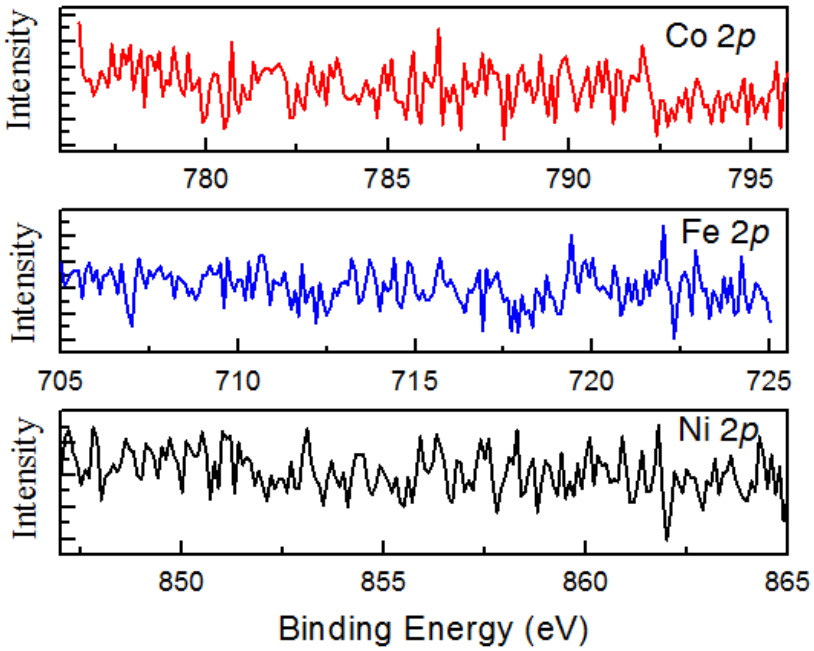

Figure 5.28. XPS spectra of the characteristic peak regions of Fe, Co and Ni. The data were collected more than 100 nm deep below the surface after 720 s etching by Ar ion milling with the ion energy of ~3 KeV. The diameter of the utilized X-ray beam is ~700 μm.

Meanwhile, XPS examination with Ar ion milling was carried out down to more than 100 nm below the surface. The wavelength regions of the

characteristic photoemission peaks of possible Fe, Co and Ni elements were carefully examined but no any signature of them was seen (Fig. 5.28).

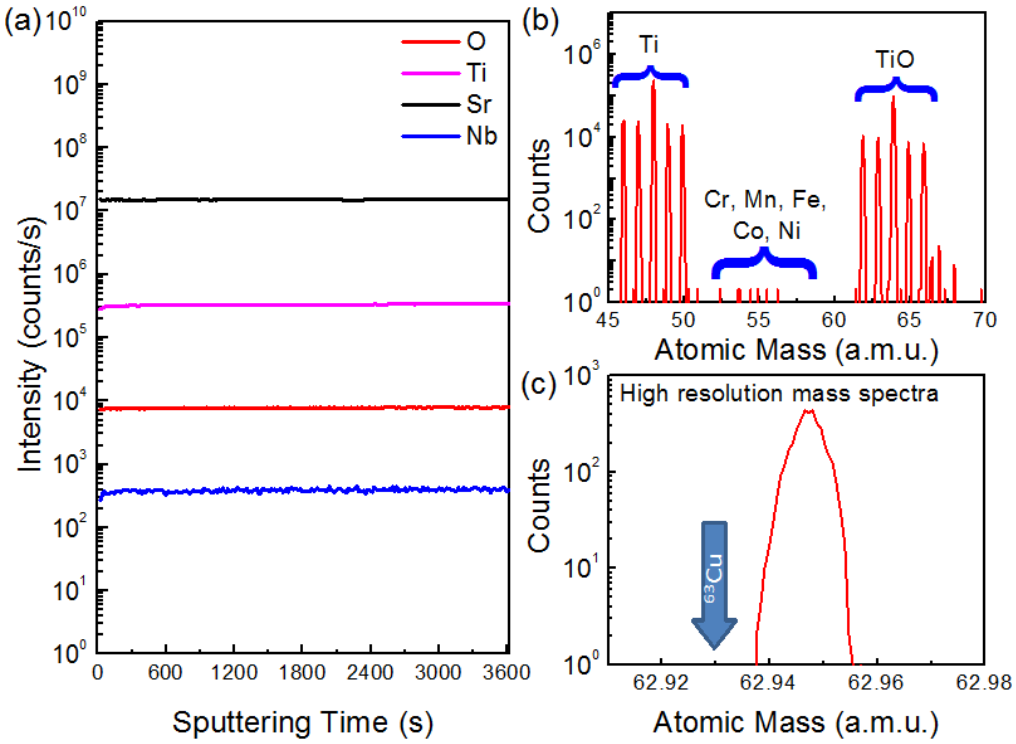

Figure 5.29. Dynamic SIMS (a) Depth profiling spectra of a vacuum-annealed 0.5 wt% NSTO single crystal. (b) Mass spectra of over the mass range of 45-70 a.m.u. (c) High resolution mass spectra at the mass range of $^{47}Ti^{16}O$.

Furthermore, to examine possible impurities of Cr, Mn, Fe, Co, Ni and Cu, we performed dynamic SIMS measurements using a Cameca IMS-6f magnetic sector spectrometer with a sensitivity of ppb, which is three orders of magnitude higher than the sensitivity of the typical static time-of-flight SIMS, for both as-received and vacuum-annealed samples. During the analysis, a Cs^+ primary ion beam of 10 KeV was rastered over an area of 250×250 μm^2, with the samples biased at a voltage of +5 kV. Positive secondary ions were acquired from a central area of approximately 40 μm in diameter. Depth profiling spectra were first acquired over a thickness of approximately 500 nm,

within which the matrix elements were observed to be uniform as shown for the vacuum-annealed sample in Fig. 5.29(a). At the specified depth, mass spectra were then collected over the mass range of interest (45-70 a.m.u.), which confirmed the absence of Cr, Mn, Fe, Co and Ni impurities [Fig. 5.29(b)]. Due to the mass interference of ^{63}Cu and ^{65}Cu with $^{47}Ti^{16}O$ and $^{49}Ti^{16}O$ respectively, high resolution mass spectra were acquired at the mass range of $^{47}Ti^{16}O$ (with mass resolution higher than 5000). No signal of ^{63}Cu was detected as demonstrated in Fig. 5.29(c).

5.2.3 Manipulation of ferromagnetism by annealing

It was found the ferromagnetism can decrease a lot or even disappear after annealing single crystals in air. After annealing of the 0.5 wt% NSTO single crystals at 600°C for 2 h, both the ferromagnetic hysteresis loops at 2 and 300 K completely disappear as shown in Fig. 5.30.

Subsequently, the sample continued to be vacuum-annealed at 950°C in ~10^{-7} Torr vacuum for 1 h, and the hysteresis loops at 2 K measured up to 0.2 and 1 T are shown in Fig. 5.31.

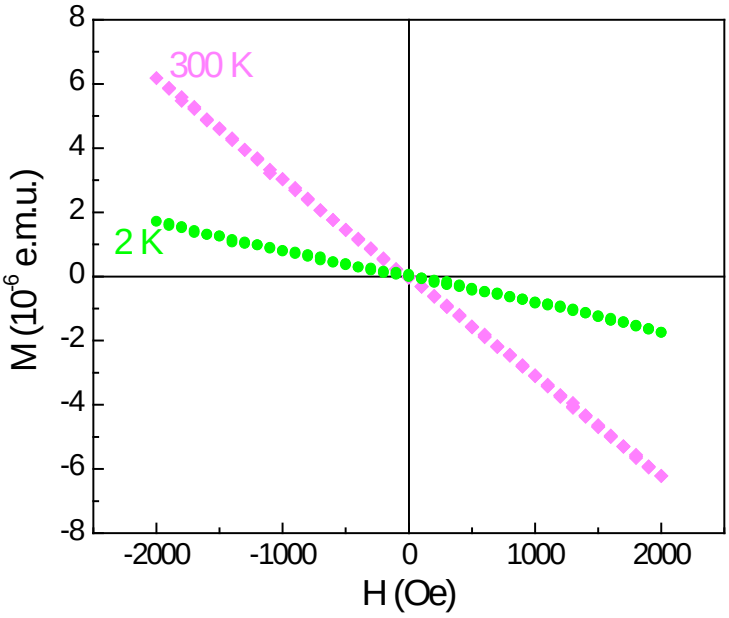

Figure 5.30. *M-H* curves of a 0.5wt% NSTO single crystal after annealing in air at 600°C for 2 h.

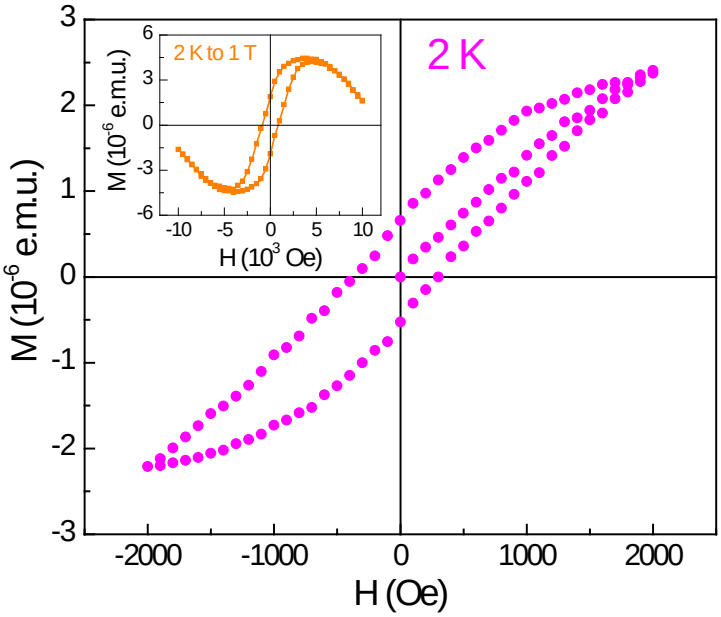

Figure 5.31. *M-H* loop at 2 K upon subsequent vacuum annealing at 950°C in ~10^{-7} Torr vacuum for 1 h. (Inset) *M-H* loop at 2 K measured up to 1 T.

Upon fitting and subtraction of the diamagnetic signal, the pure ferromagnetic loop can be extracted from the *M-H* loop up to 1 T (Fig. 5.32). The final saturation ferromagnetic moment recovered from vacuum annealing is ~8.5×10^{-6} emu, which is of the same order of magnitude with the

ferromagnetic signal in the original case. These results suggest that the ferromagnetism could be closely related to oxygen vacancies in NSTO single crystals.

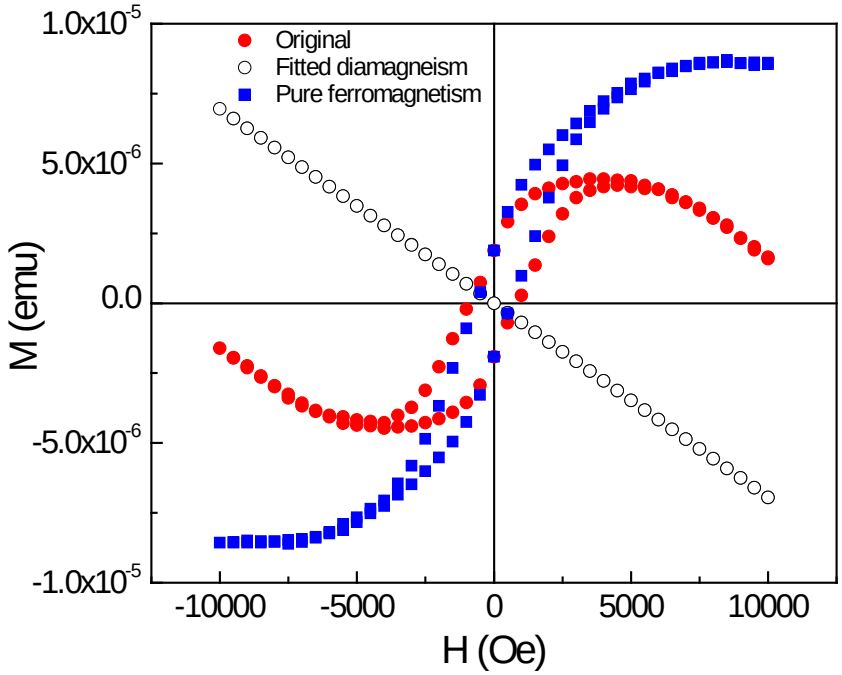

Figure 5.32. Subtraction of the fitted average diamagnetic signal from the original *M-H* curve for the vacuum-annealed 0.5wt% NSTO single crystal.

5.2.4 Relationship between magnetic moment and carrier density

The temperature dependences of carrier density (*n-T*) for as-received NSTO single crystals were measured up to ±2000 Oe via Van der Pauw Hall geometry with two voltage and two current electrodes placed at the four corners of 5 mm × 5 mm square single crystals. Surprisingly, it was found that the carrier density of NSTO peaks at a certain temperature as shown in Fig. 5.33. The peak temperature depends on the doping level. For 0.5 wt%

NSTO, the peak is well at ~60 K and also the *n-T* curve is quite similar to the *M-T* curve in Fig. 5.21.

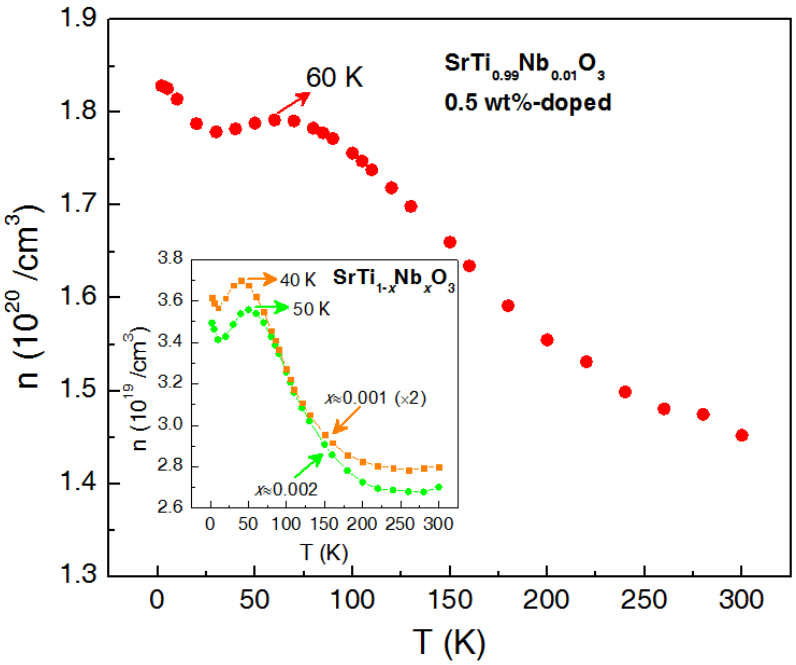

Figure 5.33. Temperature dependences of carrier density (*n-T*) of NSTO single crystals. (Inset) *n-T* curves of 0.05wt% and 0.1 wt% NSTO. The carrier density of 0.05 wt% NSTO has been multiplied by a factor of two.

After annealing in air, the *n-T* curve does not change because the carrier density generated from oxygen vacancies of 1 h vacuum annealing in STO is of the order of 10^{18} cm^{-3} carriers [119], which is two orders of magnitude smaller than the carrier density from Nb doping for 0.5 wt% NSTO. However the original peak at ~60 K in the *M-T* curve disappears, accompanied by the disappearing of the ferromagnetic hysteresis loop. Because no similarity between the *n-T* and *M-T* curves for nonmagnetic 0.05 wt% and 0.1 wt% single crystals is observed although there is also a peak in the *n-T* curve for each of them [inset of Fig. 5.33], it is plausible to believe that the close

similarity in the *n*-*T* and *M*-*T* curves is the signature of the ferromagnetic component.

For as-received 0.05 wt% and 0.1 wt% NSTO single crystals, no ferromagnetism was observed. The reason may be either the carrier density is not large enough or the initial oxygen vacancies inside are less. Because Nb^{5+} ions can attract O^{2-} more and therefore deform the crystal lattice, therefore the larger dopings could generate more defects including oxygen vacancies in the lattice.

Although both oxygen vacancies and Nb atoms can serve as donors of electrons for the Ti 3*d* orbitals in STO, they seem to be different. For example, there is no carrier deionization effect for NSTO even in the most lightly doped samples because the large dielectric constant of STO makes the activation energy of a hydrogenic-type donor quite small (0.8 meV) compared to the thermal energy at RT. But in lightly reduced STO, the carrier freeze-out [44,89] can happen for the electrons resulting from the doubly charged donor centers – oxygen vacancies, *i.e.*, the carrier density decreases dramatically with decreasing temperature and finally the whole system turns to be insulating. The donor level of oxygen vacancies is large up to 80 meV separated from the conduction band of STO [89]. This reveals that the Ti 3*d* electrons and also the magnetic moments originating from oxygen vacancies are naturally more inactive and localized.

As recently reported, localized Ti 3*d* magnetic moment in STO can serve as magnetic centers to result in Kondo scattering [20]. Meanwhile, oxygen

vacancies in the TiO_2 layer of STO can enhance the tendency for ferromagnetism considerably [139]. Therefore a possible scenario for the ferromagnetism of NSTO could be that oxygen vacancies inside NSTO single crystals are supplying localized Ti 3*d* magnetic moments and a large number of free electrons from Nb doping mediate the magnetic interactions among them via RKKY interaction, eventually yielding the ferromagnetism. It seems that sufficient oxygen vacancies as well as carrier density is essential to produce this kind of indirect ferromagnetic exchange interaction. Theoretically, the ferromagnetic RKKY interaction under the Weiss mean-field treatment can be strengthened with the increase of carrier density [165,166]. This may be able to shed light on our case.

Zhang et *al*. [167] have tried to search for ferromagnetism by doping ferromagnetic elements Fe, Co and Ni into the conductive NSTO thin films but failed. In our case, the intrinsic oxygen vacancies could be more compatible with the free electrons such that the ferromagnetism can be obtained. Here, the free electrons themselves participate in the ferromagnetic exchange interaction as mediators, so there is no Kondo scattering observed in transport data of NSTO.

5.2.5 Summary

In summary, we studied the electrical and magnetic properties of NSTO single crystals. Reversible RTFM was observed in highly-doped ($\geq$ 0.5wt%) NSTO single crystals and found to be induced by oxygen vacancies and closely related to free carriers. We proposed the RKKY interaction to explain

the ferromagnetism, where free electrons from Nb doping mediate the magnetic interaction among the localized Ti 3d magnetic moments originating from oxygen vacancies. The ferromagnetism observed here could influence the transport properties across the interface when NSTO is utilized as substrates for device applications. On the other hand, the use of this kind of substrate to search for novel ferromagnetism in oxide thin films should be exercised with care due to the existence of ferromagnetism up to RT. Since although the ferromagnetic signal observed here is small for a bulk single crystal, it is strong enough to mix up the magnetic signals of thin films grown on it.

Chapter 6 Resistive switching mediated by intragap defects

Resistive switching is a physical phenomenon where the resistance of a metal/insulator/metal sandwich structure changes upon applying a voltage or current pulse. It is a potential candidate for non-volatile data memory. The attractive points of resistive switching are the over 10 times resistance change, the capability of multi-level storage, and the fast switching rate (~ns). Moreover, the operation voltage is usually less than 10 V, which is very attractive for low-power applications.

The history of resistive switching can be dated back to the year of 1962, when Hickmott [168] found a hysteresis loop in the DC *I-V* curves in the $Al/Al_2O_3/Au$ sandwich structure and also a negative differential resistance. Nevertheless, the current highly active research in resistive switching was significantly triggered by the over three order of magnitude of resistance change in $Pr_{0.7}Ca_{0.3}MnO_3$ thin films induced by external voltage excitations under magnetic field in 1997 [10]. Following that, Liu *et al*. [11] reported the large electric-pulse-induced reversible resistance change (more than 1700%) at room temperature without magnetic field in $Ag/Pr_{0.7}Ca_{0.3}MnO_3/YBa_2Cu_3O_{7-x}$ structures in 2000. At the same time, Beck *et al.* [169] at IBM Research in Switzerland observed reproducible resistive switching in the Au/Cr-doped

$SrZrO_3/SrRuO_3$ structure. These studies opened the door for resistive switching.

Since then, reproducible resistive switching behaviors have been observed in various oxides, such as Cr-doped $SrTiO_3$ (STO) [170], Nb-doped STO [171], Ba-doped STO [172] although the role of dopants in resistive switching is still unclear. Nearly all of these studies focused on the effect of concentration on the switching performance to achieve optimal dopant concentration. Now, some better-understood mechanisms related to this area are as follows [172]: (i) trapping/detrapping effects and charge transfer processes via donor and acceptor levels (Cr^{3+}, Cr^{4+}) [169], (ii) a Mott metal-insulator transition [173], (iii) formation of local current domains [174], (iv) redox processes and filament model [175,176], and (v) conductivity due to a reversal of a local spontaneous polarization [177].

In this chapter, we present reversible metal-insulator transition (MIT) of insulating $RAlO_3$ (R = La, Pr, Nd, Y) thin films induced by the electrical population of defect levels in the bandgap of oxide insulators, which, in turn, can play a crucial role in determining the insulating nature of the material. Accordingly, our work provides an alternative mechanism for resistive switching.

6.1 Resistive switching in $LaAlO_3$ thin films

6.1.1 Reversible metal-insulator transition

The electronic state of complex oxides can be changed by chemical doping, temperature, external pressure [4,178], magnetic field [179], electric field or light [180]. In particular, the electric-field-induced metal-insulator transition (MIT) has attracted a lot of attention because of its potential for device applications. With the recent excitement in resistive switching in typical metal/insulator/metal structures, electric-field-induced MIT has been revisited as a possible mechanism [173,181,182].

A number of different mechanisms have been previously demonstrated for resistive switching, such as electric-field-induced oxygen vacancy migration resulting in the formation of conducting filaments [175] , and reversible metal migration from electrodes [183]. Such a variety of field-induced phenomena arise from the complex defects that are present in these oxides. Cationic and anionic defects can form trap states within the bandgap of even wide bandgap oxides, drastically affecting their insulating properties [184].

Typical metal/insulator/metal structures (seen in Fig. 6.1) were prepared by first depositing $LaAlO_3$ (LAO) films using a pulsed laser deposition technique from a single crystal LAO target onto (001)-oriented 0.5 wt% Nb-doped $SrTiO_3$ (NSTO) single-crystal substrates. The LAO films of various thicknesses (25~150 nm) were grown at 800 °C under an O_2 partial pressure of 1×10^{-2} Torr. During deposition, the fluence of the laser energy was 1.3 J/cm^2

and a mask was used to cover a small part of NSTO to be used as the bottom electrode. After deposition, the sample was annealed for 1 h at 600 °C in ambient O_2. Subsequently, the samples were cooled to room temperature at a very slow ramping rate of 5 °C/min to avoid cracking of the films, which can occur because of the mismatch between the thermal expansion coefficients of LAO and NSTO. Finally, 1×2 mm^2 metal top electrodes (Cu or Au) were deposited on top of the LAO film by pulsed laser deposition through a stencil mask. The temperature dependence of the sample resistance (*R*-*T*) was measured by applying a voltage of 0.05 V between the top metal electrode and bottom electrode (seen in Fig. 6.1). At this small voltage, the existing resistance state is stable over time. Using the same two-terminal geometry, current-voltage (*I*-*V)* characteristics were measured by scanning the applied voltage and reading the current with a compliance current of 0.1 A. The sign of the voltage corresponds to the sign of the voltage applied to the metal top electrode.

As shown in Fig. 6.1, typical metal/LAO/NSTO structures with different top metal electrodes (Cu or Au) and LAO layer thicknesses were prepared. As illustrated in Fig. 6.2, the temperature dependence of the sample resistance (*R*-*T*) curve of the initial state indicates typical insulating behaviour that corresponds to the initial current-voltage (*I*-*V*) curve of the system as seen from i to j in Fig. 6.3.

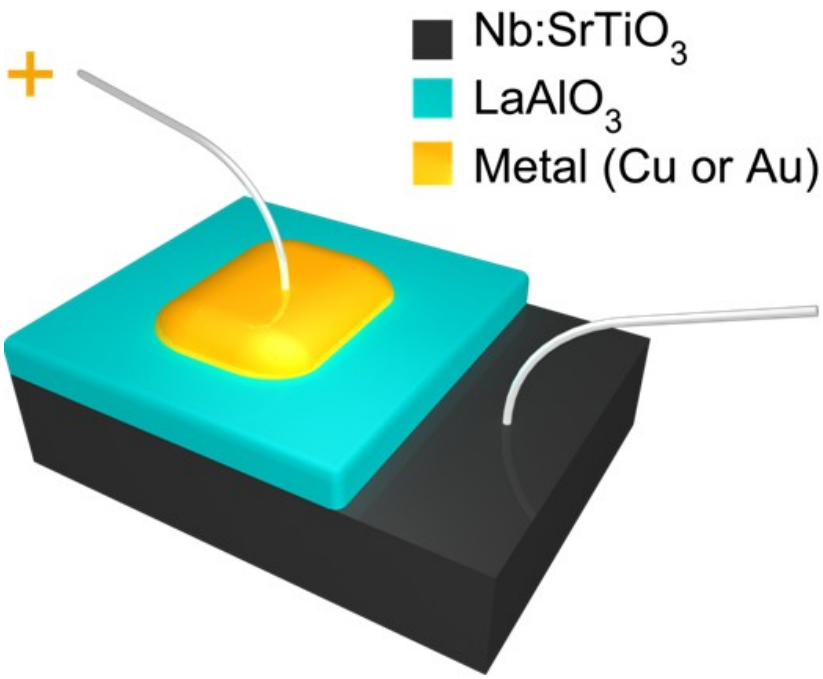

Figure 6.1. Schematic of a metal-LAO-NSTO sandwich structure.

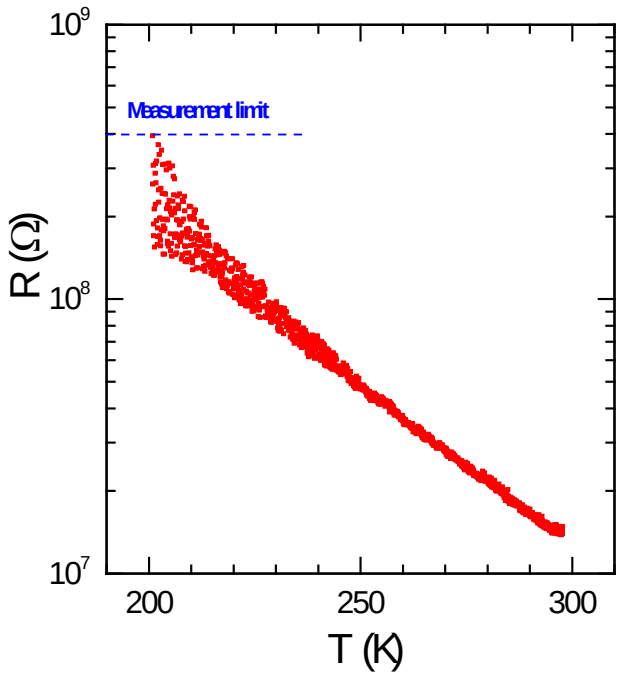

Figure 6.2. *R-T* curve of the initial resistance state for Cu/LAO (~150 nm)/NSTO structure on a semi-logarithmic scale.

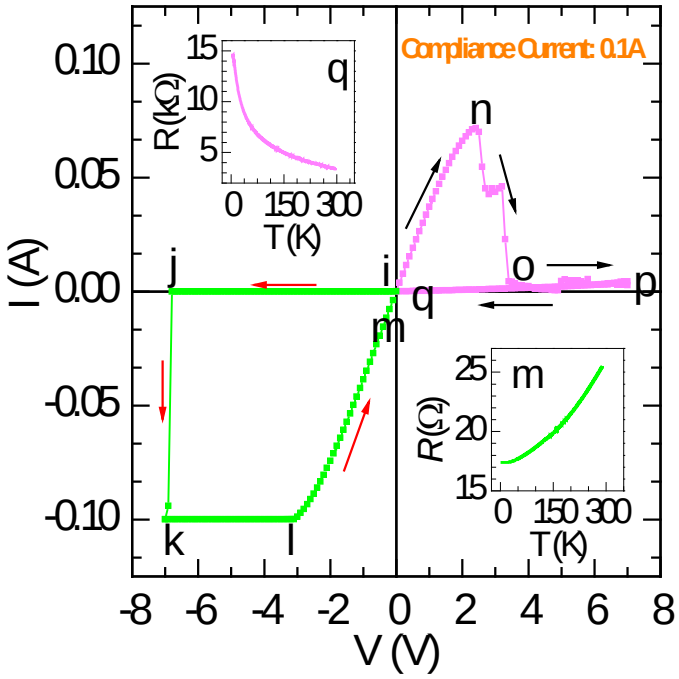

Figure 6.3. *I-V* curves obtained by scanning voltage along 0 → -7 V → 0→ 7 V → 0 and *R-T* curves of different resistance states. The insets **m** and **q** are the *R-T* curves after scanning the voltage through points m and q to zero, respectively. The horizontal data between points *k* and *l* are due to the compliance current in action.

At low voltages, the resistance is quite high but when the voltage reaches –6.8 V, a sharp jump in the current is seen. Because of the imposed compliance current of 0.1 A, which is used to prevent sample damage, the current saturates at 0.1 A. As the voltage is scanned back to 0 V, a linear *I-V* characteristic is seen, which corresponds to a stable metallic state shown in the inset **m** of Fig. 6.3. Hence, upon the dramatic switching of the resistive state at –6.8 V, the resistance changes from ~14 MΩ to ~25 Ω at room temperature, which is concomitant with a phase transition from the insulating to the metallic phase. The metallic state persists until the positive voltage scan reaches about 2.4 V; at that level, the device switches into a high-resistance (*n-o-p-q*) and non-metallic state as indicated in the inset **q** of Fig. 6.3.

The reversible phase transition is reproducible, as shown in the second *I-V* cycle in Fig. 6.4. The behaviour is totally unexpected for a wide bandgap insulator such as $LaAlO_3$.

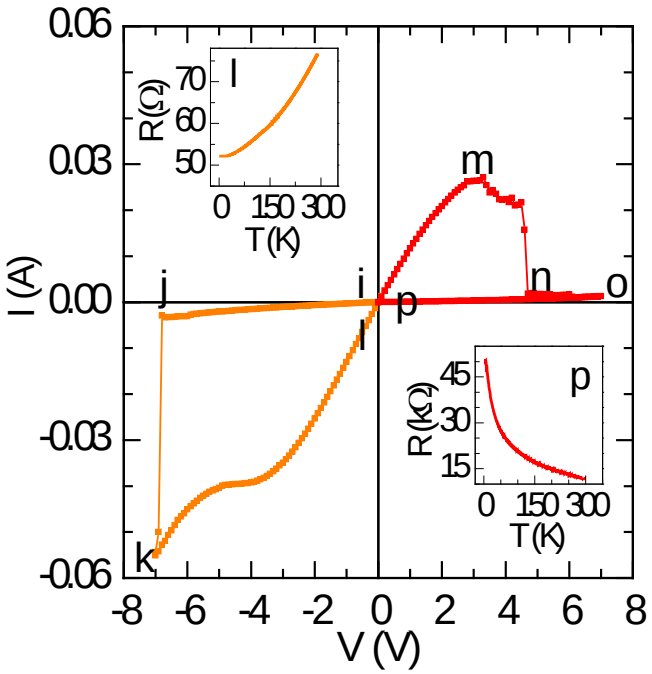

Figure 6.4. *I-V* curves after the cycle shown in Fig. 5.3 and *R-T* curves of different resistance states. The insets **l** and **p** are the *R-T* curves after scanning the voltage through points *l* and *p* to zero, respectively.

The anomalous insulating behaviour of LAO cannot be explained by artefacts such as anodization or redox of the active metal electrode [183]. In those cases, anodic dissolution of the metal electrode is possible only if adequate positive voltage is applied to an active metal electrode, and the resulting cations can be driven by the strong electric field into the insulating film where they form metallic filaments. To further eliminate this possibility, structures with inactive Au as the top electrode material were prepared and analyzed; these structures showed no observable difference in their resistive switching behaviour compared to those with Cu as the top electrode (Fig. 6.5).

This strongly suggests that the reversible phase transition cannot be caused by the diffusion of metal electrodes.

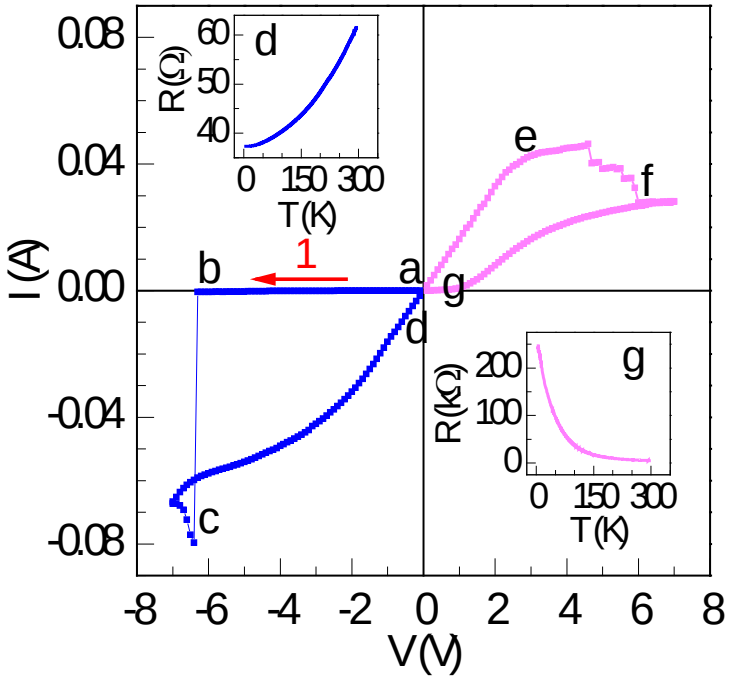

Figure 6.5. *I-V* characteristics of the Au/LAO (~150 nm)/NSTO structure. The voltage scan begins with the arrow marked with '1' and follows the sequence *a-b-c-d-e-f-g*. The upper-left and lower-right insets are the *R-T* curves after scanning the voltage through point *d* and point *g* to zero, respectively. All the lines connecting the data points are guides to the eye.

6.1.2 Low temperature switching

Another possible mechanism for this anomalous insulating phenomenon is the migration of oxygen vacancies. If such a mechanism is occurring, the applied electric field could only change the distribution of the positively charged oxygen vacancies [185]. Therefore, no insulating phase would appear, even at higher resistance states. Our case is also significantly distinct from the type of resistive switching that originates from the electro-migration of excess oxygen as described by Shi *et al.* [186]; in that experiment, the resistive switching disappeared at temperatures below 200 K because of the low

diffusion coefficient of the oxygen. To verify this, the low temperature switching properties were examined using the same structure with a Au electrode. The initial insulating state of this structure is shown in the inset **i** of Fig. 6.6. After cooling to 4.1 K, the *I-V* measurements were performed and the structure was negatively biased to –8.8 V, at which it switched to a linear state with a very small resistance of ~12 Ω as shown in Fig. 6.6, which corresponds to a metallic phase as revealed in the inset **n** of Fig. 6.6.

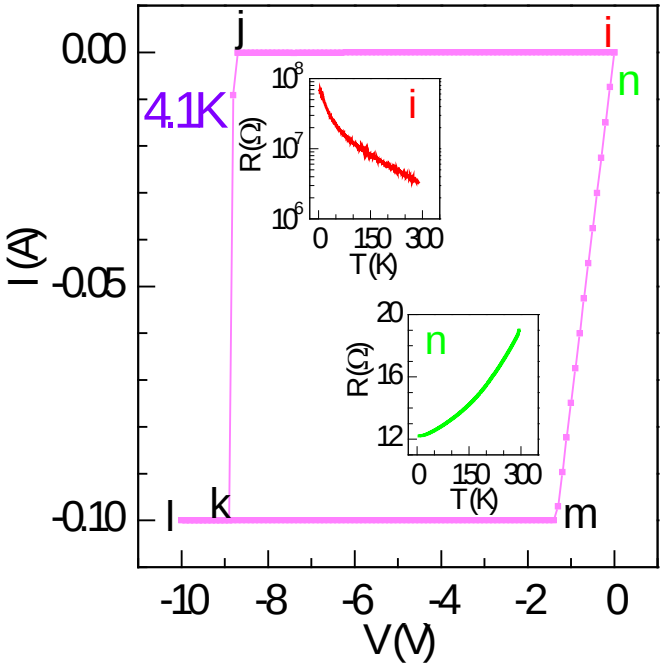

Figure 6.6. Negative switching of Au/LAO (~150 nm)/NSTO at 4.1 K. (Inset **i**) *R-T* curve of the initial state. (Inset **n**) *R-T* curve after negatively scanning voltage back to 0, *i.e.*, after 0 → -10 V → 0 at 4.1 K. The current values in the *k-l-m* sequence are confined by the compliance current.

The voltage required to obtain this switching is larger than the one at room temperature. The sample was then warmed up to 298 K, after which it was switched back to a non-metallic state as indicated by the inset m of Fig. 6.7 with a higher resistance of ~10 kΩ. These results are consistent with the results seen in the room-temperature device; it is thus very difficult to attribute

the reversible MIT observed in LAO to the oxygen vacancy or excess oxygen scenarios.

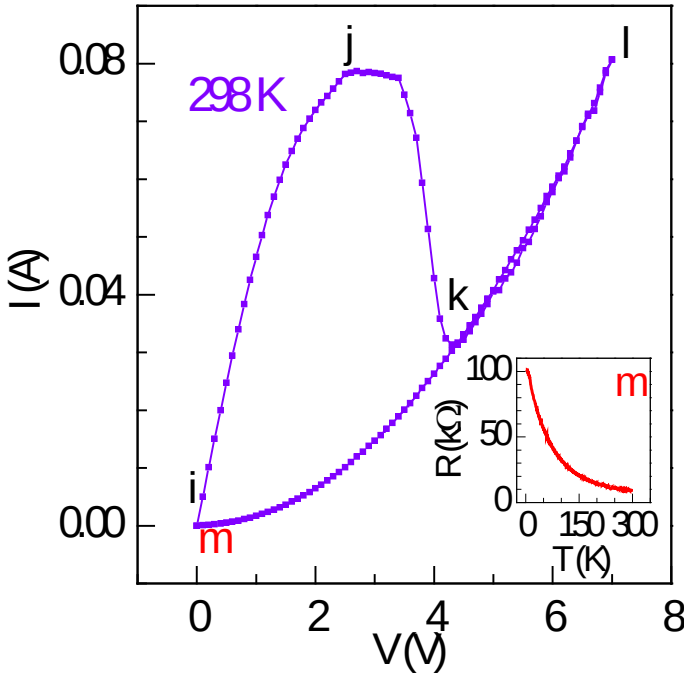

Figure 6.7. Positive scan after the switching in Fig. 5.6 at 298 K by 0 → 7 V → 0. (Inset) *R-T* curve after positive scan.

6.1.3 Structural phase transition check

To examine whether the electronic phase transition comes with any structural phase transition of the LAO film, which might be induced by the external electric field, the crystal structure of the new sample coated with a Cu electrode with a film thickness of ~150 nm was analysed by X-ray diffraction (XRD). The area not covered by the metal electrode shows good epitaxial characteristics, *i.e.*, double peaks (Fig. 6.8). Once the device was switched to the low-resistance state, the top Cu electrode was lifted off by Ar-ion beam milling, and the area originally below the Cu was examined. This area shows nearly the same diffraction peaks (Fig. 6.9) as those of the original film, which

was not covered by Cu. This indicates that there is no structural phase transition when the MIT ocurrs.

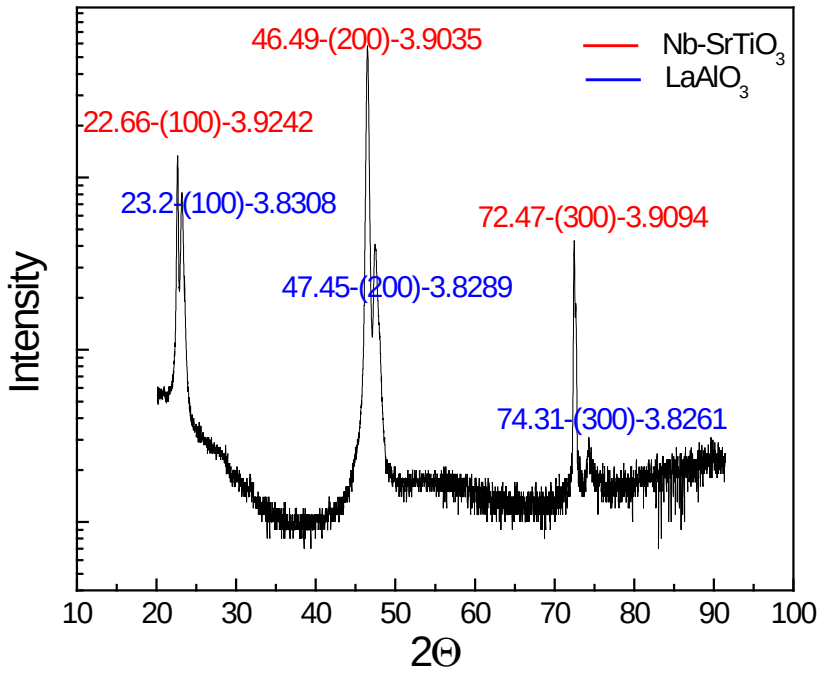

Figure 6.8. XRD of the film area not covered by the metal electrode in the initial high-resistance state of a Cu/LAO/NSTO sample.

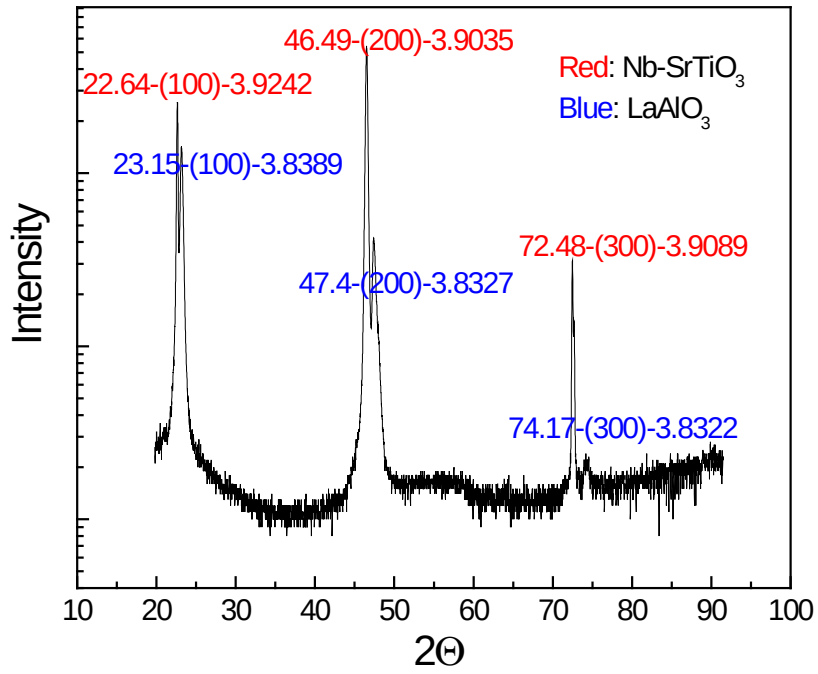

Figure 6.9. XRD of the area that was originally below the Cu electrode in a low-resistance metallic state. The blue and the red data indicate the XRD peaks of LAO and NSTO substrate, respectively.

6.1.4 Film cracking check

It was found that LAO thin films grown on STO could crack during cooling down as a result of the mismatch in the thermal coefficients of LAO and STO if the film thickness is above 10 nm and the cooling rate is too fast [187]. For example, the cracking of a 10 nm LAO film grown on STO can be clearly seen from AFM images (Fig. 6.10). Therefore it is worth checking out whether there is cracking in the thick LAO films deposited on NSTO substrates.

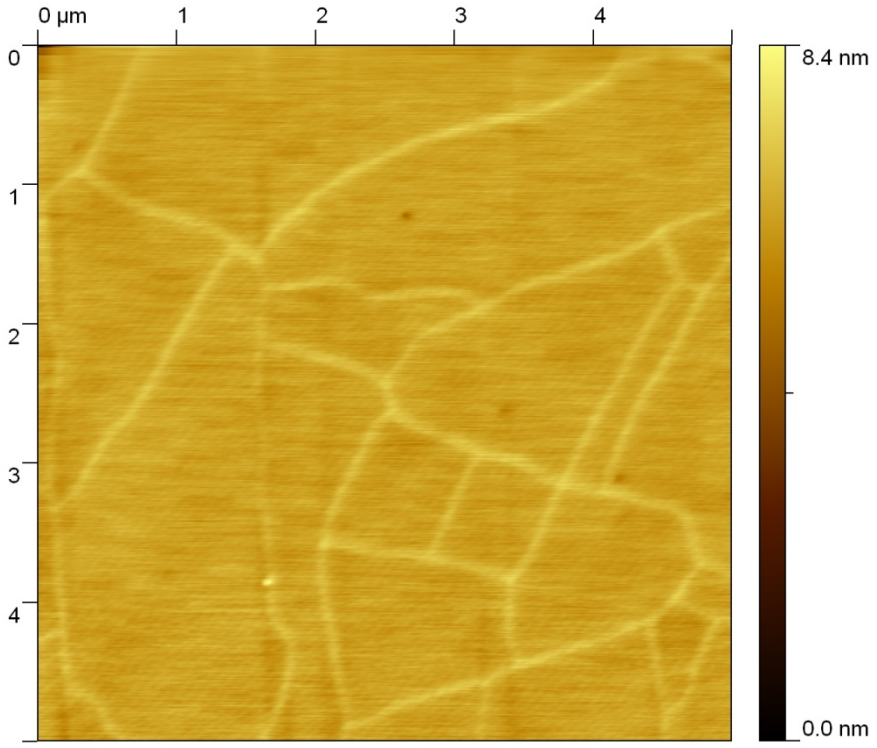

Figure 6.10. A 5×5 μm^2 AFM image of a 25 uc LAO grown on STO.

The surface topography of 150 nm LAO films grown on NSTO was examined by both AFM and optical microscope on different surface areas. A 5×5 μm^2 AFM image is shown in Fig. 6.11 and a large scale surface image obtained by optical microscope is shown in Fig. 6.12. It turns out that no

cracking exists in thick LAO films deposited on 0.5wt% NSTO substrates. This could be due to the slow cooling rate utilized in the deposition (3 °C/min).

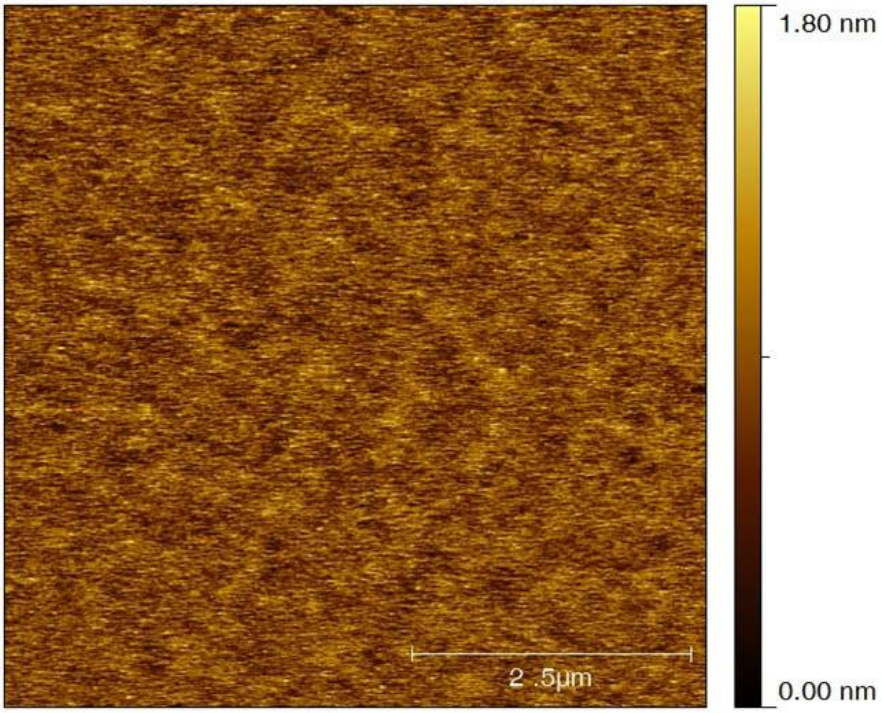

Figure 6.11. A 5×5 μm^2 AFM image of a 150 nm LAO film deposited on 0.5wt% NSTO.

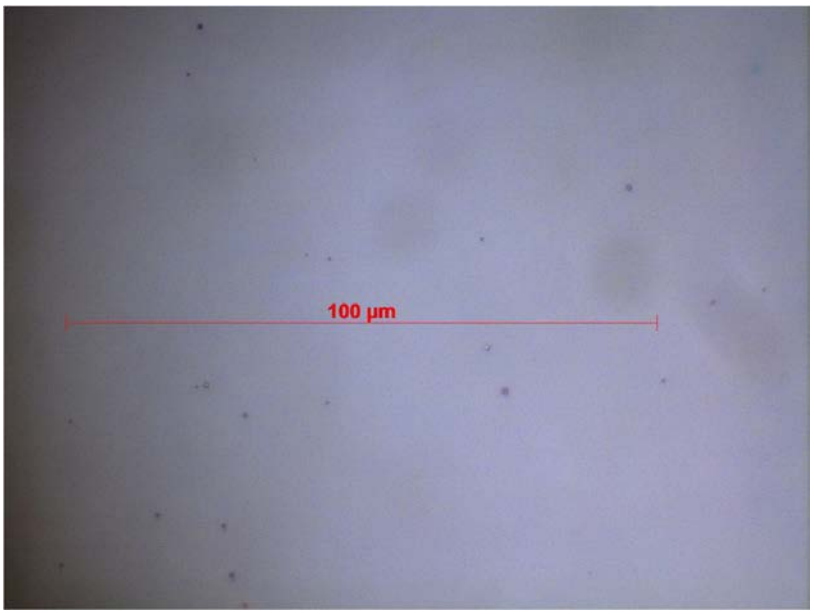

Figure 6.12. An optical microscopic image of a 150 nm LAO film deposited on 0.5wt% NSTO.

6.2 Defect mediated quasi-conduction band

6.2.1 Quasi-conduction band model

We propose a novel mechanism to describe this unusual insulating behaviour. Our femtosecond pump-probe experiments on single crystal LAO reveal that defect states can exist in LAO within a wide energy range at approximately 2.0 eV below the conduction band [136], which is consistent with the theoretical calculations of Luo *et al.* [122]. In Fig. 6.13, a sketch of the band structure of the device is depicted. For LAO, It is difficult to identify that it has a *p*-type or *n*-type band structure, so we use the term "Fermi level" to mark the middle of its bandgap.

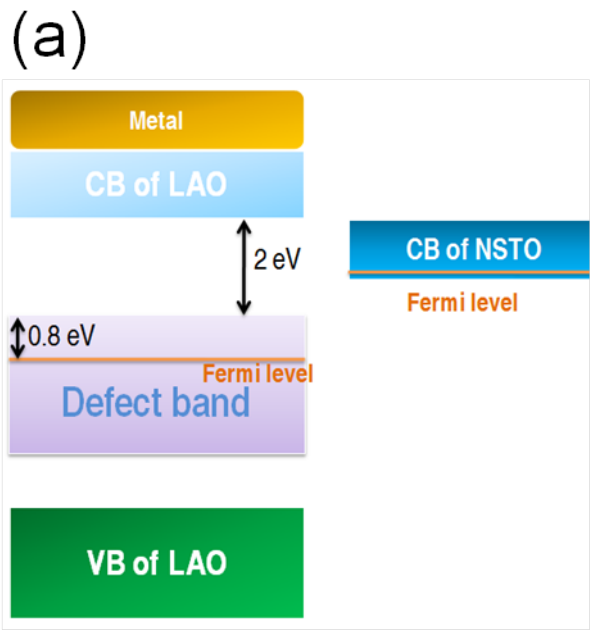

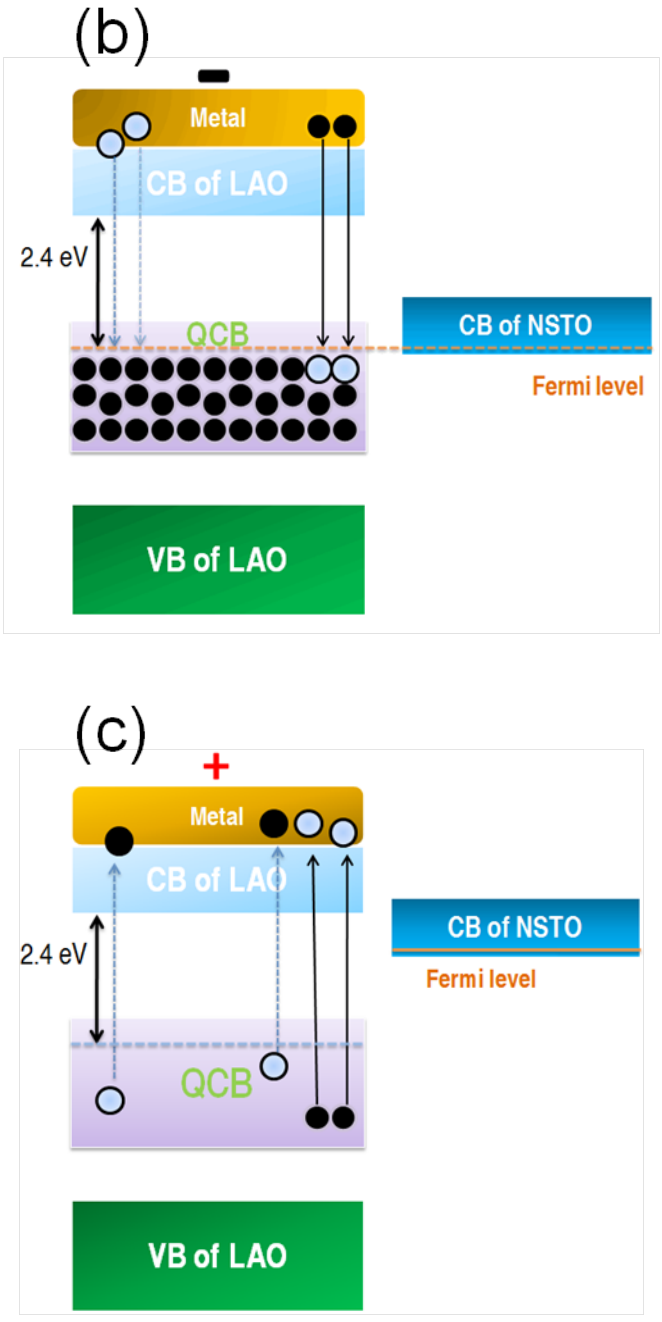

Figure 6.13. (a) Schematic of the band diagram of the device with no voltage bias. The middle defect band represents the defect levels of LAO, which are widely distributed in the bandgap at ~2 eV below the conduction band. (b) Formation of a quasi-conduction band (QCB) under an initial negative voltage bias. (c) Depletion of electrons in the QCB by a subsequent positive bias.

Additionally, the work function of the utilized 0.5wt% NSTO substrate is very small, determined to be ~3.5 eV by ultraviolet photoemission spectroscopy

measurements. Therefore, it is plausible to assume that the Fermi level of NSTO is higher than the Fermi level of LAO, as drawn in Fig. 6.13(a).

Initially, there is no conduction between the NSTO and LAO. Under sufficient negative bias, charges will be injected into and fill up the LAO defect levels from the metal side and the energy band of NSTO will be pushed down relative to the bands of LAO. At the voltage where a dramatic conductivity transition is seen, the electron population of the defect levels is high enough to form a metallic state. We call this defect-mediated conduction band a "quasi-conduction band" (QCB). As demonstrated in Fig. 6.13(b), once the energy level of QCB lines up with the Fermi level of NSTO, which is slightly above its conduction band, a continuum state is established, and this state remains even when the current is reduced to zero because of the overlap of the electron wave functions.

The effective charge transferred to the defect levels at the switching threshold of 0.22 A (Fig. 6.14) is estimated to be around 4.6×10^{19} cm^{-3} for a device area of 0.02 cm^2, a LAO thickness of 150 nm and a defect level lifetime of ~10 microseconds. While this carrier concentration is about 3.5 times smaller than that of the NSTO, which is 1.6×10^{20} cm^{-3}, it makes the LAO a stable metallic system.

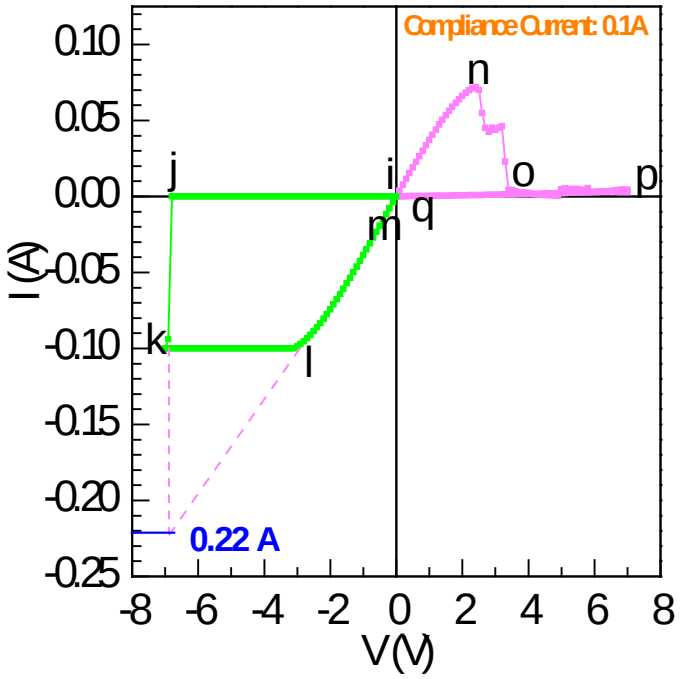

Figure 6.14. Schematic of switching threshold current. The pink dashed lines are the extension lines of the measured data points, and the abscissa of their crossing point (~0.22 A) is indicated by the short solid blue line.

6.2.2 Theoretical calculations

To validate this idea, theoretical calculations on interstitial La^{2+} defect of LAO and percolation of wave functions were performed. In order to get some insight on defect state, density functional theory calculations were carried out for LAO cubic phase with interstitial La^{2+} defects. The projector augmented-wave method was used in the framework of the generalized gradient approximation (GGA). We have chosen a 3×3×3 supercell with an interstitial La^{2+} defect in it, and relaxed all atomic positions to determine their displacements from the high-symmetry positions due to the introduced disorder. The cutoff energy of the plane-wave expansion was 400 eV, and the Brillouin zone sampling mesh was 5×5×5 with its origin at the Γ point. In the final optimized geometry, no forces on the atoms exceeded 0.01 eV/Å.

The obtained density of states (DOS) of LAO-La^{2+} using GGA+U is given in Fig. 6.15(a). On-site Coulomb repulsion U = 11 eV, and exchange J = 0.68 eV have been taken for the 4*f* electrons of La, in order to push them to higher energy. An obvious local defect state can be found in the gap of cubic LAO.

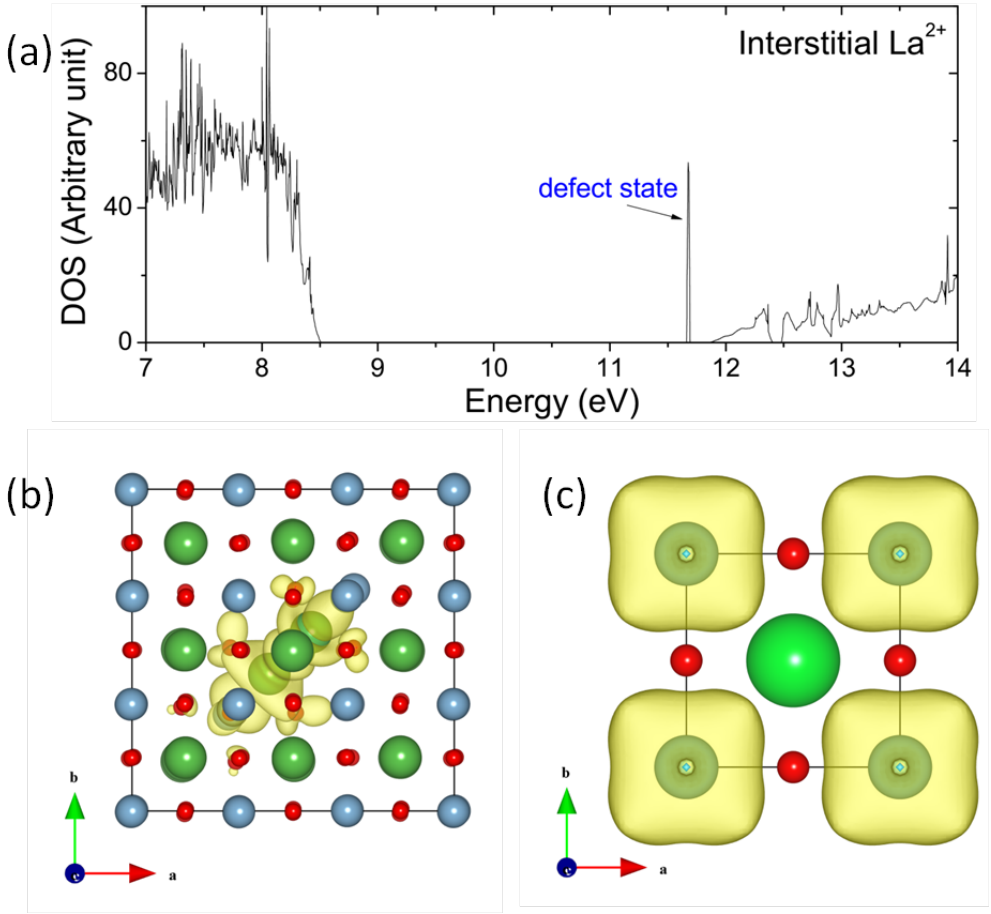

Figure 6.15. Theoretical calculations. (a) The calculated DOS for a 3×3×3 supercell of cubic LAO with an interstitial La^{2+} defect in it. (b) Partial charge density distributions of local defect state around the Fermi level in DOS. The yellow clouds represent charge densities exceeding 0.011872 electrons/Å^3. (c) Partial charge density distributions of lowest unoccupied conduction band at Γ point for cubic STO. Isosurface value is also set to be 0.011872 electrons/Å^3.

The defect state's partial charge density space distribution is plotted in Fig. 6.15(b), from which it is clearly seen that charge density—higher than 0.011872 electrons/Å^3—exists mainly at La atoms around defect with strong

d-orbital character, and extends slightly to neighboring oxygen atoms for hybridization effect. In Fig. 6.15(c), the same magnitude charge density from the lowest unoccupied conduction band at Γ point can also be found around Ti atoms in cubic STO, and the doping of Nb will make it become occupied. Thus La-*f* and Ti-*d* wave functions will overlap each other if this interstitial defect occurs at the interface between LAO and NSTO. Interestingly, the calculated charge density is of the same order of magnitude as our estimated number.

The most interesting aspect of the QCB is the inherent hysteresis; the only way that this device can be restored to the original insulating state is by applying an opposing voltage, which will then remove the carriers from the QCB and relatively pull the conduction band of NSTO up, leading to the lack of overlap between the QCB and the conduction band of NSTO, as depicted in Fig. 6.13(c).

6.2.3 Polarity and thickness dependence of resistive switching

To explore the polarity dependence of the resistive switching, an initial positive scan was also conducted but neither any stable switching behaviour nor a metallic state was observed (Fig. 6.16). Instead, the stable switching only occurs at the first negative scan. This is consistent with our model, where a negative bias is needed to pump electron from metal to LAO intragap defect levels to form the QCB.

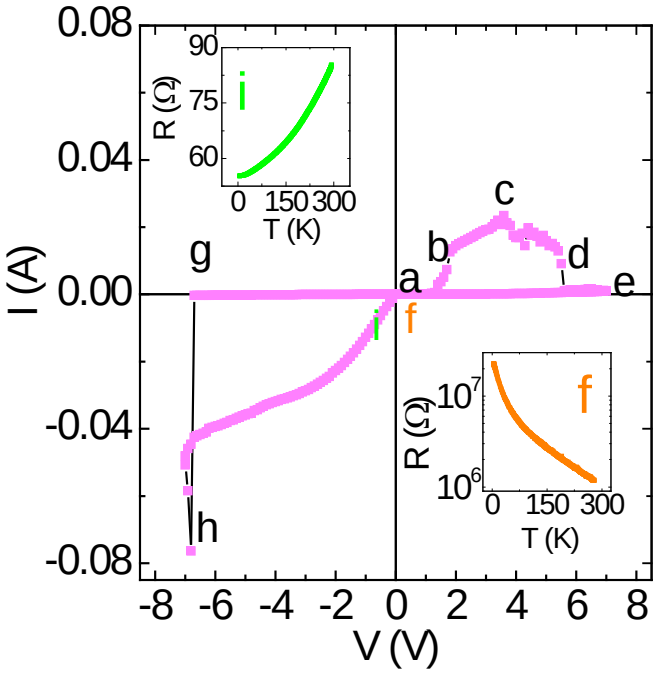

Figure 6.16. *I-V* characteristics of an Au/LAO (150 nm)/NSTO structure by scanning voltage starting from the forward bias. Insets: *R-T* curves after scanning to zero voltage via point *f* and *i*.

This QCB originates from the defect levels in the bandgap of LAO, which is supported by the change in resistive state values after several cycles; the device has slightly lower resistance values after the first cycle, and those values slightly increase in the later cycles as shown in Figs. 6.3 and 6.4. This change points to the possibility of defect production and defect rearrangement after large currents have passed through these devices. To further test this hypothesis, devices as a function of LAO thickness were studied.

Figure 6.17 shows the switching behavior as a function of thickness with the *I-V* characteristics shown for a few of the many devices studied. It is clear that a minimum thickness (70-85 nm) is required before switching occurs. This is consistent with the defect picture as the films become more defective with increasing thickness. This may arise due to the inherent lattice mismatch

between LAO and STO. In Fig. 6.17(b), the reverse switch-on voltage shows a nonlinear dependence on the thickness and this can be argued due to two effects; the need to create a threshold quantity of charge to create the QCB and to account for variations in dielectric constant as a function of thickness and

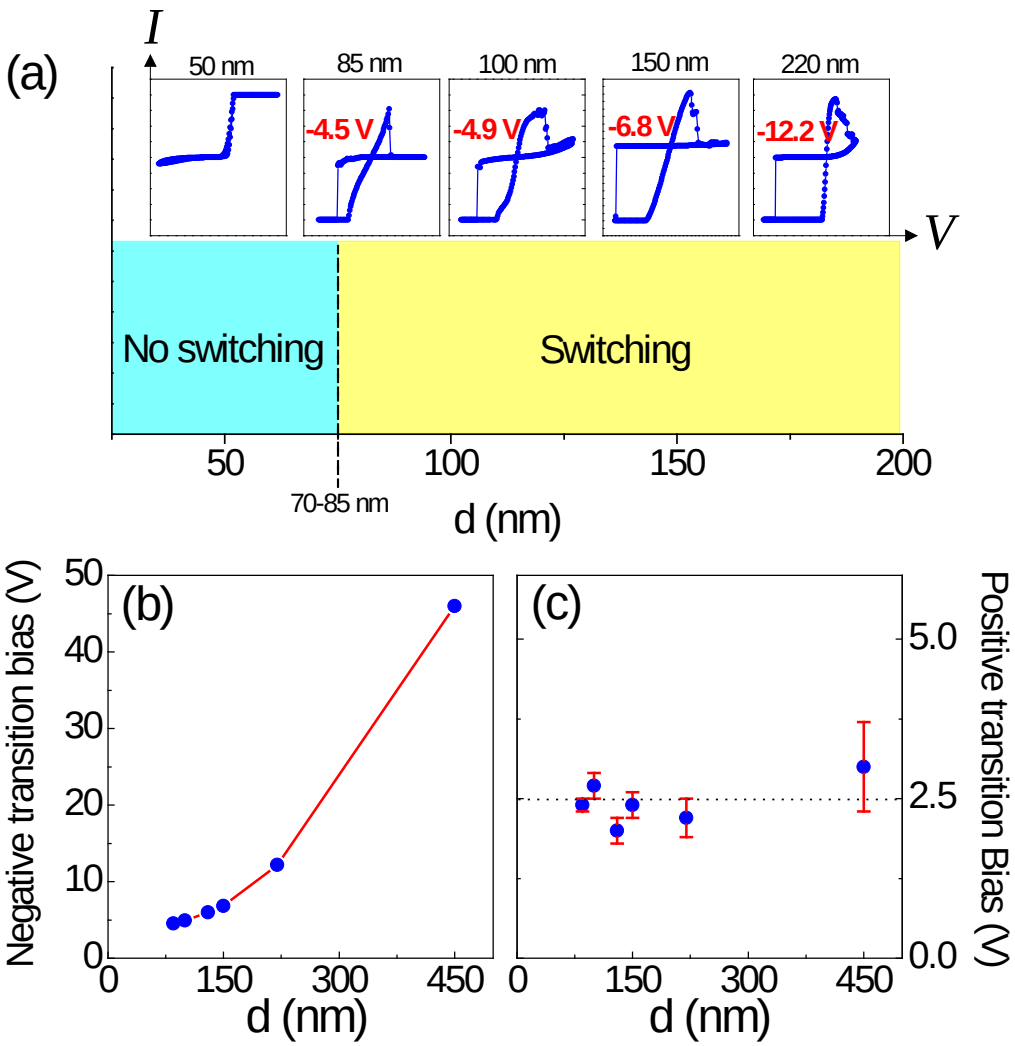

Figure 6.17. Thickness dependence of *I-V* curves of Cu/LAO/NSTO structures showing a minimum thickness threshold (70~80 nm) for appearance of resistive switching. (b) The negative switch-on voltage and (c) the forward switch-off voltage as a function of LAO thickness.

field. The forward switch-off threshold voltage is plotted in Fig. 6.17(c) and is found to be thickness independent at a value of 2.4 eV, close to the bandgap

difference between LAO and STO. The forward switch-off is very sharp for smaller thicknesses (85 nm) and tends to broaden with increasing thickness suggesting creation of more defect levels with increasing thickness. Further experiments would be needed to fully understand this behavior. The thickness dependence of the threshold voltages in the two polarities supports the basis of the proposed model.

Most of the complex oxides have predominantly ionic bonds and are prone to a variety of cationic and anionic defects including vacancies, interstitials and antisites. These defects create a plethora of electronic states within the bandgap of these oxides. In these insulators, the defect levels can be populated to form QCB, which can lead to multiple conduction states in the same system. These states can be stabilized if an adjacent metallic conduction band overlaps with them. The only way to restore the levels back to their original state is by removing the carriers from the defect levels; this phenomenon is what leads to hysteresis in the *I-V* curves.

6.3 Resistive switching of $RAlO_3$ (R=Pr, Nd, Y) films

6.3.1 $PrAlO_3$

To fabricate $PrAlO_3$ (PAO) thin films, a polycrystalline PAO target was made by grinding praseodymium oxide and aluminum oxide powder at room temperature and then sintering them at 1050 °C for 20 h. PAO films were deposited on 0.5 wt% NSTO substrates from the sintered PAO target by pulsed laser deposition at 750 °C and 10^{-2} Torr oxygen pressure. The XRD

pattern of a 150 nm PAO film grown on NSTO (Fig. 6.18) shows the epitaxial growth of PAO on NSTO. The Cu/PAO/NSTO sandwich structures were fabricated by depositing Cu top electrodes on PAO films.

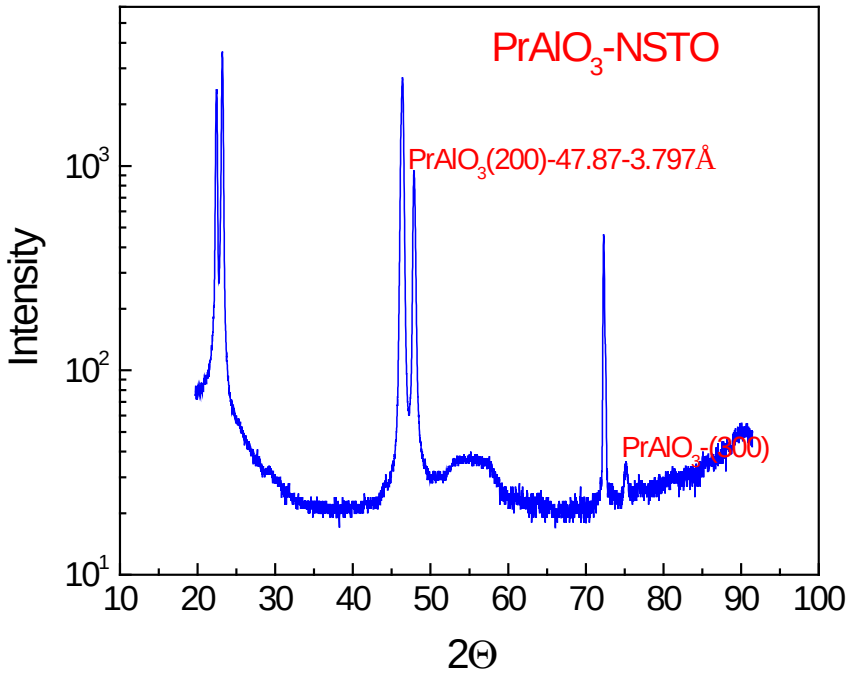

Figure 6.18. XRD of a 150 nm $PrAlO_3$ (PAO) film grown on NSTO.

The *I-V* characteristics of a Cu/PAO (150nm)/NSTO structure (Fig. 6.19) exhibit reversible MIT with voltage, which is similar to what is observed in Cu/LAO/NSTO heterostructures. The switch-on and switch-off voltages are -12.3 and 5 eV, respectively. The values are larger than those of Cu/LAO/NSTO structures, which could be because the distribution of defects as well as the density of defect states in PAO is different from those in LAO.

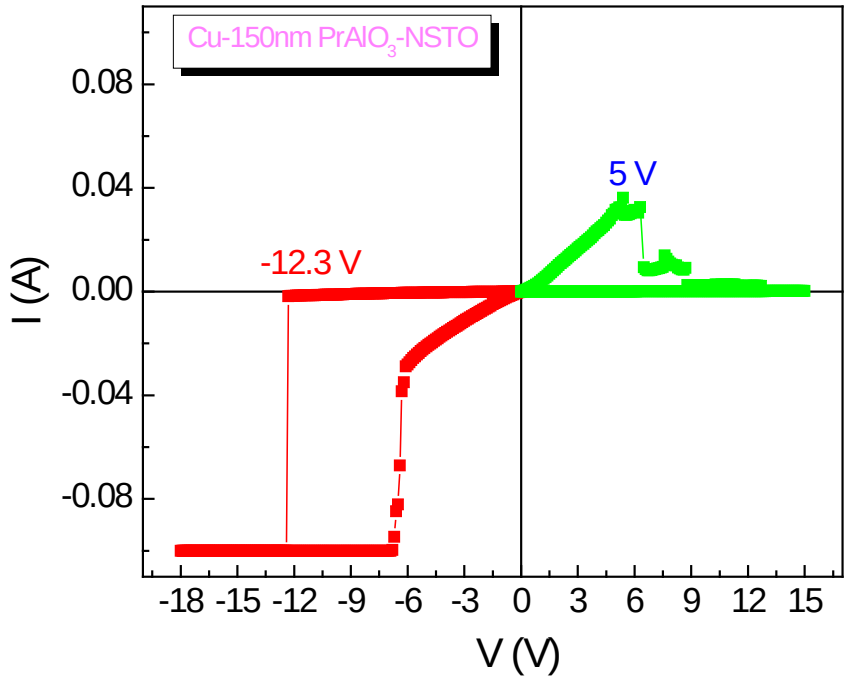

Figure 6.19. *I-V* curves of a Cu/PAO(150 nm)/NSTO structure by scanning voltage.

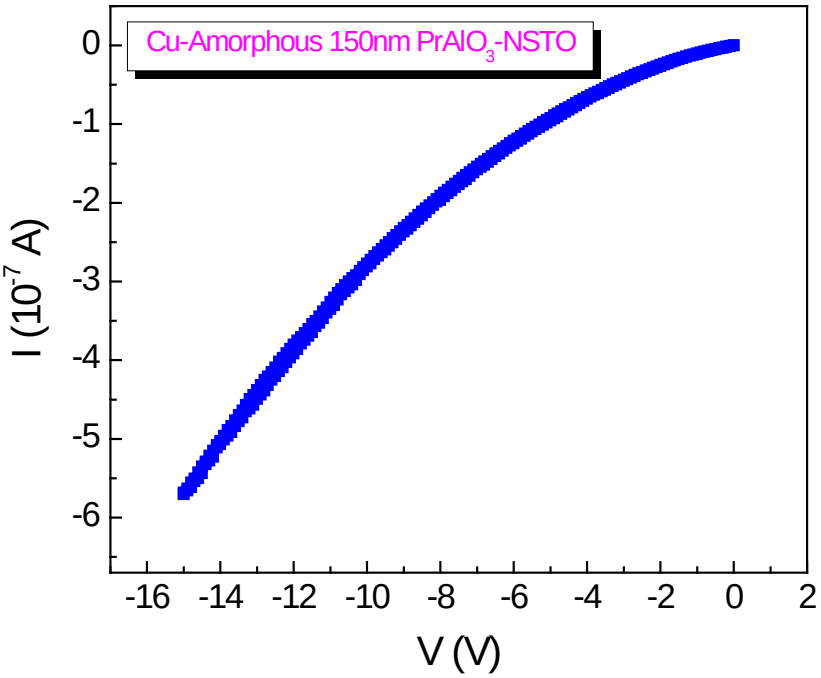

Figure 6.20. *I-V* curves of a Cu/amorphous PAO (150 nm)/NSTO structure.

In the quasi-conduction band model, the crystallinity of the middle insulating film is crucial for energy band formation. To test this idea, a 150-nm-thick amorphous PAO film was fabricated on NSTO at room temperature.

The voltage scan up to -15 V shows no pronounced switching (Fig. 6.20), which attests that the crystallinity is essential for the quasi-conduction band formation.

Similar to the thickness dependent resistive switching observed in Cu/LAO/NSTO structures, there is also a minimum thickness above which PAO films show reversible MIT. For example, there is no pronounced resistive switching in 50-nm-thick PAO films (Fig. 6.21).

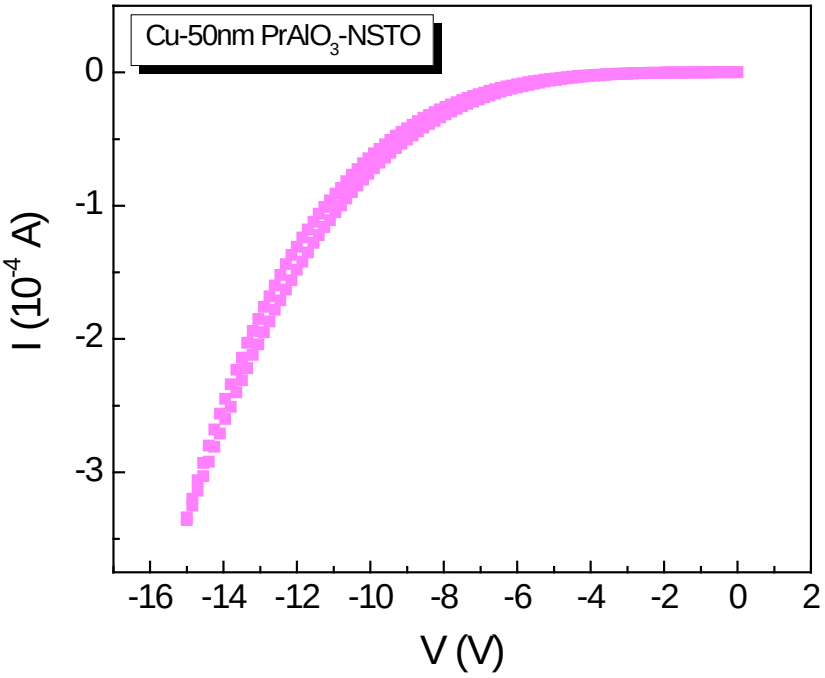

Figure 6.21. *I-V* curves of a Cu/PAO (50 nm)/NSTO structure.

6.3.2 $NdAlO_3$

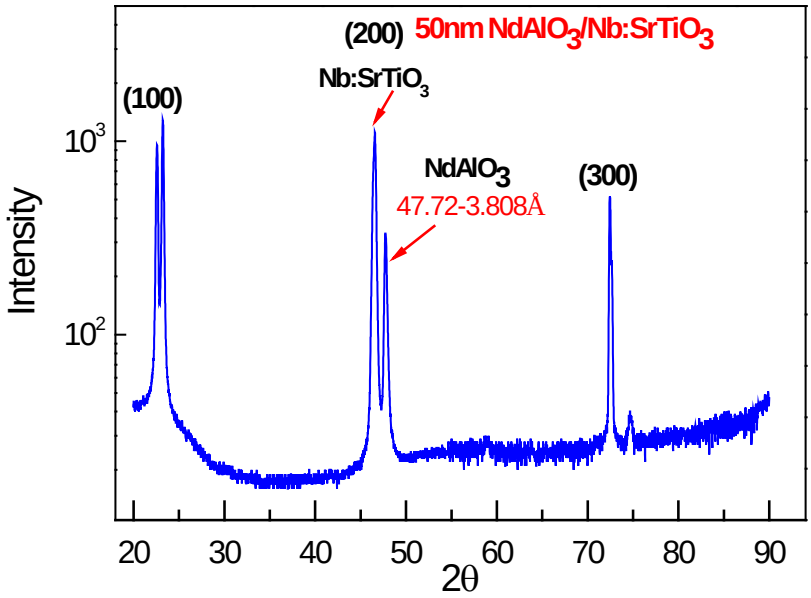

Figure 6. 22. XRD pattern of a 50-nm $NdAlO_3$ (NAO) film grown on NSTO.

$NdAlO_3$ (NAO) has a large bandgap of ~5.8 eV. Similarly, epitaxial NAO single crystal thin films (Fig. 6.22) were fabricated on NSTO substrates by pulsed laser deposition. The out-of-plane lattice constant of NAO is 3.81 Å, slightly larger than that of LAO. The resistive switching properties of NAO single crystal films were studied as a function of thickness. Figure 6.23 illustrates an *I-V* characteristic of a Cu/NAO (150nm)/NSTO structure. Reversible MIT can be clearly seen. The switch-on and switch-off voltages are close to those of a Cu/PAO/NSTO sandwich structure.

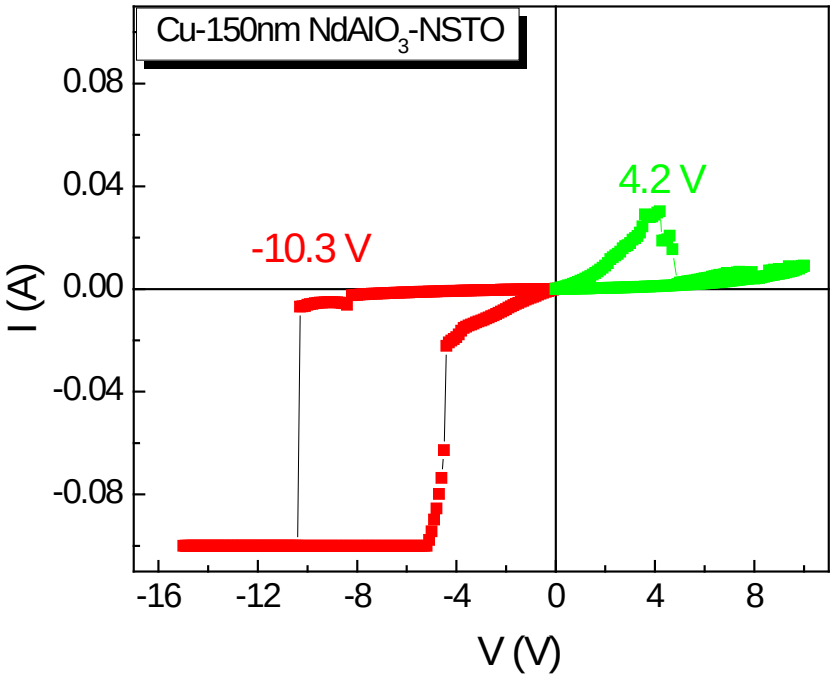

Figure 6.23. *I-V* curves of a Cu/NAO (150 nm)/NSTO structure.

The resistive switching in 100 nm NAO films (Fig. 6.24) also shows reversible MIT. The switch-on voltage value is smaller than that of 150 NAO films but the switch-off voltage is almost the same. For a thinner 50 NAO film, there is no pronounced resistive switching (Fig. 6.25). All these results are consistent with our quasi-conduction band model.

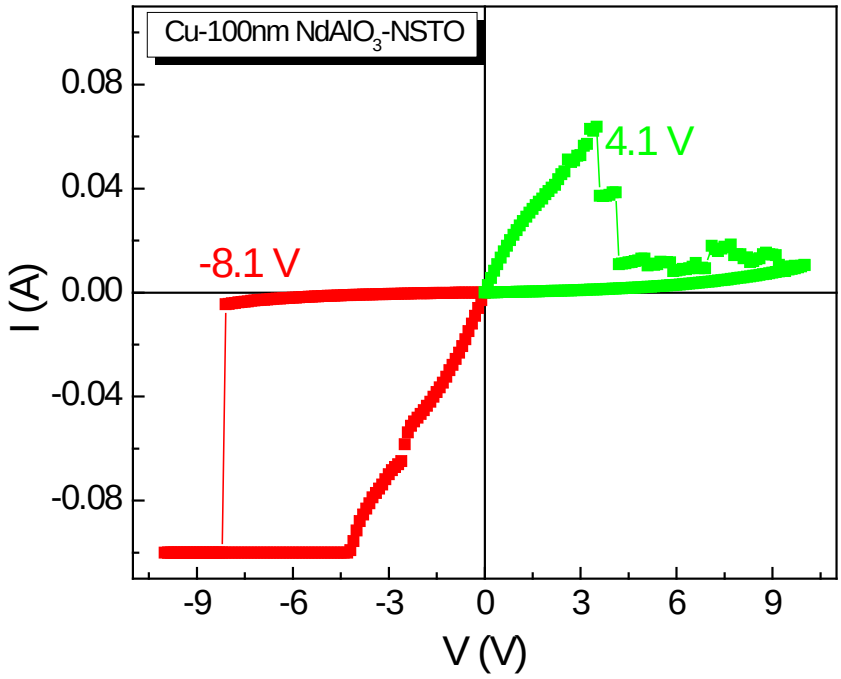

Figure 6.24. *I-V* curves of a Cu/NAO (100 nm)/NSTO structure.

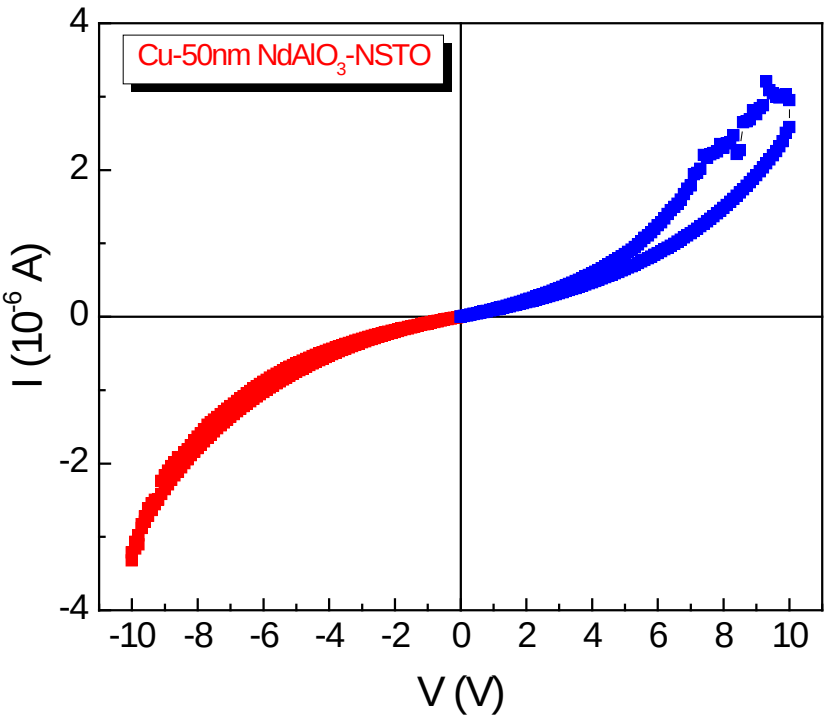

Figure 6.25. *I-V* curves of a Cu/NAO (50 nm)/NSTO structure.

6.3.3 $YAlO_3$

$YAlO_3$ (YAO) has a large bandgap of ~7.9 eV. Similarly, epitaxial YAO single crystal thin films were fabricated on NSTO substrates by pulsed laser deposition.

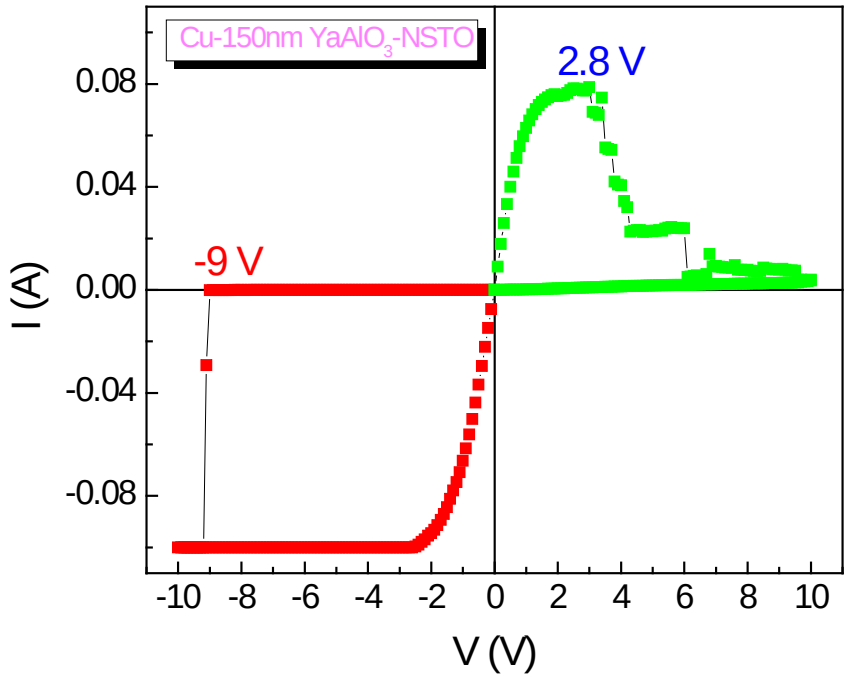

Figure 6.26. *I-V* curves of a Cu/$YAlO_3$ (YAO) (150 nm)/NSTO structure.

The resistive switching properties of YAO films were investigated as a function of thickness. The resistive switching in both 150 nm and 100 nm NAO films (Figs. 6.26 & 6.27) also shows reversible MIT. The switch-on voltage value changes with thickness but the switch-off voltage keeps the same. For a thinner 50 YAO film, there is no pronounced resistive switching (Fig. 6.28) showing up. These results further support the defect-mediated quasi-conduction band model.

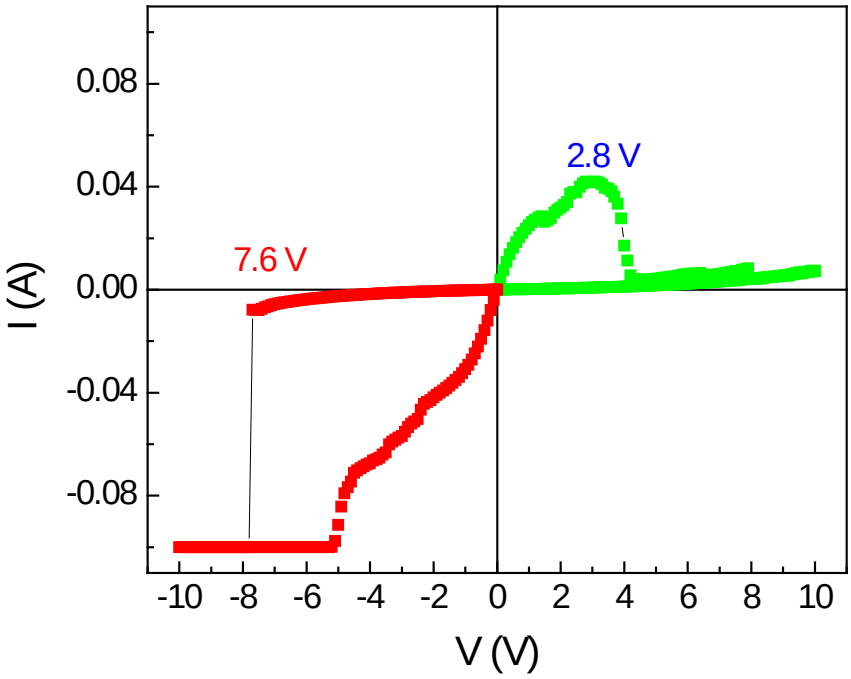

Figure 6.27. *I-V* curves of a Cu/YAO (100 nm)/NSTO structure.

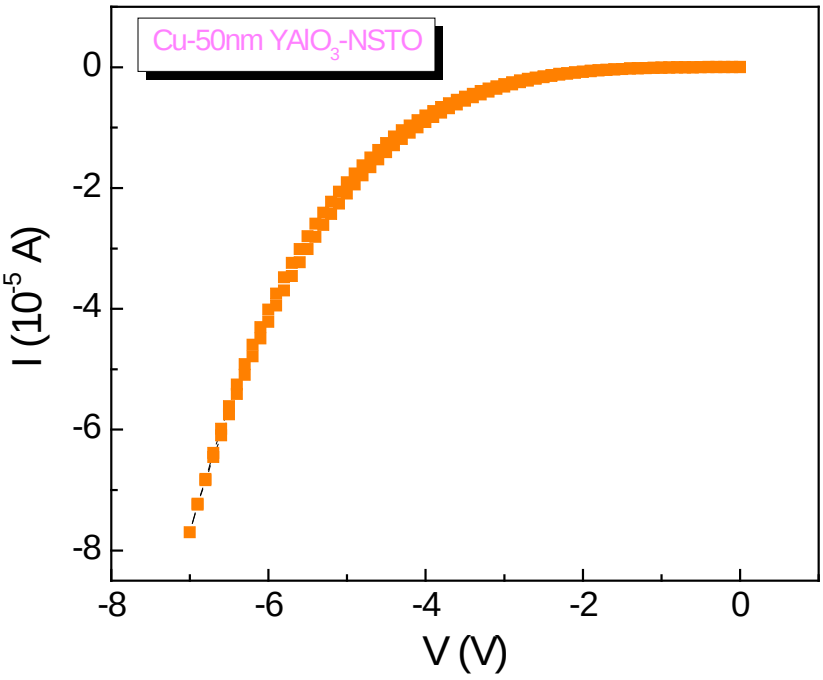

Figure 6.28. *I-V* curves of a Cu/YAO (50 nm)/NSTO structure.

6.4 Summary

In summary, we have studied the resistive switching of LAO films in metal/LAO/NSTO heterostructures and observed the electric-field-induced reversible MIT. The reversible MIT is ascribed to the population and depletion of QCB consisting of a wide range of defects states in LAO. A stable metallic state can be obtained only when the filling level of QCB inside the LAO aligns with the Fermi level of NSTO such that the wave functions of electrons inside the QCB and the conduction band of NSTO can overlap and interact with each other. The implications of this mechanism are far-reaching especially now the entire semiconductor industry is moving toward high-*k* materials. For example, the use of multi-component oxides as insulators in devices, (*e.g.*, high-*k* dielectrics in silicon CMOS devices) must be exercised with caution because of the presence of multiple defect levels within their bandgap. Furthermore, we have demonstrated that the defect medicated quasi-conduction band model also applied to other large bandgap $RAlO_3$ (R = Pr, Nd, Y) oxide materials. In addition, we have demonstrated that the effective band gap of an oxide insulator can be tuned by a QCB consisting of intragap defect states, which could be of great importance for photocatalyst and water splitting applications.

Chapter 7 Tailoring the electronic and magnetic properties of $SrRuO_3$ film in superlattices

Metallic oxides are essential to oxide electronic devices typically as electrodes and templates for integration of other oxide materials, such as in the resistive switching [188] and various tunnel junction devices [189–191]. $SrRuO_3$ (SRO) is a conductive ferromagnetic oxide [192], which has been extensively utilized as ferromagnetic electrodes in magnetic tunnel junctions [193] and normal metal electrodes in resistive switching devices [12]. Generally, technological scaling of electronic devices stresses the need of using metallic oxides in terms of ultra thin films. However, an important issue on using ultrathin films of metallic oxides is the substantially increased resistivity, which is clearly existent in SRO thin films. For example, Ahn *et al*. [194] found that room temperature resistivity of a 2 nm SRO film grown on a $SrTiO_3$ (STO) substrate reaches 20 times the bulk value; Toyota *et al*. [195] observed a metal-insulator transition in SRO films occurring at a film thickness of 4 or 5 unit cells (uc); Later, Xia *et al.* [196] observed a critical thickness of 4 uc, below which SRO films become insulating and the ferromagnetic character in magneto-optic Kerr measurements disappears.

Recently, a highly confined spin-polarized two-dimensional electron gas has been predicted in SRO-based superlattices and strong antiferromagnetic interlayer exchange coupling has been observed in SRO/$La_{0.7}Sr_{0.3}MnO_3$ superlattices with ultrathin SRO layers [197]. Furthermore, Boris *et al*. [198]

demonstrated that electronic phases of $LaNiO_3$ (LNO) can be substantially tuned by varying the thickness of LNO layers in $LaNiO_3/LaAlO_3$ (LNO/LAO) superlattices, which opens up an avenue to modulate electronic properties of strongly correlated electron systems in superlattices. The strong electron-electron correlation in SRO has been investigated by thermal and electrical transport measurements [199–201]. In addition, high quality superlattices consisting of multilayer SRO ultrathin films prevent a surface depletion typically occurring at the interface between a metallic film and air [202]. Also, a superlattice structure with multilayer SRO ultrathin films gives rise to an enhanced magnetic signal compared to that of an ultrathin SRO film with the same thickness, which can facilitate the determination of magnetic properties of an ultrathin SRO film in moment measurements. Therefore, investigating the electronic properties of ultrathin SRO films in multilayer structures (superlattices) can provide experimental basis for potential new functionalities and devices. In this chapter, we present an evolution of the electronic and magnetic properties of the SRO/LAO superlattices as a function of the SRO film thickness and demonstrate a modulation of their charge carriers in field effect device structures.

7.1 Transport properties of a 50 nm $SrRuO_3$ film

Bulk SRO is an itinerate ferromagnet with $T_c \sim 160$ K and orthorhombic with lattice parameters of $a = 5.55$ Å, $b = 5.56$ Å and $c = 7.86$ Å. Its pseudocubic structure has a lattice constant of 3.93 Å and therefore SRO films can be epitaxially grown on some common perovskite substrates (*e.g.*, STO or LAO,

both are nonmagnetic insulators with a large band gap of 3.2 and 5.6 eV, respectively).

A 50 nm SRO thin film was deposited on a STO substrate at 2×10^{-1} Torr oxygen pressure and 750 °C, which is (110)-oriented. The resistivity of the film is shown in Fig. 7.1 as a function of temperature. The room temperature resistivity is ~280 μΩ·cm, which is sufficiently low to be utilized as electrodes.

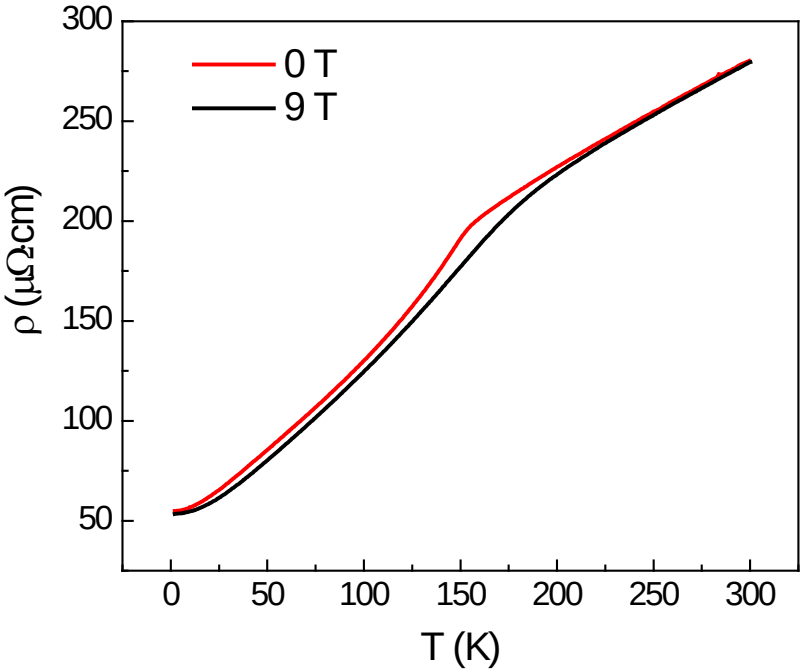

Figure 7.1. Temperature dependent resistivity of a 50 nm $SrRuO_3$ (SRO) film both under zero field and a perpendicular 9 T magnetic field.

The resistivity under a 9 T magnetic field is slightly smaller than that under zero field, especially below 200 K. Temperature-dependent magnetoresistance of a 9 T field can be extracted from Fig. 7.1 and is plotted in Fig. 7.2. The negative MR reaches maxima at 150 K and 35 K. The MR

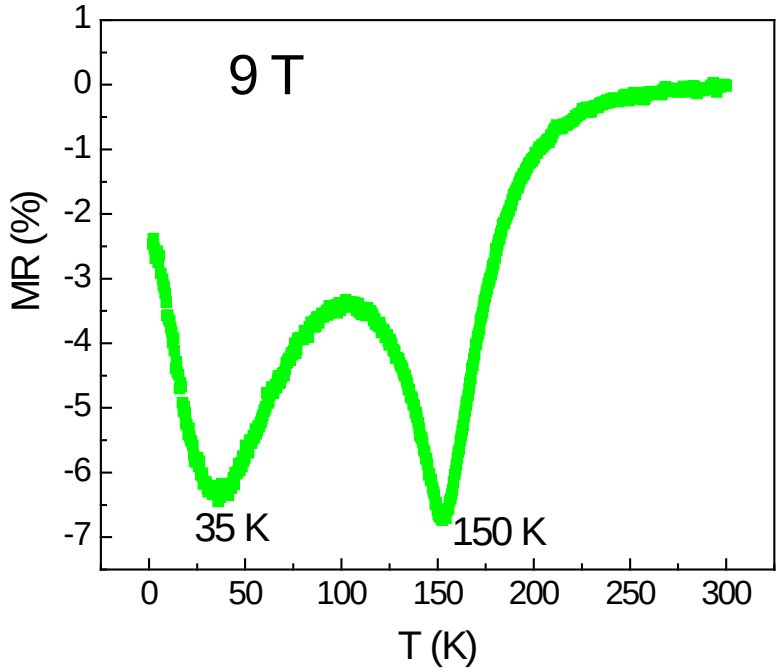

Figure 7.2. Temperature dependent MR of the SRO film under a perpendicular 9 T magnetic field.

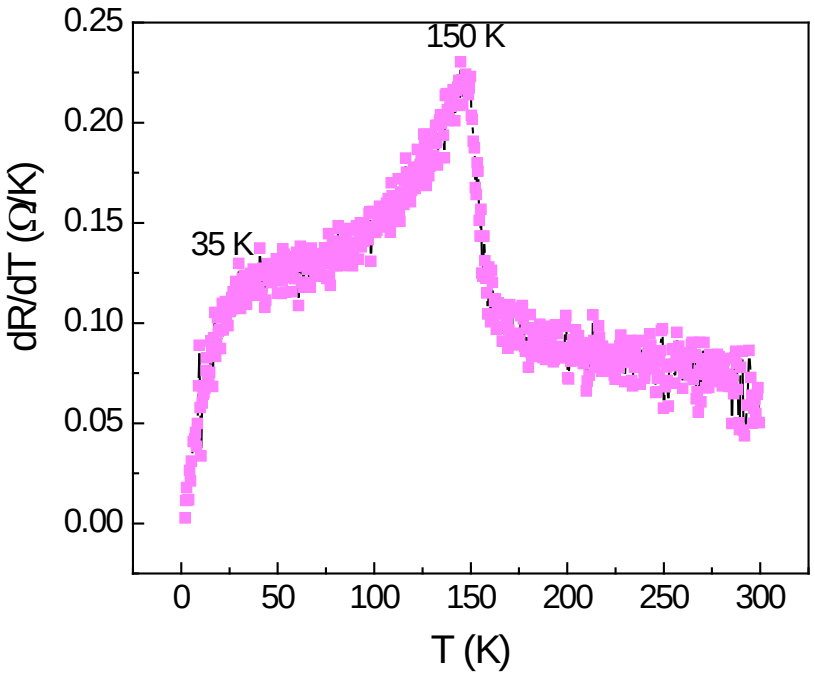

Figure 7.3. Derivative resistance as a function of temperature.

maximum at 150 K is due to the ferromagnetic transition, while the MR maximum at 35 K could be understood in terms of the large residue resistance

of SRO. As seen in Fig. 7.3, below 35 K, the rate of the resistivity change dramatically decreases with lowering temperature, which indicates the temperature-independent residual resistivity dominates. In this case, the effect of magnetic scattering on the resistance is relatively weak and therefore the negative MR resulting from the alignment of magnetic moments by an external field becomes smaller.

The room temperature Hall measurements generate linear Hall signals with the *n*-type carrier density of 1.4×10^{22} cm^{-3}, while Hall measurements of the SRO film below 160 K exhibit hysteresis signals as shown before in Fig. 2.30 as a result of the ferromagnetic state below 160 K (Fig. 2.34). Similarly, there is also hysteresis in MR curves as shown previously in Fig. 2.31.

In addition, the low temperature resistance of the SRO film was reduced while rotating a 9 T magnetic field in the sample surface plane, and the resistance show anisotropic behavior. Such anisotropic resistance measured at different temperatures is shown in Fig. 7.4. Clearly, the low temperature resistance is the smallest when the magnetic field is parallel to the current due to the alignment of magnetic moments by the external field.

Surprisingly, resistance maxima do not appear at 0, 180 and 360 degree, when magnetic field is normal to current. Instead, the resistance reaches its maxima at 30, 150, 210 and 330 degree. Such anisotropic resistance indeed indicates that there is an in-plane magnetocrystalline anisotropy in (110)-oriented SRO films and the resistance maxima angles correspond to magnetic hard axes, at which the energy is maximized. This is schematized in Fig. 7.5.

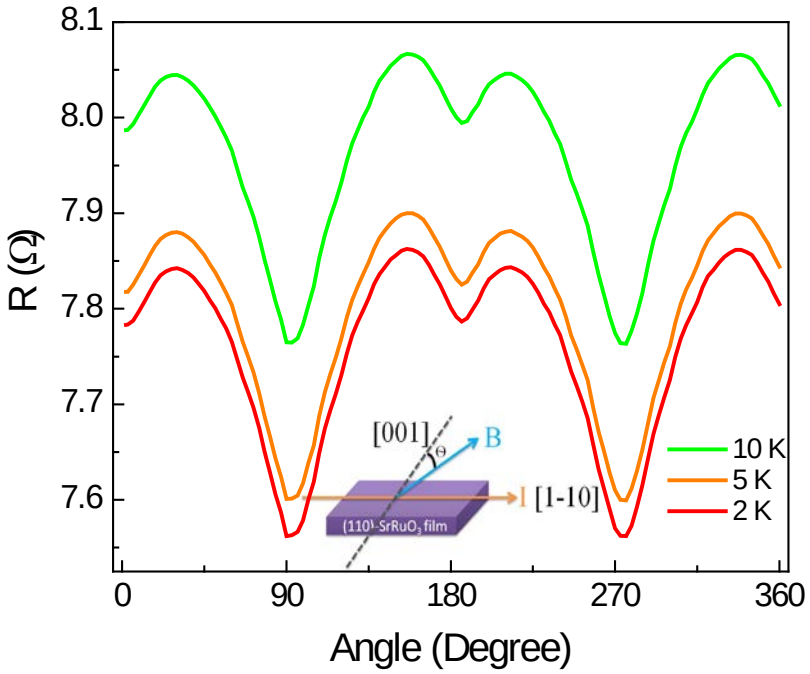

Figure 7.4. Resistance of the SRO film under a 9 T magnetic field as a function of the angle between magnetic field and the measurement current. The current direction was fixed along the [1-10] direction but the magnetic field was rotated in plane. Inset: schematic of measurement geometry.

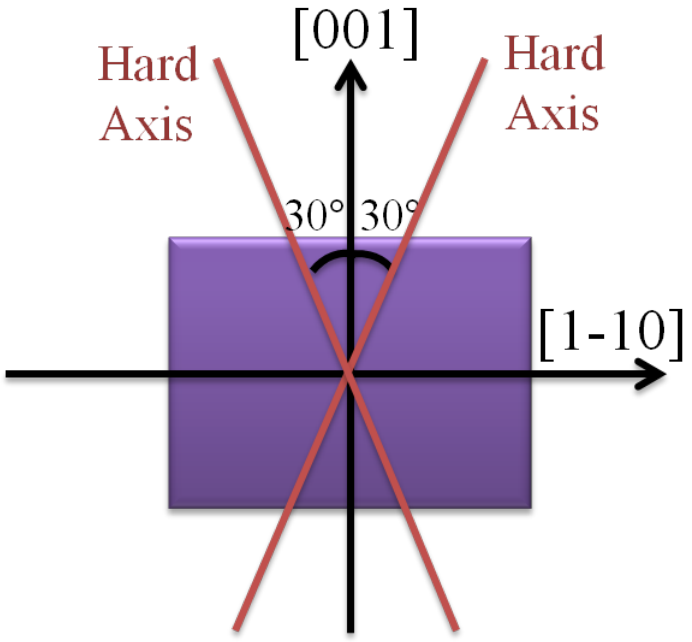

Figure 7.5. Schematic of magnetic hard axes in the (110) plane of the $SrRuO_3$ film.

7.2 $SrRuO_3/LaAlO_3$ superlattices

A series of superlattices with alternating SRO and LAO thin layers were fabricated, *i.e.*, $[SRO_{2uc}LAO_{2uc}]_{60}$, $[SRO_{3uc}LAO_{3uc}]_{40}$, $[SRO_{4uc}LAO_{4uc}]_{30}$, $[SRO_{7uc}LAO_{7uc}]_{20}$, and $[SRO_{10uc}LAO_{10uc}]_{12}$ on small-miscut TiO_2-terminated STO substrates by pulsed laser deposition, which are in sequence defined as SL2, SL3, SL4, SL7 and SL10, respectively. The superlattices with different SRO and LAO thicknesses were deposited at 750 °C under an oxygen partial pressure of 200 mTorr. During deposition, the fluence of the laser energy was kept at 1.5 J/cm^{2}and the laser repetition rate was 5 Hz. The deposition rates of SRO and LAO films were carefully calibrated by performing x-ray reflectivity measurements for thick single-layer SRO and LAO films grown on STO substrates. To avoid the effect of the two dimensional electron gas [17] at the interface between LAO and STO on electrical properties of superlattices, SRO was always the first layer deposited on the STO substrate.

Both the early study by Gan *et al*. [203] on SRO films grown on large miscut (001)-oriented STO substrates (~2°) and the recently TEM study by Ziese *et al*. [204] on SRO films grown on small-miscut (001)-oriented STO substrates (~0.1°) show that SRO films are (110)-oriented, and the [001] and [1-10] directions of SRO films are in plane and aligned with the crystalline axes of STO. Figure 7.6 shows an atomic force microscopy (AFM) image of a (001)-oriented TiO_2-terminated STO substrate with a small miscut angle of ~0.1°. Such STO substrates with an average step width of 300-400 nm are similar to what Ziese *et al*. [204] used in their study.

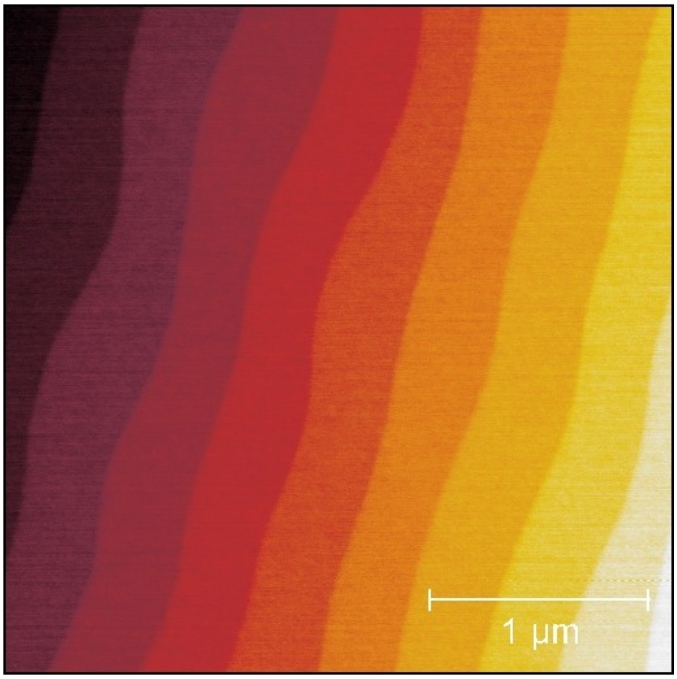

Figure 7.6. AFM image of a TiO_2-terminated STO substrate utilized for SRO/LAO superlattice deposition.

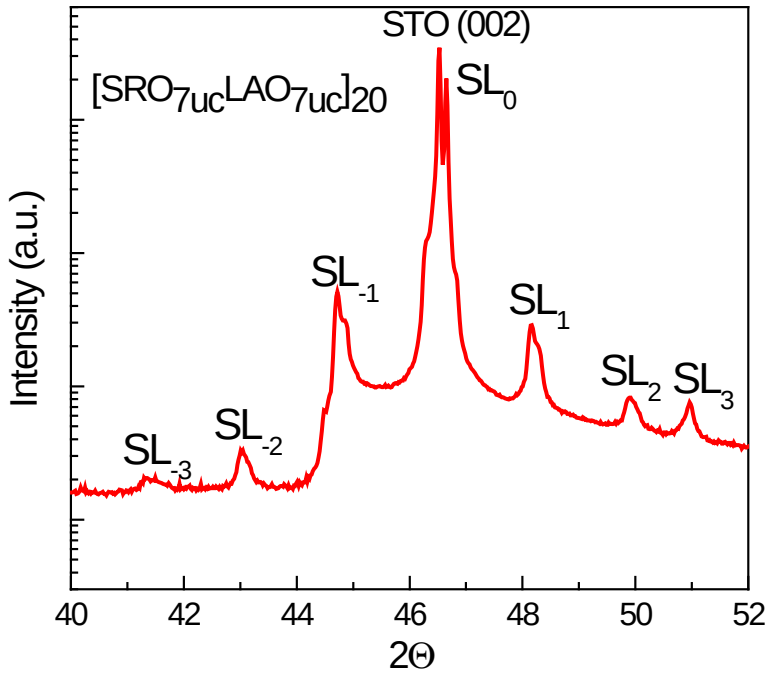

Figure 7.7. θ-2θ scan spectroscopy of a $[SRO_{7uc}LAO_{7uc}]_{20}$ superlattice grown on STO.

SRO/LAO superlattices were characterized by x-ray diffraction measurements including both θ-2θ scans and reciprocal space mappings. The

θ-2θ scan spectroscopy of a SL7 superlattice around the STO (002) Bragg peak is shown in Fig. 7.7. Satellite peaks up to the third order can be clearly seen, suggesting a good periodicity of the superlattice. The zero-order satellite peak of the superlattice is close to the STO (002) peak, which also confirms the studies by Gan *et al.* [203] and Ziese *et al.* [204] that SRO layers are (110)-oriented since the zero-order satellite peak corresponds to the average of the out-of-plane lattice constant. Furthermore, the thickness Λ of each period and the average lattice constant d of the superlattice can be fitted by satellite peak positions using the equation (2-6). A highly linear dependence (seen in Fig. 2.12) of n on $2sin\theta/\lambda$ results in Λ = 55.5 Å, which is comparable to the thickness of 7 uc SRO plus 7 uc LAO (3.93×7+3.79×7 Å=54 Å).

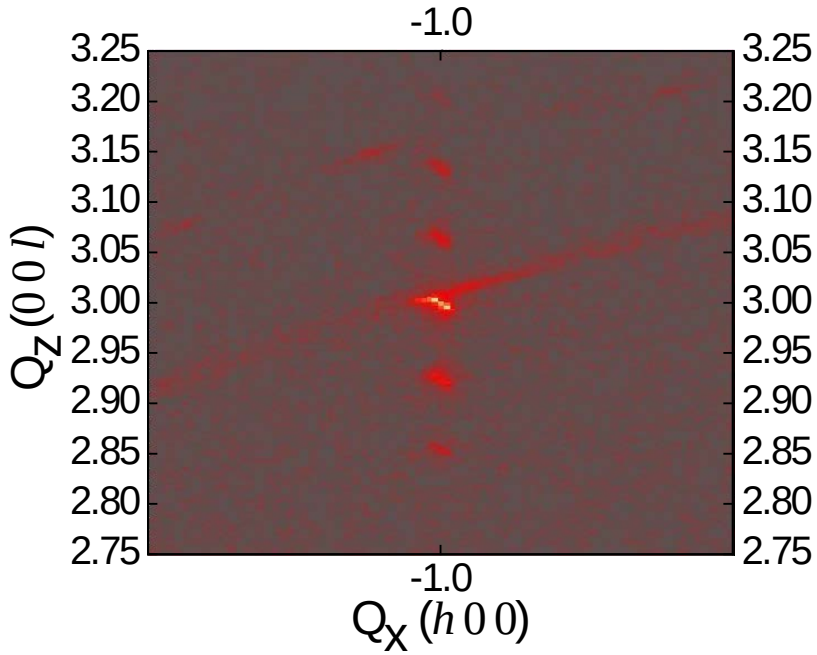

Figure 7.8. Reciprocal space mapping of the $[SRO_{7uc}LAO_{7uc}]_{20}$ superlattice in the vicinity of the STO (-103) Bragg peak.

The reciprocal space mapping of the SL7 superlattice in the vicinity of the STO (-103) Bragg peak is shown in Fig. 7.8. Satellite peaks up to the third

order are visible, which are consistent with the θ-2θ scan spectroscopy. All the satellite peaks have the same projection onto the Q_x axis as that of the STO Bragg peak indicating coherent epitaxial growth.

7.2.1 Evolution of transport properties

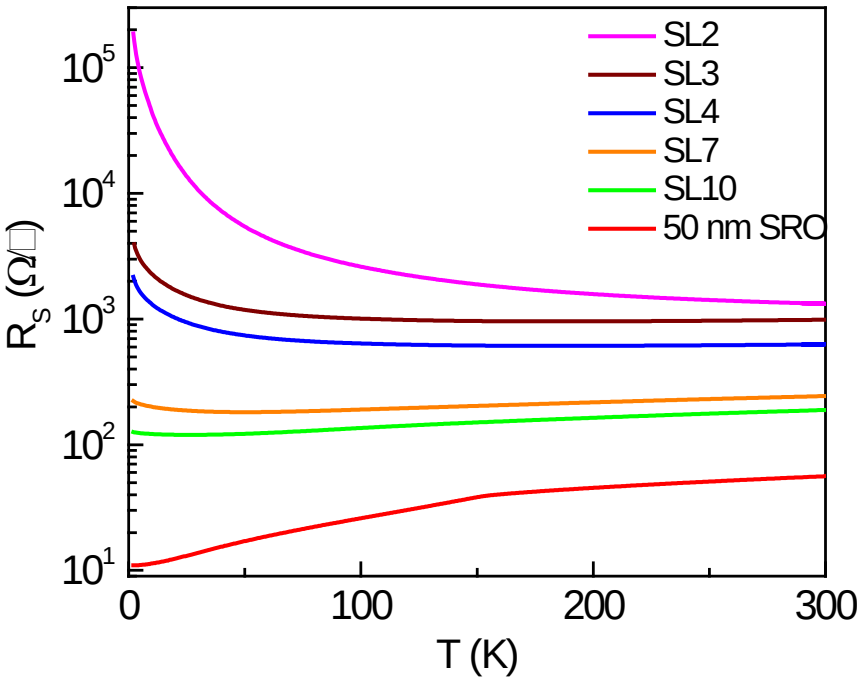

Figure 7.9. Temperature dependence of sheet resistance (R_S-T) of a 50 nm SRO film as well as different SRO/LAO superlattices.

The electrical properties of the superlattices were characterized by typical four-probe linear resistance measurements using a Quantum Design physical property measurement system (PPMS) machine. Ohmic contacts onto the 5×5 mm^2 samples were formed using Al wedge bonding directly connected to the supperlatices. Figure 7.9 summarizes the temperature dependence of the sheet resistance (R_S-T) of different superlattice samples as well as a 50 nm thick single-layer SRO film. The variation in electrical properties of superlattices with SRO layer thickness can be clearly seen. Overall, the room temperature

sheet resistance increases with decreasing thickness of SRO layers. And the metallic behaviour of bulk SRO finally transforms into a completely insulating state as SRO layer thickness is reduced to 2 uc in each period.

Such a metal-insulator transition (MIT) induced by the thickness of the SRO film was also observed on single-layer SRO films [195,196,205]. Herranz *et al*. [205] observed a resistivity upturn at ~20 K for an 8 nm SRO film grown on STO. In our superlattices, a resistivity upturn at ~30 K is present in SL10 structures. Toyota *et al*. [196] observed a completely insulating state for a 4 uc SRO single-layer film grown on STO. However, in our case, SL4 samples are metallic at high temperatures above ~185 K.

Both Herranz *et al*. [205] and Toyota *et al*. [195] attributed the observed MIT in SRO thin films to disorder. Later, Xia *et al*. [196] managed to improve the quality of single-layer SRO films by reducing the degree of disorder, and however found that SRO single-layer films with thickness below 4 uc were still insulating. In our case, the R_S-T curve of SL3 structures show a similar signature to that of SL4 structures, *i. e.*, metallic at high temperatures above ~185 K but insulating at lower temperatures. Nevertheless, based on our results, it seems that strain is not the dominant origin of the MIT observed in SRO superlattices. That is because LAO has a much smaller lattice constant (3.79 Å) than STO (3.905 Å) and SRO (3.93 Å), and thus the introduction of LAO into SRO/LAO superlattices would incur a larger compressive stress to SRO layers compared to the case of single-layer SRO films grown on STO. However, the critical thickness of SRO layers in SRO/LAO superlattices for a completely insulating state is 2 uc, which is smaller than those (4 uc and 3 uc)

of single-layer SRO films observed by Toyota *et al.* [195] and Xia *et al.* [196], respectively.

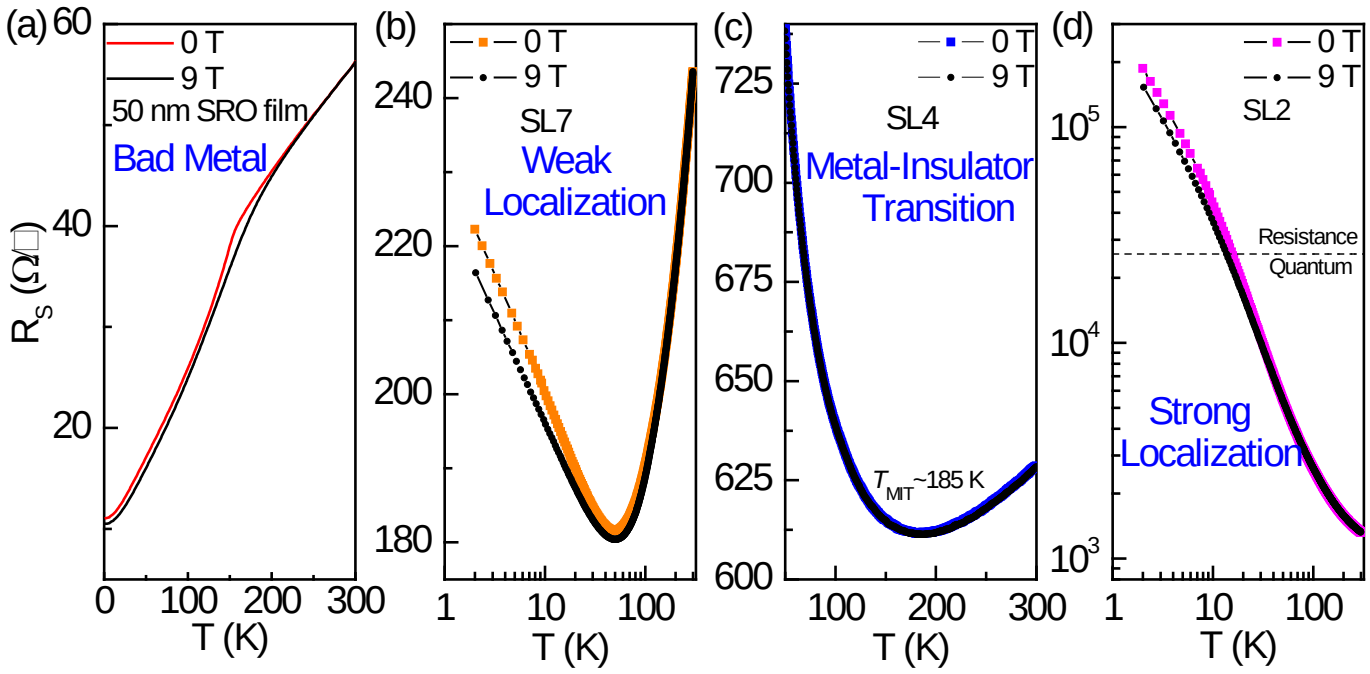

Figure 7.10. R_S-T curves of the 50 nm SRO single-layer film in (a) as well as SL7 in (b), SL4 in (c) and SL2 superlattices in (d) on different scales both under a zero-field and an out-of-plane 9 T magnetic field.

For a detailed analysis on the evolution of electrical properties of SRO/LAO superlattices with SRO layer thickness, R_S-T curves of the 50 nm SRO single-layer film, SL7, SL4 and SL2 superlattices under both zero and an out-of-plane 9 T magnetic field are plotted on different scales in Fig. 7.10(a)-(d), respectively. Room temperature sheet resistance of the 50 nm SRO film is ~56 Ω and thus corresponds to a room temperature resistivity of 280 μΩ cm, comparable to the value in previous studies [206]. A resistivity kink at ~160 K corresponding to the Curie temperature is visible due to strong magnetic scattering. Above 160 K, the sheet resistance is linearly dependent on temperature, for which SRO is referred to as a "bad metal" [207]. The

negative magnetoresistance (MR) under a 9 T magnetic field is apparent below 160 K due to the ferromagnetic phase.

As SRO layer thickness becomes 7 uc in SRO/LAO superlattices, an obvious logarithmic increase of sheet resistance with decreasing temperature as well as a negative out-of-plane MR is seen in Fig. 7.10(b), typical of a weak localization [208]. While SRO layer thickness is reduced to 4 uc in each period, a resistance upturn occurs at ~185 K, and the sheet resistance at 2 K exceeds three times that of room temperature, which can be identified as metal-insulator transition similar to the case observed in *n*-type STO [44]. Finally, when the SRO layer in each period of a superlattice is reduced to 2 uc, the whole structure turns into an insulating state. At low temperatures, the sheet resistance of the SL2 sample exceeds the resistance quantum h/e^2 = 25.8 kΩ, which means the electron mean free path becomes shorter than the Fermi wavelength so that quantum interference becomes predominant in electron transport properties, leading to a strong two-dimensional localization [209].

7.2.2 Strain effect

To examine the strain effect on the metal-insulator transition in SRO thin films, we prepared similar SRO/LAO superlattices on various other substrates including (100) $(LaAlO_3)_{0.3}(Sr_2AlTaO_6)_{0.7}$ (LSAT) and (110) $DyScO_3$ (DSC). The in-plane lattice constants of those substrates are 3.868 and 3.944 Å, respectively. In addition, atomically flat surface of LSAT and DSC can be achieved by thermal annealing and wet etching.

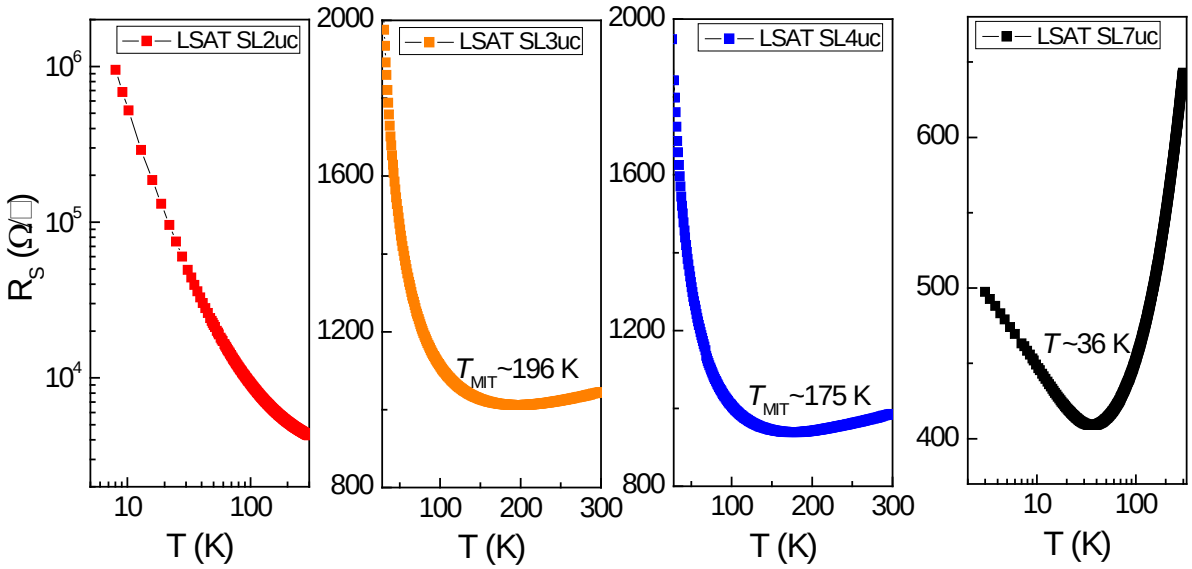

Figure 7.11. R_S-T curves of SRO/LAO superlattices grown on LSAT substrates.

As seen in Fig. 7.11, SRO/LAO superlattices fabricated on LSAT substrates exhibit a similar evolution trend of the transport properties with SRO layer thickness. As the SRO layer thickness is reduced, the whole system gradually transforms into a more localized state. This demonstrates that a larger compressive strain does not affect the electrical evolution of SRO/LAO superlattices with SRO layer thickness.

Figure 7.12 summarizes transport properties of SRO/LAO superlattices fabricated on DSC substrates. Although SL2 grown on DSC is highly insulating, the evolution trend of the degree of localization in SRO/LAO superlattices is still the same, *i.e.*, from metal to weak localization, to metal-insulator transition, and finally to strong localization as the thickness of SRO layers is decreasing. This indicates that the localization in SRO is more sensitive to a tensile strain. However, it seems that the evolution trend of the degree of localization in SRO/LAO superlattices remains under a tensile strain.

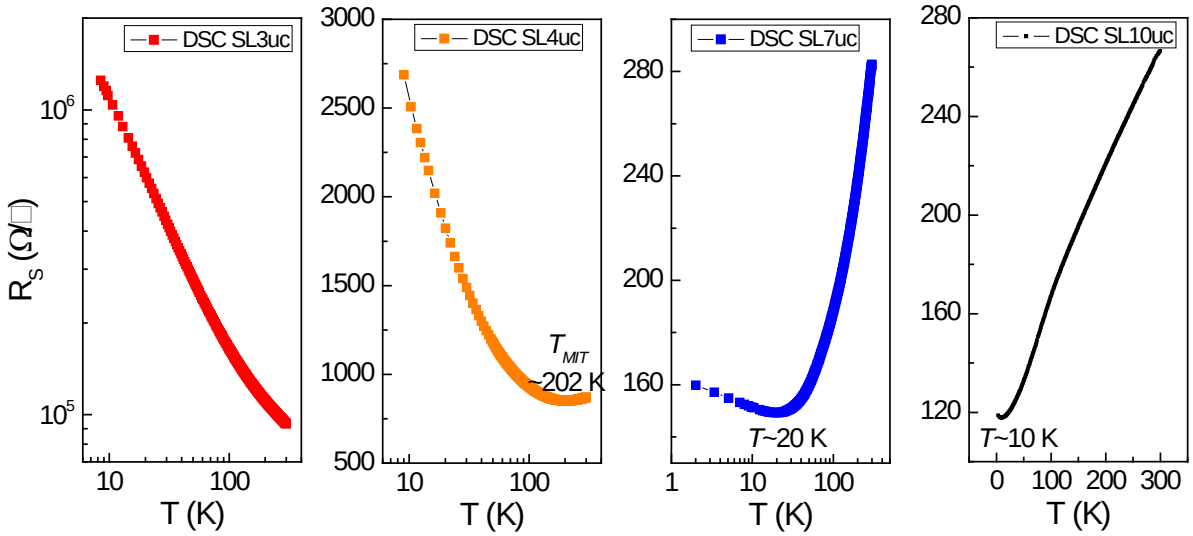

Figure 7.12. R_S-T curves of SRO/LAO superlattices grown on DSC substrates.

Overall the strain can clearly influence the resistance and degree of localization of the superlattices. However, it does not change the trend of the localization evolution with the SRO thickness. The up-turn temperatures of the resistance and the possible transport mechanisms in the SRO/LAO superlattices grown on different substrates are summarized in Table 7.1

Table 7.1 Characteristic resistance up-turn temperatures and transport categories of R_S-T curves for SRO/LAO superlattices grown on different substrates

Substrate	SL2	SL3	SL4	SL7
LSAT(a=3.868Å)	SL - >300 K	MIT - 196 K	MIT - 175 K	WL - 36 K
STO (a=3.905 Å)	SL - >300 K	MIT - 185 K	MIT - 185 K	WL - 50 K
DSC (a=3.944 Å)	-	SL - > 300 K	MIT - 202 K	WL - 20 K

Where SL, MIT and WL represents strong localization, metal-insulator transition and weak localization, respectively.

As can be seen from the table, the resistance up-turn temperature becomes higher with decreasing the thickness of SRO layers for all different substrates, which indicates that the system becomes more localized. In addition, the reproducibility of the metal-insulator transition in SRO/LAO superlattices

grown on different substrates also suggests that structural disorder is not a dominant effect since the degree of disorder should strongly depend on the lattice mismatch between substrate and SRO films.

7.2.3 Theoretical calculations for metal-insulator transition

To understand the origin of the metal-insulator transition observed in SRO/LAO superlattices, spin-polarized density functional theory calculations were performed. It was found that although the density of states (DOS) at Fermi energy in SRO/LAO superlattices decreases with reducing SRO layer thickness, it does not reach zero even if the SRO layer thickness is one uc.

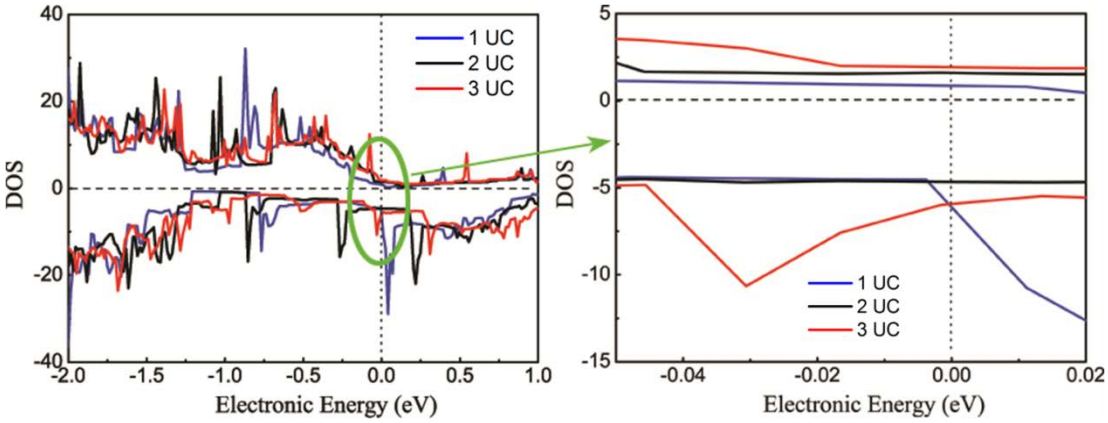

Figure 7.13. Calculated DOS for SRO/LAO superlattices with different SRO layer thickness.

The calculation results indicate that the dimensionality is contributing to the metal-insulator transition but not the only factor determining the metal-insulator transition behavior of SRO/LAO superlattices. Instead, dynamic spin scatterings which cannot be included in theoretical calculations could play an important role as well. That is because as the dimensionality is reduced, dynamic spin scattering in SRO ultrathin films could become dominant.

Therefore, we conclude that the metal-insulator transition in SRO/LAO superlattices as the SRO layer thickness is reduced is a result of the interplay between the dimensionality and dynamic spin scatterings.

7.2.4 Evolution of magnetic properties

7.2.4.1 In-plane magnetic anisotropy

Magnetic moments of the samples were measured by a Quantum Design superconducting quantum interference devices-vibrating sample magnetometer (SQUID-VSM) machine with the sensitivity of 10^{-8} emu.

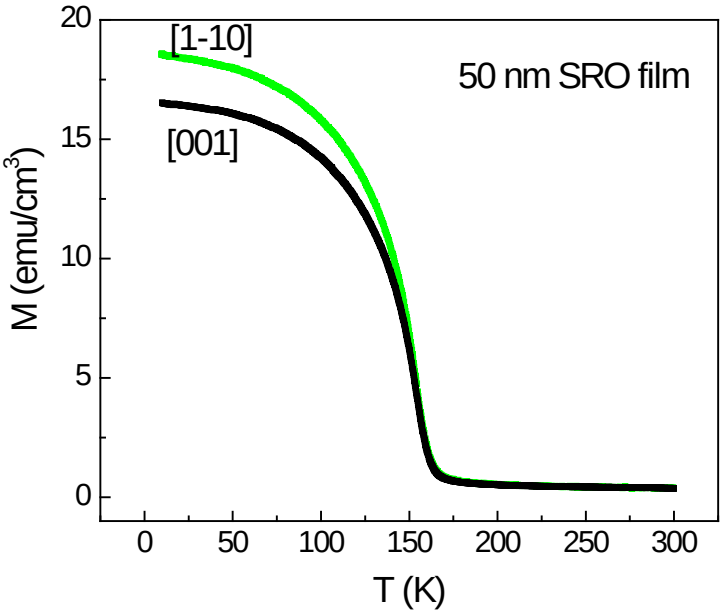

Figure 7.14. In-plane magnetic anisotropy of a 50 nm SRO film measured by a 1000 Oe field.

In-plane magnetocrystalline anisotropy was examined for all the samples. It was found that only the thick SRO single-layer film (Fig. 7.14) and the SL10 sample (Fig. 7.15) exhibit in-plane magnetocrystalline anisotropy. For other superlattices with SRO layers thinner than 10 uc, the *M-T* curves

measured along the two in-plane STO crystalline axes coincide (Fig. 7.16). This is consistent with the result obtained by Ziese *et al.* [204] that the in-plane anisotropy between [1-10] and [001] directions of a 5 nm SRO film is much smaller than that of a 40 nm SRO film.

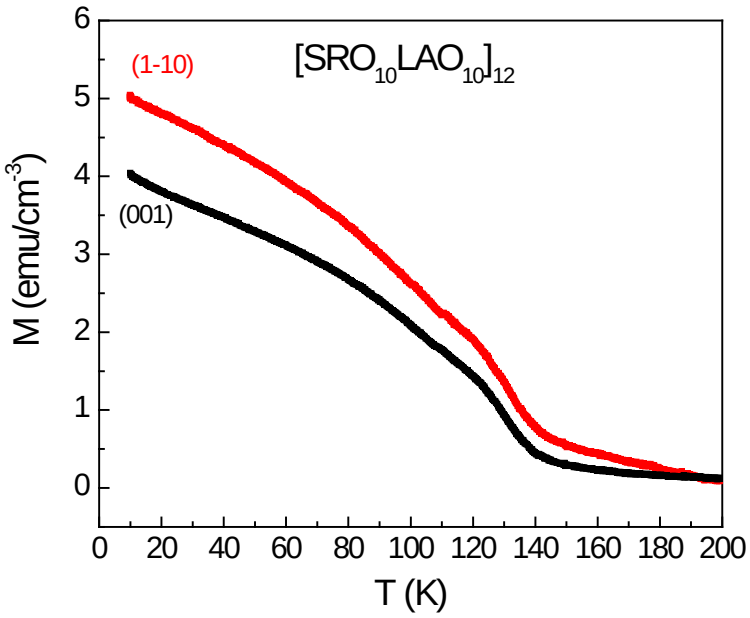

Figure 7.15. In-plane magnetic anisotropy of a SL10 superlattice measured by a 1000 Oe field.

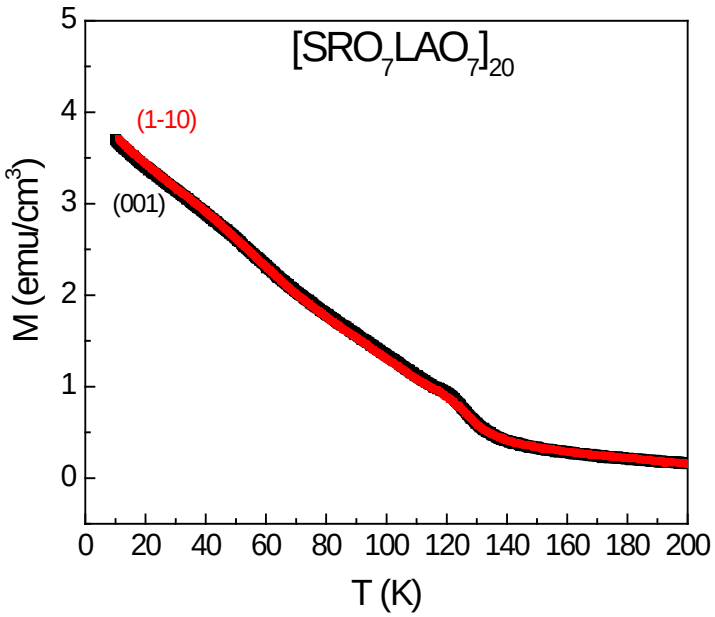

Figure 7.16. In-plane magnetizatin of a SL7 superlattice measured by a 1000 Oe field.

Moreover, it was found that the [001] direction of SRO films grown on STO is close to the STO step direction and the perpendicular in-plane [1-10] axis of SRO films is close to the in-plane easy axis. Our atomic force microscopy (AFM) and VSM measurements revealed that for both the 50 nm SRO film and the SL10 sample, the magnetic moment measured along the in-plane STO axis which is close to the step direction of a STO substrate, is smaller than that measured along the other perpendicular STO axis especially at low temperatures. This indeed confirms the results obtained by Ziese *et al*. [204].

7.2.4.2 Magnetic moment

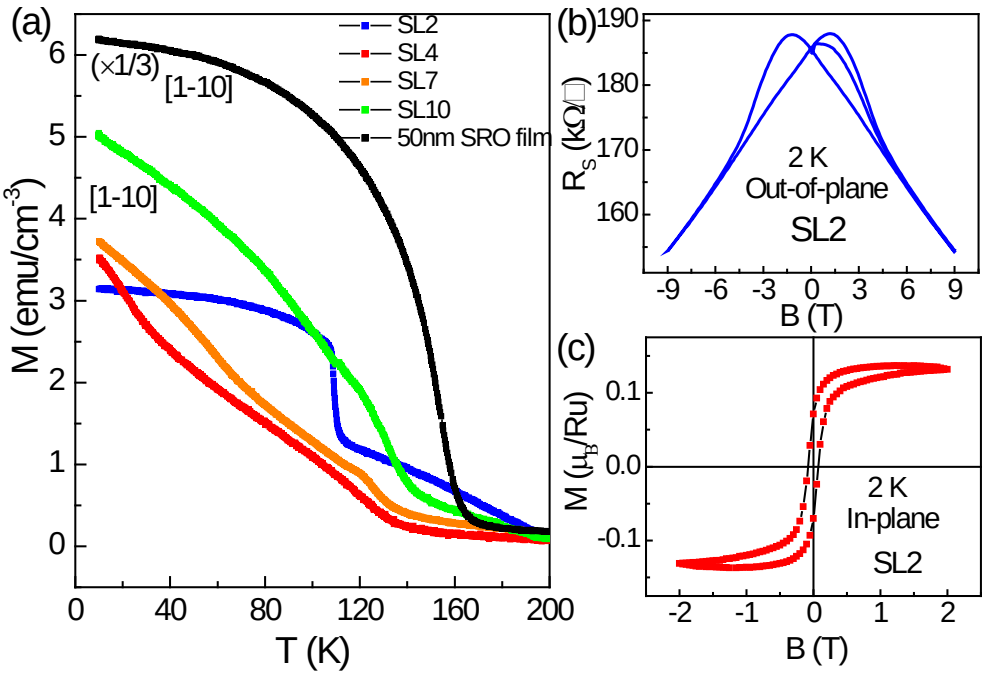

Figure 7.17. (a) Temperature dependence of magnetization of different samples measured by an in-plane 1000 Oe magnetic field. The magnetization of the 50 nm SRO single-layer film measured along its in-plane [1-10]

direction is divided by a factor of three. (b) Out-of-plane magnetoresistance of a SL2 superlattice. (c) In-plane field-dependent magnetic moment of the SL2 superlattice.

The magnetization of different superlattices as well as the thick SRO single-layer film is plotted as a function of temperature (*M*-*T*) in Fig. 7.17. The ferromagnetic transition at ~160 K can be clearly seen in the *M*-*T* curve of the thick SRO film. The Curie temperature of the SL10 structure decreases to ~140 K, which is higher than the values obtained by Herranz *et al*. [205] (~110 K) and Toyota *et al*. [195] (~127 K) for 10 uc single-layer SRO films. The Curie temperatures of the SL7 and SL4 structures are similar (~135 K), which is higher than that of a 4 uc SRO single-layer film (~120 K) observed by Xia *et al*. [196]. The *M*-*T* curve of the SL2 sample presents a different trend from other curves, which could be due to the interlayer coupling of SRO layers through ultrathin LAO intermediate layers. A sharp transition temperature of ~110 K is seen. However, for ultrathin 2 uc single-layer SRO films, neither magnetometer [195] nor Kerr measurements [196] was able to detect any possible magnetic transition due to extremely weak signals.

To further examine the low temperature magnetic phase of all the samples, electrical MR measurements as well as field-dependent moment (*M*-*B*) measurements were performed at low temperatures. It was found that all the samples exhibited butterfly hysteresis loops in low temperature out-of-plane MR measurements, and also *M*-*B* hysteresis loops in moment measurements. The out-of-plane MR and in-plane *M*-*B* curves of the SL2 sample at 2 K are shown in Fig. 7.17(b) and (c), respectively. The hysteresis loops both in electrical and magnetic measurements confirm that the low temperature phase

of such superlattices is ferromagnetic. In addition, the magnetization of superlattices is much smaller than that of the thick SRO film and further decreases with reducing SRO layer thickness, which could be due to the localization of electrons in superlattices with thin SRO layers. Since the ferromagnetism of SRO is itinerant, the localization of electrons leads to lack of electron wave function overlapping and thus the decrease of the ferromagnetic signals. Especially in the strongly localized SL2 sample, the saturation moment is ~0.15 μ_B/Ru, which is one order of magnitude smaller than 1.6 μ_B/Ru reported for bulk SRO [210].

7.2.5 Field effect modulation

Furthermore, we constructed field effect devices based on the SL2 and SL7 samples by depositing Au electrodes on the backside of STO substrates as shown schematically in Fig. 7.18.

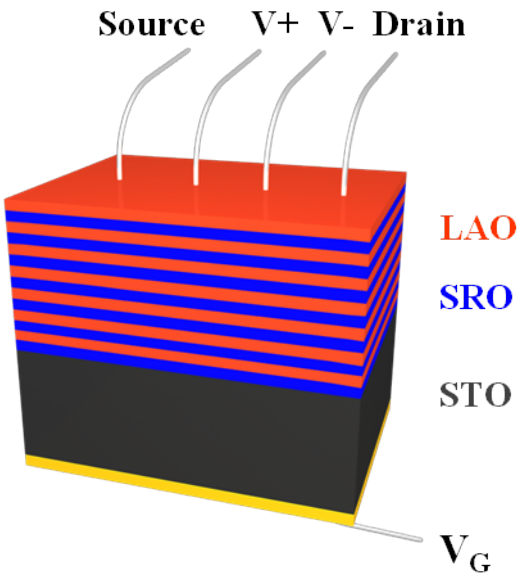

Figure 7.18. Schematic of a field effect device based on SRO/LAO superlattice structure.

STO substrates were employed as high-*k* dielectric material due to its extremely large dielectric constant at low temperatures and a gate voltage V_G was applied from Au back electrodes. During measurements, the back V_G was applied up to ±200 V and the gate leakage current was smaller than 5nA.

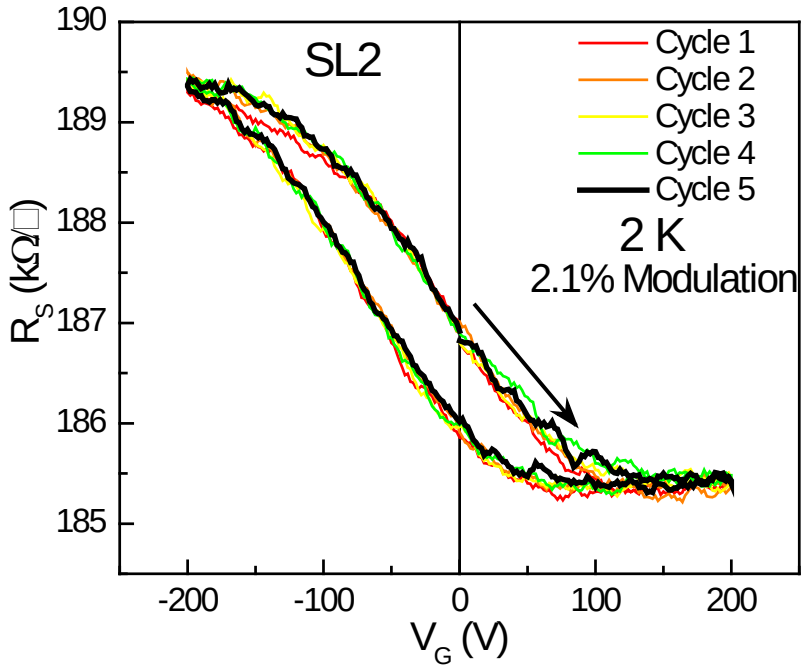

Figure 7.19. Sheet resistance of the SL2 superlattice as a function of back gate voltage.

Surprisingly, although the total film thickness of both the SL2 and SL7 samples was ~100 nm, the field modulation effect can be clearly seen in both devices (Figs. 7.19 & 7.20). For positive (or negative) V_G, R_s decreases (or increases), which is in agreement with the addition (or removal) of *n*-type carriers to (or from) the transport channels. The hysteresis loops of both devices can be continuously recycled a number of times by the sweeping the field between ±200 V, which demonstrates the interplay between external carrier injection and internal localization. The R_s in the SL2-based device

varies as much as 2.1% when changing the V_G from +200 to -200 V, which is much larger than that in the SL7-based device. That is because the

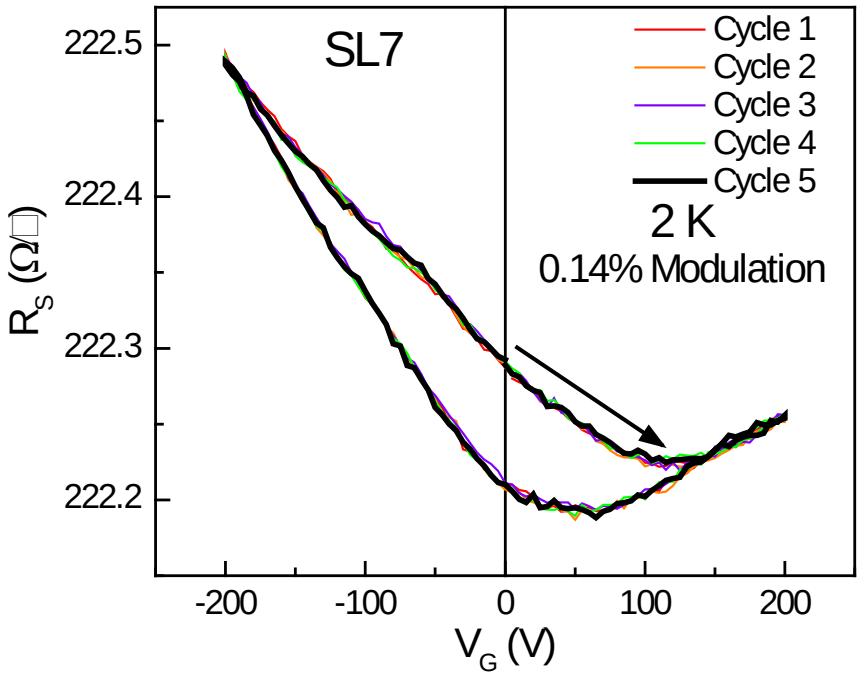

Figure 7.20. Sheet resistance of the SL7 superlattice as a function of back gate voltage.

characteristic width of the field modulation given by Thomas-Fermi screening length is inversely proportional to the one sixth power of carrier density. As the SL2 sample is more localized and expected to have less free carriers, this leads to a larger modulation length. Moreover, SRO layers in the SL2 structure are thinner than those in the SL7 structure, which further enhances the field modulation effect.

The evolution of electrical properties of SRO films from bad metal, to weak localization, then to MIT, and finally to strong localization as SRO layers become thinner and thinner could be a general evolution trend of the strongly correlated metallic systems when changing their dimensionality from

3D to 2D as also reported for $LaNiO_3$ [198,211]. Although strain can apparently affect the degree of localization of a certain SRO/LAO superlattice, it does not change the trend of the localization evolution with the thickness of the SRO films. On the other hand, ferromagnetism is clearly present in SRO films as thin as 2 uc and in bulk SRO it typically yields a kink in *R*-*T* curves as shown in Fig. 3a due to strong spin scattering. With the dimensionality of SRO films reduced, the ferromagnetic scattering could become dominant, thus leading to a metal-insulator transition. Therefore we conclude that the origin of the evolution in the electronic properties of SRO films could be the interplay between the dimensionality and dynamic spin scattering.

7.3 Summary

In summary, we studied the transport properties of single-layer SRO films and found that below 35 K residual resistance becomes pronounced. Anisotropic magnetoresistance study indicates that the magnetic hard axes in the (110) plane of SRO are 30° left and right of the SRO [001] axis. Furthermore, we studied the electronic and magnetic properties of SRO/LAO superlattices. By varying the thickness of SRO layers in the superlattices, we were able to modulate both electrical and magnetic properties of SRO films in SRO/LAO superlattices. For example, the ferromagnetic metal SRO can be tuned into a ferromagnetic insulator with a much lower T_c of ~110 K as SRO layers are reduced to 2 uc in SRO/LAO superlattices. We investigated the origin of the metal-insulator transition in ultrathin SRO films, and found that the MIT is likely due to the interplay between the dimensionality and dynamic spin

scattering. Moreover, we demonstrated field effect devices based on SRO/LAO superlattices, which reveals the possibility of realizing novel field effect devices based on multilayer structures.

Chapter 8 Ultraviolet and blue emission in $NdGaO_3$

$NdGaO_3$ (NGO) is a paramagnetic insulator, which undergoes a magnetic phase transition into an antimagnetic phase at ~1 K due to strong superexchange interaction [57]. It has an orthorhombic perovskite structure with lattice constants a = 5.43 Å, b = 5.50 Å and c = 7.71 Å while its orthorhombically distorted pseudocubic cell has a lattice constant of 3.87 Å, which is close to the lattice constants of many perovskite materials. Moreover, due to the very low dielectric loss of NGO in the GHz frequency range [212], NGO single crystals have been extensively utilized as substrates for high temperature superconducting film fabrications in microwave devices, colossal magnetoresistance thin film and other perovskite thin film depositions.

Rare earth oxides are of high interest in optical studies as rare earth ions can serve as emission centers for the construction of a laser system, such as Nd:YAG (Nd-doped $Y_3Al_5O_{12}$). The photoluminescence properties of the Nd^{3+} ion in NGO single crystals were studied by Orera *et al.* [58], where the samples were excited by light from a tungsten lamp. But no emission was detected in NGO even at low temperature. In this chapter, we report ultraviolet (UV) and blue emission in NGO single crystals and thin films obtained by the excitation of a 325 nm laser. There are two clusters of UV emission peaks around 360 and 390 nm while blue emission peaks are centered at 420 nm. In

crystalline NGO including bulk single crystals, polycrystalline films and single crystal films, the UV emission peak at 388 nm is very sharp and the strongest. Nevertheless, all the emission peaks in amorphous NGO films deposited on commercial SiO_2/Si substrates are broadened and the emission at 365 nm becomes the strongest. The photoluminescence (PL) intensity is significantly enhanced by lowering temperature and the blue emission becomes visible at low temperatures. To the best of our knowledge, such UV and blue emission in NGO has not been reported and therefore this report may open the path for NGO to be used in photonic devices and as laser material in terms of both bulk crystal and thin film.

The (110)-oriented NGO single crystals (5×5×0.5 mm^3) were obtained from CrysTec GmbH, Germany. Various NGO thin films were deposited from an NGO single crystal target (diameter: 25 mm, thickness: 5 mm) on different substrates using pulsed laser deposition. The deposition oxygen pressure was 10^{-2} Torr and the deposition temperature was 700 °C. During pulsed laser deposition, the laser fluence was fixed at 1.5 J/cm^2 and the repetition rate was 5 Hz. PL properties of NGO single crystals and thin films were determined by a 325 nm laser PL system with a laser spot size of ~800 nm and an excitation intensity of 1 MW/cm^{-2}.

8.1 UV and blue emission in NGO single crystals

PL spectra were measured in the range of 330 to 700 nm for all samples. However, no photoemission was detected above 450 nm, which is consistent with the results reported by Orera *et al.* [58]. Figure 8.1 shows the room-

temperature PL spectra of two NGO single crystals. Indeed, the PL spectra of different NGO single crystals are the same and all of them exhibit a very sharp UV emission peak at 388 nm. There are a few of emission peaks apparently existing in the PL spectra, which are labeled by wavelength in the figure. Overall, the emission peaks can be categorized into three sets. The first set around 360 nm and the second set around 390 nm are UV emission while the third emission peak set around 420 nm pertains to blue emission.

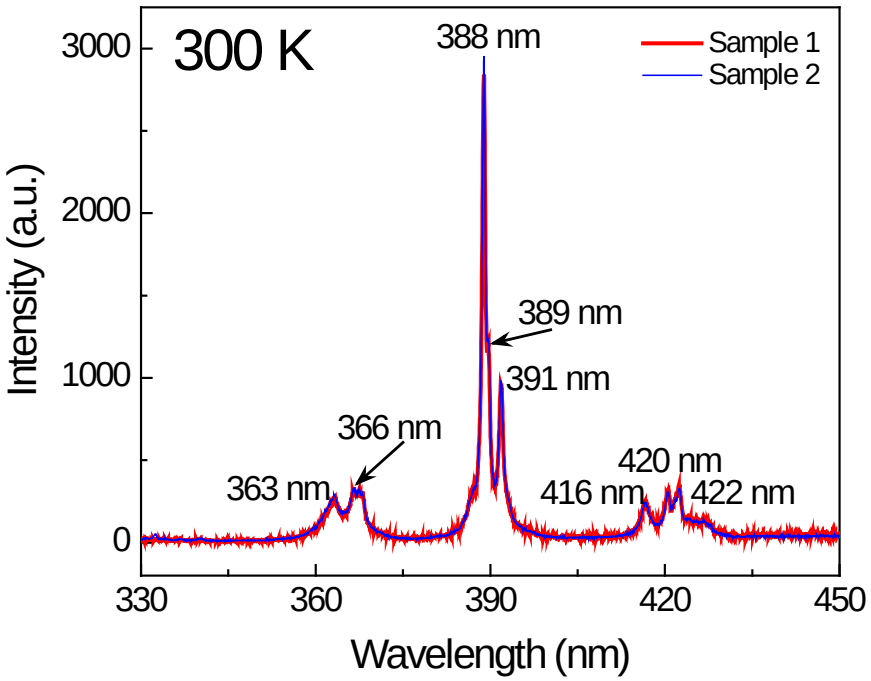

Figure 8.1. Room temperature photoluminescence (PL) spectra of two $NdGaO_3$ (NGO) single crystals excited by a 325 nm laser.

It was found that the emission peak wavelength does not shift but only the emission intensity is pronouncedly enhanced as the temperature is lowered. The low temperature PL spectra in the range of 380 to 396 nm are shown in Fig. 8.2(a). The 388 nm emission peak intensity at 20 K is increased by a factor of ten compared to that at room temperature. In addition, the emission peaks at 389 and 391 nm can be clearly seen in low temperature spectra.

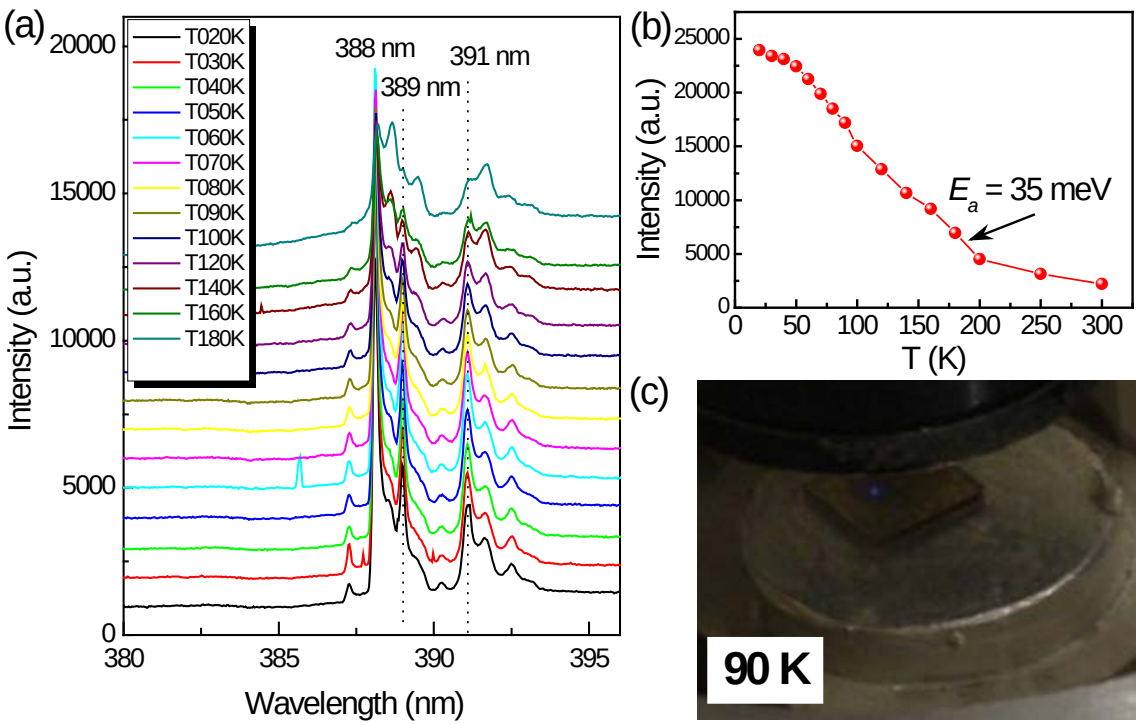

Figure 8.2. Low temperature PL properties of NGO. (a) Low temperature PL spectra of a NGO single crystal. (b) Integrated intensity of the 388 nm emission peak as a function of temperature. (c) Blue emission of NGO at 90 K excited by a 325 nm laser with the laser spot size of ~800 nm.

To investigate the effect of thermal activation on the PL emission of NGO, the integrated intensity of the 388 nm emission peak is plotted as a function of temperature in Fig. 8.2(b). As the temperature increases, the recombination rate and accordingly the emission intensity decrease due to the thermal activation of photo-excited electrons. Such processes can be described by [213]

$$I(T) = I_0/[1 + \exp(-E_a/kT)] \tag{8-1}$$

where E_a is the activation energy. The integrated intensity above 140 K can be well fitted by the above formula and the fitted activation energy is 35 meV. This value is comparable to that of UV emission in GaN [213]. In addition, the

blue emission around 420 nm in NGO is visible at 90 K, which is shown in Fig. 8.2(c).

8.2 UV and blue emission in NGO thin films

8.2.1 Polycrystalline films

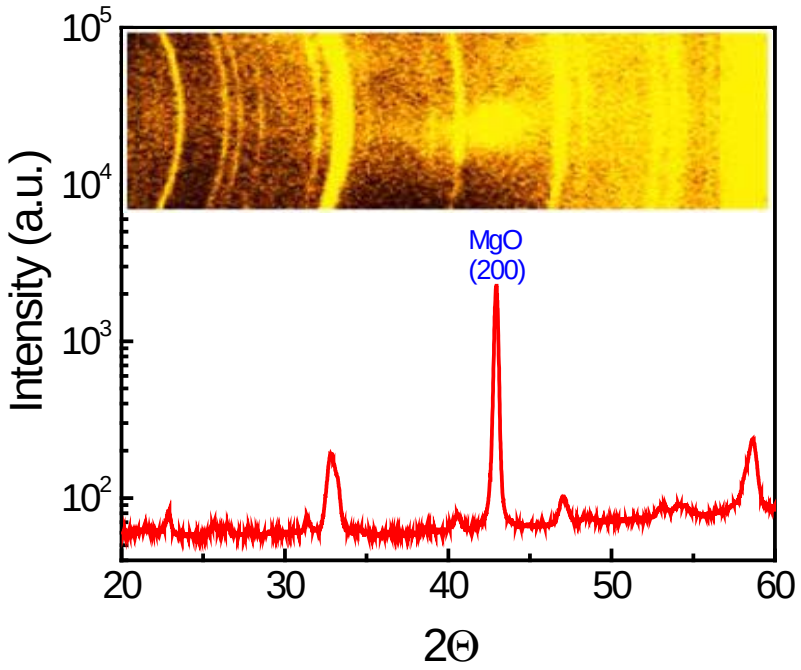

Figure 8.3. X-ray diffraction (XRD) spectrum of a 1 μm NGO film grown on an MgO single crystal substrate. The inset is the corresponding 2D diffraction pattern.

NGO films of ~1 μm thickness were deposited on MgO and Al_2O_3 substrates. The crystal structure of the deposited films was examined by an x-ray diffraction (XRD) machine with a 2D detector. It was found all the NGO films grown on MgO and Al_2O_3 substrate are polycrystalline due to the lattice mismatch. Multiple diffraction rings in the 2D diffraction pattern and the corresponding multiple diffraction peaks in the spectrum demonstrate the polycrystalline signature of an NGO film grown on MgO (Fig. 8.3). It was

found that all the NGO films fabricated on MgO and Al_2O_3 substrates exhibit similar PL properties (Fig. 8.4). Generally, the PL emission peaks of a polycrystalline NGO film are the same with those of bulk NGO single crystals.

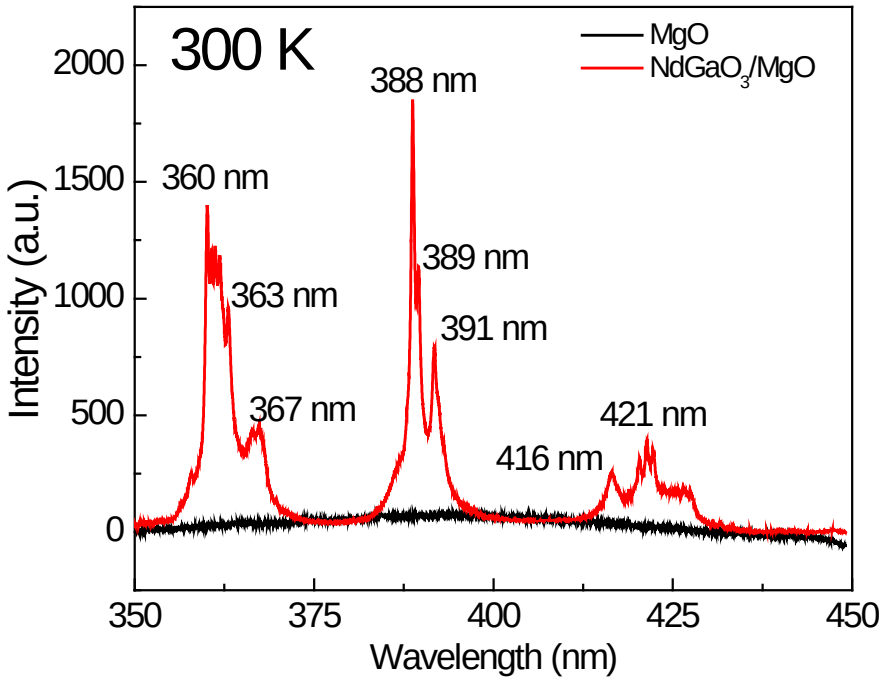

Figure 8.4. PL spectra of the NGO film grown on MgO (red line) and the MgO substrate.

8.2.2 Epitaxial single crystal films

Epitaxial single crystal thin films are potential for laser filter applications and UV detectors. However, the difficulty in fabricating epitaxial NGO films for PL studies is that most of perovskite substrates such as $SrTiO_3$ (STO) and $LaAlO_3$ (LAO) have plethora of oxygen vacancies and intragap defects, which result in strong photoemission in these substrates [44,136]. To overcome this issue, we first deposited a 300 nm Nb-doped STO (NSTO) buffer layer on a LAO single crystal substrate and then grew a 1-μm-thick NGO film on it. Nb-doped STO is metallic and has a large number of free electrons. The free

electrons in this buffer layer can absorb the laser light effectively so that the PL signal of the substrate will not be excited.

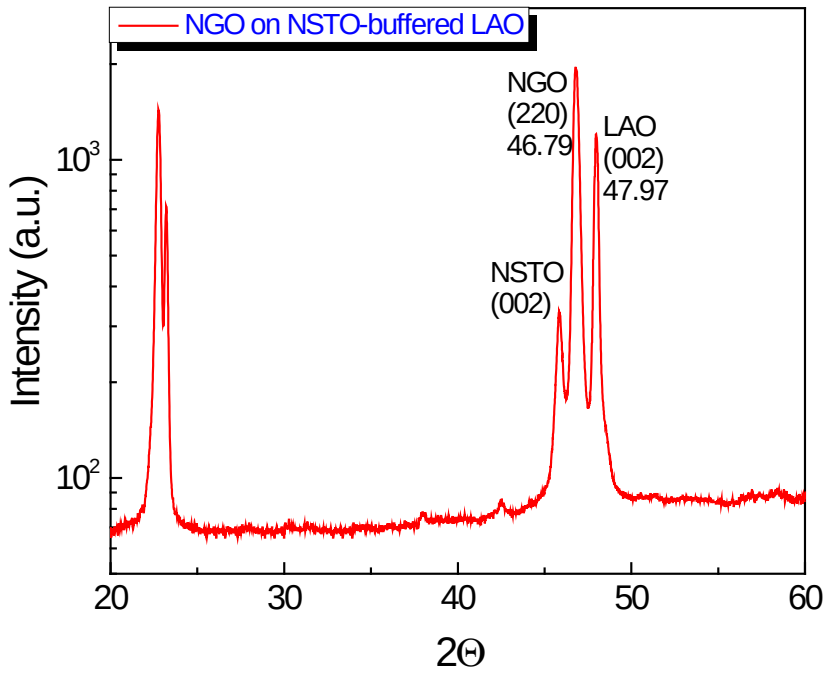

Figure 8.5. XRD spectrum of a 1 μm NGO film grown on a 300 nm Nb-doped $SrTiO_3$ (NSTO) buffered $LaAlO_3$ (LAO) substrate.

The XRD spectrum of a NGO/NSTO/LAO heterostructure (Fig. 8.5) shows that the NGO film is epitaxially grown on NSTO-buffered LAO. The PL spectrum of this heterostructure is shown in Fig. 8.6. Surprisingly, although the emission peaks around 390 and 420 nm are similar to those of a bulk crystal, there is no emission around 360 nm. The emission around 360 nm may have been absorbed by the underlying NSTO buffer layer as the band gap of STO is 3.27 eV (~380 nm). In this aspect, the NSTO buffer layer could have served as a filter to the 360 nm PL emission.

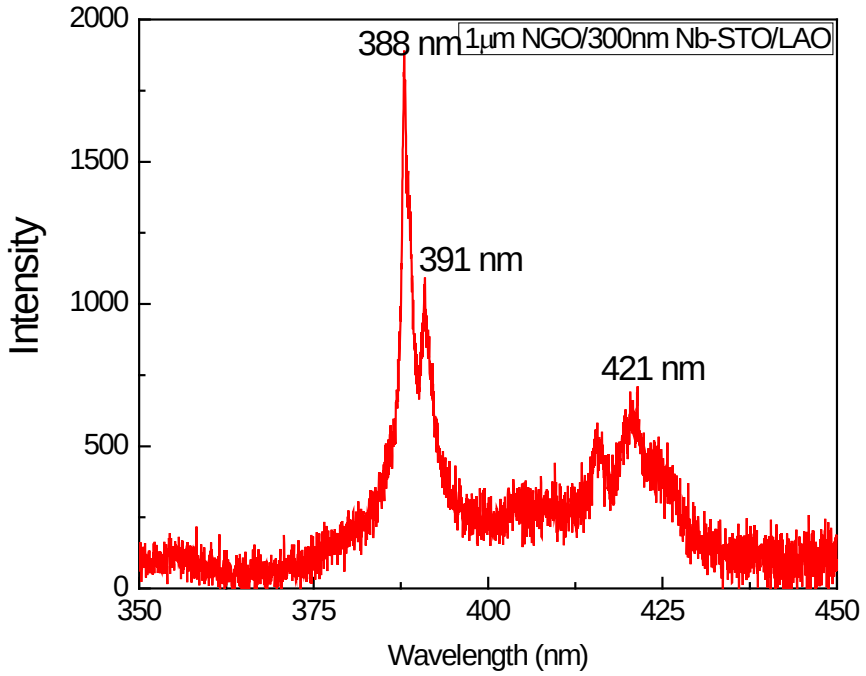

Figure 8.6. PL spectrum of the NGO film (red line). The black line is the PL spectrum of 300 nm NSTO grown on LAO.

8.2.3 Amorphous films

For practical applications, amorphous substrates such as SiO_2/Si have technological and cost advantages. Therefore 1 μm NGO films were also fabricated on commercial SiO_2/Si substrates. An atomic force microscopy image of an NGO film grown on Si substrate is shown in Fig. 8.7(a). The surface of the film is quite flat with a rms roughness of 0.24 nm for a 1 μm×1 μm area. The XRD spectrum shown in Fig. 8.7(b) indicates that the crystallinity of the film is very poor and the film is amorphous. The PL emission exhibits three broad peaks at 365, 391 and 423 nm [Fig. 8.7(c)]. The broadening of emission peaks in such an amorphous film can be attributed to the Stark effect, which is the splitting of spectral lines due to the present of an electric field. The internal crystal field in crystalline material is closely

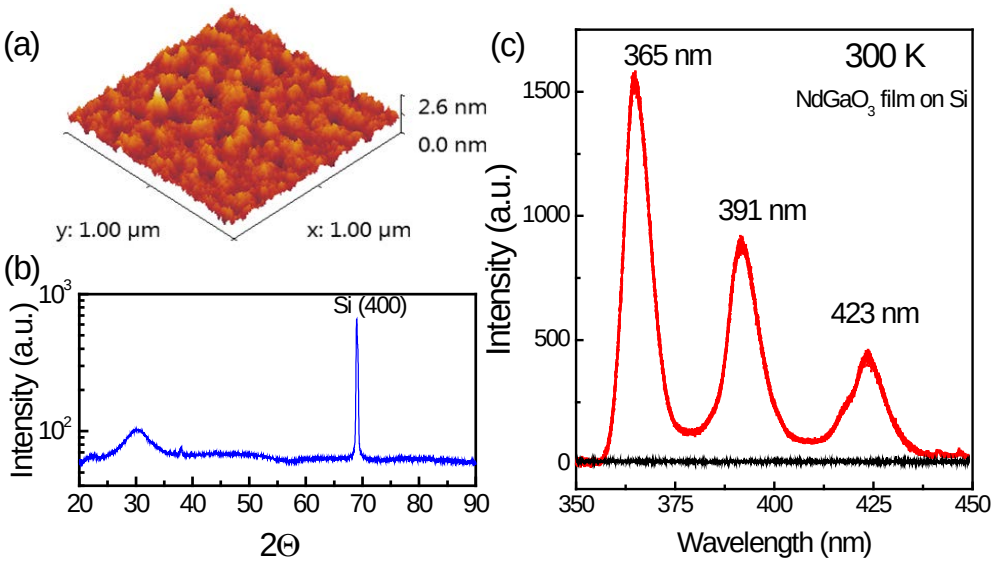

Figure 8.7. PL emission of amorphous NGO film. (a) Atomic force microscopy image of a1 µm×1 µm area of a 1 µm thick NGO film grown on an amorphous SiO_2/Si substrate. (b) XRD data of the NGO/SiO_2/Si heterostructure. (c) PL spectrum of the NGO film grown on amorphous SiO_2/Si (red line). The black line is the PL spectrum of the amorphous SiO_2/Si substrate.

related to the crystallinity and in amorphous material it could be ideally zero. Accordingly, no splitting of emission peaks is present in the PL spectrum of the amorphous NGO film and the emission peaks get broadened.

8.3 Mechanism of photoemission

The optical absorption edge of NGO single crystal was found to be ~220 nm [58], corresponding to an optical band gap of 5.6 eV, which is much larger than the excitation energy of the 325 nm laser (3.8 eV). Therefore, the PL emission observed in NGO single crystals and thin films is obviously not a band gap emission. Instead, the emission peaks observed in NGO can be readily understood by looking at the energy levels of Nd^{3+}. The characteristic

energy level structure of rare earth ions Ln^{3+} is known as Dieke diagram and only slightly changes in different crystal structures.

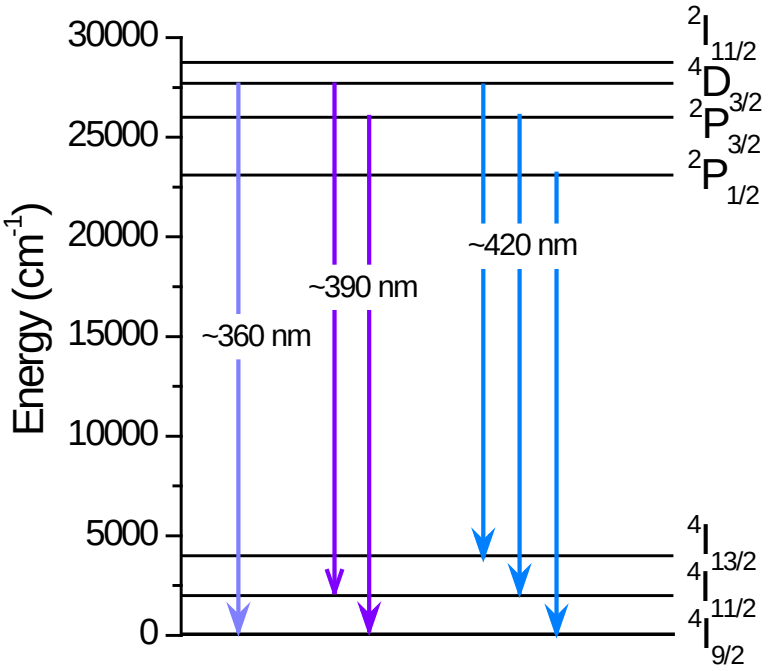

Figure 8.8. Schematic of possible photoemission processes in NGO.

The wavelengths of three emission centers 360, 390 and 420 nm correspond to the wavenumbers of 27700, 25600 and 23800 cm^{-1}, respectively. The ground state of Nd^{3+} is $^4I_{9/2}$. Based on the energy levels of Nd^{3+} [214], the PL emission around 360 nm pertains to the optical transition $^4D_{3/2} \rightarrow {}^4I_{9/2}$; the emission around 390 nm corresponds to the optical transitions $^4D_{3/2} \rightarrow {}^4I_{11/2}$ and $^2P_{3/2} \rightarrow {}^4I_{9/2}$; and the emission around 420 nm can be ascribed to the optical transitions $^4D_{3/2} \rightarrow {}^4I_{13/2}$, $^2P_{3/2} \rightarrow {}^4I_{11/2}$ and $^2P_{1/2} \rightarrow {}^4I_{9/2}$. Such possible emission processes are schematized in Fig. 8.8. Definitely, the crystal field in NGO participates in optical emissions, mainly resulting in energy level and emission peak splitting, which is however not included in the schematic.

8.4 Summary

In summary, we studied PL properties of NGO single crystals and thin films. The UV (~360 and ~390 nm) and blue emissions (~420 nm) were observed in both NGO single crystals and thin films. The PL emission of NGO is significantly enhanced at low temperatures and the high temperature activation energy was found to be 35 meV. It was found that the crystallinity of NGO is essential for sharp emissions by virtue of Stark splitting. The observed UV and blue emissions can be understood based on the energy level diagram of the Nd^{3+} ion. Our observation is expected to open a path for NGO to be utilized as laser material or in photonic devices. In addition, the UV and blue emission in amorphous NGO films grown on commercial SiO_2/Si substrates is potential for large-scale photonic device applications.

Chapter 9 Conclusion and future work

9.1 Conclusion

Defects in oxides are extensively existent, which affect electrical, magnetic and optical properties significantly. In this thesis, we have investigated the effect of defects on electronic, magnetic and optical properties of oxides. Specifically, we have fabricated various oxide thin films and heterostructures by pulsed laser deposition. We started with detailed studies on oxygen vacancies in $SrTiO_3$. The metal-insulator transition was observed in $SrTiO_{3-x}$ films and was found to be induced by the carrier freeze-out effect. In addition, the reversible room-temperature ferromagnetism was observed in Nb-doped $SrTiO_3$ single crystals, which was found to be induced by oxygen vacancies. These are important findings to clarify many pending issues in the conflicting reports of different properties of $SrTiO_3$-based oxides and heterostructures including the two-dimensional electron gas at the $LaAlO_3/SrTiO_3$ interface.

Moreover, the electronic and magnetic properties of $SrRuO_3$ thin films were systematically tuned by varying the thickness in $SrRuO_3/LaAlO_3$ superlattices. This study investigated to what extent in terms of thickness $SrRuO_3$ films can maintain its conductivity and ferromagnetism. The effect of disorder on the electronic and magnetic phases of ultrathin $SrRuO_3$ films was

intensively explored. It is rather important for practical applications as $SrRuO_3$ is typically used as bottom electrodes for oxide electronic devices and ferroelectric materials characterization.

Regarding the device applications, ReRAM devices were fabricated based on $LaAlO_3$ films. It was found that rich intragap defects in $LaAlO_3$ play a dominant role in its resistive switching performance, leading to reversible metal-insulator transition. A quasi-conduction band model consisting of those intragap defects was proposed to understand the electric-field-induced reversible metal-insulator transitions in metal/$LaAlO_3$/Nb-$SrTiO_3$ ReRAM devices.

Last but not least, room-temperature ultraviolet and blue emission in $NdGaO_3$ single crystals and thin films was found. The fact that similar emission can be obtained in poorly-crystallized $NdGaO_3$ films deposited on SiO_2/Si substrates provides the great possibility for $NdGaO_3$ to be used in large scale optoelectronic devices.

9.2 Future work

$SrTiO_3$ is the central platform for complex oxide heterostructure fabrications. If we can modulate the properties of $SrTiO_3$ itself by virtue of defects, the functions of $SrTiO_3$-based heterostructures could be significantly changed. Some novel phenomenon may appear. This is extremely worth trying in my future work, *i.e.*, tailoring $SrTiO_3$-based heterostructures by defects engineering in $SrTiO_3$.

In addition, the integration of oxides into Si is an essential approach to push oxide electronic devices into applications. Hereinto, $SrTiO_3$ will be again the “bridge” to connect Si with other oxide films and heterostructure. Therefore, epitaxial growth of $SrTiO_3$ on Si by a less-expensive technique such as pulsed laser deposition (compared with molecular beam epitaxy) becomes rather important. This is technically attractive, *i.e.*, oxide electronics on a Si chip – $SrTiO_3$ being the bridge.

Bibliography

[1] J. A. Bednorz and K. A. Müller, Possible high T_c superconductivity in the Ba-La-Cu-O System. *Zeitschrift Fur Physik B: Condensed Matter* **64**, 189 (1986).

[2] M. K. Wu, J. R. Ashburn, C. J. Torng, P. H. Hor, R. L. Meng, L. Gao, Z. J. Huang, Y. Q. Wang, and C. W. Chu, Superconductivity at 93 K in a new mixed-phase Y-Ba-Cu-O compound system at ambient pressure. *Phys. Rev. Lett.* **58**, 908 (1987).

[3] N. F. Mott, Metal-insulator transition. *Reviews of Modern Physics* **40**, 677 (1968).

[4] M. Imada, A. Fujimori, and Y. Tokura, Metal-insulator transitions. *Reviews of Modern Physics* **70**, 1039 (1998).

[5] R. von Helmolt, J. Wecker, B. Holzapfel, L. Schultz, and K. Samwer, Giant negative magnetoresistance in perovskitelike $La_{2/3}Ba_{1/3}MnO_x$ ferromagnetic films. *Phys. Rev. Lett.* **71**, 2331 (1993).

[6] S. Jin, T. H. Tiefel, M. Mccormack, R. A. Fastnacht, R. Ramesh, and L. H. Chen, Thousandfold change in resistivity films magnetoresistive. *Science* **264**, 413 (1994).

[7] S. Yunoki, J. Hu, A. Malvezzi, A. Moreo, N. Furukawa, and E. Dagotto, Phase Separation in electronic models for manganites. *Phys. Rev. Lett.* **80**, 845 (1998).

[8] M. Uehara, S. Mori, C. H. Chen, and S.-W. Cheong, Percolative phase separation underlies colossal magnetoresistance in mixed-valent manganites. *Nature* **399**, 560 (1999).

[9] Ariando, X. Wang, G. Baskaran, Z. Q. Liu, J. Huijben, J. B. Yi, A. Annadi, A. R. Barman, A. Rusydi, S. Dhar, Y. P. Feng, J. Ding, H. Hilgenkamp, and T. Venkatesan, Electronic phase separation at the $LaAlO_3/SrTiO_3$ interface. *Nature Communications* **2**, 188 (2011).

[10] A. Asamitsu, Y. Tomioka, and H. Kuwahara, Current switching of resistive states in magnetoresistive manganites. *Nature* **388**, 50 (1997).

[11] S. Q. Liu, N. J. Wu, and a. Ignatiev, Electric-pulse-induced reversible resistance change effect in magnetoresistive films. *Appl. Phys. Lett.* **76**, 2749 (2000).

[12] A. Sawa, Resistive switching in transition metal oxides. *Materials Today* **11**, 28 (2008).

[13] M. Dawber, K. M. Rabe, and J. F. Scott, Physics of thin-film ferroelectric oxides. *Reviews of Modern Physics* **77**, 1083 (2005).

[14] R. Ramesh and N. A. Spaldin, Multiferroics: progress and prospects in thin films. *Nature Materials* **6**, 21 (2007).

[15] C. Yoshida, K. Tsunoda, H. Noshiro, and Y. Sugiyama, High speed resistive switching in $Pt/TiO_2/TiN$ film for nonvolatile memory application. *Appl. Phys. Lett.* **91**, 223510 (2007).

[16] H. Y. Hwang, Y. Iwasa, M. Kawasaki, B. Keimer, N. Nagaosa, and Y. Tokura, Emergent phenomena at oxide interfaces. *Nature Materials* **11**, 103 (2012).

[17] A. Ohtomo and H. Y. Hwang, A high-mobility electron gas at the $LaAlO_3/SrTiO_3$ heterointerface. *Nature* **427**, 423 (2004).

[18] N. Nakagawa, H. Y. Hwang, and D. A. Müller, Why some interfaces cannot be sharp. *Nature Materials* **5**, 204 (2006).

[19] N. Reyren, S. Thiel, A. D. Caviglia, L. F. Kourkoutis, G. Hammerl, C. Richter, C. W. Schneider, T. Kopp, A.-S. Ruetschi, D. Jaccard, M. Gabay, D. A. Muller, J.-M. Triscone, and J. Mannhart, Supeconducting interfaces between insulating oxides. *Science* **317**, 1196 (2007).

[20] A. Brinkman, M. Huijben, M. van Zalk, J. Huijben, U. Zeitler, J. C. Maan, W. G. van der Wiel, G. Rijnders, D. H. A. Blank, and H. Hilgenkamp, Magnetic effects at the interface between non-magnetic oxides. *Nature Materials* **6**, 493 (2007).

[21] J. H. Haeni, P. Irvin, W. Chang, R. Uecker, P. Reiche, Y. L. Li, S. Choudhury, W. Tian, M. E. Hawley, B. Craigo, A. K. Tagantsen, X. Q. Pan, S. K. Streiffer, L. Q. Chen, S. W. Kirchoefer, J. Levy, and D. G. Schlom, Room-temperature ferroelectricity in strained $SrTiO_3$. *Nature* **430**, 758 (2004).

[22] P. Yu, W. Luo, D. Yi, J. X. Zhang, M. D. Rossell, C. Yang, L. You, G. Singh-bhalla, S. Y. Yang, Q. He, Q. M. Ramasse, R. Erni, L. W. Martin, Y. H. Chu, S. T. Pantelides, S. J. Pennycook, and R. Ramesh, Interface control of bulk ferroelectric polarization. *Proc. Natl. Acad. Sci. U. S. A.* **109**, 9710 (2012).

[23] D. Satapathy, M. Uribe-Laverde, I. Marozau, V. Malik, S. Das, T. Wagner, C. Marcelot, J. Stahn, S. Brück, A. Rühm, S. Macke, T. Tietze, E. Goering, A. Frañó, J. Kim, M. Wu, E. Benckiser, B. Keimer, A.

Devishvili, B. Toperverg, M. Merz, P. Nagel, S. Schuppler, and C. Bernhard, Magnetic proximity effect in $YBa_2Cu_3O_7/La_{2/3}Ca_{1/3}MnO_3$ and $YBa_2Cu_3O_7/LaMnO_{3+\delta}$ superlattices. *Phys. Rev. Lett.* **108**, 197201 (2012).

[24] I. N. Chan, D. C. Vier, J. Hasen, J. Guimpel, S. Schultz, and I. K. Schuller, Thicknes dependence of the superconducting transition temperature of YBCO. *Phys. Lett. A* **175**, 241 (1993).

[25] G. Logvenov, A. Gozar, and I. Bozovic, High-temperature superconductivity in a single copper-oxide plane. *Science* **326**, 699 (2009).

[26] E. Detemple, Q. M. Ramasse, W. Sigle, G. Cristiani, H.-U. Habermeier, E. Benckiser, A. V Boris, A. Frano, P. Wochner, M. Wu, B. Keimer, and P. A. van Aken, Polarity-driven nickel oxide precipitation in $LaNiO_3$-$LaAlO_3$ superlattices. *Appl. Phys. Lett.* **99**, 211903 (2011).

[27] J. L. Blok, X. Wan, G. Koster, D. H. A. Blank, and G. Rijnders, Epitaxial oxide growth on polar (111) surfaces. *Appl. Phys. Lett.* **99**, 151917 (2011).

[28] M. Huijben, G. Rijnders, D. H. a Blank, S. Bals, S. Van Aert, J. Verbeeck, G. Van Tendeloo, A. Brinkman, and H. Hilgenkamp, Electronically coupled complementary interfaces between perovskite band insulators. *Nat. Mater.* **5**, 556 (2006).

[29] S. Thiel, G. Hammerl, A. Schmehl, C. W. Schneider, and J. Mannhart, Tunable quasi–two-dimensional electron gases in oxide heterostructures. *Science* **313**, 1942 (2006).

[30] A. D. Caviglia, S. Gariglio, N. Reyren, D. Jaccard, T. Schneider, M. Gabay, S. Thiel, G. Hammerl, J. Mannhart, and J.-M. Triscone, Electric field control of the $LaAlO_3/SrTiO_3$ interface ground state. *Nature* **456**, 624 (2008).

[31] D. A. Dikin, M. Mehta, C. W. Bark, C. M. Folkman, C. B. Eom, and V. Chandrasekhar, Coexistence of superconductivity and ferromagnetism in two dimensions. *Phys. Rev. Lett.* **107**, 056802 (2011).

[32] L. Li, C. Richter, J. Mannhart, and R. C. Ashoori, Coexistence of magnetic order and two-dimensional superconductivity at $LaAlO_3/SrTiO_3$ interfaces. *Nature Physics* **7**, 762 (2011).

[33] J. A. Bert, B. Kalisky, C. Bell, M. Kim, Y. Hikita, H. Y. Hwang, and K. A. Moler, Direct imaging of the coexistence of ferromagnetism and superconductivity at the $LaAlO_3/SrTiO_3$ interface. *Nature Physics* **7**, 767 (2011).

[34] L. Li, C. Richter, S. Paetel, T. Kopp, J. Mannhart, and R. C. Ashoori, Very large capacitance enhancement in a two-dimensional electron system. *Science* **332**, 825 (2011).

[35] J. W. Park, D. F. Bogorin, C. Cen, D. A. Felker, Y. Zhang, C. T. Nelson, C. W. Bark, C. M. Folkman, X. Q. Pan, M. S. Rzchowski, J. Levy, and C. B. Eom, Creation of a two-dimensional electron gas at an oxide interface on silicon. *Nature Communications* **1**, 94 (2010).

[36] D. G. Schlom and J. Mannhart, Oxide electronics: Interface takes charge over Si. *Nature Materials* **10**, 168 (2011).

[37] Z. Popović, S. Satpathy, and R. Martin, Origin of the two-dimensional electron gas carrier density at the $LaAlO_3$ on $SrTiO_3$ Interface. *Phys. Rev. Lett.* **101**, 256801 (2008).

[38] R. Pentcheva and W. Pickett, Avoiding the polarization catastrophe in $LaAlO_3$ overlayers on $SrTiO_3$ (001) through polar distortion. *Phys. Rev. Lett.* **102**, 107602 (2009).

[39] P. R. Willmott, S. A. Pauli, R. Herger, C. M. Schleputz, D. Martoccia, B. D. Patterson, B. Delley, R. Clarke, D. Kumah, C. Cionca, and Y. Yacoby, Structural basis for the conducting interface between $LaAlO_3$ and $SrTiO_3$. *Phys. Rev. Lett.* **99155502**, (2007).

[40] A. Kalabukhov, R. Gunnarsson, J. Börjesson, E. Olsson, T. Claeson, and D. Winkler, Effect of oxygen vacancies in the $SrTiO_3$ substrate on the electrical properties of the $LaAlO_3/SrTiO_3$ interface. *Physical Review B* **75**, 121404 (2007).

[41] G. Herranz, M. Basletic, M. Bibes, C. Carre, E. Tafra, E. Jacquet, K. Bouzehouane, C. Deranlot, A. Barthe, A. Fert, A. Hamzic, J.-M. Broto, and A. Barthelemy, High mobility in $LaAlO_3/SrTiO_3$ heterostructures: origin, dimensionality, and perspectives. *Phys. Rev. Lett.* **98**, 216803 (2007).

[42] W. Siemons, G. Koster, H. Yamamoto, W. Harrison, G. Lucovsky, T. Geballe, D. Blank, and M. Beasley, Origin of charge density at $LaAlO_3$ on $SrTiO_3$ heterointerfaces: Possibility of intrinsic doping. *Phys. Rev. Lett.* **98**, 196802 (2007).

[43] J. N. Eckstein, Watch out for the lack of oxygen. *Nat. Mater.* **6**, 473 (2007).

[44] Z. Q. Liu, D. P. Leusink, X. Wang, W. M. Lü, K. Gopinadhan, A. Annadi, Y. L. Zhao, X. H. Huang, S. W. Zeng, Z. Huang, A. Srivastava, S. Dhar, T. Venkatesan, and Ariando, Metal-insulator transition in

$SrTiO_{3-x}$ thin films induced by frozen-out carriers. *Phys. Rev. Lett.* **107**, 146802 (2011).

[45] M. L. Reinle-Schmitt, C. Cancellieri, D. Li, D. Fontaine, M. Medarde, E. Pomjakushina, C. W. Schneider, S. Gariglio, P. Ghosez, J.-M. Triscone, and P. R. Willmott, Tunable conductivity threshold at polar oxide interfaces. *Nature Communications* **3**, 932 (2012).

[46] Z. Q. Liu, Z. Huang, W. M. Lü, K. Gopinadhan, X. Wang, A. Annadi, T. Venkatesan, and Ariando, Atomically flat interface between a single-terminated $LaAlO_3$ substrate and $SrTiO_3$ thin film is insulating. *AIP Advances* **2**, 12147 (2012).

[47] Y. Chen, N. Pryds, J. E. Kleibeuker, G. Koster, J. Sun, E. Stamate, B. Shen, G. Rijnders, and S. Linderoth, Metallic and insulating interfaces of amorphous $SrTiO_3$-based oxide heterostructures. *Nano Lett.* **11**, 3774 (2011).

[48] S. W. Lee, Y. Liu, J. Heo, and R. G. Gordon, Creation and control of two-dimensional electron gas using Al-based amorphous oxides/$SrTiO_3$ heterostructures grown by atomic layer deposition. *Nano Lett.* **12**, 4775 (2012).

[49] K. van Benthem , C. Elsässer, and R. H. French, Bulk electronic structure of $SrTiO_3$: Experiment and theory. *J. Appl. Phys.* **90**, 6156 (2001).

[50] K. A. Müller and H. Burkard, SrTiO3: An intrinsic quantum paraelectric below 4 K. *Physical Review B* **19**, 3593 (1979).

[51] Y. Du, M.-S. Zhang, J. Wu, L. Kang, S. Yang, P. Wu, and Z. Yin, Optical properties of $SrTiO_3$ thin films by pulsed laser deposition. *Applied Physics A: Materials Science & Processing* **76**, 1105 (2003).

[52] M. Kawasaki, K. Takahashi, T. Maeda, R. Tsuchiya, M. Shinohara, O. Ishiyama, T. Yonezawa, M. Yoshimoto, and H. Koinuma, Atomic control of the $SrTiO_3$ crystal surface. *Science* **266**, 1540 (1993).

[53] A. Kaestner, M. Volk, F. Ludwig, M. Schilling, and J. Menzel, $YBa_2Cu_3O_7$ Josephson junctions on $LaAlO_3$ bicrystals for terahertz-frequency applications. *Appl. Phys. Lett.* **77**, 3057 (2000).

[54] T. Ohnishi, K. Takahashi, M. Nakamura, M. Kawasaki, M. Yoshimoto, and H. Koinuma, A-site layer terminated perovskite substrate: $NdGaO_3$. *Appl. Phys. Lett.* **74**, 2531 (1999).

[55] S. Yamanaka, T. Maekawa, H. Muta, T. Matsuda, S. Kobayashi, and K. Kurosaki, Thermophysical properties of $SrHfO_3$ and $SrRuO_3$. *J. Solid State Chem.* **177**, 3484 (2004).

[56] A. H. Reshak, M. Piasecki, S. Auluck, I. V Kityk, R. Khenata, B. Andriyevsky, C. Cobet, N. Esser, a Majchrowski, M. Swirkowicz, R. Diduszko, and W. Szyrski, Effect of U on the electronic properties of neodymium gallate ($NdGaO_3$): theoretical and experimental studies. *The Journal of Physical Chemistry. B* **113**, 15237 (2009).

[57] F. Luis, M. D. Kuzmin, F. Bartolome, V. M. Orera, J. Bartolome, M. Artigas, and J. Rubin, Magnetic susceptibility of $NdGaO_3$ at low temperatures: A quasi-two-dimensional Ising behavior. *Physical Review B* **58**, 798 (1998).

[58] V. M. Orera, L. E. Trinklerz, R. I. Merinot, and A. Larreat, The optical properties of the Nd^{3+} ion in $NdGaO_3$ and $LaGaO_3$:Nd : temperature and concentration dependence. *Journal of Physics: Condensed Matter* **7**, 9657 (1995).

[59] O. Chaix-Pluchery, D. Sauer, and J. Kreisel, Temperature-dependent Raman scattering of $DyScO_3$ and $GdScO_3$ single crystals. *Journal of Physics. Condensed Matter* **22**, 165901 (2010).

[60] S. C. Tidrow, A. Tauber, W. D. Wilber, R. T. Lareau, C. D. Brandle, G. W. Berkstresser, A. J. V. Graitis, D. M. Potrepka, J. I. Budnick, and J. Z. Wu, New substrates for HTSC microwave devices. *IEEE Transactions on Appiled Superconductivity* **7**, 1766 (1997).

[61] B. C. Chakoumakos, D. G. Schlom, M. Urbanik, and J. Luine, Thermal expansion of $LaAlO_3$ and $(La,Sr)(Al,Ta)O_3$, substrate materials for superconducting thin-film device applications. *J. Appl. Phys.* **83**, 1979 (1998).

[62] J. E. Mazierska, M. V Jacob, D. O. Ledenyov, and J. Krupka, Loss tangent measurements of dielectric substrates from 15 K to 300 K with two resonators : investigation into accuracy issues. *Arxiv* **1210**, 2230 (2012).

[63] K. Shimamura, H. Tabata, H. Takeda, V. V. Kochurikhin, and T. Fukuda, Growth and characterization of $(La,Sr)(Al,Ta)O_3$ single crystals as substrates for GaN epitaxial growth. *J. Cryst. Growth* **194**, 209 (1998).

[64] H. Bo-Qing, W. Xiao-Ming, Z. Tang, Z. Zong-Yuan, W. Xing, and C. Xiao-Long, Transmittance and Refractive Index of the Lanthanum Strontium Aluminium Tantalum Oxide Crystal. *Chinese Physics Letters* **18**, 278 (2001).

[65] T. H. Maiman, Stimulated optical radiation in ruby. *Nature* **187**, 493 (1960).

[66] J. C. Miller, A brief history of laser ablation. *AIP Conference Proceedings* **288**, 619 (1993).

[67] H. M. Smith and A. F. Turner, Vacuum deposited thin films using a ruby laser. *Applied Optics* **4**, 147 (1965).

[68] J. T. Cheung and T. Magee, Recent progress on LADA growth of HgCdTe and CdTe epitaxial layers. *Journal of Vacuum Science & Technology A: Vacuum, Surfaces, and Films* **1**, 1604 (1983).

[69] D. Dijkkamp, T. Venkatesan, X. D. Wu, S. A. Shaheen, N. Jisrawi, Y. H. Min-Lee, W. L. McLean, and M. Croft, Preparation of Y-Ba-Cu oxide superconductor thin films using pulsed laser evaporation from high Tc bulk material. *Appl. Phys. Lett.* **51**, 619 (1987).

[70] T. Venkatesan, X. D. Wu, A. Inam, and J. B. Wachtman, Observation of two distinct components during pulsed laser deposition of high Tc superconducting films. *Appl. Phys. Lett.* **52**, 1193 (1988).

[71] Y. Zhang, H. Gu, and S. Iijima, Single-wall carbon nanotubes synthesized by laser ablation in a nitrogen atmosphere. *Appl. Phys. Lett.* **73**, 3827 (1998).

[72] D. B. Geohegan, A. A. Puretzky, and D. J. Rader, Gas-phase nanoparticle formation and transport during pulsed laser deposition of $Y_1Ba_2Cu_3O_{7-d}$. *Appl. Phys. Lett.* **74**, 3788 (1999).

[73] Q. Dai, J. Chen, L. Lu, J. Tang, and W. Wang, Pulsed laser deposition of CdSe Quantum dots on Zn_2SnO_4 nanowires and their photovoltaic applications. *Nano Letters* **12**, 4187 (2012).

[74] J. Choi, C. B. Eom, G. Rijnders, H. Rogalla, and D. H. A. Blank, Growth mode transition from layer by layer to step flow during the growth of heteroepitaxial $SrRuO_3$ on (001) $SrTiO_3$. *Appl. Phys. Lett.* **79**, 1447 (2001).

[75] E. E. Fullerton, I. K. Schuller, H. Vanderstraeten, and Y. Bruynseraede, Structural refinement of superlattices from x-ray diffraction. *Physical Review B* **45**, 9292 (1992).

[76] F. M. Smits, Measurement of sheet resistivities with the four-point probe. *The Bell System Technical Journal* **37**, 711 (1958).

[77] H. P. R. Frederikse, W. R. Hosler, and W. R. Thurber, Shubnikov-de Haas Effect in $SrTiO_3$. *Physical Review* **158**, (1967).

[78] H. P. R. Frederikse and W. R. Hosler, Galvanomagnetic effects in n-type indium antimonide. *Physical Review* **108**, 1136 (1957).

[79] A. Tsukazaki, A. Ohtomo, T. Kita, Y. Ohno, H. Ohno, and M. Kawasaki, Quantum Hall effect in polar oxide heterostructures. *Science* **315**, 1388 (2007).

[80] Y. B. Zhang, Y. W. Tan, H. L. Stormer, and P. Kim, Experimental observation of the quantum Hall effect and Berry's phase in graphene. *Nature* **438**, 201 (2005).

[81] P. N. Argyres and E. N. Adams, Logitudinal magnetoresistance in the quantum limit. *Physical Review* **104**, 900 (1956).

[82] S. Zhang, S. B. Ogale, W. Yu, X. Gao, T. Liu, S. Ghosh, G. P. Das, A. T. S. Wee, R. L. Greene, and T. Venkatesan, Electronic manifestation of cation-vacancy-induced magnetic moments in a transparent oxide semiconductor: Anatase Nb:TiO_2. *Advanced Materials* **21**, 2282 (2009).

[83] P. A. Stampe, H. P. Kunkel, Z. Wang, and G. Williams, Influence of spin-orbit coupling on the transport and magnetic properties of Co_3Pd_{97}. *Physical Review B* **52**, 335 (1995).

[84] J. O'Donnell, J. N. Eckstein, and M. S. Rzchowski, Temperature and magnetic field dependent transport anisotropies in $La_{0.7}Ca_{0.3}MnO_3$ films. *Appl. Phys. Lett.* **76**, 218 (2000).

[85] K. Binder and A. P. Young, Spin glasses: Experimental facts, theoretical concepts, and open questions. *Reviews of Modern Physics* **58**, 801 (1986).

[86] I. J. Ferrer, D. M. Nevskaia, C. de las Heras, and C. Sanchez, About the band gap nature of FeS_2 as determined from optical and photo-electrochemical measurements. *Solid State Commun.* **74**, 913 (1990).

[87] D. Kan, T. Terashima, R. Kanda, A. Masuno, K. Tanaka, S. Chu, H. Kan, A. Ishizumi, Y. Kanemitsu, Y. Shimakawa, and M. Takano, Blue-light emission at room temperature from Ar+-irradiated $SrTiO_3$. *Nat. Mater.* **4**, 816 (2005).

[88] H. P. R. Frederikse, W. R. Thurber, and W. R. Hosler, Electron transport in strontium titanate. *Physical Review* **134**, A442 (1964).

[89] O. N. Tufte and P. W. Chapman, Electron mobility in semiconducting strontium titanate. *Physical Review* **155**, 796 (1967).

[90] J. F. Schooley, W. R. Hosler, and M. L. Cohen, Superconductivity in semiconducting $SrTiO_3$. *Phys. Rev. Lett.* **12**, 474 (1964).

[91] R . B . Dingle, Scattering of electrons and holes by charged donors and acceptors in semiconductors. *Philos. Mag.* **46**, 831 (1955).

[92] W. S. Baer, Free-carrier absorption in reduced $SrTiO_3$. *Physical Review* **144**, 734 (1966).

[93] S. Nuclear, Temperature dependence of mobility in heavily doped n-type PbTe layres grown by LPE. *Physics Letters* **98A**, 451 (1983).

[94] S. Ikeda, M. N. Ohara, T. Fujita, A. P. Mackenzie, N. E. Hussey, J. G. Bednorz, and F. Lichtenberg, Two-dimensional Fermi liquid behavior of the superconductor Sr_2RuO_4. *J. Phys. Soc. Jpn.* **66**, 1405 (1997).

[95] Y. Yafet, R. W. Keyes, and E. N. Adams, Hydrogen atom in a strong magnetic field. *J. Phys. Chem. Solids* **1**, 137 (1956).

[96] Y. Kozuka, T. Susaki, and H. Hwang, Vanishing Hall coefficient in the extreme quantum limit in photocarrier-doped $SrTiO_3$. *Phys. Rev. Lett.* **101**, 96601 (2008).

[97] L. M. Falicov and H. Smith, Linear magnetoresistance and anisotropic quantum fluctuations. *Phys. Rev. Lett.* **29**, 124 (1972).

[98] A. A. Abrikosov, Quantum linear magnetoresistance. *Europhys. Lett.* **49**, 789 (2000).

[99] R. T. Bate, R. K. Willardson, and A. C. Beer, Transverse magnetoresistance and Hall effect in *n*-type InSb. *J. Phys. Chem. Solids* **9**, 119 (1959).

[100] W. R. Branford, A. Husmann, S. A. Solin, S. K. Clowes, T. Zhang, Y. V Bugoslavsky, and L. F. Cohen, Geometric manipulation of the high-field linear magnetoresistance in InSb epilayers on GaAs (001). *Appl. Phys. Lett.* **86**, 202116 (2005).

[101] J. Hu and T. F. Rosenbaum, Classical and quantum routes to linear magnetoresistance. *Nat. Mater.* **7**, 697 (2008).

[102] J. W. Mcclure and W. J. Spry, Linear magnetoresistance in he quantum limit in graphite. *Physical Review* **165**, 809 (1968).

[103] P. B. L. R. Xu, A. Husmann, T. F. Rosenbaum, M.-L. Saboung, J. E. Enderby, Large magnetoresistance in non-magnetic silver chalcogenides. *Nature* **390**, 57 (1997).

[104] A. A. Abrikosov, Quantum magnetoresistance. *Physical Review B* **58**, 2788 (1998).

[105] K. Szot, W. Speier, R. Carius, U. Zastrow, and W. Beyer, Localized Metallic Conductivity and Self-Healing during Thermal Reduction of $SrTiO_3$. *Phys. Rev. Lett.* **88**, 75508 (2002).

[106] D. Cuong, B. Lee, K. Choi, H.-S. Ahn, S. Han, and J. Lee, Oxygen Vacancy Clustering and Electron Localization in Oxygen-Deficient $SrTiO_3$: LDA+U Study. *Phys. Rev. Lett.* **98**, 115503 (2007).

[107] D. A. Muller, N. Nakagawa, A. Ohtomo, J. L. Grazul, and H. Y. Hwang, Atomic-scale imaging of nanoengineered oxygen vacancy profiles in $SrTiO_3$. *Nature* **430**, 657 (2004).

[108] A. F. Santander-Syro, O. Copie, T. Kondo, F. Fortuna, S. Pailhès, R. Weht, X. G. Qiu, F. Bertran, A. Nicolaou, A. Taleb-Ibrahimi, P. Le Fèvre, G. Herranz, M. Bibes, N. Reyren, Y. Apertet, P. Lecoeur, A. Barthélémy, and M. J. Rozenberg, Two-dimensional electron gas with universal subbands at the surface of $SrTiO_3$. *Nature* **469**, 189 (2011).

[109] W. Meevasana, P. D. C. King, R. H. He, S. Mo, M. Hashimoto, A. Tamai, P. Songsiriritthigul, F. Baumberger, and Z. Shen, Creation and control of a two-dimensional electron liquid at the bare $SrTiO_3$ surface. *Nat. Mater.* **10**, 114 (2011).

[110] A. Ohtomo, D. A. Muller, J. L. Grazul, and H. Y. Hwang, Artificial charge-modulationin atomic-scale perovskite titanate superlattices. *Nature* **419**, 378 (2002).

[111] J. M. Rondinelli, M. Stengel, and N. A. Spaldin, Carrier-mediated magnetoelectricity in complex oxide heterostructures. *Nature Nanotechnology* **3**, 46 (2008).

[112] J. F. Schooley, W. R. Hosier, E. Ambler, J. H. Becker, M. L. Cohen, and C. S. Koonce, Dependence of the supercondcucting transition temperature on carrier concentration in semiconducting $SrTiO_3$. *Phys. Rev. Lett.* **14**, 305 (1965).

[113] C. S. Koonce, M. L. Cohen, J. F. Schooley, W. R. Hosler, and E. R. Preiffer, Superconducting transition temperatures of semiconducting $SrTiO_3$. *Physical Review* **163**, 380 (1967).

[114] A. E. Paladino, L. G. Rubin, and J. S. Waugh, Oxygen ion diffusion in single crystal $SrTiO_3$. *J. Phys. Chem. Solids* **26**, 391 (1964).

[115] C. Herring, Effect of random inhomogeneities on electrical and galvanomagnetic measurements. *J. Appl. Phys.* **31**, 1939 (1960).

[116] H. Fujisada, S. Kataoka, and A. C. Beer, Electric field dependence of galvanomagnetic properties in *n*-type Insb at 77 K. *Physical Review B* **3**, 3249 (1971).

[117] A. Dejneka, M. Tyunina, J. Narkilahti, J. Levoska, D. Chvostova, L. Jastrabik, and V. A. Trepakov, Tensile strain induced changes in the optical spectra of $SrTiO_3$. *Phys. Solid State* **52**, 2082 (2010).

[118] T. C. Harman, H. L. Goering, and A. C. Beer, Electrical properties of *n*-type InAs. *Physical Review* **104**, 1562 (1956).

[119] Z. Q. Liu, W. M. Lü, X. Wang, Z. Huang, A. Annadi, S. W. Zeng, T. Venkatesan, and Ariando, Magnetic-field induced resistivity minimum with in-plane linear magnetoresistance of the Fermi liquid in $SrTiO_{3-x}$ single crystals. *Physical Review B* **85**, 155114 (2012).

[120] C. Yu, M. L. Scullin, M. Huijben, and R. Ramesh, Thermal conductivity reduction in oxygen-deficient strontium titanates. *Appl. Phys. Lett.* **92**, 191911 (2008).

[121] K. Nomura, S. Okami, X. Xie, M. Mizuno, K. Fukunaga, and Y. Ohki, Effect of annealing on optical absorption of $LaAlO_3$ at terahertz frequencies. *Japanese Journal of Applied Physics* **50**, 21502 (2011).

[122] X. Luo, B. Wang, and Y. Zheng, First-principles study on energetics of intrinsic point defects in $LaAlO_3$. *Physical Review B* **80**, 104115 (2009).

[123] J. Yao, P. B. Merrill, S. S. Perry, D. Marton, and J. W. Rabalais, Thermal stimulation of the surface termination of $LaAlO_3${100}. *J. Chem. Phys.* **108**, 1645 (1998).

[124] Z. L. Wang and A. J. Shapiro, Studies of LaA103{100} surfaces using RHEED and REM II : 5 X 5 surface reconstruction. *Surf. Sci.* **328**, 159 (1995).

[125] P. W. Tasker, The stability of ionic crystal surfaces. *Journal of Physics C: Solid State Physics* **12**, 4977 (1979).

[126] J. Jacobs, M. Angel, S. Miguel, J. E. Sfinchez, and L. J. Alvarez, On the origin of the reconstruction of $LaA1O_3${100} surfaces. *Surf. Sci.* **389**, L1147 (1997).

[127] R. E. Watson and J. W. Davenport, Ionic-charge modification at the surface of polar crystals. *Physical Review B* **27**, 6418 (1983).

[128] D. B. Holt, Surface polarity and symmetry in semiconducting compounds. *J. Mater. Sci.* **23**, 1131 (1988).

[129] M. Breitschaft, V. Tinkl, N. Pavlenko, S. Paetel, C. Richter, J. R. Kirtley, Y. C. Liao, G. Hammerl, V. Eyert, T. Kopp, and J. Mannhart, Two-dimensional electron liquid state at $LaAlO_3$-$SrTiO_3$ interfaces. *Physical Review B* **81**, 153414 (2010).

[130] J. A. Bert, B. Kalisky, C. Bell, M. Kim, Y. Hikita, H. Y. Hwang, and K. A. Moler, Direct imaging of the coexistence of ferromagnetism and superconductivity at the $LaAlO_3/SrTiO_3$ interface. *Nature Physics* **7**, 767 (2011).

[131] K. Michaeli, A. C. Potter, and P. a. Lee, Superconducting and ferromagnetic phases in $SrTiO_3/LaAlO_3$ oxide interface structures: possibility of finite momentum pairing. *Phys. Rev. Lett.* **108**, 117003 (2012).

[132] K. Shibuya, T. Ohnishi, M. Lippmaa, and M. Oshima, Metallic conductivity at the $CaHfO_3/SrTiO_3$ interface. *Appl. Phys. Lett.* **91**, 232106 (2007).

[133] J. Son, P. Moetakef, B. Jalan, O. Bierwagen, N. J. Wright, R. Engel-Herbert, and S. Stemmer, Epitaxial $SrTiO_3$ films with electron mobilities exceeding 30,000 cm2V-1s-1. *Nature Materials* **9**, 482 (2010).

[134] C. W. Bark, D. a. Felker, Y. Wang, Y. Zhang, H. W. Jang, C. M. Folkman, J. W. Park, S. H. Baek, H. Zhou, D. D. Fong, X. Q. Pan, E. Y. Tsymbal, M. S. Rzchowski, and C. B. Eom, Tailoring a two-dimensional electron gas at the $LaAlO_3/SrTiO_3$ (001) interface by epitaxial strain. *Proceedings of the National Academy of Sciences* **108**, 4720 (2011).

[135] J. Delahaye and T. Grenet, Metallicity of the $SrTiO_3$ surface induced by room temperature evaporation of alumina. *J. Phys. D: Appl. Phys.* **45**, 315301 (2012).

[136] J. Q. Chen, X. Wang, Y. H. Lu, A. Roy Barman, G. J. You, G. C. Xing, T. C. Sum, S. Dhar, Y. P. Feng, Q.-H. Xu, and T. Venkatesan, Defect dynamics and spectral observation of twinning in single crystalline $LaAlO_3$ under subbandgap excitation. *Appl. Phys. Lett.* **98**, 41904 (2011).

[137] M. Ben Shalom, C. Tai, Y. Lereah, M. Sachs, E. Levy, D. Rakhmilevitch, A. Palevski, and Y. Dagan, Anisotropic magnetotransport at the $SrTiO_3/LaAlO_3$ interface. *Physical Review B* **80**, 140403(R) (2009).

[138] M. Lee, J. R. Williams, S. Zhang, C. D. Frisbie, and D. Goldhaber-Gordon, Electrolyte gate-controlled Kondo effect in $SrTiO_3$. *Phys. Rev. Lett.* **107**, 256601 (2011).

[139] N. Pavlenko, T. Kopp, E. Y. Tsymbal, J. Mannhart, and G. A. Sawatzky, Oxygen vacancies at titanate interfaces : Two-dimensional magnetism and orbital reconstruction. *Physical Review B* **86**, 064431 (2012).

[140] J. Kondo, Resistance minimum in dilute magnetic alloys. *Progress of Theoretical Physics* **32**, 37 (1964).

[141] A. D. Caviglia, M. Gabay, S. Gariglio, N. Reyren, C. Cancellieri, and J. Triscone, Tunable Rashba Spin-orbit interaction at oxide interfaces. *Phys. Rev. Lett.* **104**, 126803 (2010).

[142] C. T. Campbell, Ultrathin metal films and particles on oxide surfaces: structural, electronic and chemisorptive properties. *Surf. Sci. Rep.* **27**, 1 (1997).

[143] P. Calvani, M. Capizzi, F. Donato, S. Lupi, P. Maselli, and D. Peschiaroli, Observation of a midinfrared band in $SrTiO_{3-y}$. *Physical Review B* **47**, 8971 (1993).

[144] S. Na-Phattalung, M. Smith, K. Kim, M.-H. Du, S.-H. Wei, S. Zhang, and S. Limpijumnong, First-principles study of native defects in anatase TiO_2. *Physical Review B* **73**, 125205 (2006).

[145] S. Gariglio, N. Reyren, A. D. Caviglia, and J.-M. Triscone, Superconductivity at the $LaAlO_3/SrTiO_3$ interface. *Journal of Physics: Condensed Matter* **21**, 164213 (2009).

[146] G. Singh-Bhalla, C. Bell, J. Ravichandran, W. Siemons, Y. Hikita, S. Salahuddin, A. F. Hebard, H. Y. Hwang, and R. Ramesh, Built-in and induced polarization across $LaAlO_3/SrTiO_3$ heterojunctions. *Nature Physics* **7**, 80 (2010).

[147] B. Huang, Y. Chiu, P. Huang, W. Wang, V. T. Tra, J. C. Yang, Q. He, J. Y. Lin, C. S. Chang, and Y. H. Chu, Mapping band alignment across complex oxide heterointerfaces. *Phys. Rev. Lett.* **109**, 246807 (2012).

[148] H. M. Chan, M. P. Harmer, and D. M. Smyth, Compensating defects in highly donor-doped $BaTiO_3$. *J. Am. Ceram. Soc.* **69**, 507 (1986).

[149] M. Ahrens, R. Merkle, B. Rahmati, and J. Maier, Effective masses of electrons in *n*-type $SrTiO_3$ determined from low-temperature specific heat capacities. *Physica B: Condensed Matter* **393**, 239 (2007).

[150] H. Ohno, Making Nonmagnetic Semiconductors Ferromagnetic. *Science* **281**, 951 (1998).

[151] G. A. Prinz, Magnetoelectronics. *Science* **282**, 1660 (1998).

[152] T. Dietl, H. Ohno, F. Matsukura, J. Cibert, and D. Ferrand, Zener model description of ferromagnetism in zinc-blende magnetic semiconductors. *Science* **287**, 1019 (2000).

[153] Y. Matsumoto, M. Murakami, T. Shono, T. Hasegawa, T. Fukumura, M. Kawasaki, P. Ahmet, T. Chikyow, S. Koshihara, and H. Koinuma, Room-temperature ferromagnetism in transparent transition metal-doped titanium dioxide. *Science* **291**, 854 (2001).

[154] S. Ogale, R. Choudhary, J. Buban, S. Lofland, S. Shinde, S. Kale, V. Kulkarni, J. Higgins, C. Lanci, J. Simpson, N. Browning, S. Das Sarma, H. Drew, R. Greene, and T. Venkatesan, High temperature ferromagnetism with a giant magnetic moment in transparent Co-doped $SnO_{2-\delta}$. *Phys. Rev. Lett.* **91**, 77205 (2003).

[155] J. He, S. Xu, Y. K. Yoo, Q. Xue, H.-C. Lee, S. Cheng, X.-D. Xiang, G. F. Dionne, and I. Takeuchi, Room temperature ferromagnetic n-type semiconductor in $(In_{1-x}Fe_x)_2O_{3-\sigma}$. *Appl. Phys. Lett.* **86**, 52503 (2005).

[156] J. M. D. C. M. Venkatesan, C. B. Fitzgerald, Unexpected magnetism in a dielectric oxide. *Nature* **430**, 630 (2004).

[157] S. D. Yoon, Y. Chen, A. Yang, T. L. Goodrich, X. Zuo, D. a Arena, K. Ziemer, C. Vittoria, and V. G. Harris, Oxygen-defect-induced magnetism to 880 K in semiconducting anatase $TiO_{2-\delta}$ films. *J. Phys.: Condens. Matter* **18**, L355 (2006).

[158] N. Hong, J. Sakai, N. Poirot, and V. Brizé, Room-temperature ferromagnetism observed in undoped semiconducting and insulating oxide thin films. *Physical Review B* **73**, 132404 (2006).

[159] N. H. Hong, J. Sakai, and V. Briz, Observation of ferromagnetism at room temperature in ZnO thin films. *Journal of Physics. Condensed Matter* **036219**, (2007).

[160] N. H. Hong, N. Poirot, and J. Sakai, Ferromagnetism observed in pristine SnO2 thin films. *Physical Review B* **77**, 33205 (2008).

[161] G. Binnig, A. Baratoff, H. E. Hoenig, and J. G. Bednorz, Two-band superconductivity in Nb-doped $SrTiO_3$. *Phys. Rev. Lett.* **45**, 1352 (1980).

[162] O. Cedex, A. Barato, J. G. Bednorz, and G. Binnig, Temperature dependence of plasmons in Nb-doped $SrTiO_3$. *Physical Review B* **47**, 8187 (1993).

[163] J. L. M. van Mechelen, D. van der Marel, C. Grimaldi, A. Kuzmenko, N. Armitage, N. Reyren, H. Hagemann, and I. Mazin, Electron-phonon interaction and charge carrier mass enhancement in $SrTiO_3$. *Phys. Rev. Lett.* **100**, 226403 (2008).

[164] D. P. Young, D. Hall, M. E. Torelli, Z. Fisk, J. L. Sarrao, J. D. Thompson, H.-R. Ott, S. B. Oseroff, R. G. Goodrich, and R. Zysler, High-temperature weak ferromagnetism in a low-density free-electron gas. *Nature* **397**, 412 (1999).

[165] T. Dietl, H. Ohno, and F. Matsukura, Hole-mediated ferromagnetism in tetrahedrally coordinated semiconductors. *Physical Review B* **63**, 195205 (2001).

[166] S. Das Sarma, E. Hwang, and J. D. J. Priour, Enhancing Tc in ferromagnetic semiconductors. *Physical Review B* **70**, 161203(R) (2004).

[167] S. X. Zhang, S. B. Ogale, D. C. Kundaliya, L. F. Fu, N. D. Browning, S. Dhar, W. Ramadan, J. S. Higgins, R. L. Greene, and T. Venkatesan, Search for ferromagnetism in conductive Nb:$SrTiO_3$ with magnetic transition element (Cr, Co, Fe, Mn) dopants. *Appl. Phys. Lett.* **89**, 12501 (2006).

[168] T. W. Hickmott, Low-frequency negative resistance in thin anodic oxide films. *J. Appl. Phys.* **33**, 2669 (1962).

[169] a. Beck, J. G. Bednorz, C. Gerber, C. Rossel, and D. Widmer, Reproducible switching effect in thin oxide films for memory applications. *Appl. Phys. Lett.* **77**, 139 (2000).

[170] Y. Watanabe, J. G. Bednorz, A. Bietsch, C. Gerber, D. Widmer, A. Beck, and S. J. Wind, Current-driven insulator–conductor transition and nonvolatile memory in chromium-doped $SrTiO_3$ single crystals. *Appl. Phys. Lett.* **78**, 3738 (2001).

[171] T. Fujii, M. Kawasaki, A. Sawa, H. Akoh, Y. Kawazoe, and Y. Tokura, Hysteretic current–voltage characteristics and resistance switching at an epitaxial oxide Schottky junction $SrRuO_3/SrTi_{0.99}Nb_{0.01}O_3$. *Appl. Phys. Lett.* **86**, 12107 (2005).

[172] R. Oligschlaeger, R. Waser, R. Meyer, S. Karthäuser, and R. Dittmann, Resistive switching and data reliability of epitaxial $(Ba,Sr)TiO_3$ thin films. *Appl. Phys. Lett.* **88**, 42901 (2006).

[173] M. Rozenberg, I. Inoue, and M. Sánchez, Nonvolatile memory with multilevel switching: A basic model. *Phys. Rev. Lett.* **92**, 1 (2004).

[174] C. Rossel, G. I. Meijer, D. Brémaud, and D. Widmer, Electrical current distribution across a metal–insulator–metal structure during bistable switching. *J. Appl. Phys.* **90**, 2892 (2001).

[175] D.-H. Kwon, K. M. Kim, J. H. Jang, J. M. Jeon, M. H. Lee, G. H. Kim, X.-S. Li, G.-S. Park, B. Lee, S. Han, M. Kim, and C. S. Hwang, Atomic structure of conducting nanofilaments in TiO_2 resistive switching memory. *Nature Nanotechnology* **5**, 148 (2010).

[176] R. Waser and M. Aono, Nanoionics-based resistive switching memories. *Nat. Mater.* **6**, 833 (2007).

[177] R. Meyer, J. R. Contreras, A. Petraru, and H. Kohlstedt, On a novel ferro resistive random access memory (FRRAM): basic model and first experiments. *Integrated Ferroelectrics* **64**, 77 (2004).

[178] P. Limelette, A. Georges, D. Jérome, P. Wzietek, P. Metcalf, and J. M. Honig, Universality and critical behavior at the Mott transition. *Science* **302**, 89 (2003).

[179] H. Kuwahara, Y. Tomioka, A. Asamitsu, Y. Moritomo, and Y. Tokura, A first-order phase transition induced by a magnetic field. *Science* **270**, 961 (1995).

[180] S. Shamoto, H. Tazawa, Y. Ono, T. Nakano, Y. Nozue, and T. Kajitani, Light-induced metal–insulator transition in $Lu_2V_2O_7$. *J. Phys. Chem. Solids* **62**, 325 (2001).

[181] T. Oka and N. Nagaosa, Interfaces of Correlated Electron Systems : Proposed Mechanism for Colossal Electroresistance Hubburd model. *Phys. Rev. Lett.* **95**, 266403 (2005).

[182] M. J. Rozenberg, I. H. Inoue, and M . J. Sánchez, Strong electron correlation effects in nonvolatile electronic memory devices. *Appl. Phys. Lett.* **88**, 033510 (2006).

[183] B. R. Waser, R. Dittmann, G. Staikov, and K. Szot, Redox-Based Resistive Switching Memories – Nanoionic Mechanisms , Prospects , and Challenges. *Advanced Materials* **21**, 2632 (2009).

[184] D. Muñoz Ramo, A. Shluger, J. Gavartin, and G. Bersuker, Theoretical prediction of intrinsic self-trapping of electrons and holes in monoclinic HfO2. *Phys. Rev. Lett.* **99**, 1 (2007).

[185] M. Janousch, G. I. Meijer, U. Staub, B. Delley, S. F. Karg, and B. P. Andreasson, Role of oxygen vacancies in Cr-Doped $SrTiO_3$ for resistance-change memory. *Advanced Materials* **19**, 2232 (2007).

[186] J. P. Shi, Y. G. Zhao, H. J. Zhang, H. F. Tian, and X. P. Zhang, Oxygen electromigration induced nonvolatile resistance switching at Ag/La_2CuO_{4+x} interface. *Appl. Phys. Lett.* **94**, 192103 (2009).

[187] J. Mannhart, D. H. A. Blank, H. Y. Hwang, A. J. Millis, and J.-M. Triscone, Two-dimensional electron gases at oxide interfaces. *MRS Bulletin* **33**, 1027 (2008).

[188] Z. Q. Liu, D. P. Leusink, W. M. Lü, X. Wang, X. P. Yang, K. Gopinadhan, Y. T. Lin, A. Annadi, Y. L. Zhao, a. R. Barman, S. Dhar, Y. P. Feng, H. B. Su, G. Xiong, T. Venkatesan, and Ariando, Reversible metal-insulator transition in $LaAlO_3$ thin films mediated by intragap defects: An alternative mechanism for resistive switching. *Physical Review B* **84**, 165106 (2011).

[189] L. Antognazza, K. Char, T. H. Geballe, L. L. H. King, and a. W. Sleight, Josephson coupling of $YBa_2Cu_3O_{7-x}$ through a ferromagnetic barrier SrRuO3. *Appl. Phys. Lett.* **63**, 1005 (1993).

[190] D. Darminto, H. Smilde, V. Leca, D. Blank, H. Rogalla, and H. Hilgenkamp, Phase-Sensitive Order Parameter Symmetry Test Experiments Utilizing $Nd_{2-x}Ce_xCuO_{4-y}$/Nb Zigzag Junctions. *Phys. Rev. Lett.* **94**, 2 (2005).

[191] M. Minohara, I. Ohkubo, H. Kumigashira, and M. Oshima, Band diagrams of spin tunneling junctions $La_{0.6}Sr_{0.4}MnO_3/Nb:SrTiO_3$ and $SrRuO_3/Nb:SrTiO_3$ determined by in situ photoemission spectroscopy. *Appl. Phys. Lett.* **90**, 132123 (2007).

[192] G. Koster, L. Klein, W. Siemons, G. Rijnders, J. S. Dodge, C.-B. Eom, D. H. A. Blank, and M. R. Beasley, Structure, physical properties, and applications of SrRuO3 thin films. *Reviews of Modern Physics* **84**, 253 (2012).

[193] K. Takahashi, a. Sawa, Y. Ishii, H. Akoh, M. Kawasaki, and Y. Tokura, Inverse tunnel magnetoresistance in all-perovskite junctions of $La_{0.7}Sr_{0.3}MnO_3/SrTiO_3/SrRuO_3$. *Physical Review B* **67**, 2 (2003).

[194] C. H. Ahn, R. H. Hammond, T. H. Geballe, M. R. Beasley, J.-M. Triscone, M. Decroux, O. Fischer, L. Antognazza, and K. Char, Ferroelectric field effect in ultrathin $SrRuO_3$ films. *Appl. Phys. Lett.* **70**, 206 (1997).

[195] D. Toyota, I. Ohkubo, H. Kumigashira, M. Oshima, T. Ohnishi, M. Lippmaa, M. Takizawa, A. Fujimori, K. Ono, M. Kawasaki, and H. Koinuma, Thickness-dependent electronic structure of ultrathin $SrRuO_3$ films studied by in situ photoemission spectroscopy. *Appl. Phys. Lett.* **87**, 162508 (2005).

[196] J. Xia, W. Siemons, G. Koster, M. Beasley, and a. Kapitulnik, Critical thickness for itinerant ferromagnetism in ultrathin films of $SrRuO_3$. *Physical Review B* **79**, 2 (2009).

[197] M. Verissimo-Alves, P. García-Fernández, D. I. Bilc, P. Ghosez, and J. Junquera, Highly confined spin-polarized two-dimensional electron gas in $SrTiO_3$/$SrRuO_3$ superlattices. *Phys. Rev. Lett.* **108**, 107003 (2012).

[198] A. V Boris, Y. Matiks, E. Benckiser, A. Frano, P. Popovich, V. Hinkov, P. Wochner, E. Detemple, V. K. Malik, C. Bernhard, T. Prokscha, A. Suter, Z. Salman, E. Morenzoni, G. Cristiani, H. Habermeier, and B. Keimer, Dimensionality control of electronic phase transitions in nickel-oxide superlattices. *Science* **332**, 937 (2011).

[199] P. Allen, H. Berger, O. Chauvet, L. Forro, T. Jarlborg, a Junod, B. Revaz, and G. Santi, Transport properties, thermodynamic properties, and electronic structure of $SrRuO_3$. *Physical Review. B, Condensed Matter* **53**, 4393 (1996).

[200] G. Cao, S. Mccall, M. Shepard, and J. E. Crow, Thermal , magnetic , and transport properties of single-crystal $Sr_{1-x}Cax RuO_3$. *Physical Review B* **56**, 321 (1997).

[201] A. P. Mackenzie, J. W. Reiner, A. W. Tyler, L. M. Galvin, S. R. Julian, M. R. Beasley, T. H. Geballe, and A. Kapitulnik, Observation of quantum oscillations in the electrical resistivity of $SrRuO_3$. *Physical Review B* **58**, 318 (1998).

[202] A. Ohtomo and H. Y. Hwang, Surface depletion in doped $SrTiO_3$ thin films. *Appl. Phys. Lett.* **84**, 1716 (2004).

[203] Q. Gan, R. A. Rao, C. B. Eom, L. Wu, and F. Tsui, Lattice distortion and uniaxial magnetic anisotropy in single domain epitaxial (110) films of $SrRuO_3$. *J. Appl. Phys.* **85**, 5297 (1999).

[204] M. Ziese, I. Vrejoiu, and D. Hesse, Structural symmetry and magnetocrystalline anisotropy of $SrRuO_3$ films on $SrTiO_3$. *Physical Review B* **81**, 184418 (2010).

[205] G. Herranz, B. Martínez, J. Fontcuberta, F. Sánchez, C. Ferrater, M. García-Cuenca, and M. Varela, Enhanced electron-electron correlations in nanometric $SrRuO_3$ epitaxial films. *Physical Review B* **67**, 1 (2003).

[206] C. B. Eom, R. J. Cava, R. M. Fleming, J. M. Philips, R. B. van Dover, J. H. Marshall, J. W. P. Hsu, J. J. Krajewski, and J. W. F. Peck, Single-crystal epitaxial thin films of the isotropic metallic oxides $Sr_{1-x}Ca_xRuO_3$ ($0<x<1$). *Science* **258**, 1766 (1992).

[207] P. Kostic, Y. Okada, N. Collins, Z. Schlesinger, J. Reiner, L. Klein, A. Kapitulnik, T. Geballe, and M. Beasley, Non-Fermi-liquid behavior of $SrRuO_3$: evidence from infrared conductivity. *Phys. Rev. Lett.* **81**, 2498 (1998).

[208] G. Bergmann, Consistent temperature and field dependence in weak localization. *Physical Review B* **28**, 515 (1983).

[209] L. a. Ponomarenko, a. K. Geim, a. a. Zhukov, R. Jalil, S. V. Morozov, K. S. Novoselov, I. V. Grigorieva, E. H. Hill, V. V. Cheianov, V. I. Fal'ko, K. Watanabe, T. Taniguchi, and R. V. Gorbachev, Tunable metal–insulator transition in double-layer graphene heterostructures. *Nature Physics* **7**, 958 (2011).

[210] L. Klein, J. S. Dodge, C. H. Ahn, J. W. Reiner, L. Mieville, T. H. Geballe, M. R. Beasley, and A. Kapitulnik, Transport and magnetization in the badly metallic itinerant ferromagnet $SrRuO_3$. *J. Phys.: Condens. Matter* **8**, 10111 (1996).

[211] R. Scherwitzl, S. Gariglio, M. Gabay, P. Zubko, M. Gibert, and J.-M. Triscone, Metal-Insulator Transition in Ultrathin $LaNiO_3$ Films. *Phys. Rev. Lett.* **106**, 246403 (2011).

[212] J. M. Phillips, Substrate selection for high-temperature superconducting thin films. *J. Appl. Phys.* **79**, 1829 (1996).

[213] A. S. Zubrilov, S. A. Nikishin, G. D. Kipshidze, V. V Kuryatkov, H. Temkin, T. I. Prokofyeva, and M. Holtz, Optical properties of GaN grown on Si (111) by gas source molecular beam epitaxy with ammonia. *J. Appl. Phys.* **91**, 1209 (2002).

[214] M. Karbowiak and N. M. Edelstein, Spectroscopic studies and dynamics of Nd^{3+} ions in RbY_2Cl_7 single crystals. *Chem. Phys.* **277**, 341 (2002).